The University Of Sheffield.

Improved Characterisation of the Cell Wall Mechanics of *Staphylococcus aureus* using Atomic Force Microscopy

By:

David Spencer Owen BSc (Hons)

(Sheffield Hallam University)

A thesis submitted in partial fulfilment of the requirements for the degree of Doctor of Philosophy

The University of Sheffield

Faculty of Science

Department of Physics & Astronomy

September 2018

Summary

The cell wall represents the major structural determinant of a bacterium. Its integrity and tightly coordinated growth are vital for the survival of a bacterium, and consequently many antibiotics target the cell wall proteins or other accessory polymers in an aid to disrupt these important processes. Despite the 80 year use of antibiotics, surprisingly, little is known about the bacterial cell wall. The precise mode of antibiotic-induced lysis of the cell and the molecular organisation of the structural components are still under debate.

The mechanical properties of the cell wall may lend us clues towards a better understanding of the life, and ultimately, death of a bacterium. Elasticity represents a biophysical property of a cell that can influence, and be influenced by its environment. Plant, animal and bacterial cells all display a changing elasticity during normal and abnormal physiologies. However, the methods available to measure these properties are varied, and the reported values display orders of magnitude disparity, even for the same cell type, and when gathered using the same techniques, equipment and methodologies.

Immobilisation of microbial cells presents a technical challenge and has often proven to be a problematic step in the imaging of samples under aqueous conditions. The immobilisation must be enough to constrain the bacterium, but not impose a stress that may alter the physiological and nanomechanical properties of the cell.

This study has investigated the mechanical properties of the model bacterium *Staphylococcus aureus*, using atomic force microscopy (AFM). A range of substrates were tested for their abilities to immobilise, yet confer normal growth of the cell. The silicone elastomer, polydimethysiloxane (PDMS) was extensively studied and characterised, and used as a calibrant when analysing mechanical data. The elasticity and stiffness of the cell wall were evaluated from living cells and from extracted cell wall sacculi, and compared in their native states, and following antibiotic challenge. We have developed a model that more accurately defines the geometry of an indenting probe to report elasticity values that are considerably lower than many reported in the literature. We have shown – for the first time, the molecular architecture of PDMS and true unperturbed growth, division and death of a bacterium, obtaining the mechanical changes throughout these events.

Acknowledgements

I am extremely grateful to my supervisors Professor Jamie Hobbs and Professor Simon Foster for giving me the opportunity to undertake this PhD and for their help, good nature and support throughout. I would also thank the University of Sheffield and the Imagine: Imaging Life and 2022 Futures for funding my PhD.

Many thanks to my colleagues in the department of Physics and the department of MBB for their friendship, help, support and advice. Thanks to Laia Pasquina Lemonche for preparing the extracted cell wall sacculi, and Viral Panchal for putting bacterial overnights on for me, whilst I wrote this thesis. My initial AFM training was provided by Dr Richard Bailey and Dr Jonathan Burns and for that I should remain eternally grateful. Extra special thanks to Jonny for making the 2.5 μm silicon wafer that failed in your experiments, but ultimately gave me the successful growth and division that had eluded me for over three years!

Thanks also to Dr Kenneth Kennedy and Saurabh Kumar at the Kroto Research Institute for their assistance in the design and fabrication of the etched silicon wafers and Saurabh for the very useful SEM and photolithography sessions. Many thanks to Chris Hill at the Faculty of Science Electron Microscopy Unit for his assistance and training with SEM, TEM and microtomed-sections. My gratitude to Dr Chris Holland at the Department of Materials Science and Engineering for his assistance with the tensile testing of the PDMS substrate, and Dawn Bussey for her assistance with nanoindentation of the PDMS substrate. All the confocal microscopy was performed at the Wolfson Light Microscopy Facility and I thank Dr Darren Robinson for his assistance with these experiments.

I would like to thank the staff and students of the Imagine cohort, both past and present, for their friendship throughout this study, and for their joint efforts with the organisation of the annual Imagine symposia.

Finally I would like to dedicate this work to my friends, family, extended family and Katy, which have offered their continual support and encouragement throughout my whole belated University journey.

Abbreviations

3D	Three dimensional
°	Angular degree
° C	Degree Celsius
Å	Ångstrom
AFM	Atomic force microscopy / Atomic force microscope
β	Beta
BHI	Brain heart infusion
cfu	Colony forming units
DMT	Derjaguin-Muller-Toporov
DNA	Deoxyribonucleic acid
dH_2O	Deionised water
E	Young's (elastic) modulus
ECM	Extracellular matrix
EM	Electron microscopy
EPS	Extracellular polysaccharide
F_{min}	Minimum detectable force
F-D	Force-Distance curve
F-V	Force-Volume
Glc*N*Ac	*N*-acetyl glucosamine
GPa	Gigapascal
g	Grams
Hz	Hertz
h	Hours
InvOLS	Inverse optical lever sensitivity
JKR	Johnson-Kendall-Roberts
K	Kelvin
kHz	Kilohertz
KOH	Potassium hydroxide
kPa	Kilopascal

kV	Kilovolt
k	Spring constant
LPS	Lipopolysaccharide
LTA	Lipoteichoic acid
l	Litre
MIC	Minimum inhibitory concentration
MPa	Megapascal
Mur*N*Ac	*N*-acetyl muramic acid
mg	Milligrams
min	Minutes
ml	Millilitres
mW	Milliwatt
n =	Number of samples / experiments
N_2	Nitrogen gas
N	Newton
N/m	Newton per metre
nm	Nanometre
nN	Nanonewton
OD_{600}	Optical density at 600 nm wavelength
Pa	Pascal
PBP	Penicillin-binding protein
PBS	Phosphate buffered saline
PDMS	Polydimethylsiloxane
PF-QNM	PeakForce-Quantitative Nanomechanical Mapping
PG	Peptidoglycan
PID	Proportional-Integral-Derivative
pN	Piconewton
psi	Pounds per square inch
PV	Process variable
Q	Quality factor
QI™	Quantitative imaging

RMS	Root mean square
rpm	Revolutions per minute
SA	*Staphylococcus aureus*
SD	Standard deviation
SDS	Sodium dodecyl sulphate
SE	Standard error
SEM	Scanning electron microscopy
SI	International system of units
s	Seconds
TEM	Transmission electron microscopy
TSB	Tryptone soy broth
t	Time
UV	Ultraviolet
µg	Microgram
µl	Microlitre
µm	Micrometre
V	Volts
vs.	Versus
v/v	Volume for volume
W	Watt
WT	Wild type
WTA	Wall teichoic acid
w/v	Weight for volume
x	Times
x g	Times gravity
Z	Piezo height
~	Approximately
>	Greater than
<	Less than
%	Percentage

Table of Contents

List of Figures

List of Tables

Chapter 1

Staphylococcus aureus

1.1 Introduction

Staphylococcus aureus (SA) is a nominally spherical, non-motile and non-spore forming Gram-positive bacterium, with a diameter of 1 ± 0.5 µm. Most *Staphylococci* are facultative anaerobes and catalase-positive, with a low G+C content. SA tests positive for coagulase and produces a carotenoid pigment, staphyloxanthin, which gives a characteristic golden colour, leading to its species name. Its genus name is derived from 'staphyle', meaning bunch of grapes, and was first coined in 1883 by the British surgeon Sir Alexander Ogston, who was famed with the discovery of the *Staphylococcus* genus. *Staphylococci* may occur singly or in pairs and tetrads, or form grape-like clusters as observed by Ogston (Götz, Bannerman and Schleifer, 2006; Jensen and Lyon, 2009). SA is a commensal of the human skin and anterior nares, and is estimated to reside permanently within a third of the human population, whilst the remaining populace are intermittent carriers (Neumann *et al.*, 2014). It is a significant human pathogen and is responsible for a wide-ranging array of disease states from localised infections, such as skin abscesses, to systemic and life-threatening infective endocarditis. These pathologies are mediated by a diverse molecular arsenal including efflux pumps, proteases, exotoxins and specific enzymes that can destroy host tissues, evade the host immune response and inactivate many antimicrobials (Lowy, 2000; Costa *et al.*, 2013). The now infamous hospital 'superbug' methicillin resistant *Staphylococcus aureus* (MRSA) has evolved sophisticated genetic processes to inhibit the action of antimicrobials, leading to its pathogenesis.

1.1.1 A brief timeline of antimicrobials

The introduction of antibiotics was a milestone of 20th century medicine. They have saved countless lives and extended the human lifespan. The modern antibiotic era is generally thought to have started when Paul Erlich posited his famous 'magic bullet' concept, where a drug could selectively target disease-causing microbes whilst not harming the host. His large-scale search for a compound to treat syphilis, which was endemic and almost incurable at the time, lead to the discovery of the organoarsenic compound 'Salvarsan'. This drug enjoyed great success and was the most widely prescribed drug until the 1940s, when

a new compound rose to prominence. That compound was penicillin. This drug needs little introduction and most of us are familiar with the famous and serendipitous event that lead to its discovery in 1928 by Alexander Fleming. It is hard to conceive that it took a further 12 years, until 1940, for the widespread manufacturing of the drug. Previously problematic with regards to purity and yield Howard Florey and Ernst Chain published a protocol outlining the purification of the compound. This lead to mass production by the end of the Second World War and has been attributed to saving countless allied lives on and off the battlefield, and perhaps influencing the final outcomes of the war (Aminov, 2010; Quinn, 2013). Erlich, Fleming, Florey and Chain were all awarded Nobel Prizes. Such were the impacts of their research.

1.1.2 Antimicrobial resistance

The rise of antimicrobial resistance poses a serious threat to humanity. In the EU, 25,000 people die each year due to multidrug resistant bacterial infections and 63,000 hospital patients die each year in the US as a result of hospital-acquired bacterial infections (Aminov, 2010). In her 2011 annual report, the UK's chief medical officer Professor Dame Sally Davies stated that 'antimicrobial resistance is a ticking timebomb' and 'is a threat arguably as important as climate change' (Davies, 2013). Bacteria appear to not only be a modern problem, as traces of tetracycline and artemisinin have been found in human skeletal remains dating back over thousands of years. These compounds were thought to have been present in the diets and through the use of traditional remedies at the time (Aminov, 2010). In the modern era resistance to penicillin was observed mere years after it was first introduced into clinical practice, and since then the development of new antimicrobials has been shadowed by a steady increase of antimicrobial resistant strains (Costa *et al.*, 2013).

1.1.2.1 Genetic mechanisms of antimicrobial resistance

Spontaneous gene mutations can be typically generated at frequencies ~ 10^{-7} per cell in the laboratory, but in most instances antimicrobial resistance is driven by horizontal gene transfer between related bacterial strains, or even between different species and genera. This pathway leads to the acquisition of mobile genetic elements that incorporate antimicrobial resistance genes (Jensen and Lyon, 2009). The biosynthetic pathway of the peptidoglycan (PG) component of the cell wall is a critical process in the bacterial cell and is

a major target for antimicrobials. Penicillin belongs to the so-called Beta-Lactam (β-Lactam) class of antimicrobials, named for the β-Lactam ring moiety within the chemical structure of the penicillin. During bacterial growth and division the PG must be synthesised and remodelled by endogenous cell wall hydrolases to allow the cell to divide. The covalent binding of the penicillin to one or more of these enzymes - subsequently termed the penicillin-binding proteins (PBPs), can inhibit this highly regulated process. The resistance to penicillin within MRSA is due to the expression of a low affinity PBP, termed PBP2a. This is a homologue of PBP2, which is one of four key PBPs within SA (named PBP1 – 4 respectively). The chromosomes of MRSA carry a mobile genetic element termed the *Staphylococcal* cassette chromosome *mec* (SCC*mec*), which contains the *mec*A gene and encodes PBP2a. β-Lactam antimicrobials cannot bind PBP2a and thus cell wall synthesis can continue (Götz, Bannerman and Schleifer, 2006; Jensen and Lyon, 2009; Foster, 2017).

1.1.3 The Gram-positive bacterial cell wall

The cell wall of SA acts as a tough protective coat that is thought to resist the high intracellular turgor pressures that have been reported to be as high as 20 atmospheres (Mitchell and Moyle, 1957). In SA, and other Gram-positive species, the cell wall forms the outer surface of the bacterium. It is composed of PG and often with anionic polymers called teichoic acids. Under the transmission electron microscope (TEM) the SA cell wall appears as a relatively homogenous, and not particularly electron dense structure between 20 – 40 nm in thickness (Giesbrecht, Kersten and Maidhof, 1998; Matias and Beveridge, 2006), and is thought to be multi-layered, with an inner and outer zone (Fig 1.1). It encloses a single lipid membrane-bound cytoplasm. The septum, which leads to daughter cell separation has been shown to comprise two high density zones, sandwiched between three lower density zones within a structural region termed the splitting system (Giesbrecht, Kersten and Maidhof, 1998; Matias and Beveridge, 2006). 50% of the cell wall mass is composed of PG, with 40% composed of wall teichoic acid (WTA) or cell membrane associated lipoteichoic acid (LTA), whilst proteins make up the final 10% (Harris, Foster and Richards, 2002) (Fig. 1.2b). It appears to be a mesh-like structure of significant porosity (Fig. 1.3). Once thought to be the sole domain of Gram-negative species, a periplasmic space exists between the lipid membrane and the PG layer within SA and other Gram-positive bacteria (Matias and Beveridge, 2008).

1.1.4 The Gram-negative bacterial cell wall

Gram-negative species, such as *Escherichia coli* (*E.coli*) contain a thin single layer (or very few layers) of PG within the periplasmic space. The PG has a reported thickness between 2 – 7 nm (Silhavy, Kahne and Walker, 2010; Gumbart *et al.*, 2014). In further contrast to Gram-positive species, this thin PG layer is enveloped by a second lipid membrane mainly containing anionic lipopolysaccharides (LPS) on its outer leaflet, that extend into the extracellular space (Fig. 1.2a). The outer membrane is secured to the underlying PG layer by a specialised lipoprotein. LPS performs a critical barrier function for the outer membrane. It is composed of a combination of disaccharides, including an extended polysaccharide chain called the O-antigen. Pathogenic strains of *E. coli* are typically classified by the antigenic properties of this disaccharide chain (Silhavy, Kahne and Walker, 2010).

1.1.5 Structural architecture of the cell wall

Peptidoglycan is a largely conserved, huge macromolecular sacculus and is a component of nearly all bacterial species, but the chemistry is diverse and the architecture is a matter of debate (Turner, Vollmer and Foster, 2014). Most of the structural studies of PG have been performed with *E. coli*. Several competing models have posited some kind of order to the structural arrangement; either with a planar orientation of PG architecture, where glycan chains are ordered parallel to the lipid membrane (Koch, 1998), a scaffold model, where the glycan strands are oriented perpendicular to the lipid membrane (Dmitriev *et al.*, 2003) and more recently a coiled-coil model where helical cables are arranged circumferentially around the cell (Hayhurst *et al.*, 2008). This more recent work, from our laboratory, using the atomic force microscope (AFM), was expanded further to describe a PG-architecture-related model of growth and aging of the cell wall (Turner *et al.*, 2013). Using a combination of TEM and AFM the nascent cell wall has been observed to exhibit a spherical array of circumferentially oriented bands, while the mature cell wall has a knobbled appearance (Touhami, Jericho and Beveridge, 2004), whose morphology may have changed due to the action of PG hydrolases. For a review see (Turner, Vollmer and Foster, 2014). It has since been identified that the knobbled appearance may be due to the dehydrated nature of the cells studied or the image resolution available at the time. Recent advancements have allowed the study of intact and isolated cell walls in an aqueous environment and identified that the knobbles are more porous and mesh-like, and the ultrastructure displays very little

structural organisation. Recent work in our laboratory has identified both of these cell wall features using AFM on intact, living SA cells (Fig. 1.3).

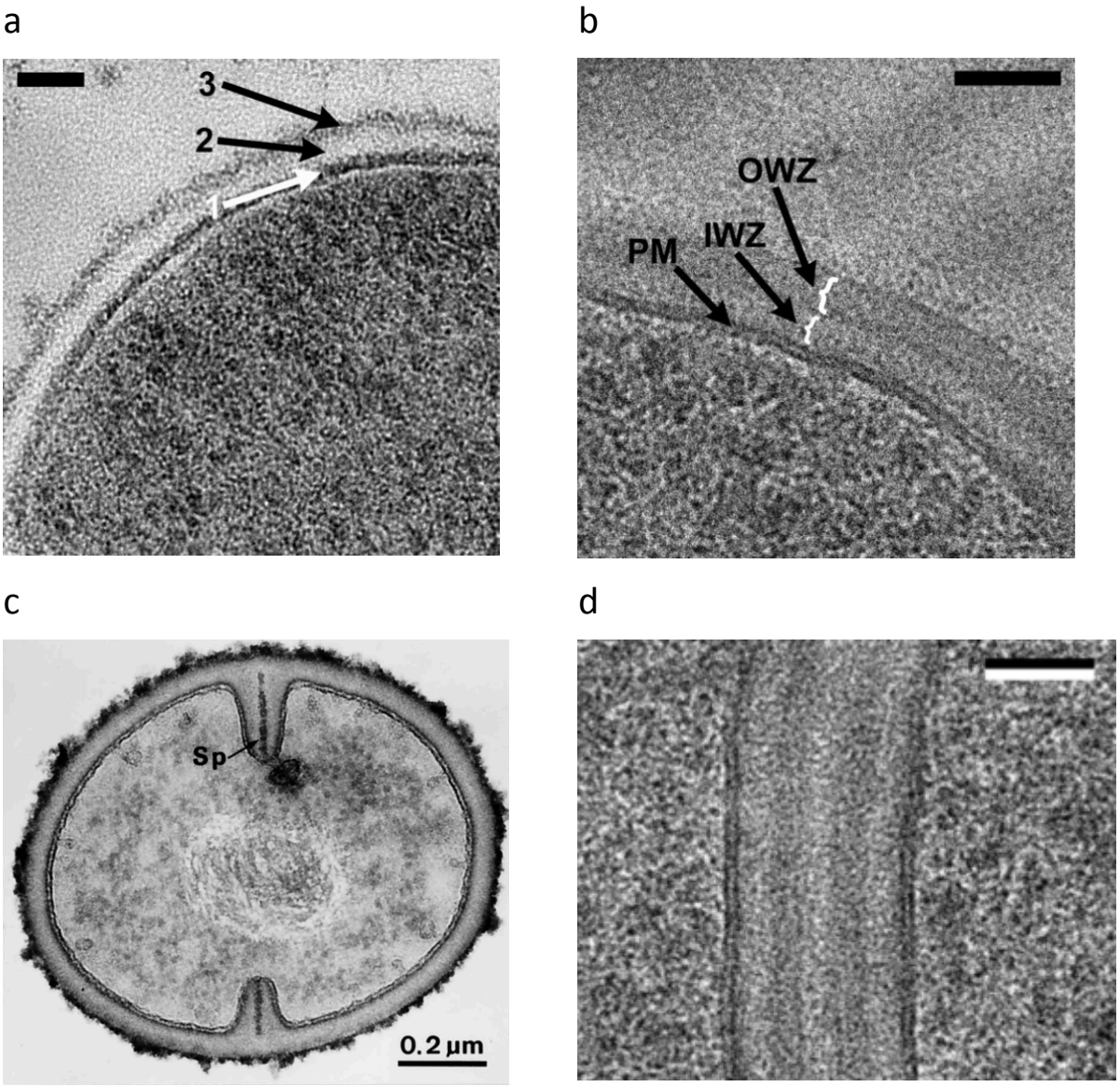

Figure 1.1. TEM micrographs of the SA cell wall and septum. The cell wall of SA is a 20 – 40 nm thick layer composed of peptidoglycan and teichoic acid. (a, b) The peptidoglycan surrounds the plasma membrane (1) and is composed of an inner wall zone (2) and outer wall zone (3) (c) The 'fluffy' outer coat is thought to be the wall teichoic acids. The dark line, Sp (arrow) is the splitting system within the newly forming septum. (d) Increased magnification of the septal splitting system shows two regions of high density sandwiched between three regions of lower density. Image a, b and d adapted from (Matias and Beveridge, 2006). Image c adapted from (Giesbrecht, Kersten and Maidhof, 1998). Scale bar a, b and d = 50 nm.

a

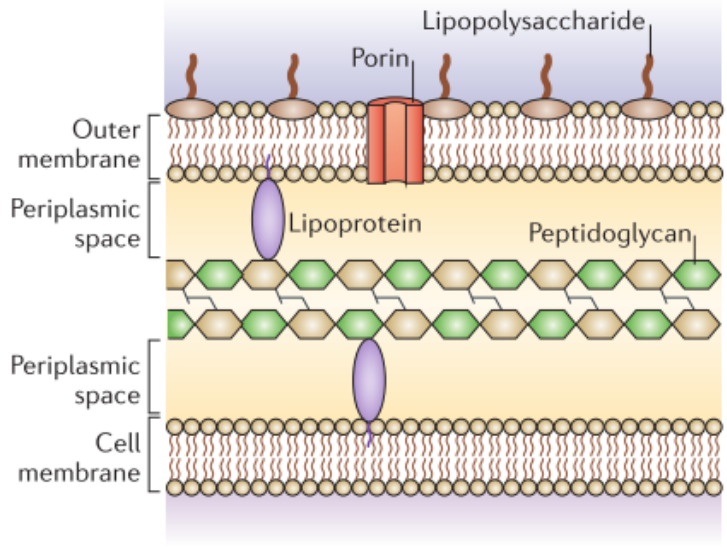

b

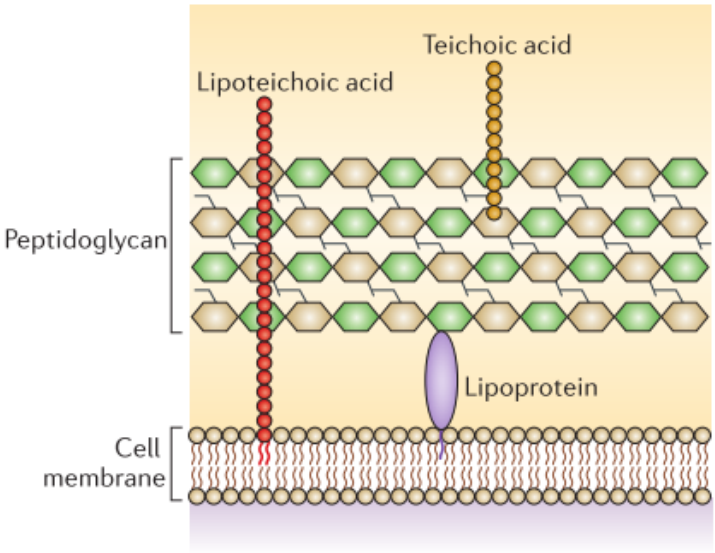

Figure 1.2. Cell wall structure of Gram-negative and Gram-positive bacteria. Cartoon representations of the ultrastructure of the bacterial cell wall. (a) In Gram-negative species a thin layer of peptidoglycan resides in the periplasmic space between the inner and outer lipid membranes. The outer membrane contains lipopolysaccharides. (b) The Gram-positive cell wall is considerably thicker and is thought to consist of multiple layers of peptidoglycan. A periplasmic space exists between the lipid membrane and the cell wall, which is anchored to the membrane by lipoproteins and lipoteichoic acid. The extracellular region of the cell wall contains wall teichoic acid and proteins. Image adapted from (Brown *et al.*, 2015).

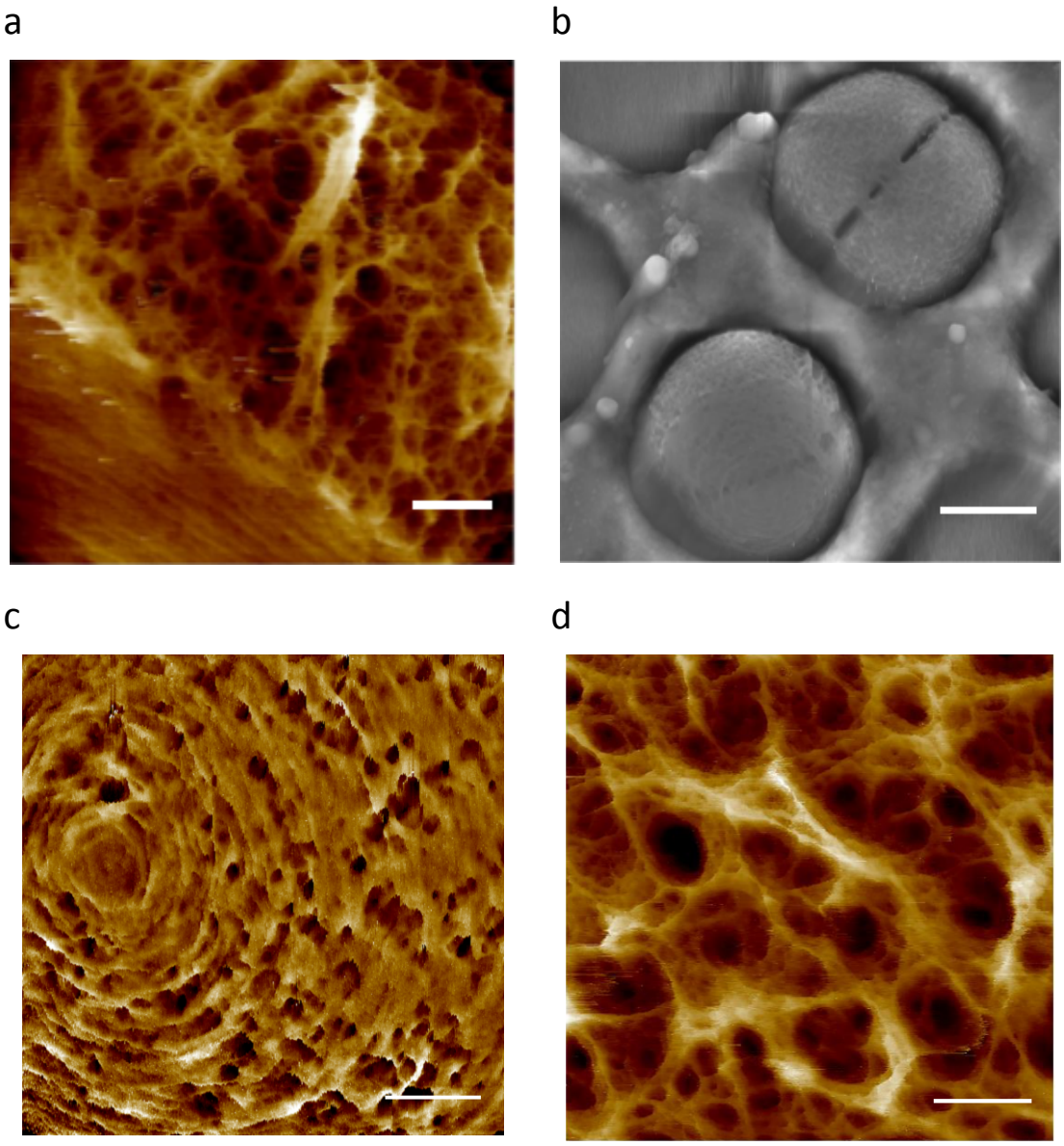

Figure 1.3. AFM images of the architecture of the SA cell wall. AFM height images at varying length scales and image resolution show the structural architecture of specific regions of the SA bacterial cell wall. Considerable porosity is evident throughout. (a) There is a clear region demarking the mature mesh-like cell wall from the nascent circumferential rings. (b) Two SA cells immobilised within a patterned silicon wafer show the onset of septation, with discontinuous breaks in the cell wall. (c) High resolution of the nascent concentric rings. (d) High resolution of the mature cell wall. Images adapted from, and with permission of Dr Jonathan Burns (currently unpublished). Scale bar = (a, c) 100 nm (b) 500 nm (d) 50 nm. *Z* scale = (a) 29.6 nm (b) 1.34 µm (c) 24.9 nm (d) 17.2 nm

1.1.6 Chemical properties of the cell wall

1.1.6.1 Peptidoglycan biochemistry

The chemical structure of peptidoglycan (formerly murein) is similar in both Gram-positive and Gram-negative species and is a network of disaccharide-peptide repeat units connected with β-1,4 glycosidic bonds to form linear glycan strands. The glycan strands are a repeating dissacharide of *N*-acetylmuramic acid (Mur*N*Ac) and *N*-acetylglucosamine (Glc*N*Ac). Peptide stems are covalently attached to the Mur*N*Ac residues and are composed of alternating L- and D- isoforms, usually with the composition L-Alanine – D-Glutamate – L-Lysine (or *meso*-diaminopimelic acid) - D-Alanyl – D-Alanine, with the last D-Alanine residue being lost in the mature macromolecule (Fig. 1.4). The peptide stem composition is less conserved than that of the glycan strands, either through the specificity of the enzymes during its biosynthesis, or occurring at a later step of biosynthesis (Vollmer, Blanot and de Pedro, 2008).

In SA the PG is crosslinked via a pentaglycine interpeptide bridge, which branches off the L-Lysine of the peptide stem and interconnects one PG chain to the D-Alanine in position four of a neighbouring PG chain. This is a characteristic feature of the *Staphylococcal* cell wall and is essential for the full expression of antimicrobial resistance in MRSA as the PBP2a couples only to the pentaglycine-bridged substrates (Schneider *et al.*, 2004; Silhavy, Kahne and Walker, 2010). The main variation of PG chemistry throughout the bacterial kingdom relates to the average glycan chain length. Interestingly, the chain length does not dictate the cell wall thickness. SA has short chain lengths with an average ~ 6 disaccharides, but a relatively thick cell wall, compared to *Bacillus subtilis*, which shares a similar cell wall thickness, but has glycan strands of up to ~ 5 µm in length, which is longer than the actual bacterium. Similarly, there are Gram-negative species with short or long glycan strands; such as *Helicobacter pylori* and *Proteus morganii* respectively (Vollmer, Blanot and de Pedro, 2008).

PG plays an important role in human health, mood and behaviour. Mammals have a PG recognition protein that is upregulated once it binds to the PG of living bacteria. It is involved in innate immunity and has been shown to influence the homeostatic regulation of sleep in rats (Götz, Bannerman and Schleifer, 2006). Estimates suggest that there are > 100 species and over 7000 strains of bacteria in the human gut, which are capable of

synthesising and releasing neurotransmitters or neuromodulators (Rea, Dinan and Cryan, 2016). Recently, it has been shown that circulating fragments of gut-derived PG from the microbiome in humans activates inflammatory cytokines within the brain – influencing mood and alcohol dependence (Leclercq *et al.*, 2017).

1.1.6.2 Teichoic acid biochemistry

Teichoic acids are anionic glycopolymers found in a variety of Gram-positive organisms. They are composed largely of glycerol phosphate, ribitol phosphate or glucosyl phosphate. In SA the WTA are composed of poly-glycerol phosphate (Silhavy, Kahne and Walker, 2010). The WTA are covalently attached to the Mur*N*Ac residues in PG and extend through the wall into the extracellular space creating a 'fluffy' layer, (as seen in Fig. 1.1c). The chain can consist of up to 60 repeats. The LTA are anchored to the lipid membrane and typically contain fewer repeats. They extend only into the PG and not beyond. Collectively both polymers provide a reservoir of anionic charge that play an important role in the sequestering of cations (Silhavy, Kahne and Walker, 2010).

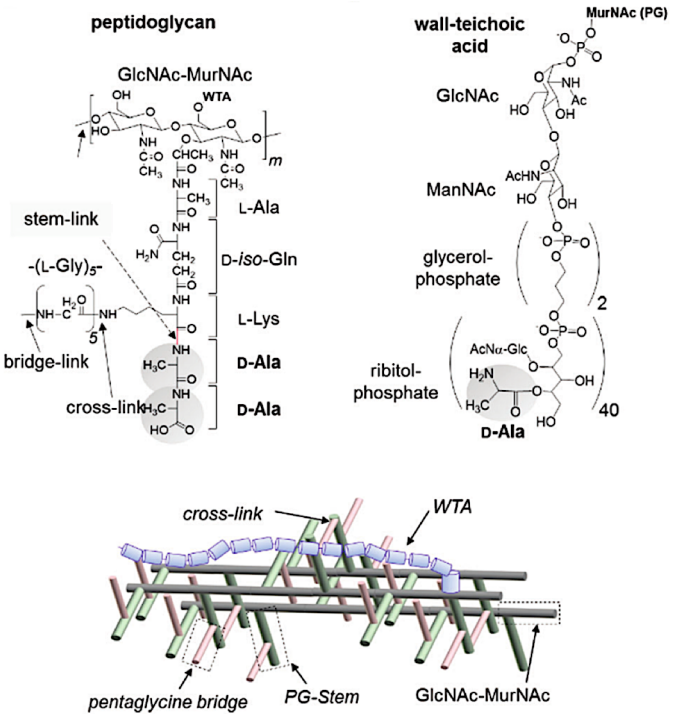

Figure 1.4. Chemical structure of SA peptidoglycan and wall teichoic acid. Cartoon representation of the structure, bonding and organisation of the cell wall PG and WTA. Adapted from (Chang, Coffman and Kim, 2017).

1.1.7 Growth and division

A growing bacterium typically divides into two genetically identical sister cells through the process of binary fission, and ultimately gives rise to a clonal population. The cellular machinery of growth and division – termed the divisome, is comprised of a number of proteins, of which many are conserved amongst different species (Typas *et al.*, 2012). Cells typically divide at the mid-cell location via the production of a septum. In order to preserve the genetic information within the cytoplasm a high degree of spatial and temporal coordination must be employed to replicate and segregate the chromosome and create the mid-cell septum. The primary component within most bacteria is a eukaryotic tubulin-like homologue called FtsZ that forms a ring (the Z-ring) at the midcell (Typas *et al.*, 2012). A further system, termed the nucleoid occlusion system (*noc*) prevents Z-ring formation near the nucleoid to prevent the chromosome from being bissected by the septum. In *Bacillus subtilis* the *noc* provides a molecular basis for the process but the DNA-binding site for the SA *noc* remains elusive (Wu and Errington, 2012). In *Bacillus subtilis* PG synthesis at the septum was seen to occur via discrete enzyme-filament complexes being directed around the division plane by FtsZ treadmilling (Bisson-Filho *et al.*, 2017). This model of PG insertion may not apply in SA, however. Using fluorescently labelled D-amino acids visualised with localisation microscopy the septum was seen to be thinner at the leading edge and progressively thicker at the lagging edge, suggesting that PG insertion cannot be confined to the leading edge of the septum. It was shown that the division proteins were distributed throughout the septum, with no discernable pattern and that multiple proteins may be inserting PG at any one time (Lund *et al.*, 2018). It remains a matter of debate how *Staphylococci* are able to divide on orthogonal planes, leading to the 'bunch of grapes' pattern of division that gives the genus its name.

1.1.7.1 A mechanical basis for growth and division

Each round of division occurs orthogonally at 90° from the previous, thus SA must 'remember' the planes of the previous two rounds. As these spatial effects are modified at each round, they cannot be encoded by DNA (Turner, Ratcliffe, *et al.*, 2010). Using AFM and fluorescence microscopy, these investigators identified a number of architectural details on the cell wall that they proposed could offer a mechanical cue to enable this orthogonal division process. A thick band of PG (termed the 'piecrust') was shown to encircle the

presumptive septum and was divided between the two daughter cells following division. These then resembled a thinner 'rib' of material. After the second round of division these ribs are shared again, leading to half-ribs whilst also retaining full ribs from the most recent round of division. The third round of division leads to a quarter rib bounded by two T-junctions, in addition to a half rib and whole rib from the previous two rounds. The authors suggest that these ribs can encode enough information to determine the position for the next round (Turner, Ratcliffe, *et al.*, 2010) (Fig. 1.5). The synthesis and hydrolysis of PG is essential for growth of a bacterium, however, it is not fully understood how these two distinct processes are linked (Lee and Huang, 2013). During the formation of a septum and the subsequent generation of a daughter cell, the action of cell wall hydrolases are thought to contribute to the eventual splitting and cell separations. Giesbrecht and colleagues postulated that either hydrolase activity or mechanical forces are responsible for cell splitting in SA (Giesbrecht *et al.*, 1997). Recently, it was shown that both processes play their part in daughter cell separation (Zhou *et al.*, 2015). These authors showed that when a SA daughter cell is generated, they are initially connected via a narrow peripheral ring 'or hinge point'. Prior to cell separation small perforations were seen to form (analogous to Fig. 1.3b), that were likely mediated by hydrolase activity, but the likelihood of popping relied on the amount of mechanical stress, which the authors could control via changing osmotic gradients. However, the actual moment of cell separation occurred in milliseconds, suggesting that it was entirely dependent on the intracellular turgor pressure and subsequent cell wall stress propagating around the peripheral ring, as hydrolase activity would not be quick enough to give rise to these events (Zhou *et al.*, 2015).

1.1.7.2 Mechanical properties of cells

Biological tissues, including the bacterial cell wall have a robust architecture that must allow for their stability and resistance to stress, whilst also displaying considerable levels of plasticity to allow for remodelling (Lecuit and Lenne, 2007; Vadillo-Rodriguez, Beveridge and Dutcher, 2008). The mechanical properties of mutated, or chemically challenged cells have been shown to exhibit altered properties, and the resultant data could be used to infer a structure-function relationship. Investigators found that the stiffness of metastatic human cancer cells was more than 70% softer, and with a much lower standard deviation than the non-benign cell, and that a range of different cancer types was found to share a similar

stiffness (Cross *et al.*, 2007). The authors further showed that they could determine a cancerous cell, even if it shared the same morphology as a benign cell, entirely on the basis of its mechanical properties. They corroborated their findings by comparing against immunohistochemical analysis, suggesting that nanomechanical assessment has the potential for the detection of cancer, where accurate diagnoses based on cell morphology has been otherwise challenging (Cross *et al.*, 2007). Scleroderma is a disease caused by crosslinking of collagen, and results in painful skin, diminished organ function and death in ~ half of patients. Using histological imaging and the AFM, researchers identified that collagen fibrils became crosslinked in diseased tissue biopsies, leading to increased elastic moduli (Strange *et al.*, 2017). When challenged with antimicrobial compounds the stiffness of *Bacillus subtilis* was seen to initially increase, but eventually decrease during extended incubation times and under augmented antimicrobial concentrations (Pogoda *et al.*, 2017). Determining the mechanical properties of cells by using the AFM is a relatively recent area of research, with the first articles dating only from the early 1990s, and whilst the technique is capable of producing quantitative information there is a significant disparity between the reported data, even for similar cell types (Benitez and Toca-herrera, 2014). The reported elastic moduli for SA span many orders of magnitude. This suggests that the topic is complex and more investigations and theoretical models are required – something that we seek to address in this study.

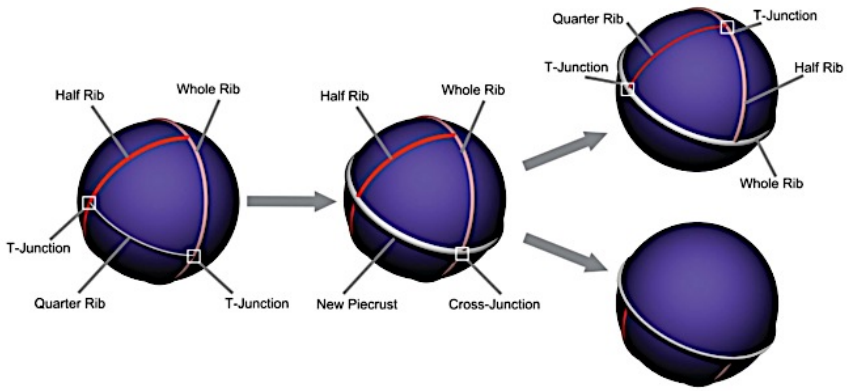

Figure 1.5. Model for maintaining orthogonal division planes in SA. The location and inheritance of structural remnants of peptidoglycan 'ribs' can specify division planes in SA. Following division each daughter cell will inherit a portion of the 'piecrust', such that a quarter rib is inherited from the first round, a half rib from the second round and a full rib from the third round. Image adapted from (Turner, Ratcliffe, *et al.*, 2010).

1.1.8 Attachment to surfaces and biofilm formation

The laboratory setting for the study of bacteria, where bacteria are grown planktonically and nutrient supply is plentiful, does not particularly reflect the natural habitat of a bacterium. Bacteria found in the environment typically grow in nutrient-limited conditions and often form multicellular aggregations – or biofilms, and their formation on indwelling medical devices poses a serious problem in the biomedical field, leading to significant increases in morbidity and mortality (Moormeier and Bayles, 2017). Titanium implants are considered the gold standard in dentistry, but surface infection remains a problem. Using the AFM, SA was gently pressed against a titanium surface with a loading force of 0.5 nanonewton (nN) and held between 1- 60 s. The unbinding events due to adhesion were observed in ~ 10% of the cells at 1 s contact time, but increased to ~ 90% after 60 s contact time, which is consistent with the time-dependent binding of surface proteins (Aguayo *et al.*, 2015). SA biofilm development has been seen to progress through a five-stage process including; (i) attachment (ii) multiplication (iii) exodus (iv) maturation (v) dispersal (Moormeier *et al.*, 2014). Initial attachment of planktonic cells is frequently mediated by a variety of cell wall proteins that are specific for different substrates, typically belonging to the microbial surface components recognising adhesive matrix molecules (MSCRAMM) family (Götz, Bannerman and Schleifer, 2006; Moormeier *et al.*, 2014). Investigators looked at a variety of substrates with different surface chemistries and found that SA was unlikely to form initial attachments on uncharged, hydrophobic polystyrene surfaces, and that the surface required modifications to make it hydrophilic and negatively charged (Kennedy and O'Gara, 2004). Although WTA is negatively charged, suggesting that repulsion would occur against a negatively charged surface, the direct interaction of bacteria and surfaces is dependent on van der Waals forces, which can overcome charge repulsion (Gross *et al.*, 2001). Patterned surface topography of polycarbonate was investigated for its ability to promote, or inhibit SA adhesion, and to determine if the reported elastic modulus of the bacterium was influenced by differences in the topography (Aguayo *et al.*, 2016). Smooth, or patterned polycarbonate with a repeating lattice of ~ 100 nm diameter wells and a depth of ~ 70 nm showed no surface-induced changes in the elastic modulus of the cells, but adhesion forces between the cell and the patterned surface were greater than the smooth surface, which the authors suggest is due to higher short range forces, compared to

repulsive longer range forces acting on cells on the smooth surface (Aguayo *et al.*, 2016). Biofilms are stabilised by a self-produced extracellular matrix (ECM) composed of proteins, extracellular DNA and extracellular polysaccharides (EPS), which allow the cells to mature into three-dimensional structures (Gazzè *et al.*, 2013). However, even after initial cell attachment to a surface SA cells are vulnerable to detachment, particularly from the shear forces induced by fluid flow (Moormeier and Bayles, 2017). With regards to bacterial study using the AFM, in addition to fluid motion induced by the AFM cantilever as it moves through the medium, there is the extra challenge of repeated contact with the scanning probe.

Moreover, this study, and similar studies (Louise Meyer *et al.*, 2010; Moffitt, Lee and Cluzel, 2012b; Formosa *et al.*, 2015) performed single cell force spectroscopy. The behaviours of individual bacteria may differ from the collective behaviours of a population of cells. In their normal collective communities bacteria may exchange small molecules that drive antimicrobial resistance, cell differentiation and quorum sensing for example. The implications of confining single cells and potentially disrupting their normal behaviour are yet to be understood (Moffitt, Lee and Cluzel, 2012b). Collectively, these factors present a challenging scenario for the analysis of individual cells. This study aims to design and explore a variety of different substrates that may prove suitable to the confinement of SA for repeated scanning with the AFM, whilst hopefully providing the ability for unperturbed growth and division, that has not previously been reported in the literature. We hope to be able to monitor any changes in the mechanical properties of the cells throughout the cell cycle, during growth, division and ultimately death of the bacterium.

Chapter 2

The atomic force microscope

2.1 Introduction

2.1.1 Development of the atomic force microscope

The atomic force microscope (AFM) is a sensitive scanning probe microscope that can investigate sub-nanometre (nm) length scales with picoNewton (pN) forces. It was invented in 1986 by Gerd Binnig, Calvin Quate and Christoph Gerber (Binnig, Quate and Gerber, 1986) as an update from the scanning tunnelling microscope (STM) which Binnig also co-devised with Heinrich Rohrer and colleagues in 1982 (Binnig *et al.*, 1982). Both of these were reported in surprisingly short papers in Physical Review Letters, but such was the impact of these microscopies that Binnig and Rohrer were jointly awarded the Nobel Prize in Physics 1986 for the development of the STM. The AFM is now widely used in the nanotechnology field. Initially the preserve of physicists and engineers, in 1989 Paul Hansma's group introduced the world of biology to the AFM, specifically by looking at amino acid polymers in liquid (Drake *et al.*, 1989).

2.1.2 Comparisons to other forms of microscopy

Because samples are interrogated with a scanning probe, rather than lenses and light, any image is built up through topographic maps. This method of image capture allows the microscope to exceed the resolution limits of diffraction-limited optical microscopy by up to three orders of magnitude. High resolution images, such as the structural details of individual membrane proteins, can be obtained (Kumar *et al.*, 2017) and the mechanical (Bailey *et al.*, 2014) and electrochemical (Pobelov *et al.*, 2013) properties of samples can also be investigated. Additionally, nanoparticles can be physically manipulated, moved and dissected (Liu *et al.*, 2006). When compared to the STM or electron microscopy (EM), the sample under investigation does not need to be electrically conducting. This allows for the analysis of unadulterated samples – free from the contrast dyes or heavy metal addition that could alter the chemical nature of the sample and render biological samples non-physiological in nature. The AFM can be used in ambient conditions, or in a dedicated gaseous medium giving a distinct advantage over the need for working in a vacuum, as is

required for most EM techniques. The ability to work in an aqueous environment means that biological samples can be assessed in their native states – a feature that the AFM community is increasingly exploiting. What this all means, of course, is that the samples can be kept alive and observed at a molecular level - a milestone breakthrough in the analysis of biological materials.

2.1.3 The AFM scanner

The AFM scanner houses piezoelectric translators that expand and contract proportionally according to the magnitude of an applied voltage. These piezo dynamics can precisely control the scanner, and attached probe, movement in the *XYZ* directions. A major benefit of scanning in the *Z*-direction is that it allows for three-dimensional (3D) imaging. The shape of the probe (radius and geometry) influences the lateral dimensions - and the experimenter should exercise some caution when interpreting the image, but the *Z*-resolution is ultimately limited by thermal fluctuations (Frederix, Bosshart and Engel, 2009). Typically, the scanner moves along the surface of a stationary sample in an *XY* raster fashion – similar to the motion of an inkjet printer, whilst the *Z*-piezo precisely controls the height of the scanner.

2.1.4 The feedback-loop

The AFM ensures that the probe accurately tracks the sample surface topography by means of a sophisticated feedback-loop system. A reference value, known as the setpoint is defined. This could be an arbitrary voltage, such as 0.5 Volts (V) for example. As the scanner moves the probe into the imaging regime the detector signal is monitored, and the defined value is compared against the actual value, with the electronics working to make both values the same. Once the setpoint is reached scanning can begin. Lateral resolutions around 0.5 - 1 nm and vertical resolutions of around 0.1 nm are achievable (Zhong *et al.*, 1993; Müller *et al.*, 1999; Dufrene *et al.*, 2013). Alternative sample-scanning systems utilise a stationary probe above a piezo-controlled stage that precisely moves the sample in the *XYZ* directions. The AFM user can provide inputs to the system in an effort to control the *Z*-sample position, typically as 'feedback gain' values. These gains control how quickly the system responds to perturbations from the setpoint value. A proportional-integral-derivative (PID) controller is often used to control the imaging. It monitors the setpoint (input) value and compares it to the actual value – the process variable (PV) and attempts to

reduce any discrepancies to zero (Ando, Uchihashi and Scheuring, 2014). The AFM utilises the proportional and integral calculations of the PID algorithm and rarely uses the derivative term. The gain value refers to the percentage by which the error signal will lose or gain strength on its way through the controller towards becoming the output. The 'proportional gain' value multiplies the PV error by the user-inputted gain value, such that a proportional gain of 2 doubles the signal compared to a proportional gain of 1. This is a linear function, and although it works well there always remains some residual error. To correct for this residual error the 'integral gain' monitors these errors over time and attempts to narrow the error closer to the setpoint. These gains can be adjusted in real-time but over-tuning them can lead to overshooting the setpoint and also drive the system into oscillation, introducing noise into the image.

2.1.5 The photodiode

The deflection of the cantilever is typically measured by using the optical lever technique (Meyer and Amer, 1988). In this system a laser diode provides a beam onto the back of the cantilever, which is often coated with a reflective metal, such as gold (Fig. 2.1) and its position can be finely adjusted for the best signal to noise ratio. This beam is reflected onto a position-sensitive photodiode, usually with four quadrants and the alignment can be fine-tuned by an adjustable mirror (Fig. 2.2). A voltage is generated from each quadrant that is proportional to the amount of light hitting it. The cantilever deflection signal is the difference between the voltages in the top and bottom halves of the detector (A + B) – (C + D)/(A + B) + (C + D) and the lateral signal is the difference between the voltages in the left and right halves of the detector (A + C) – (B + D)/(A + C) + (B + D) (D'Costa and Hoh, 1995; Butt, Cappella and Kappl, 2005). The laser spot is aligned in the centre of the photodiode when the cantilever is far from the surface. Following a repulsive force, when the cantilever hits the surface it deflects upwards, moving the laser spot up into the A and B segments. Because more light now hits the top of the photodiode this leads to a greater voltage at the top and a reduced signal at the bottom, denoting a positive deflection. When the cantilever experiences an attractive force it deflects downwards. This changes the position of the laser spot into the C and D segments, leading to a greater voltage at the bottom, denoting a negative deflection (Butt, Cappella and Kappl, 2005). These signals are fed into the deflection-to-amplitude converter and its output amplitude signal is subtracted from a

setpoint voltage corresponding to the setpoint amplitude. This signal – the feedback error, is fed into the PID controller, and the output signal is input to the Z-piezo. The signal is then amplified to displace the Z-scanner to bring the feedback error towards zero (Ando, Uchihashi and Scheuring, 2014). The deflection of a cantilever could be as a result of the topography, or the adhesive properties of the sample under investigation. These both lead to characteristic distortions of the cantilever and the resultant photodiode signal and are described in greater detail in Section 2.8.4 Force spectroscopy.

The cantilever deflection, and thus the differential signal from the altered position of the laser spot on the photodiode, is used to translate this information into an image, via sophisticated control from the feedback loop (Fig. 2.2). The distance between the detector and cantilever is typically three orders of magnitude greater than the cantilever length and so the optical lever method amplifies the motion of the tip to provide high sensitivity and resolution.

a b

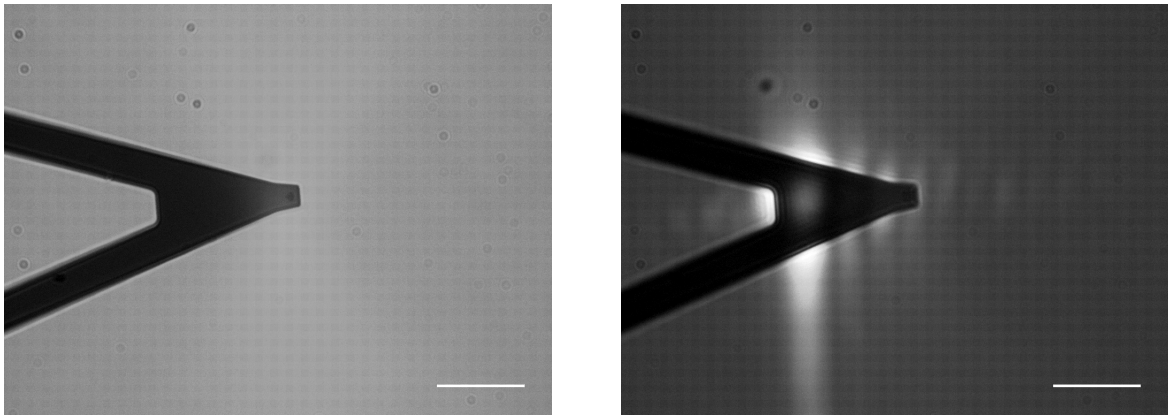

Figure 2.1. Laser positioning on an AFM cantilever. A 10X optical micrograph, from a Nikon Ti inverted microscope, shows a triangular cantilever, from the MLCT silicon nitride six-cantilever chip (Bruker Corporation). (a) Without the laser. The pyramidal tip is just visible at the narrow periphery of the cantilever. (b) The laser is positioned above the widest part of the cantilever for maximum signal to noise sensitivity, but radiates beyond the edges. Scale bar is 50 µm.

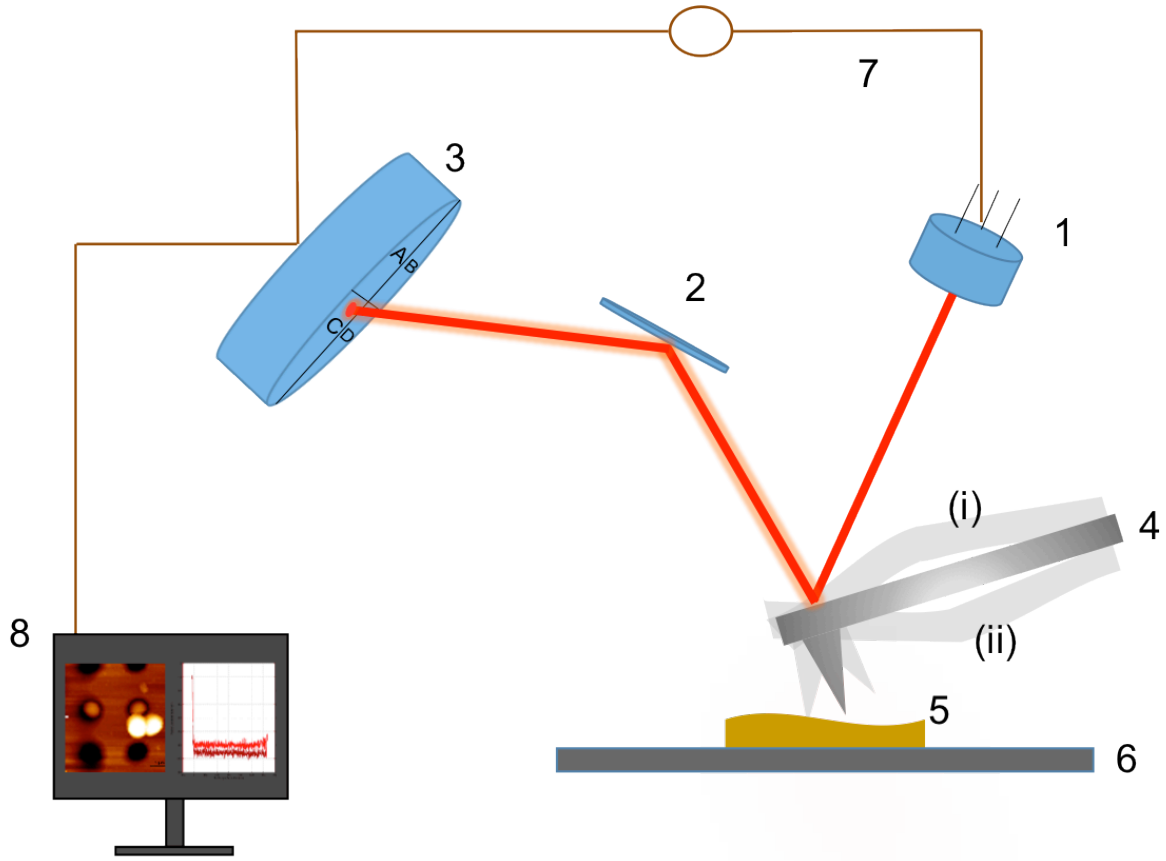

Figure 2.2. Schematic representation of an AFM. A laser beam is focused on the back of a cantilever with a sharp tip (probe) mounted on it. This probe interacts with the sample surface and the resultant forces displace the cantilever, and thus, the reflected laser beam placement on a position-sensitive quadrant photodetector. In a scanned probe system the cantilever, connected to the scanner, rasters in an *XY* direction over a fixed stage and sample. In alternative 'sample-scanning' systems the stage raster scans under a fixed probe. Piezoelectric translators precisely control the *XY* and *Z* movements to Ångstrom resolution. *1*, Laser diode; *2*, adjustable mirror; *3*, position-sensitive photodetector; *4*, cantilever and tip (i) adhesion (ii) deflection; *5*, sample; *6*, stage; *7*, feedback loop electronics; *8*, computer.

2.1.6 The AFM cantilever

The cantilever forms the heart of an AFM system. It behaves as a Hookean spring where its deflection is resultant on the properties of the sample surface. Hooke's law states that the force F in Newtons (N) required to compress or extend a spring by a distance x in metres (m) is proportional to that distance and is subject to the spring constant (k) of the spring, measured in Newton per metre (N/m) and is represented by the equation

$$F = -k\,x \tag{1}$$

Early incarnations of the cantilever were handmade from thin films of gold with a diamond tip glued onto it (Binnig, Quate and Gerber, 1986) or tungsten wires which were electrochemically etched and bent to provide the tip (Meyer and Amer, 1988). Today the cantilever and tip are typically made of silicon or silicon nitride and micromachined in a process similar to integrated circuit fabrication, which involve a silicon wafer being processed through deposition, photolithography and etching (Tortonese, 1997). This batch process enables thousands of cantilevers to be made simultaneously providing high levels of reproducibility and at a relatively low cost. The mechanical properties of the cantilever are a key component of the AFM system. The spring (force) constant, physical dimensions and resonant frequency are critical design requirements and are dependent upon on the length, width and thickness of the cantilever. A common cantilever may be around 100 - 400 µm in length, 10 - 50 µm in width and 0.3 – 2 µm in thickness. The two most commonly used designs of cantilever are a rectangular or triangular shape, which have different torsional properties. These properties, and hence the choice of cantilever, are chosen dependent upon the mode of operation and the choice of sample under investigation.

Typical spring constants for non-contact and intermittent contact mode are 1 N/m – 100 N/m and for contact mode values of 0.01 N/m – 1 N/m are common. The spring constant of a rectangular cantilever is represented by the equation

$$k = \frac{Et^3\,w}{4l^3} \tag{2}$$

where E is the Young's (elastic) modulus, t is the thickness, w is the width and l is the length. The formula is expanded for a triangular cantilever and represented by the equation

$$k = \frac{Et^3wb}{2b({L_1}^3 - {L_2}^3) + 6w{L_2}^3} \quad (3)$$

where b is the triangular apex, L_1 is the total length of the triangle and L_2 is the length of the triangular apex (Cleveland *et al.*, 1993; Butt, Cappella and Kappl, 2005) (Fig. 2.3). The resonant frequency, F_r of a rectangular cantilever can be calculated by the equation

$$F_r = \frac{1}{2\pi}\sqrt{\frac{k}{m*}} \quad (4)$$

where k is the spring constant and $m*$ is equal to 0.24 times the mass of the cantilever. This equation also provides a good approximation for triangular cantilevers (Tortonese, 1997).

The quality factor (Q) describes the relative width of the resonance peak and is equal to the resonance frequency divided by the half width of the square amplitude resonance peak (Butt, Cappella and Kappl, 2005). It is a dimensionless number whose value can elucidate the damping response of the cantilever, and be tuned to alter the response (Martin, Williams and Wickramasinghe, 1987; Rodríguez and García, 2003). In a vacuum the Q typically falls in the 10^4 - 10^8 range and is reduced to 10 – 200 in air. In liquid this is reduced further by around two orders of magnitude to give values of 1 – 5 (Butt *et al.*, 1993).

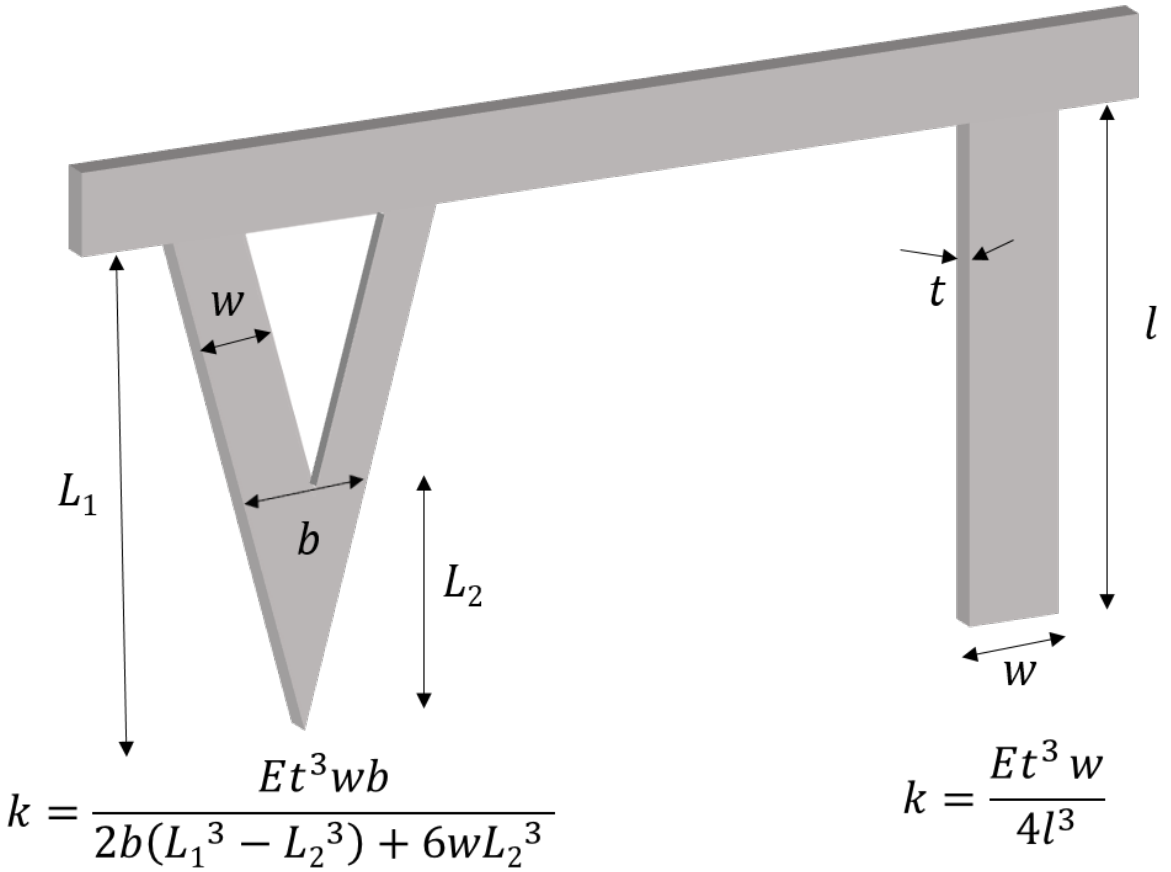

Figure 2.3. Schematic representation of triangular and rectangular cantilevers. The mechanical properties, such as spring constant k, and resonant frequency depend on the length *L*, width *w*, and thickness *t*, of the material.

2.1.7 The cantilever tip

The sharpness of the tip apex, which is defined by the radius of curvature, r, and the aspect ratio of height to width, are determining factors in the lateral resolution of the AFM (Frederix, Bosshart and Engel, 2009) (Fig. 2.4). The standard silicon nitride tip is usually a 3 - 6 µm tall pyramid with an end radius between 5 nm – 50 nm, for contact mode tips. Tip length can be up to 15 µm for intermittent contact mode cantilevers, with an end radius between 1 – 10 nm. Tips may also be manufactured in a conical shape. Smaller and sharper tips can be created, sometimes by using electron beam deposition or using a focused ion beam to mill away material. These milled tips are more fragile and the user has to decide if the potential for increased resolution is worth the risk. Indeed, many of the operating procedures on the AFM involve compromises between resolution, speed, stability and quality of results – and this present study is no exception. Whilst a sharper tip may improve

the resolution on hard, flat surfaces, often a larger radius tip may be better suited to a particular application. Soft biological samples, such as cells and membranes, are less likely to be damaged by a blunter tip for example, where a sharper tip may lead to a rupturing of the material. Forces as low as 10^{-10} N can damage or destroy biological samples (Radmacher, Cleveland and Hansma, 1995). The cantilever tip shall be discussed in greater detail in (Chapter 5).

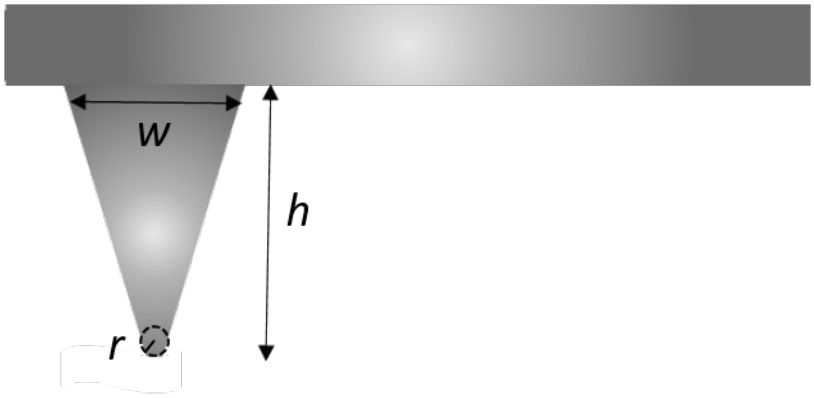

Figure 2.4. Schematic representation of an AFM tip. The cantilever tip is typically made from silicon or silicon nitride. The sharpness of the tip apex, which is defined by the radius of curvature, *r*, and the aspect ratio (*h* to *w*) are determining factors in the lateral resolution of the AFM. The tip is usually between 3 – 6 µm in length for contact tips, with tip radii between 5 – 50 nm. Intermittent contact tips are commonly up to 15 µm in length, with tip radii between 1 – 10 nm.

2.1.8 Imaging modes

There are a number of different modes used to acquire AFM images but the basic premise is similar, however. The tip raster scans over a sample (or the stage raster scans under a fixed tip in alternate systems) and the topography, and other information, is obtained line-by-line in the *X* and *Y* direction. These different modes all have their advantages and disadvantages. The choice of one versus the other could be the difference between success and failure of an experiment. Previous work from this laboratory (data not shown) and from this current study, have found that the oscillations from a cantilever in intermittent contact mode may lead to displacement of cells in a liquid medium, whereas other modes may facilitate

successful scanning. Methods to improve on the imaging capabilities of AFM are continually under development, and many groups use home-built systems towards this goal. Additionally, cantilever manufacturing has become more sophisticated in recent years, with shorter and much higher resonant frequency cantilevers now routinely available.

2.1.8.1 Contact mode

In contact mode, or static mode, the tip is brought into contact with the sample and the deflection of the cantilever is kept constant during scanning by the feedback loop. Image contrast depends on the applied force. The voltage applied to the feedback amplifier of the *Z*-height electrode keeps the deflection signal constant. When the cantilever is deflected through the surface interactions the scanner moves in the *Z*-axis in order to maintain the constant height. The amount the scanner has to move is taken to be the equivalent of the sample topography. This allows for accurate height measurements and images to be taken. Both the servo input and output can provide images, with the deflection (error) signal used mainly to provide topographical detail of features with large height differences (Ducker and Cook, 1990; Leckband, 2000; Tamayo *et al.*, 2001). The error signal is the difference between the setpoint and the effective deflection of the cantilever that results from the finite time response of the feedback loop. This loop acts as a high-pass filter that removes the low spatial frequency aspects of the surface and thus highlighting the high spatial frequency components. The tip is usually attracted to the surface due to capillary condensation. Common problems, particularly for soft samples in contact mode, result from the compressive forces of the tip contact and shear forces from the lateral scan movement (Zhong *et al.*, 1993). Soft and low-resonance frequency cantilevers are required in contact mode to prevent undue pressure on the sample surface.

2.1.8.2 Non-contact mode

Non-contact mode, or frequency modulation mode, shares similarities with intermittent contact mode. In non-contact mode the cantilever oscillates near its resonant frequency a short distance away from the sample surface. To prevent the ‘snap-in’ effect from van der Waals forces the cantilever needs to be stiff and with a high resonance frequency. An oscillating probe is brought into the proximity of a surface, but does not touch it. The van der Waals forces induce a frequency shift in the resonant frequency of the cantilever. Images are taken by keeping the frequency constant, by monitoring the amplitude of the

cantilever via the feedback loop and translating the information as a function of tip-sample spacing (Martin, Williams and Wickramasinghe, 1987). The technique is regarded as capable of providing true atomic resolution (Gross *et al.*, 2009), and is not damaging to soft samples, as there is no contact. It was generally restricted to vacuum conditions, however, recent advances in instrumentation have enabled atomic resolution in liquid studies (Morita *et al.*, 2000; Fukuma *et al.*, 2012). The minimum detectable force (F_{min}) required for atomic resolution typically lies between 10 – 100 pN. The spring constant, resonance frequency and the Q determine the theoretical limit of F_{min} in frequency modulation mode. In vacuum the Q can be between 1000 – 100,000, which more than satisfies this requirement, but as the Q in liquid is typically around 1 – 10 this can lead to a low efficiency and poor reproducibility of results (Fukuma *et al.*, 2012). Fukuma and co-workers managed to improve F_{min} in liquid by using small cantilevers that possess megahertz-order resonance frequencies. They compared four different cantilevers and found that their experimental results corresponded well to the theoretical estimates, using the rectangular beam model. To avoid squeeze damping of Q a sufficiently long tip was required. An electron beam deposition provided this but the interaction between it and the relatively inert sample led to difficulties in obtaining atomic resolution. This was overcome by sputtering silicon onto the tip. To excite the cantilever into resonance they used the photothermal method, which relies on the different thermal expansion coefficients of the cantilever and its reflective gold backing. A specially modified laser diode module and driver enabled a smaller, temperature-controlled laser spot onto the cantilever (Fukuma *et al.*, 2012). More recently, a group from the Department of Chemical Engineering at Pennsylvania State University reported the ability to image soft materials in liquid, in the non-contact regime using regular silicon cantilevers (Marchand, Hsiao and Kim, 2013). The authors conclude that the AC voltage applied to the cantilever in water causes it to vibrate at a specific frequency that is used to provide local surface information, but that a second frequency, twice that of the AC oscillation amplitude could be used for feedback control and topographical imaging. The end result is chemical and topographical detail with enhanced resolution when compared to air.

2.1.8.3 Intermittent contact mode

The same characteristics of non-contact mode are also required for intermittent contact mode (TappingMode™ or AC mode), where the cantilever oscillates near its resonant frequency via an additional driving signal. This leads to the cantilever tip only periodically touching the sample at the end of its oscillation cycle, which can reduce the forces that are transferred to a sample (Cleveland *et al.*, 1993; Tortonese, 1997; Frederix, Bosshart and Engel, 2009). The oscillation amplitude is made to be sufficient to overcome the stickiness of the surface, typically in the 20 – 100 nm range. It is measured as the root mean square (RMS) value of the deflection detector signal, with the feedback system set to detect the changes of the oscillation amplitude resulting from the intermittent surface contact (Zhong *et al.*, 1993). Height images are obtained in a similar manner to contact mode, but with the oscillation amplitude used as the feedback signal. The phase lag of the cantilever oscillation relative to the driving signal is also used to provide an image (Magonov, Elings and Whangbo, 1997). This lag is sensitive to variations in material properties, such as surface contaminants and differences in surface modulus and viscoelasticity. These images can be analysed to provide much greater detail about a sample than topography alone. Alternative systems of intermittent contact are possible. Instead of oscillating the cantilever the sample is tapped against the tip and uses a feedback loop to maintain the force at very low levels (Hansma *et al.*, 1994). This method of intermittent contact does not appear to be reported in the literature nowadays but amendments of the tapping technique are routinely reported, especially with regard to biological sample studies. Because the Q is greatly reduced in liquid this can have pronounced effects when working in intermittent contact mode. Tamayo and colleagues devised a dynamic force microscopy technique for use in liquid (Tamayo *et al.*, 2001). A cantilever in amplitude modulation mode can be thought of as a damped harmonic oscillator where its response (z) to the incident forces (F) can be expressed as $z(\omega) = X(\omega)\, F(\omega)$ according to the equation

$$X(\omega) = \frac{\omega_0^2/k}{\omega_0^2 - \omega^2 + i\omega_0\omega/Q} \tag{5}$$

where ω_0 and ω are the resonant and incident force frequencies respectively, k is the spring constant and Q is the quality factor. In their system an AC magnetic field is used to excite magnetically coated cantilevers. The authors claim to be able to increase the Q by up

to three orders of magnitude than that of traditional intermittent contact mode systems in liquid (Tamayo *et al.*, 2001). In liquid experiments the van der Waals and electrostatic forces are important, as the surfaces can become charged due to dissociation of surface groups. Van der Waals are typically attractive forces and the electrostatic forces repulsive. In air a water neck forms between the tip and the surface due to capillary condensation and adsorption of thin water films at the surfaces, leading to an attractive force (Hooton *et al.*, 2004; Butt, Cappella and Kappl, 2005).

2.1.8.4 Force spectroscopy

A major advantage of the AFM, when compared to other forms of microscopy, is the ability to obtain measurements of mechanical elasticity, stiffness, adhesion and viscosity of a sample, in addition to an image. Even single molecules can be assayed and the forces required to bond, stretch or break bonds can be measured (Butt, Cappella and Kappl, 2005). One could functionalise a tip with a ligand, such as an antibody for example, and use it to bind to a membrane protein. From this, it is possible to deduce the binding energies of this antibody-antigen interaction, such as from van der Waals, hydrogen bonds and hydrophobic and steric contacts (Leckband, 2000). The principles of obtaining a force measurement (force-distance curve, or F-D curve) (Fig. 2.5) involve approaching the sample until the distance becomes small enough for the tip and sample to interact, which leads to a shift in the resonant frequency. Attractive forces reduce and repulsive forces increase the frequency. This change in frequency can be used to analyse surface forces (Ducker and Cook, 1990). If the interaction is strongly attractive, and greater than the spring constant of the cantilever, the tip accelerates towards the sample. When they come into contact with each other, the deflection of the cantilever is directly coupled to the piezo movement (Senden, 2001). The point of contact, often called the ‘snap in’ leads to a characteristic dip in the curve, although this can be overcome by using stiffer cantilevers, and is often absent in liquid studies. The cantilever bends until it reaches the specified force limit (setpoint) voltage defined by the user (Fig. 2.2 (4ii)). Depending on the setpoint value the tip may indent the sample, and this is dependent upon the stiffness of the sample. A linear slope represents this part of the F-D curve. At this point the cantilever is the most compliant component of the system and directly measures the optical sensitivity of the detector with respect to the cantilever deflection. Under application of the retraction force the tip

detaches from the sample surface. The adhesive properties of the surfaces may result in a primary adhesion between the cantilever and the sample (Fig. 2.2 (4i)) until a spring instability occurs again. Further secondary adhesions, typically resulting from the bridging of macromolecules, occur away from contact. These adhesion events, sometimes termed the 'snap off' lead to another characteristic peak/s on the F-D curve, before returning to the baseline value (Senden, 2001). The amplitude and frequency of the vertical movement of the scanner can be adjusted to control the speed and distance that the AFM travels during the force measurement. A F-D curve is a measurement of cantilever deflection, Z_c, versus height position of the piezo scanner, $Z_{p,}$ normal to the surface (Butt, Cappella and Kappl, 2005). The photodiode signal has to be calibrated to accurately measure this deflection and it is essential to leave the laser alignment unchanged after calibration. Usually the software has simple calibration settings. The measured voltage at this stage is converted into cantilever deflection using either a measured sensitivity value or more routinely the inverse optical lever sensitivity (InvOLS). To calculate InvOLS a force measurement is typically performed on a hard surface, such as mica or glass, to measure the voltage response of the photodiode as a function of the known distance moved by the piezo. This process creates a linear slope whose inverse can then be given as the InvOLS (Cleveland *et al.*, 2006). This value can then be fitted to the curve of the experimental data. The spring constant of the cantilever must also be accurately determined and is routinely found using the thermal noise method (Hutter and Bechhoefer, 1993).

A spring constant of 0.05 N/m, at room temperature, may show thermal fluctuations in the order of 3 Å. Such small deflections allow the cantilever to be approximated as a simple harmonic oscillator with one degree of freedom. If the RMS fluctuations of a freely moving cantilever are sampled with frequencies much higher than the resonant frequency of the cantilever, to avoid averaging out the fluctuations, you can estimate the spring constant. Additional noise sources may also be present and it is unlikely that they will share the same resonant frequency of the cantilever. By subtracting these from the thermal response you are left with an area under the remaining peak that is a measure of the power of the cantilever fluctuations (Hutter and Bechhoefer, 1993). Once these calibrations are performed, and in order to make the force curve into a quantifiable measurement, the obtained values of deflection (Voltage) versus height have to be converted into force versus

distance. The force F is obtained by multiplying the deflection of the cantilever with its spring constant k, and the tip – sample separation (distance) *D* is calculated by adding the piezo height (Z_p) to the cantilever deflection (Z_c) (Butt, Cappella and Kappl, 2005). The F-D curve is then usually analysed by fitting against mathematical models of contact mechanics – typically the Hertz model for soft biological samples.

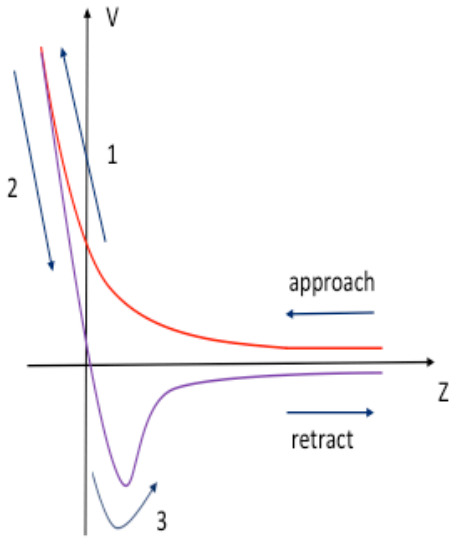

Figure 2.5. Sketch of a force - distance curve plot of voltage, V against piezo height, *Z*. Approach and retract represents the non-contact movement of the scanner in the *Z*-direction, when the tip is far from the surface. 1, repulsive contact regime, where the cantilever is deflected until the defined setpoint limit is reached. 2, retraction of the cantilever, where the *Z*-piezo withdraws the scanner upon reaching the setpoint value. 3, adhesive 'snap off' location (if the sample is sufficiently adhesive).

2.1.8.5 Multiparametric imaging

Traditionally, force measurements were taken in a force spectroscopy regime, whereby ranges of indents were collected over a random, or ordered region of a sample and the relevant F-D curves gathered. Combining these curves with imaging would be a huge advantage. A number of manufacturer's have developed methods that allow the AFM to obtain force measurements, whilst collecting image data at the same time. A solution proposed in 1994 by Manfred Radmacher and colleagues, then part of the Hansma group (Radmacher *et al.*, 1994), was to gather an ordered array of F-D curves, individually analyse them and spatially organise them against a topographic image. The method was licensed to

Digital Instruments (formerly Veeco) – now Bruker Corporation. This force-volume (F-V), or force mapping technique proved very useful for soft samples, as the lateral forces are virtually non-existent as the tip detaches from the surface between indents. The spatial and temporal resolution were quite limited however, and limited the acquisition of many dynamic processes in the life sciences (Dufrene *et al.*, 2013). In recent years improved techniques have enabled researchers to capture quantitative 3D images with F-D curves at speeds similar to conventional AFM topography imaging. In PeakForce Quantitative Nanomechanical Mapping (PF-QNM), also from Bruker Corporation (Alsteens *et al.*, 2012) the tip is oscillated with a frequency of 0.25 – 10.0 kHz and with an amplitude of 100 – 300 nm (Alsteens *et al.*, 2012; Dufrene *et al.*, 2013; Smolyakov *et al.*, 2016). The approach and retract from the sample surface are performed in a sinusoidal waveform, as opposed to a simple rectangular up-down-and move pattern used in F-V (Fig. 2.6). The oscillating system allows for direct control of lateral forces, and at frequencies that are up to three orders of magnitude greater than F-V. In addition, the pixel resolution can be much greater – up to 2048 x 2048 pixels, compared to the 64 x 64 pixel resolution of traditional F-V imaging (Alsteens *et al.*, 2012).

2.1.8.6 Quantitative Imaging (QI™) mode

A further development of multiparametric imaging came from JPK Instruments under the guise of Quantitative Imaging (QI™) (JPK Instruments AG, 2011; Chopinet *et al.*, 2013). This imaging mode works without applying any lateral force and gives the user the ability to control the force at every pixel - up to a 512 x 512 pixel resolution. There is no feedback loop and thus no requirement for setpoint or gain adjustment while scanning. Cantilevers with spring constants from <0.01 N/m to >40 N/m can be used, to determine the mechanical properties of soft material such as living cells, to hard substrates such as glassy polymers respectively, and the interaction force can be controlled to <50 pN. Sample rates up to 800 kHz can be used to allow for fast F-D measurements even at approach and retract velocities >50 µm/s. The large *Z*-range of 15 µm (on the NanoWizard® III AFM) allows for imaging tall samples and ensures that any surface asperities are avoided during the retract portion of the scan. Additionally, any surface adhesions from sticky samples are overcome. In contrast to PF-QNM there is no sinusoidal oscillation of the cantilever, and the frequency range is similar to that of F-V – being around 0.5 – 100 Hz. Crucially, QI™ uses a novel tip

movement algorithm (Fig. 2.7). The approach and retract from the sample are performed via a sawtooth waveform, which provides even less chance of lateral distortion, when compared to F-V or PF-QNM. Moreover, there is no movement in the *XY* direction whilst a F-D curve is being recorded. This ensures that the F-D curve is measured under a constant velocity. There is a sinusoidal deceleration movement at the end of the retract motion that the user can manipulate, both for height and length, before the next sawtooth approach. A 'dynamic baseline correction' corrects the viscous drag of the cantilever in the F-D curves (Braunsmann *et al.*, 2014). The collected F-D curve can be analysed by the Hertz, Sneddon or DMT (for adhesion study) contact mechanics models provided in the software. If preferred, the user could export the data for analysis with a model of their choosing (Chopinet *et al.*, 2013). Because of the ability to control the forces exerted on a sample this technique allows for gentle imaging, even where quantitative mechanical data may not be required. QI™ AFM has been widely used in the literature for eukaryotic cells (Chopinet *et al.*, 2013; Horimizu *et al.*, 2013; Braunsmann *et al.*, 2014) and prokaryotic cells (Chopinet *et al.*, 2013; Francois *et al.*, 2013; Formosa-Dague *et al.*, 2016; Smolyakov *et al.*, 2016; Solopova *et al.*, 2016) respectively. This study found that living, hydrated and loosely bound bacteria could be repeatedly scanned, for up to many hours, without being displaced. Conversely, other imaging methods, (such as contact or intermittent contact) both on the JPK NanoWizard III® or other systems, (including PF-QNM), routinely failed. In addition to topographical images, elasticity and stiffness (slope) images can also be obtained, with brighter regions of the images representing the less elastic or stiffer regions respectively. The slope image is generated by making a linear fit to the approach region of the F-D curve at every pixel.

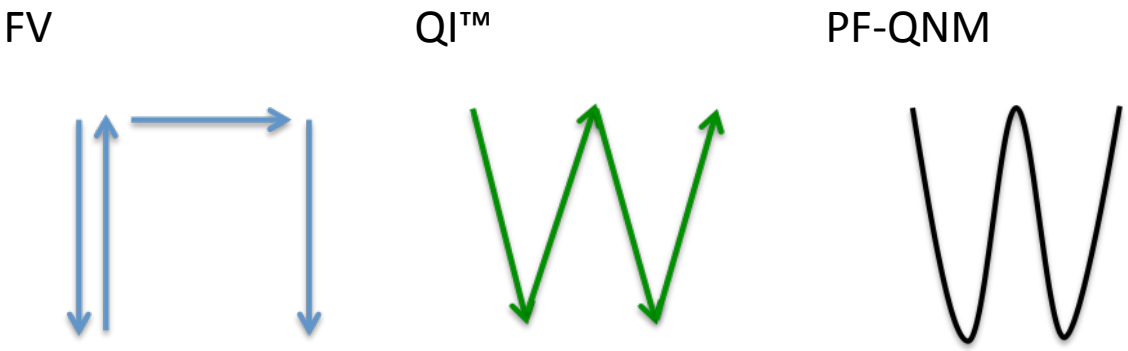

Figure 2.6. Schematic representation of tip motion in FV, QI™ and PF-QNM. In FV, the scanner motion is ordered in a simple linear direction during the approach, retract and movement to the next pixel. In QI™ the approach and retract are performed via a sawtooth waveform. The approach and retract is sinusoidal in PF-QNM.

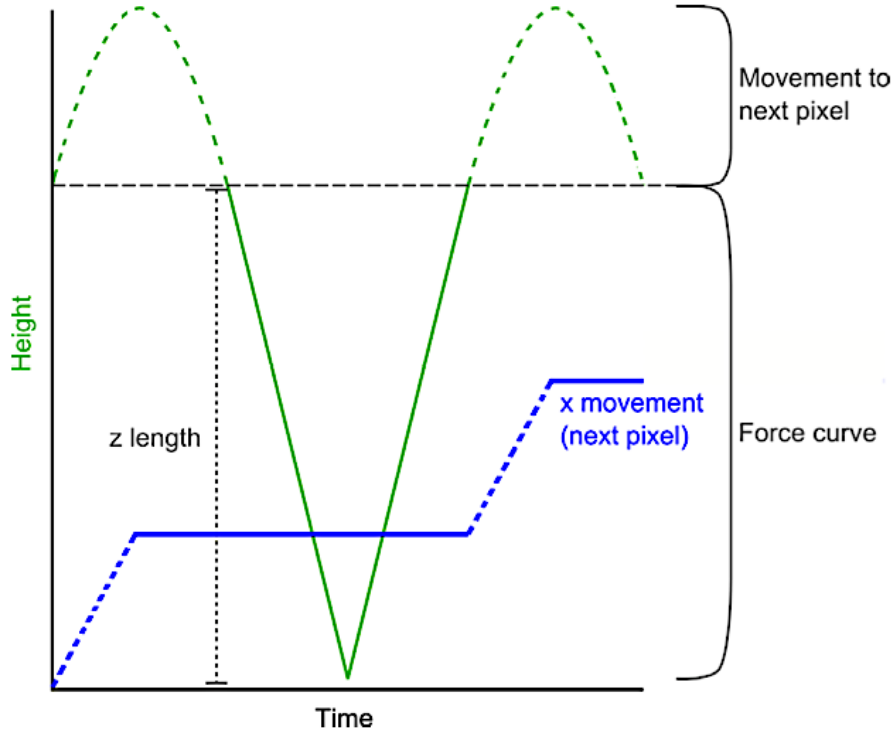

Figure 2.7. JPK QI™ tip algorithm. Schematic views of the cantilever movement during a QI™ scan. The green line depicts the *Z*-movement of the cantilever. The blue line shows the *X*-movement. A complete force-distance curve is recorded at every pixel of the image while there is no *XY* movement of the tip. The user can control the sinusoidal deceleration and movement to the next pixel. Reproduced from JPK Instruments (2011).

Etienne Dague's group compared FV, PF-QNM and QI™ modes at high-speed indentation on the bacterium *Pseudomonas aeruginosa* (Smolyakov *et al.*, 2016). They used the Hertz model for FV and QI™ and the Sneddon model for PF-QNM. They found that the difference between modulus values was as low as 10% for F-V data between the Hertz and Sneddon contact models, suggesting that both models could be applied. The difference between different operating modes and systems, however, was more varied. They found that elastic modulus remained consistent for indentation frequencies below 20 Hz in all three modes. When increasing the scanning frequency above 20 Hz, and up to 79 Hz, in F-V and QI™ modes on the JPK NanoWizard III® there was an increase in elastic modulus vs. frequency. Conversely, F-V and PF-QNM modes on the Bruker BioScope Catalyst™ showed the opposite relationship, with a decrease of elastic modulus vs. scanning frequency. The authors attribute this phenomenon to creep relaxation of the bacterial cell wall. They concluded that all three modes provided consistent modulus maps, and cellular morphology, and that one may benefit from lower acquisition times within QI™ or PF-QNM. The elastic modulus data presented in this study were all gathered in QI™ mode at a scanning frequency of 22.5 Hz (Chapter 3.8.3). Previous research from our laboratory (data not shown) has suggested that viscoelastic creep relaxation of the SA cell wall is negligible between 1 – 60 s, with relatively little measurable change.

2.1.9 Using AFM in a liquid medium

Because biological samples may benefit from study in a liquid medium there are certain considerations that must be met when planning such an experiment. The temperature, and particularly the variation of it are critical to the outcome of an experiment. The cantilever is extremely sensitive to temperature changes and thus the control of temperature is desirable (Workman and Manne, 2000). It is important to allow the system to equilibrate prior to image capture. If the temperature changes during an experiment the resulting thermal deflections of the cantilever may lead to aberrations in the image. The thermally-induced bending of a cantilever can increase the imaging force applied to a sample, which may be damaging to a soft sample in contact mode, if restorative intervention from the user is not applied. The thermally-induced bend has been estimated to be in the order of 100 nm/Kelvin) for a typical cantilever (Workman and Manne, 2000). Using typical silicon or silicon nitride cantilevers with a length of 200 µm and a thickness of 0.5 µm as an example, a

temperature change of only 0.1 K will result in a relative change of 1 x 10^{-6} between the cantilever material and the gold reflective backing, due to the differences in the thermal expansion coefficients of the two materials. This results in a bending which can raise the end of the cantilever by 40 nm and a change in force of 4 nN (Radmacher, Cleveland and Hansma, 1995). The AFM utilises two different methods in an attempt to manage the temperature control. These are either by a high gain feedback loop with a system that can provide fast thermal response, or an open-loop operation that has a slower thermal response (Workman and Manne, 2000). The high gain (closed loop) system uses highly conductive materials with large thermal expansive properties, for example, copper. The fast temperature response of these materials is limited by the liquid, which may negate the efficiency of this system. In an open-loop system, a moderate thermal mass prevents fast temperature drift, once the system has equilibrated to its target temperature.

The forces interacting between liquid-solid interfaces are equally important. When immersed in a liquid the cantilever experiences drag due to increased viscosity and density effects than in air, resulting in a decrease of the resonance frequency and the Q, in addition to the fluid mass being accelerated by the cantilever motion (O'Shea and Welland, 1998). A means of improving the Q can be achieved by decreasing the size of the AFM probe. Reducing the dimensions of the cantilever will increase its resonance frequency (Hoogenboom and Leung, 2013). This can be seen from the mass term in equation (4). The higher resonance leads to a decreased thermal noise, as it is spread over a larger bandwidth. Further, by increasing the resonance frequency and Q, while decreasing, or keeping the k constant, the F_{min} can be decreased, contributing to improved resolution (Hoogenboom and Leung, 2013)

2.1.10 Elastic contact models

2.1.10.1 Hertz and Sneddon

Indentation of elastic solids has been studied for over a century. Heinrich Hertz first pioneered the contact between elastic bodies (Hertz, 1882) where he approximated shallow indentations for a smooth elastic sphere onto a rigid flat surface, according to the equation

$$F = \frac{4}{3}\frac{E_s}{1-v_s^2}\sqrt{r}\delta^{\frac{3}{2}} \quad (6)$$

where E_s is the sample surface modulus, v_s is the Poisson's ratio, r is the tip radius of curvature, and δ is the displacement of the indenter. The model was extended to study the contact problem between two linearly isotropic solids (Boussinesq, 1885). Ian Sneddon took the approach by Boussinesq to derive the load-displacement relationship for a rigid conical indenter (Sneddon, 1948) to derive the equation

$$F = \frac{2}{\pi}\frac{E_s}{1-v_s^2}\tan(\alpha)\delta^2 \quad (7)$$

where α is the half opening angle of the indenting cone. He later extended his work for other indenter geometries (Sneddon, 1965).

Both models are still widely used today – even at the nanoscale, with certain limiting constraints; (i) that the sample is an infinite half-space, (ii) the material is linearly elastic, isotropic and incompressible, and (iii) the indenter has an ideal geometry with known parameters (i.e. a perfect sphere or cone). Biological samples rarely satisfy these criteria and defining the indenter geometry is difficult. Additionally, neither Hertz nor Sneddon consider surface forces, that may interact with an indenter prior to hard contact, nor the adhesive interactions during retraction. Despite these limitations, the Hertz and Sneddon models are widely used in material (Domke and Radmacher, 1998; Mesarovic and Fleck, 1999; Lim and Chaudhri, 2004; Denisin and Pruitt, 2016) and biomechanical sciences (Eaton *et al.*, 2008; Chopinet *et al.*, 2013; Smolyakov *et al.*, 2016; Solopova *et al.*, 2016).

2.1.10.2 Alternative contact models

In order to address the limitations of the Hertz and Sneddon models, several other models were developed that consider adhesion effects, and are equally widely used in the materials and biological sciences. These include the Johnson-Kendall-Roberts (JKR) model (Johnson, Kendall and Roberts, 1971) and the Derjaguin-Muller-Toporov (DMT) model (Derjaguin, Muller and Toporov, 1975). The JKR model is applicable for elastic deformation with large adhesion, on soft materials indented with large tips. Conversely, the DMT model considers elastic deformation with small adhesion, on soft samples with small tips.

2.1.10.3 Young's modulus

The Young's (elastic) modulus is a numerical constant, named after the 18th-century physician and physicist Thomas Young. It is a property that represents how much resistance a material offers to being elastically deformed along an axis, under the application of a load (Khan and Hoffmann, 2016), and is equal to the longitudinal stress divided by the strain, according to the equation

$$E = \frac{\sigma}{\varepsilon} \tag{8}$$

where E is the Young's modulus, σ is the tensile stress and ε is the tensile strain. Tensile stress is derived according to the equation

$$\sigma = \frac{F}{A} \tag{9}$$

where F is the tensile force and A is the cross-sectional area. Tensile strain is derived according to the equation

$$\varepsilon = \frac{\Delta L}{L} \tag{10}$$

where ΔL is the amount by which the length L of the object changes. Substituting equations (9) and (10) into (8) gives

$$E = \frac{FL}{\Delta LA} \tag{11}$$

The stress has units of pressure, whose SI unit is the Pascal (Pa or N/m^2). The strain is a dimensionless number, thus the Young's modulus has units of pressure. When a metal bar under tension is elongated, its width is slightly reduced. This lateral shrinkage represents a strain that is equal to the change in width, divided by the original width. The ratio of the lateral strain to the longitudinal strain is called the Poisson's ratio, which is also a dimensionless value. Most materials have a Poisson's ratio between 0.0 and 0.5. Most steels typically exhibit a value ~ 0.3 (Dejun *et al.*, 2004). A perfectly incompressible rubber, for example, would have a Poisson's ratio of 0.5 (Poon, Rittel and Ravichandran, 2008). Polymers, cells and bacteria are routinely considered to be elastic, incompressible materials and are given a Poisson's ratio of 0.5 (Magonov and Reneker, 1997; Chen, 2014; Pogoda *et al.*, 2017). Young's modulus is meaningful only in the range where the stress is proportional to the strain, and the material resumes its original dimensions once the external load is

removed. Because AFM tips could be considered as sharp cones, there is a danger that indenting could cause plastic deformation (Domke and Radmacher, 1998). In principle, however, the semi-included angle of the cone should not affect the measured elastic properties, if appropriate models are used (Chen, 2014). Repetitive measurements on a bacterial surface have been shown to exhibit no significant changes in morphology, suggesting plastic deformation was not considered to play an important role (Smolyakov *et al.*, 2016). Equally, this study has taken multiple scans of the bacterial surface, over a sustained timeframe, and no obvious signs of plastic deformations were observed (discussed in Chapter 6). The Young's modulus is often called the elastic modulus in the literature and both terms are used interchangeably.

Chapter 3

Materials and Methods

3.1 Growth media

All media were prepared using deionised water (dH_2O) and autoclaved at 121° C for 20 min, 15 pounds per square inch (psi) unless otherwise stated. For filtered growth medium a sterile Millex® (0.22 µm pore) syringe filter was used (Merck Millipore). For solid medium Bacteriological agar (Oxoid) 1.5% (w/v) was added.

3.1.1 Brain heart infusion (BHI)

Brain heart infusion broth (Fluka)	37 g l^{-1}

3.1.2 Tryptone soy broth (TSB)

Tryptone soy broth (Sigma)	30 g l^{-1}

3.2 Antibiotics

Oxacillin (Sigma)	0.25 µg ml^{-1}

Oxacillin was prepared in a dH_2O stock solution, filter sterilised (0.22 µm pore) and stored at -20° C. Stock concentration was 512 µg ml^{-1} and working concentrations were diluted in dH_2O. The MIC was established to be 0.25 µg ml^{-1} from a minimum inhibitory concentration evaluator strip (Thermo Scientific) (data not shown) and 10x MIC (2.5 µg ml^{-1}) was used for experiments (unless stated).

Methicillin (Sigma)	4.0 µg ml^{-1}

Methicillin was prepared in a dH_2O stock solution, filter sterilised (0.22 µm pore) and stored at 4° C. Stock concentration was 10 mg ml^{-1} and working concentrations were diluted in dH_2O. The MIC was established to be 4.0 µg ml^{-1} (data not shown) and 10x MIC (40 µg ml^{-1}) was used.

3.3 Buffers and solutions

Stock solutions were prepared using dH_2O and stored at room temperature, unless otherwise stated.

3.3.1 Phosphate buffered saline (PBS)

NaCl	8.0 g l^{-1}
KCl	0.2 g l^{-1}
KH_2PO_4	0.2 g l^{-1}
Na_2HPO_4	1.15 g l^{-1}

Five P4417 tablets (Sigma) were dissolved in 1l dH_2O. pH 7.4, at 25° C.

3.3.2 AFM imaging buffer

KCl	300 mM
Tris HCl (pH 7.8)	10 mM

CHROMASOLV™ dH_2O (Honeywell) to required final volume and stored at 4° C.

3.3.3 Porcine serum

Porcine serum (Sigma)	500 ml

5 ml aliquots were prepared from undiluted USA origin, sterile-filtered stock and stored at -20° C.

3.4 Bacterial strains

Staphylococcus aureus strains were taken from a Microbank™ storage bead (Pro-Lab) kept at -80° C and grown on BHI or TSB agar plates. The plates were incubated overnight at 37° C and stored at 4° C for up to 4 weeks. All the strains used in this study are listed in (Table 3.1)

Strain	**Genotype / Marker**	**Source**
SH1000	Functional *rsbU*$^+$ derivative of 8325-4	(Horsburgh *et al.*, 2002)
SH1000-GFP	geh::Pma1M-gfp	(Pollitt *et al.*, 2018)

Table 3.1. *S.aureus* strains used in this study.

3.5 Bacterial growth and cell culture

A single colony was used to inoculate 10 ml BHI or TSB in a 50 ml Falcon tube and grown overnight at 37° C, with aeration at 250 rpm. A 10 ml growth medium control was incubated with all cultures. The overnight starter culture was used to inoculate fresh media (10 ml) to a target optical density (OD_{600}) of 0.05. Cultures were grown at 37° C, with aeration at 250 rpm for ~ 1.5 h until an OD_{600} of typically ~ 0.2 - 0.5 for mid-exponential phase cells. For stationary phase cell studies, cells were taken from the overnight culture with an OD_{600} routinely around 8 – 15. All steps were prepared aseptically near a flame.

3.5.1 Optical density measurements (OD_{600})

Bacterial concentration was determined by spectrophotometry (WPA Biowave) by calculating the optical density at 600 nm (OD_{600}). All cultures were diluted 1:10 in the overnight control media.

3.6 Centrifugation

Various centrifuges were used in this study and are listed below. Centrifugation was performed at room temperature unless otherwise stated.

a) Sigma SciQuip 3K15 — Max load, 16 x 50 ml; Max speed, 15,300 rpm (23,031 *x* g)
b) Eppendorf™ centrifuge 5424 — Max load, 24 x 2 ml; Max speed 15,000 rpm (21130 *x* g)

3.7 Etched silicon wafer design, processing and experimental usage

A 2-inch silicon wafer was used for contact mask photolithographic patterning of custom designs similar to a method previously described (Kailas *et al.*, 2009). Saurabh Kumar at the Kroto Research Institute performed the design and fabrication.

Two types of silicon wafers were processed. A raised pillar design that would be used to imprint holes onto a PDMS substrate, cast from the wafer; and an inverted pillar design to imprint pillars onto a PDMS substrate. Additionally, the inverted pillar design was used regularly to directly trap bacteria onto the silicon surface within the inverted pillars (wells). To process between raised or inverted pillars simply requires changing the photoresist between a positive, or negative tone photoresist respectively.

3.7.1 Design of the mask templates

Three distinct designs were created in WaveMaker® LAYOUT design software (Barnard Microsystems) for patterning onto the silicon wafer (Chapter 4). 1) A repeating lattice of ~ 1.5 µm diameter circles separated by ~ 1 µm between them. 2) A repeating lattice of 5 µm circles arranged to achieve a 4 sided star shape between them similar to (Kailas *et al.*, 2009) with a diagonal spacing of 2.5 µm between the circles. 3) A ~ 36 µm width x ~ 100 µm length grid comprised of 8 repeating arrays of 10 x 1.5 µm circles, 10 x 2.5 µm circles, 10 x 3.5 µm circles and 2 repeating arrays of 2 x 5.5 µm length x 1.5 µm wide rod shaped features. The whole grid was separated from the next grid ~ 93 µm horizontally and ~ 64 µm vertically. Below each individual grid is an *XY* grid reference numbering system.

3.7.2 Fabrication of raised pillar wafers

A 2-inch silicon wafer was given a three-stage clean in >99.9% (v/v) *n*-Butyl acetate, acetone and isopropanol for 30 s respectively and pre-baked at 100° C for 1 min. A 750 nm silicon oxide (SiO_2) layer was deposited using Plasma Enhanced Chemical Vapour Deposition (PECVD). The wafer was spin-coated with hexamethyldisilazane (HDMS) adhesion promoter at 4000 rpm, 30 s and MEGAPOSIT™ SPR™ 350 positive photoresist (Dow Corning) at 4000 rpm, 30 s. The wafer was baked at 100° C for a further 1 min. The wafer was exposed, via vacuum contact, with the relevant mask on an MJB 3 mask aligner (SÜSS MicroTec) under UV at a 300 nm wavelength for 15 s, and developed for 1 min in a MICROPOSIT™ MF-26A developer (Dow Corning). The wafer was blow-dried under Nitrogen gas (N_2) and the developed pattern checked with optical microscopy. To remove any traces of photoresist the wafer was given oxygen plasma etching for 1 min in a Reactive Ion Etching (RIE) system. The pattern etching was performed in the RIE system with Fluoroform (CHF_3) and Argon at 20 cm^3 min^{-1} and 35 cm^3 min^{-1} respectively, to a depth of ~ 750 nm. The wafer was given a three-stage clean (as previously) to remove any photoresist residue. The wafer was scribed through the centre of the etched holes in the SiO_2 layer to check the etch depth. Finally, the wafers were checked with SEM (Raith EO) and images collected at 10.0 kV using a 125 eV secondary electron detector (Bruker Corporation). For assays with the photoresist-coated wafer the RIE etching and three-stage clean were omitted.

3.7.3 Fabrication of inverted pillar wafers

All steps were performed as for raised pillar wafers, but substituted with ma-N 1410 (Micro resist) negative photoresist. A negative photoresist polymerises under exposure to UV light and becomes less soluble than a positive photoresist, and thus, extremely difficult to dissolve. This results in the negative photoresist remaining on the surface while the developer solution works to remove the areas that are unexposed.

3.7.4 Experimental use of silicon wafers

Small ~ 4 mm^2 sections were removed by diamond scribe and secured to a 35 mm plastic tissue culture dish with rubber elastomer.

3.8 PDMS substrate preparation and experimental usage

Polydimethylsiloxane (PDMS) substrate was prepared using SYLGARD® 184 silicone elastomer kit (Dow Corning). The pre-polymer and curing agent were mixed 10:1 (unless otherwise stated), following the manufacturers' instructions (routinely 6.0 g: 0.6 g respectively) and degassed for ~ 5 min under vacuum at room temperature. This mixture was poured onto a silicon stamp template (placed in a glass dish) that had been briefly immersed in 10% (w/v) Brij® 52 (Sigma) surfactant, prepared following the manufacturers' instructions. This surfactant coats the silicon stamp and allows for easier removal of the PDMS. They were heated in an oven at 70° C (routinely checked with thermocouple) for 2 h. The PDMS was carefully removed and both it, and the silicon stamp, were given a three-stage clean, with sonication, in 5 ml of mild detergent, anhydrous, 99.5% isopropanol (Sigma) and dH_2O for 10 min respectively and dried under N_2. Multiple PDMS substrates were made throughout this study, with each being used for a single assay.

3.8.1 Tensile analysis of PDMS

Chris Holland at the Department of Materials Science and Engineering performed the tensile testing.

Five pieces of PDMS of varying thickness, with a total area between 3 – 12 mm^2 and from freshly made to 4 weeks old, were trimmed into rectangles, to fit into the specimen grips of a zwickiLine Z0.5 testing machine (Zwick Roell). A mean force of 3.7 ± 0.5 N was used to break the PDMS samples and the modulus was determined from a gradient of ~ 14% of their

strain curves, using testXpert® II software (Zw*i*ck Roell). The outputted data were exported into Microsoft Excel (2013) v.15.0.5015 for Windows and analysed further.

3.8.2 Nanoindentation analysis

Dawn Bussey at the Department of Materials Science and Engineering performed the nanoindentation experiments.

Freshly prepared and aged PDMS samples were analysed on a TI Premier TriboIndenter® (Hysitron) using a 5 µm *Z*-axis transducer. The transducer was calibrated at the start of every experiment, following the manufacturers tip to optics calibration routine, by performing an 'H' pattern on a hard substrate, such as polycarbonate, fused quartz or aluminium. An 'area function' for each indenter was created by generating load-displacement curves over a range of increasing depths. The transducer piezo was allowed a rest period prior to PDMS analysis, to minimise drift. Various diamond indenter probes (with differing geometries) and a range of loading forces were used. A Berkovich indenter with a 142.3° included angle and 100 nm radius of curvature was used in dH_2O. Automated and single indents with loading forces of 3 µN – 100 µN were taken via load control and displacement control feedback tests. The load function was set to a trapezoid with 5 s load time – 50 s hold time – 5 s unload time, with a lift height of 10 nm. A 100 µm radius conospherical probe with a 90° included angle was used in dH_2O. Single indents were taken at loading forces between 0.8 µN – 20 µN. The load function was set to a trapezoid with 5 s – 2 s – 5 s and a lift height of 500 nm – 2.0 µm. Tests were done in air with a 1 µm radius conospherical probe with a 90° included angle. Loading forces of 3 µN – 15 µN and a lift height of 180 nm – 2 µm were used. The load function was set to a trapezoid with 5 s – 50 s – 5 s load control. A 1 mm diameter sapphire flat punch was used in air. No area function was required as the indenter geometry is not assumed to change on increased indentation. Loading forces between 3 µN – 100 µN and a load function of 5 s – 5 s – 5 s were used, with a lift height of 500 nm – 2 µm. The 1 mm diameter flat punch was used for a further experiment, and was operated in open-loop (no feedback) mode for a comparative assessment of sample modulus, with a pre-load of 1 µN – 2 µN. Loading forces of 10 µN – 30 µN and a trapezoid load function of 5 s – 5 s – 5 s were used. All indentation data were analysed with TriboScan™ software v. 9.41.0 (Hysitron) and exported into Microsoft Excel (2011) for Mac, v.14.0.0 for further quantification

3.8.3 AFM multiparametric imaging of PDMS and hydrated bacteria

A NanoWizard® 3 AFM, software v. 5.0.51 or NanoWizard® ULTRA speed, software v. 6.1.81 (JPK Instruments) were used for all live cell experiments on all substrates, in Quantitative Imaging (QI™) mode. Both AFM systems were coupled with optical imaging capacity for easier visualisation of samples and substrates. The NanoWizard® 3 AFM was mounted onto a Nikon T*i* inverted optical microscope fitted with a 10X Plan Fluor 0.30 NA objective. The NanoWizard® ULTRA speed was equipped with an MVL12X3Z top view modular 12X optical zoom lens (Thorlabs Inc.). All experiments were performed with the same settings unless otherwise stated. MLCT silicon nitride cantilevers (Bruker Corporation) with silicon nitride tips were used throughout unless otherwise stated, with a new cantilever used for every experiment. The probe layout consists of 6 different cantilevers labelled A to F, each with a different resonant frequency and spring constant. In order to standardise the experiments, and the acquired mechanical data, cantilever D was used throughout. The other cantilevers were not removed. Cantilever D has a nominal resonant frequency of 15 KHz and a nominal stiffness of 0.03 N/m. It is triangular with a nominal length of 225 µm and a nominal width of 20 µm. The backside is coated with reflective gold and the top layer is 45 ± 5 nm of titanium/gold. The tip geometry is rotated (symmetric) with the height between 2.5 – 8.0 µm and a nominal radius of 20 nm (maximum 60 nm). Typical frequencies in liquid were ~ 3 kHz, integrated amplitude ~ 3 pm/√Hz, and Q ~ 1.5. The inverse optical lever sensitivity (InvOLS) (Cleveland *et al.*, 2006) was performed at the start of each experiment in air and liquid on freshly cleaved mica or potassium hydroxide (KOH)-cleaned glass coverslip. The thermal noise method (Hutter and Bechhoefer, 1993) was used to determine the cantilever spring constant using the calibration routine in the JPK software with corrections applied for the 10° cantilever tilt (Hutter, 2005). The spring constant from the air calibration routine was used with the InvOLS value from the liquid measurements. All images and force curves were analysed using JPK Data Processing software v.spm-5.1.13 (JPK Instruments). QI™ setpoint was typically either 1 nN or 5 nN for cell wall or whole cell respectively. *Z*-length was set to 900 nm with an additional 50 nm added before going to the next pixel. Values lower than these led to unfavourable adhesion between the sample and cantilever. Approach and retract times were 40 ms, which equated to 22.5 µm/s. Motion and acceleration times were 1.0 ms and sample rate was 100 kHz. These settings consistently

produced favourable F-D curves and data. The time taken to complete each full scan was 5.76 min, at a resolution of 64 x 64 pixels over a 10 x 10 µm scan region. This scan time was found to yield results comparable with a slower force mapping study, previously performed and published from this laboratory (data not shown) (Bailey *et al.*, 2014).

3.9 AFM F-D curve modulus analysis

All F-D curves were analysed using JPK Data Processing software v.spm-5.1.13 (JPK Instruments) using the approach portion of the curves. The inbuilt operators were loaded in a specific, necessary order, and were saved as a user 'process'. This process could be easily loaded for all future batch, or individual, curve processing. At least 10 F-D curves were analysed for every sample unless otherwise stated.

3.9.1 Batch processing F-D curves

Experimental QI™ F-D curves are saved in individual folders for each saved scan. After choosing a scan of interest, all of the F-D curves were batch processed using the inbuilt software operators. Several steps have to be performed before the elastic modulus and/or stiffness values could be determined (Chapter 4.2.4). An individual F-D curve is loaded and the operators fitted to the approach region of that curve. The 'cantilever calibration' operator was loaded to check that the values matched those calculated during the experiment. These values could be changed, if required, in the operator. To remove any offset from the raw F-D curve, and to bring the *X* and *Y*-axis towards zero, the 'subtract baseline' operation was applied. Next, the cantilever deflection 'contact point' was manually chosen by selecting the desired region with the mouse. This adjusts the *X*-axis offset to bring it to zero. These routines are variable fit parameters and do not influence the fit results, thus they do not need to be exactly determined. Following this, the 'correct height for cantilever bending' operator is applied. This crucial operation calculates the tip-sample separation (indentation depth) by subtracting the difference of the cantilever vertical deflection from the piezo height in units of length. Finally, the 'Hertz fit' operator was applied, with default settings. These routines were applied to every force curve within the individual folder – typically 4096 curves for a 64 x 64 pixel scan.

3.9.2 Individual F-D curve processing

Applying the operators during batch processing enables the majority of F-D curves to be oriented about the zero offset in the *X* and *Y*-axis. Some further adjustment was typically required to more accurately define the actual contact point, using the 'subtract baseline', 'contact point' and the 'correct height for cantilever bending' operators. Further operators were loaded and described below.

3.9.3 Measuring the slope

The 'measure slope' operator was loaded. This allows one to measure the slope of the approach curve by fitting a line tangent to the curve over a chosen length. This feature was used to determine stiffness values of PDMS and SA in units of nN/µm. For both samples the indentation at -10 nm was studied. A region was drawn between -12 to -8 nm on the *X*-axis to constrain the slope around -10 nm and the resulting value recorded. Where the noise within a slope at this region led to a negative slope, the drawn region was shifted ~ 1 nm in either direction on the *X*-axis until a positive value was recorded.

3.9.4 Curve statistics

The 'curve statistics' operator was used to calculate statistical quantities – the minimum, maximum, mean and RMS cantilever deflection of the F-D curve. A region was drawn from 0 to -10 nm on the *X*-axis, or subject to noise in the F-D curve, as close as possible to report the values at this location. Where the value was considerably less than -10 nm, this was due to a stiffer sample location, leading to an F-D curve that was less than -10 nm. Where the value was greater than 10 nm of indentation, i.e. -12 nm, this was due to noise in the F-D curve.

3.9.5 Editing the Hertz/Sneddon model

The inbuilt Hertz/Sneddon model in the software allows the user to change the indenter geometry. Both the Hertz fit for a spherical indenter and the Sneddon fit for a conical indenter were used. The sphere radius can be modified and cantilever manufacturer's nominal values and SEM-calculated radii were used (40 nm for MLCT D). It was found that the conical indenter (Sneddon) consistently gave better results, as the inputted sphere radii (Hertz) had to be considerably larger in the software model than the actual radii. The cone half-opening angle can be modified from the preset 15° value. Following the elucidation of

the tip angles (discussed in chapter 5), a half-angle of 85° was used for all PDMS and SA modulus data. All the other indenter geometries available in the software were explored; paraboloid, triangular pyramid, quadratic pyramid and flat cylinder. Editing the radii or half-angle in these parameters did not provide the expected modulus values and/or apply a sufficient modulus fit to an F-D curve.

3.9.6 Measuring the elastic modulus

The Young's modulus fitting curve within the Hertz/Sneddon operator was applied between the zero contact point and -10 nm indentation and the values recorded. Where the fitting curve did not follow the F-D curve faithfully it may over, or underestimate the modulus value. Accordingly, the fitting curve may have been applied to the entire F-D curve – at indentation depths greater than 10 nm. Where this was required, the reported modulus was checked at multiple points across the F-D curve for consistency. Where consistency was not evident, these F-D curves were discarded and alternative ones used.

3.9.7 Exporting F-D values

Once the numerical values were obtained from each of the operators, the values were added into statistical software – both Microsoft Excel (2013) v.15.0.5015 for Windows or Microsoft Excel (2011) for Mac, v.14.0.0. The raw data was taken into Excel and briefly statistically analysed. These data were copied into GraphPad Prism version 7.03 for Windows or GraphPad Prism version 8.0.2 for Mac (GraphPad Software Inc., La Jolla, California) for further quantification, statistical analysis and generation of histograms.

3.9.8 Statistical analysis

For SA modulus and stiffness data two-tailed unpaired non-parametric t-test was performed, with the Mann-Whitney (Wilcoxon rank sum) test. Although the before and after modulus and stiffness values (either t = 0 h and t = 1.5 h, or prior to and following oxacillin incubation) were taken on the same cell the individual F-D curves may have been sampled at a slightly different pixel location. Thus, the unpaired test was chosen over a paired t-test. The same tests were performed for extracted cell wall sacculi. Where population distributions are presented the averages ± one standard deviation (SD) are shown. Where averages of 10 replicate F-D curves are shown they are also presented with their standard error (SE). Averages may be calculated from the mean or median and this is

detailed in the figure legends. All values are reported to 2 significant figures. Significance was considered at an alpha (α) level < 0.05.

3.9.9 AFM indentation model

When formulating the model that lead to the adoption of the 85° cone angle settings a range of cantilevers was used for comparative analysis of the PDMS substrate modulus. Standard MLCT cantilevers (Bruker Corporation) using the triangular D or F cantilever, or B500_CONTR (nanotools) were used. Additionally, functionalised Arrow™ CONT (NanoWorld AG) or functionalised TESPA-V2 cantilevers (Bruker Corporation) were used. A range of QI™ setpoints were used to either ensure that large spherical indenters reached the same indentation depth of smaller radii tips, or to specifically determine the modulus at increased depths, when exploring the indentation depth and tip angle relationship. Freshly made PDMS substrates were scanned at 0.5 nN and immediately after at 1 nN to establish if there was a loading force dependence on the reported modulus and the tip geometry at differing indentation depths. Where indentation was less than 10 nm, the slope fitting method (section 3.9.3) was followed as faithfully as possible, but by constraining the slope ± 2 nm from the maximum indentation reached. Data were exported and analysed as previously described (section 3.9.7 and 3.9.8).

3.10 Functionalisation of cantilevers

MLCT cantilevers (A, D and F) (Bruker Corporation), Arrow™ CONT cantilevers (NanoWorld AG) and TESPA-V2 cantilevers (Bruker Corporation) were functionalised with 10 ± 0.2 µm and 25 ± 0.4 µm polystyrene beads (Sigma) for comparative AFM indentation assays on SA and PDMS. Colloidal solutions of the beads were stored at room temperature in dH_2O. A 20 µl droplet of the required colloidal solution was pipetted onto a clean glass slide and the liquid gently removed with lens tissue. The slide was mounted on an Eclipse T*i* inverted optical microscope (Nikon) using a 10X Plan Fluor 0.30 NA objective (Nikon) and the beads located. A small droplet of optical adhesive was placed onto a region of glass slide devoid of beads. The cantilever to be functionalised was mounted on a NanoWizard® 3 AFM (JPK Instruments) and brought into gentle contact with the leading edge of the glue. It was lowered into the glue 1 nm at a time until a capillary neck was formed, at which point the cantilever was quickly raised by ~ 100 nm. A single polystyrene bead was located and the

cantilever was brought into gentle contact with the glass slide surface adjacent to the bead, before being retracted by 1 nm. The trailing face of the tip was manipulated into contact with the polystyrene bead and quickly retracted ~ 1000 nm, with the bead attached. The cantilever/bead combination was placed under a UV lamp and the adhesive was cured for 1 min. Multiple cantilevers were functionalised and stored at room temperature.

3.11 AFM imaging of PDMS

TESPA-V2 (Bruker Corporation) or Arrow™ UHF (NanoWorld AG) cantilevers were used in air. Images captured with a TESPA-V2 were with a drive amplitude ~ 47 mV and scan rate was 1.49 Hz. Images captured with an Arrow™ UHF were with a drive amplitude ~ 1400 mV and a scan rate of 2.99 Hz. Pixel density was 512 x 512. *Z*-range was 0.2 – 0.5 µm. To look at the internal structure of PDMS, a small piece ~ 2 cm^2 was briefly immersed in liquid nitrogen and carefully placed in a glass dish. A pestle was used to crack the PDMS in half. The non-imaged side was carefully sliced to create a level piece of PDMS and it was secured to the microscope stage with rubber elastomer. The internally exposed face was scanned with a TESPA-V2 in air with a drive amplitude of 160-170 mV and a scan rate of 1.49 Hz. Pixel densities were 512 x 512. *Z*-range was 0.5 µm.

3.11.1 Alternative modulus PDMS samples

Commercially available PDMS samples with low modulus values of 15 kPa and 28 kPa were obtained - µ-Dish 35 mm, high ESS (Ibidi). Softer modulus samples were made by adjusting the ratio of pre-polymer and curing agent to 30:1. The modulus was tested with a range of functionalised cantilevers; MLCT A, D and F with 10 µm spheres, and TESPA-V2 with 25 µm spheres, using QI™ and force spectroscopy modes on the NanoWizard® 3 AFM.

3.11.2 High-resolution AFM imaging

All high-resolution imaging was performed on a Dimension FastScan, software v.9.1 (64 bit) (Bruker Corporation) in intermittent contact mode. A number of different cantilevers were used (section 3.10). All imaging was performed in imaging buffer (section 3.3.2). Jonathan Burns performed the high-resolution imaging of SA used in (Fig. 1.3) at a 1024 x 1024 pixel density.

3.12 PDMS roughness

PDMS was regularly monitored for its roughness parameters during acquisition of F-D curves, at 64 x 64 pixel resolution, by creating line profiles and quantifying peak to valley measurements (data not shown). To more accurately determine the roughness, 10:1 PDMS was cast from clean, unused 4-inch silicon wafers, with no lithographic patterning, with and without Brij® 52 coatings for comparative analysis. Following the 2 h curing at 70° C, small sections of PDMS were removed from the wafer; immediately, 1 day later, 1 week later and 1 month later. The smooth face (facing the silicon wafer) was analysed for roughness on the AFM from images captured at 1 µm, 500 nm and 80 nm at a 512 x 512 pixel density. The arithmetic mean roughness, R_a, the RMS roughness, R_q, and the skewness, R_{sk} and kurtosis, R_{ku} were established, using NanoScope Analysis and Gwyddion (32 bit) software v. 2.36 (http://gwyddion.net). Data were copied into Microsoft Excel and the mean values calculated and compared. The R_a was automatically calculated from the whole image. All other measurements were taken by drawing individual horizontal lines, evenly spaced apart. For the 1 µm and 500 nm images 3 x 1 µm or 3 x 500 nm length lines respectively, were drawn in the top third, middle, and bottom third of the images. 1 µm/512 pixels = 2.0 nm/pixel. For the 500 nm images, 500 nm/512 pixels = 1.0 nm/pixel. The 80 nm images were analysed in greater detail with 10 x 80 nm length horizontal lines evenly spaced ~ 7.5 nm apart. 80 nm/512 pixels = 0.16 nm/pixel (all to 2 significant figures). All images were processed with first order plane fitting in both software packages.

3.13 AFM image processing

All images were processed with first order (linear) plane fitting to remove any tilt. Streaks or similar artefacts were removed with the relevant manufacturer software routine. Height measurements were taken from streak-free regions, and prior to removal of any streaks. Where images required more levelling (high resolution PDMS and PG cell wall images), third order plane fitting was applied. Additionally, a low pass filter may have been applied, to remove any high frequency artefacts. Details of any editing, beyond first order plane fitting, are described in the image legends.

3.13.1 QI™ image processing

Where sample topography and measurements were required, the QI™ files were saved as QI™ images using the inbuilt saving settings, and imported back into the software. The raw data contains 'channels' that can be selected for export. These include height, slope (stiffness) and Young's modulus. The *XY*-axes of 3D height profiles were manually adjusted and the *Z*-aspect ratio was increased to 20%. Colour scales were adjusted where preferred (cantilever tip images). Scale bars were manually displayed on the image, via the manufacturers AFM software and the colour inverted where required. Images were exported in PNG or TIFF format.

3.13.2 Intermittent contact image processing

Where sample topography and measurements were required, height images were exported in PNG or TIFF format. Where phase images are used instead of height images, the figure legend provides a description. Scale bars were added via the manufacturers AFM software and the colour inverted where required. The *Z*-axis aspect ratio was set to 0.100 on 3D images.

3.13.3 Optical micrograph processing

Optical micrographs, from all of the optical microscopes used throughout this study, were enhanced in various ways. Where brightness and/or contrast adjustments were required, these were performed directly in Microsoft Word (2013) v.15.0.5015 for Windows or Microsoft Word (2011) for Mac, v.14.0.0, using the format picture option. Scale bars were added in the Fiji distribution of ImageJ v. 2.0.0-rc-65/1.51s (Schindelin *et al.*, 2012). Firstly, by drawing a straight line across a region of known size and using the Analyse - Set Scale option to calibrate the micrograph. From this, the Analyse – Tools – Scale Bar option was used to display a scale bar at the lower right of the image. Micrographs may have been cropped for a region of interest within Fiji, by drawing a rectangle around the region and using the Image – Crop option. The image retains its calibrated scale and a scale bar was displayed by following the previous options. Images were further scaled and/or cropped within Microsoft Word where required.

3.14 Scanning electron microscopy of AFM cantilevers

Saurabh Kumar at the Kroto Research Institute performed the SEM imaging. Sputter coating of samples was performed by Chris Hill at the Faculty of Science electron microscopy unit.

3.14.1 Imaging of functionalised Arrow™ cantilever

A functionalised Arrow™ CONT cantilever (NanoWorld AG) was coated with gold for 1.5 min, 20 mA on an S150B sputter coater (Edwards) and secured onto an SEM mounting with carbon tape. Images were collected on a SEM (Raith EO) at 10.0 kV and aperture size 30.0 µm.

3.14.2 SEM imaging of MLCT cantilevers and tips

A number of MLCT cantilevers were assayed with SEM. Initial imaging was performed with gold-sputter coated samples. Where the radius and angles of the tips were to be measured it was found that the sputter-coated material was not of a uniform distribution and altered the topography. This made absolute quantification of values difficult to obtain. It was found that uncoated cantilevers could be observed on the SEM, as the reflective coating of gold (on the back side) and/or the titanium/silver (on the top layer) were sufficient to enable high-contrast imaging. Additionally, despite the lack of the conductive coating, there was very little observed charging. Uncoated images were collected at 3.0 kV and aperture size 30.0 µm.

3.14.3 SEM micrograph processing

Calibration of the micrograph size was performed by drawing a straight line over a previously SEM-calibrated marker, such as a scale bar, or cursor region, and using the set scale option within Fiji. Various size and angle measurements were added and appear yellow on the micrographs. All original SEM-calculated cursor and diameter measurements appear in white. Angle measurements were obtained using the angle tool within the Fiji toolbar and using the Analyse – Measure option to find the values. Circle diameters were obtained by first drawing a straight line of a required length (checking with the Measure option) and permanently adding this to the image, using the Image – Overlay – Add Selection option. The circle was drawn over the line using the oval selection and holding down Shift on the computer keyboard to constrain the drawing as a circle. Where sample charging was evident on the detailed AFM tip micrographs, the Process – Find Edges option

was used to enable easier visualisation of the tip shape. AFM tip images were rotated 180° using the Image – Transform – Rotate… option, for easier assessment of indentation angles. Values of resolution, height and width from scaled micrographs were found using the Image – Show Info… option. These data and angle values were copied and pasted into a Microsoft Word text box (in white font) and placed at the top left of the micrographs. Images were further scaled and/or cropped within Microsoft Word where required.

3.15 AFM imaging of MLCT cantilever tips

Individual cantilevers from the MLCT chip were gently removed with a blade and tweezers, and glued to a 35 mm plastic tissue culture dish, tip side facing up, with optical adhesive (Chapter 5). The tip was carefully scanned using another MLCT D in QI™ mode, or TESPA-V2 cantilever in intermittent contact mode on a NanoWizard® 3 AFM (JPK Instruments). Images were analysed for topography. The *XY*-axes of 3D height profiles were manually adjusted and the *Z*-aspect ratio was increased to 20%. Colour scales were adjusted to match SEM micrographs, for easier comparative assessments. A horizontal cross section was drawn across the tallest section of the tip height image and the numerical data was exported as an ASCII file containing height against offset. The file was opened in JMP Pro® v.12.2 for Microsoft Windows x64 (SAS Institute Inc.) and the *XY*-axes were made isometric, to attempt to elucidate the true geometry of the tip. Further editing was performed, by removing a large proportion of numerical data to leave only the peak, ~ 1 µm, of the tip for more detailed analysis.

3.16 *Staphylococcus aureus* sample preparation for AFM

3.16.1 Reducing the cell concentration for AFM substrates

Where a less concentrated SA sample was required, and following the OD_{600} readings, arbitrary calculations were performed and the culture diluted in fresh, filtered growth medium until a desired OD_{600} was achieved; typically between 0.02 – 2.0.

3.16.2 Increasing the cell concentration for AFM substrates

Conversely, when a more concentrated SA sample was required, the cells were collected by centrifugation (5500 rpm, 5 min) and supernatant discarded. The cells were resuspended in 0.5, 1.0 or 1.5 ml fresh filtered growth medium.

3.16.3 Cell deposition onto silicon wafers

Where bacterial cell entrapment was required, 20 µl of bacterial suspension was pipetted onto the wafer and left for 30 min. The liquid droplet was then dried under N_2 for ~ 5 - 15 min until no observable liquid remained. The cells were immediately re-hydrated with 20 µl filtered growth medium and given a further 5 min equilibration. Omitting this drying step often resulted in a poor yield of immobilised bacteria.

3.16.4 Cell deposition onto PDMS substrate

Two methods for cell deposition were tried. Where data is presented, the actual method used will be listed.

3.16.5 Glass coverslip deposition

The bacterial sample was prepared in filtered growth medium. 20 µl was pipetted onto the PDMS and allowed to settle for 10 min. A glass coverslip was used to gently scrape the cells into the holes of the PDMS grid in multiple directions, orthogonal to the previous in a manner similar to previously described (Formosa *et al.*, 2015). The liquid droplet was then dried under N_2 for ~ 15 min until no observable liquid remained.

3.16.6 Non-glass coverslip deposition

Alternatively, the glass coverslip step was omitted, and 20 µl was pipetted onto the PDMS and left for 30 min. The liquid droplet was then dried under N_2 for ~ 15 min until no observable liquid remained.

3.16.7 Sample rehydration

Following the N_2 drying step (section 3.11.4), the cells were immediately re-hydrated with 20 µl filtered growth medium and given a further 5 min equilibration. The PDMS was placed in a 35 mm plastic tissue culture dish and inserted into a heated stage on a NanoWizard® 3 AFM and ~ 4 ml filtered growth medium was pipetted evenly around and onto the substrate for heating evenly, and to increase the relative humidity during a scan. The temperature setting on the heated stage required setting to 46° C to allow heating the chosen medium to 37° C. Medium temperature was routinely checked using a K-type thermocouple (Digitron). For room temperature assays the heated stage was not activated. For room temperature assays on a NanoWizard® ULTRA speed AFM (JPK Instruments) the PDMS was either placed

in a 35 mm plastic tissue culture dish that was secured to a glass slide with rubber elastomer, or the PDMS was placed directly onto a glass slide. Samples were not immersed in ~ 4 ml filtered growth medium for room temperature assays, but instead, a droplet between 20 – 100 µl was pipetted onto the region of interest.

3.17 Transmission electron microscopy

SA was grown to mid-exponential phase, with an OD_{600} ~ 0.5 and centrifuged at 5500 rpm, 5 min. The pellet was resuspended in 1 ml filtered BHI. Cells were fixed in 2.5% (v/v) glutaraldehyde in 0.1 M sodium cacodylate buffer (Agar Scientific) and incubated overnight at 4° C. Cells were washed x 2 in 0.1 M sodium cacodylate buffer for 30 min at 4° C, followed by secondary fixation in 2% (w/v) aqueous osmium tetroxide (Agar Scientific) for 2 h at room temperature. Dehydration was achieved stepwise at room temperature in ethanol; 75% (v/v) and 95% (v/v) for 15 min respectively, followed by absolute ethanol for 2 x 15 min. Finally, absolute ethanol dried over anhydrous copper sulphate for 2 x 15 min. Cells were washed in propylene oxide for 2 x 15 min. All steps were taken at room temperature. Infiltration was performed by resuspending the cell pellet in ~ 1 ml of a 1:1 mixture of propylene oxide/epoxy resin (Araldite® CY212) 10 ml, dodecenyl succinic anhydride (DDSA) 10 ml, with 10 drops benzyldimethylamine (BDMA) (Agar Scientific)**.** The mixture was made up to 20 ml in propylene oxide, with shaking at each step. The cell/resin mixture was incubated overnight in a rotor at 2 rpm. 15 ml of full strength epoxy resin mixture (without propylene oxide) was used to embed the cells for 2 x 3 h at room temperature. Pellets were placed into a silicone mould, filled with 100% (v/v) epoxy resin and polymerised for 72 h at 60° C. Ultrathin sections ~ 90 nm were obtained using a diamond knife (DiATOME) on a UC6 microtome (Leica) and placed onto a 400 mesh copper TEM grid (Agar Scientific). The sections were stained with saturated aqueous uranyl acetate for 25 min, followed by staining with Reynold's lead citrate for 5 min. Images were collected on a Tecnai G2 Spirit (FEI), with an Orius SC1000A CCD camera (Gatan) at 80.0 kV and edited using Digital Micrograph software v. 2.32.888.0 (Gatan).

3.18 Imaging SA

FastScan-D (Bruker Corporation) cantilevers were used in small amplitude intermittent contact mode. The low thermal energy laser spot was employed. Typical amplitudes were 1 – 2 nm, with a scan rate of 1 Hz and 1024 x 1024 pixel densities. The overnight analysis

(Chapter 6.2.1.3) was performed at a pixel density of 256 x 256 at a scan rate of 1.99 Hz. Drive amplitude was 2340 mV. A realtime bow planefit was used for image acquisition. To correct for drift, the 15 h image was shifted laterally. Both images were cropped to display the regions of interest.

3.19 SA whole cell wall sample modulus

Following cell deposition, previously described, and to limit the influence of curvature of the cell surface, and any impacts that this may have on the cantilever, F-D curves were taken from a narrow region about the centre of a cell. At 64 x 64 pixel resolution from a cell imaged in a 10 x 10 µm scan, this typically comprised 2 x rows of 2 F-D curves and 2 x rows of 3 F-D curves closely oriented together – with < 2 pixels between F-D curves and rows. On smaller scan sizes (where the cell occupied more of the scan region), or with scans at pixel densities greater than 64 x 64 pixels the F-D curves were more widely distributed with > 2 pixels between F-D curves and rows. New MLCT D cantilevers were used for every modulus experiment.

3.19.1 SA extracted cell wall sacculi sample modulus

Once a sacculi sample was adhered to a substrate there was little to no curvature to influence the cantilever, and F-D curves could be taken from a wider area of the cell surface. However, to maintain consistency the curves were largely taken from the central region of the sacculi and the edges were avoided.

3.20 Purification of cell wall sacculi

Laia Pasquina Lemonche prepared all cell wall sacculi and generously provided samples for analysis.

3.20.1 Extraction of cell walls

A 1 L mid-exponential phase culture with OD_{600} ~ 0.5 was harvested by centrifugation (5500 rpm, 10 min) and the supernatant discarded. The pellet was resuspended in 1 ml PBS in an eppendorf and boiled in a water bath at 100° C. The boiled cells were added to FastPrep® Lysing Matrix B, 2 ml tubes, containing 0.1 mm silica spheres (MP Biomedicals). Samples were mechanically sheared using a FastPrep-24® homogeniser (MP Biomedicals) at least eleven times at 6.0 m s^{-1} for 30 s and samples chilled on ice in-between, with a 5 min pause

between each run. Shearing efficiency was checked with optical microscopy and further shearing performed if necessary. The beads were collected as a pellet by centrifugation x 2 (1000 rpm, 30 s) and separated from the cell extracts in the supernatant. Insoluble material was collected by centrifugation (13500 rpm, 3 min) and resuspended in 5% (w/v) sodium dodecyl sulphate (SDS) at 100° C and boiled for 25 min to remove non-covalently bound cell wall components. Pellets were collected by centrifugation (13500 rpm, 3 min) and resuspended in 5% (w/v) SDS at 100° C. They were boiled for 15 min, and stored at room temperature overnight. The pellets were washed six times in dH_2O (13500 rpm, 3 min) and resuspended into a single eppendorf in 1 ml trisaminomethane-hydrochloride (Tris-HCl) (50 mM, pH 7.4), containing 2 mg ml^{-1} pronase, to degrade proteins. The sample was incubated at 60° C for 90 min and washed twice in dH_2O (13500 rpm, 3 min). Samples were stored in dH_2O at 4° C.

3.20.2 Methicillin-treated cell walls

An overnight culture was resuspended in 1 l TSB (in a 3 l flask), with shaking at 120 rpm for 2 h, until an OD_{600} ~ 0.2 – 0.3. A control flask was cultured as above, and placed on ice after 2 h. 4 ml (equivalent to 10x MIC) Methicillin was added and the cells grown for a further 30 min. Immediately, 250 ml was removed and aliquoted into individual falcon tubes, with 35 ml in each. The falcon tubes were placed in a water bath at 100° C for 10 min to kill the cells, and stop any further action of antibiotic. These steps were repeated at 60 min and 120 min. All samples were removed at 37° C to prevent any heat-shock to the culture. Once the 30, 60 and 120 min cultures were boiled, the cells were harvested by centrifugation (5500 rpm, 10 min) and the supernatant discarded. The pellet was resuspended in 1 ml PBS in an eppendorf and added to FastPrep® Lysing Matrix tubes and further preparation was performed as described previously (section 3.20.1).

3.21 AFM multiparametric imaging of cell wall sacculi

A KOH-cleaned glass coverslip was prepared by washing in 150 ml of 1 M KOH (Fisher), with sonication for 15 min, followed by rinsing in 150 ml dH_2O, with sonication for 15 min. The coverslips were then stored in 150 ml fresh dH_2O. The coverslip was dried under N_2 and fastened to a glass slide with nail varnish. 50 µl of 0.01% (w/v) poly-L-lysine (Sigma) was pipetted onto the coverslip and left for 20 min. It was gently rinsed with dH_2O and 5 µl sacculi solution was pipetted onto the surface. 20 µl of 10 mM TRIS was immediately added

and triturated with the sacculi solution. The mixture was left for 40 min before a gentle rinse with 10 mM TRIS. A further 200 µl TRIS was added before AFM was performed.

3.22 Modified substrate growth assays

To address the apparent lack of immobilisation and growth and division observed with SA cells, a number of techniques were employed and compared. The surface chemistry of PDMS and glass coverslips were adjusted with various coatings and SA cells were grown under a range of differing conditions and time scales on the modified substrates (Chapter 7).

3.22.1 PDMS substrate functionalisation

To render PDMS more hydrophobic a 10 µl droplet of 35,000 M_W atactic polystyrene (Sigma) dissolved in toluene, to a concentration of 1 mg/ml, was pipetted onto a patterned PDMS substrate and the toluene allowed to evaporate in a fume hood. Conversely, to render the PDMS more hydrophilic multiple substrates were treated with O_2 plasma under vacuum for 15 – 60 s. Native PDMS was placed face down onto a 100 µl droplet of 0.01% (w/v) poly-L-lysine for 20 min at room temperature, and gently rinsed with dH_2O. A 60 s O_2 plasma-treated PDMS substrate was immersed in 0.01% (w/v) poly-L-lysine and left for 24 h at room temperature. The sample was removed and left to air dry for ~ 30 min. The chemistry of the MEGAPOSIT™ SPR™ 350 positive photoresist was tested, to see if it promoted the attachment and/or growth of SA. A small droplet was pipetted onto a piece of 10:1 PDMS and 30:1 PDMS and spin coated at 4000 rpm, 30 s, followed by baking on a hotplate at 100° C for 1 min. To test if mammalian serum proteins could bind to PDMS and afford immobilisation of SA cells, a 60 s O_2 plasma-treated PDMS substrate was immersed in 5 ml porcine serum for ~ 22 h. It was gently rinsed with dH_2O and dried under N_2. All the samples were either used immediately following functionalisation, or sealed in 35 mm plastic tissue culture dishes for later usage. Porcine serum treated samples were stored at 4° C.

3.22.2 Glass coverslip functionalisation

Glass coverslips were given a four-stage clean, with sonication, in 5 ml of mild detergent, HPLC grade acetone (Fisher), isopropanol and dH_2O for 10 min respectively. They were gently scrubbed with lens tissue and dried under N_2. Alternatively, KOH-cleaned coverslips were used (section 3.21) and spin coated with MEGAPOSIT™ SPR™ 350 positive photoresist, at 4000 rpm, 30 s, followed by baking on a hotplate at 100° C for 1 min. Native, and plasma-

cleaned coverslips were immersed in porcine serum for ~ 22 h and gently blotted on tissue paper to remove large droplets.

3.22.3 6 well plate SA binding assay

To test the ability of SA cells to preferentially bind to either glass or PDMS substrates, against the action of gravity and simply dropping out of solution, glass coverslips and PDMS samples were supported at ~ 45° angles in individual wells and fully immersed in 12 ml BHI per well, inoculated with an overnight culture of SA to a target OD_{600} = 0.05. 2 PDMS samples were used; 10:1 and 30:1 that were both photoresist coated. 4 glass coverslips were used; 1 x photoresist coated, 1 x plasma-cleaned and serum treated, 1 x serum treated, and 1 x native, cleaned glass only. The plate was carefully placed on a shelf, with no shaking at 37° C for 4 h. This assay was repeated using 3 KOH-cleaned coverslips and 3 native PDMS substrates, all with no treatment or coatings. To each of the 3 wells per substrate type was added; BHI, BHI plus 10% porcine serum, and RPMI 1640 growth medium (Gibco™) respectively. The plate was placed on a shelf at 37° C, with no shaking, for 8 h. Each substrate was carefully removed and gently rinsed on both sides with dH_2O and quickly passed over a flame to heat fix any bound cells. The trailing face of each substrate (the one that would have required SA cell deposition against the action of gravity) was covered in 300 µl crystal violet solution for 1 min, and rinsed with dH_2O. The dH_2O was gently blotted from both sides of the substrate and cell adhesion was checked with optical microscopy, with 10X and 40X objectives, and a 100X 1.25 NA oil objective.

3.23 Confocal microscopy of SA immobilisation and growth

Darren Robinson at the Wolfson Light Microscopy Facility performed the confocal microscopy.

Glass, PDMS and silicon were tested for their ability to both immobilise, and encourage growth and division of GFP-expressing SA cells (section 3.4) over a 20 h period, using two different confocal systems.

3.23.1 Glass surface

SA was grown to an OD_{600} = 0.5 and 20 µl sample droplet at this concentration was pipetted directly onto a µ-Dish 35 mm, high glass bottom imaging dish (Ibidi). 4 ml filtered BHI was added and the dish placed onto an inverted A1 confocal system (Nikon) with Nikon

Elements software. An environmental control chamber (Okolab) was used to control the temperature at 37° C. Cells were visualised with a 60X NA 1.4 CFI Plan Apochromat VC oil objective. Excitation source was a 457-514 nm argon laser. A single emission filter for GFP was used. Detection was with photomultiplier tubes. Images were captured every 1 min for 20 h.

3.23.2 PDMS surface

SA was grown to an OD_{600} = 0.27 and was resuspended to an OD_{600} ~ 0.1. 40 µl sample suspension was pipetted onto 3 day old repeating lattice (section 3.7.1 (3)) PDMS substrate, that was placed onto the base of a µ-Dish 35 mm, high glass bottom imaging dish. The dish was filled with 4 ml filtered BHI and observed on the A1 confocal system described above (section 3.23.1). The focal length of the 60X objective was not sufficient to focus on the surface of the PDMS and a 20X NA 0.75 CFI Plan Fluor MI objective was used. The temperature was controlled at 37° C as previously. To attempt to capture any growth and division at an increased frame rate, images were collected every 20 s for the first 2 h. Subsequent images were collected every 1 min for 18 h.

3.23.3 Silicon surface

SA was grown to OD_{600} = 0.30 and was resuspended to an OD_{600} ~ 0.1. 20 µl sample suspension was pipetted onto the inverted pillar silicon wafer and left to settle out of suspension for 10 min. The droplet was dried under N_2 for ~ 5 min. The silicon wafer was secured to the base of a 35 mm plastic tissue culture dish and filled with 4 ml filtered BHI. The dish was placed on an upright FV1200 confocal system (Olympus) with Olympus Fluoview FV-ASW software. A LUMPlan FI 40X NA 0.8 water-dipping objective was used at room temperature, and the system was set to reflection, rather than emission microscopy mode, to aid the imaging. To correct for any drift, and SA sample motion above the silicon surface, a 40 µm *Z*-stack, set up over 10 x 4 µm slices, with each complete *Z*-stack taking ~ 1 min. Excitation source was a 488 nm argon laser. A single emission filter for GFP was used. Detection was with photomultiplier tubes. To test the potential of a photoresist-coated silicon wafer allowing for immobilisation and growth, a wafer previously used in our laboratory (Kailas *et al.*, 2009) was observed, as above, with minor changes. An overnight culture of SA was grown to an OD_{600} = 0.24 and was resuspended to an OD_{600} ~ 0.1. 20 µl sample suspension was pipetted onto the wafer and left to settle out of suspension for 10

min. The droplet was dried under N_2 for ~ 10 min and the dish filled with 4.5 ml filtered BHI. Images were captured every 1 min for 20 h.

3.24 Agar and agarose substrate preparation

Agar and agarose was tested as an alternative substrate to PDMS, for patterning from the various lithographically prepared silicon wafers, and for their ability to immobilise and promote growth and division of SA. Concentrations of 4%, 6% and 10% (w/v) were tested for their durability, and ability to assume and retain the patterns. 6% agarose was found to imprint more efficiently than the other concentrations. 4% agar and agarose did not imprint at all, and 10% agar and agarose were thick and viscous, and cured too quickly. At 6% concentrations agarose yielded slightly better performance and agar was discontinued. 6% (w/v) USB® 32830 low melt agarose (Affymetrix Inc.) was prepared by adding 0.3 g into 5 ml dH_2O in a 50 ml falcon tube and briefly shaken by hand. It was microwave heated at full power for 20 s and immediately placed into the neck of a 250 ml Duran® bottle filled with boiling water. The agarose was left for 10 min to degas. A 65 µl Gene Frame (Thermo Scientific) was stuck to a glass slide with the easy release adhesive side face up. A piece of silicon, with a chosen pattern, was placed in the centre of a plastic 90 mm petri dish. The tip of a 1000 µl pipette tip was removed with scissors and 400 µl of the degassed agarose was pipetted onto the silicon. The Gene Frame / glass slide was immediately pressed onto the agarose, expelling any air bubbles, and left for at least 30 min at room temperature, by flame, until the agarose had cured. The adhesive seal was broken with a blade and the glass slide was secured onto an AFM stage, with the imprinted agarose side face up.

3.24.1 Further agarose assay modifications

It was found that the expected ~ 750 nm depth holes, cast from the silicon substrates were routinely between 30 nm – 200 nm only. Multiple 6% agarose substrates were made, with a differing range of preparatory and curing methods employed, to improve the hole depth patterning. The numbers of Gene Frames was increased, and up to 10 were adhered to each other, to create a deeper cavity over the chosen silicon template. The volume of degassed agarose was increased up to ~ 1 ml to allow sufficient filling of the increased depth cavity. To improve the wettability of the silicon templates they were plasma-cleaned for 30 s - 3 min, or UV-ozone cleaned (home built) for 30 min. Additionally, following the pressing down of the glass slide / Gene Frame onto the agarose, various weights between ~ 500 g – 3 kg

were placed onto the glass slide and left for 5 min – 1 h. To further test for the influence of hydrophobicity, PDMS substrates were cast from silicon wafers with wells, to create PDMS with ~ 750 nm height pillars. 6% agarose was cast from this PDMS, in addition to silicon wafers. These PDMS substrates were also cleaned under plasma, or UV-ozone. The curing temperature was explored on both these PDMS substrates and silicon wafers. Both substrates were pre-heated to ~ 65° C (tested with thermocouple), which was the typical temperature the 6% agarose reached, after degassing for 10 min. Following agarose deposition the samples were left to cure at 37° C, room temperature, or 4° C for 30 min. Both substrates were tested over varying combinations using these modified steps. Agarose samples were routinely left for a further ~ 3 h at room temperature to allow for further curing, prior to AFM analysis. The agarose that remained in place on the glass slide / Gene Frame routinely dehydrated, but appeared to sufficiently rehydrate upon application of liquid.

3.24.2 Agarose imaging and SA cell seeding assays

When attempting to capture AFM images of hydrated agarose, or when testing the immobilisation or growth and division of SA cells, the agarose sample was removed from the glass slide / Gene Frame combination by carefully slicing with a blade. The patterned agarose was secured to the base of a 35 mm plastic tissue culture dish with either optical adhesive or rubber elastomer, and the dish filled with ~ 3 ml filtered growth medium. The agarose typically swelled, bowed, or detached from the dish. A layer of agarose was poured into the base of a 35 mm plastic tissue dish, during the initial patterning steps and was left to cure for 30 min – 3 h at room temperature. A small volume of 6% agarose was separately prepared and smeared onto the cured agarose layer on the 35 mm dish, to act as glue. The patterned agarose was quickly placed onto this and carefully flattened out. Once cured, SA cells were seeded and the dish filled with ~ 3 ml filtered growth medium.

3.25 SA cell growth and division

Jonathan Burns fabricated the silicon wafer following a similar protocol as previously described (section 3.7.2).

3.25.1 Growth and division assays

Following the repeated, unsuccessful growth and division events, using silicon wafers, PDMS or agarose substrates, an alternate lithographically patterned silicon wafer was found to support growth and division (Chapter 7). The design featured ~ 2 µm diameter pillars, ~ 750 nm in height, separated by channels ~ 2.5 µm in diameter. A small ~ 4 mm^2 piece was secured to a 35 mm plastic tissue culture dish using rubber elastomer. SA cells were grown to an OD_{600} between 0.27 – 0.33 and resuspended in 500 µl – 1.5 ml filtered TSB throughout various repeated assays. 15 – 20 µl of SA sample suspension was pipetted onto the silicon wafer and left for time scales between 1 h 25 min – 2 h 30 min. Following this wait, the samples were briefly dried under N_2 and rehydrated in 2 – 3 ml filtered TSB. Samples were left for a further period of time ranging between 4 h 20 min – 6 h to allow sufficient attachment and immobilisation prior to AFM scanning. AFM was performed on both the NanoWizard® 3 at room temperature or 37° C, or the NanoWizard® ULTRA speed at room temperature only. The room temperatures ranged between 23.7 – 26.3° C across both instruments. Five independent experiments were performed and SA cells became over confluent in four of them – 2 at room temperature and 2 at 37° C. Removing the growth medium and squirting some across the silicon surface gently rinsed the cells, leaving only the sufficiently immobilised ones. The culture dish was refilled with 2 – 3 ml filtered growth medium and left for at least 30 min prior to AFM scanning. All scans were performed with a new MLCT D cantilever at 0.5 nN QI™ setpoint, following the settings previously described (section 3.8.3). Growth and division events were observed for at least 30 min - 4 h 30 min prior to cell detachment or poor scanning conditions ending the experiments. Two unattended, overnight scans were performed, with cell detachment or poor scanning conditions occurring between 1 h – 3 h 30 min later.

3.25.2 Antibiotic assay

A single assay was performed in a similar manner to those above (section 3.25.1). SA cells were grown to an OD_{600} = 0.31 and resuspended in 1 ml filtered TSB. 15 µl cell suspension was pipetted onto the silicon wafer and left for 1 h 45 min. The sample was briefly dried under N_2 and rehydrated with 15 µl filtered TSB, and the dish filled with 3 ml filtered TSB. The sample was left for 3 h and became over confluent. It was rinsed, as previously described and fresh 3 ml filtered TSB was added. Following a further 1 h equilibration – and

5 h 45 min after initial cell seeding, growth and division events were captured for a further 1.5 h. 3 µl oxacillin (section 3.2) was carefully pipetted into the growth medium during a repeated AFM scan. From the oxacillin stock this equated to 0.5 µg ml^{-1} and a 20 x MIC. It was not possible to pipette 1.5 µl oxacillin (at 10 x MIC), as this small volume would not drop from the pipette tip under the restricted AFM scanning conditions. Repeated scans were performed for another 2 h 15 min prior to cell detachments. AFM scans were performed with a QI™ setpoint of 0.5 nN and following the settings previously described (section 3.8.3). F-D curves were processed as previously described (section 3.20) and QI™ images were processed as previously described (section 3.9). To correct for drift and the differing aspect ratios of multiple, repeated scans, QI™ images were edited in Adobe® Photoshop® CS6 for Mac v. 13.0 x64 (Adobe Systems Inc.), by aligning the *XY*-axes of a specific region in each image to a fixed location.

Chapter 4

The design and fabrication of lithographically patterned PDMS

4.1 Introduction

Polydimethylsiloxane (PDMS) is a widely used organosilicon elastomer in the life sciences. It is extensively used in microfluidic devices (Fujii, 2002; Tsai *et al.*, 2011; Johnston *et al.*, 2014) as it has shown biocompatibility with a diverse range of biomolecules (Bélanger *et al.*, 2001). It is routinely available as a two-part liquid polymer kit, comprising a pre-polymer base and a curing agent that creates crosslinking when mixed together. It is curable at room temperature, or by heating at elevated temperatures. It is relatively cheap, and easy to use. Its soft and elastic nature allows for reversible deformations and it can be lithographically moulded with high fidelity (Liu *et al.*, 2009). PDMS has been extensively covered in the literature, particularly in the semiconductor industry, due to its good electrical properties, thermal stability, low surface energy and unique hydrophobic character (Meincken, Berhane and Mallon, 2005). Our laboratory was interested in utilising PDMS for correlative fluorescence assays and for its potential to immobilise bacteria for AFM analysis. A major feature of this study utilised our experimentally derived mechanical properties of PDMS, from a variety of instruments, and compared these to the values widely reported in the literature. From these values, the AFM was used to indent PDMS to a range of indentation depths and the Hertzian contact model was modified to constrain the elastic modulus to our chosen value. In this regard, we used the PDMS as a method of calibrating the experimental environment. In this chapter we will further explore the mechanical properties and the molecular organisation of PDMS in an attempt to correlate the structure with the mechanical properties, and to address the disparity of the elastic moduli that are reported in the literature. Further, we will investigate the geometry of the AFM probe in corroboration of this calibration method in Chapter 5.

4.1.1 Lithographic patterning

There are numerous ways to produce patterns on a PDMS substrate. Chemical patterning sees a photomask applied to the PDMS surface, which is degraded with O_2 plasma into a distinct, user-defined pattern. A similar method - bond-detach lithography, utilises an O_2

plasma-treated PDMS film, and patterning is bonded onto another similarly treated PDMS film on silicon. For a review see (Zhou *et al.*, 2012). Previous work in our laboratory utilised contact mask photolithography to make arrays of holes patterned onto a negative tone photoresist material that had been spin-coated onto a silicon wafer (Kailas *et al.*, 2009; Bailey *et al.*, 2014) (Chapter 3.7). In this regime, the photoresist is not dissolved in the developer and remains in place, while the patterned region is removed – leaving wells of the chosen pattern. Living cells can be immobilised within the wells of the silicon substrate and analysed by AFM or other methods. An alternative to this technique simply swaps the negative tone photoresist for a positive tone photoresist. Once irradiated with UV light the photoresist is dissolved, leaving pillars of the underlying material adopting the user-defined pattern and geometry. The liquid PDMS can then be poured onto this topographic stamp, and following curing it will retain this microstructure, leading to wells within the substrate that can be used to immobilise cells for analysis (Dague *et al.*, 2011; Formosa *et al.*, 2015). This technique was adopted for our study.

4.1.2 Optical properties

PDMS is optically transparent to wavelengths from NIR to UVB (Liu *et al.*, 2009) and displays little autofluorescence (Piruska *et al.*, 2005). Additionally it has a refractive index of ~ 1.4 (Piruska *et al.*, 2005; Schneider *et al.*, 2009) which is close to water (Schiebener *et al.*, 1990) and common soda-lime window glass (Rubin, 1985). These combined properties thus render PDMS perfect for use in optical and fluorescence microscopy.

4.1.3 Mechanical properties

PDMS is a soft, amorphous and elastic polymer. It can be moulded to a resolution of a few nanometres and is able to maintain this moulded shape (Hua *et al.*, 2004). The blending ratio of the elastomer base and curing agent can be adjusted to effectively tune the elastic modulus to a desired value (Palchesko *et al.*, 2012). Alternatively, the curing temperature can have a marked effect on the final modulus (Johnston *et al.*, 2014). The elastic modulus has been widely characterised throughout the industrial and academic literature. The most commonly used methods to characterise the elastic modulus are by tensile testing, whereby the sample is stretched and the stress-strain curve is analysed to derive the modulus, or by

nanoindentation, where the piezo displacement from a dedicated nanoindenter instrument, or AFM is monitored, and the resultant data are analysed by Hertzian contact models.

Commonly available products, such as Dow Corning's SYLGARD® 184 have reported elastic moduli between ~ 1 – 9 MPa, when mixed and cured in a 10:1 (w/w) mass ratio following the manufacturer instructions. However, the majority of reported moduli have come from ill-defined curing temperatures or time scales (Johnston *et al.*, 2014). Johnston and co-workers sought to fully characterise the elastic modulus of PDMS when cured at a varied range of temperatures. Using a tensile testing instrument, which is the engineering standard for comparison of the mechanical properties of different materials, they reported a modulus of 1.32 ± 0.07 MPa at 25° C, 2.05 ± 0.12 MPa at 100° C, and up to 2.97 ± 0.04 MPa when cured at 200° C. (Johnston *et al.*, 2014).

The influence of curing time on the elastic modulus has also been investigated (Hocheng *et al.*, 2010). The author's mixed ratios of 6:1 – 12:1. When cured at 85° C, the modulus of their 10:1 sample increased from 1.49 MPa at 60 min to 1.67 MPa by 120 min. When curing at 150° C, after 15 min the elastic modulus was 1.75 MPa. This increased to 2.27 MPa by 60 min, and there was no further change by 90 min. At room temperature the 10:1 mix had an elastic modulus of exactly 1.00 MPa. Their data suggest that the elastic modulus value is increased at higher curing temperatures (Hocheng *et al.*, 2010).

The Poisson's ratio of SYLGARD® 184 has value ranging between 0.45 – 0.5 in the literature, and often a value of 0.499 is employed, to avoid incorrect calculation of the shear and bulk moduli (Johnston *et al.*, 2014). An alternative method reported an elastic modulus of 750 kPa for a 10:1 mixing ratio of PDMS cured for 15 min at 90° C (Armani, Liu and Aluru, 1999). These investigators measured the vertical deflection of a PDMS cantilever using an optical microscope, and derived the value from an equation that considered the geometry and density of the cantilever. They assumed that the shear modulus of PDMS was 250 kPa (as reported elsewhere) and calculated a Poisson's ratio of 0.5 for their 10:1 mix. Based on these data, we would expect our 10:1 mix ratio PDMS – which was cured at ~ 70° C for ~ 2 h, to have an elastic modulus ~ 1.5 MPa.

4.1.4 Nanoindentation

Much like the AFM, dedicated nanoindentation instruments were developed in the 1980's and further paved the way for a nano-revolution. In contrast to AFM, where a calibrated displacement is applied to the probe and its deflection measured optically, during a nanoindentation experiment a calibrated force is applied to the probe, which is constrained vertically by leaf springs in a three-plate capacitor, and the displacement is measured independently. The accurate determination of the contact point is then used to define the depth of indentation. However, for soft materials, the initial contact point is difficult to determine, which can lead to erroneous reporting of indentation depth and modulus (Cohen and Kalfon-cohen, 2013).

Dedicated nanoindentation relies on the accurate calculation of the indenter tip geometry. Sneddon assumed an infinitely sharp tip, when considering the geometry of the cone, but in reality, the indenter has a finite tip radius of curvature. Many researchers have explored this effect. Doerner and Nix considered that the exact shape of the indenter is critical to determine the measurements of hardness and elastic modulus for depths < 1 µm (Doerner and Nix, 1986). They produced two-stage carbon replicas of plastically deformed indentations in a brass substrate and imaged them with a TEM. From this, they derived an effective area equation of the indenter and tested it on hard substrates, such as tungsten. They calculated an elastic modulus of 480 GPa at shallow indentation depths and took the Poisson's ratio to be 0.28. Moreover, the measured area deviated from an ideally sharp indenter by up to a factor of three, when reducing from ~ 1 µm down to a depth of 20 nm. Thus, they further concluded, "The indenter tip is considerably more blunt than the ideal pyramid". From this area equation, Shih and colleagues (Shih, Yang and Li, 1991) modelled the blunt end of the indenter as a spherical cap of various radii. They used a triangular-base pyramid indenter with nominal angles of 65.3° between the faces and the vertical axis and 77.0° between the edges and the vertical axis. They used simple geometry to derive an equation where a single parameter *R*, the tip radius, is used to calculate the relationship between area and depth.

4.1.4.1 Oliver and Pharr

The previous theory was extended to account for the changes in contact area at different locations along the unloading (retract) portion of a F-D curve (Oliver and Pharr, 1992). Their experiments suggested that the assumption by Doerner and Nix - that the unloading curve was linear and the elastic behaviour could be described by a flat punch geometry, was not entirely adequate. They extended the theory and proposed a new model, based on a conical indenter. As its cross-sectional area changes at different depths of contact - and as no real indenter is ever perfectly sharp, the tip assumes a spherical geometry. To obtain values of elastic modulus the authors assume that the indenter geometry can be described by an area function $F(h)$ which relates the cross-sectional area of the indenter to the distance from its tip. The projected contact area, A at peak load can be computed from the relation $A = F(h_c)$ where F is determined experimentally prior to analysis and h_c is the contact depth. To correct for any effects of non-rigid indenters on the load-displacement behaviour a reduced elastic modulus, E_r can be defined according to the equation

$$\frac{1}{E_r} = \frac{(1-v_i^2)}{E_i} + \frac{(1-v_s^2)}{E_s} \tag{12}$$

where v is the Poisson's ratio and i and s denote the indenter and sample respectively.

As the elastic modulus of the PDMS is orders of magnitude lower than that of the indenter, the indenter term in Eq. (12) can be neglected (Ebenstein and Pruitt, 2004). The reduced elastic modulus could be solved according to the equation

$$E_r = \frac{\sqrt{\pi}S}{2\sqrt{A}} \tag{13}$$

where the stiffness, S is experimentally measured from the upper portion of the unloading curve according to the derivatives of the indenter load with respect to the indenter displacement (dF/dh). Eq. (13) holds for any indenter that can be described as a body of revolution, and thus, is not limited to a specific geometry (Oliver and Pharr, 1992). In the formulation of their contact model Oliver and Pharr made the assumption that the elastic modulus was independent of indentation depth. Further, they defined a geometric constant for various indenter geometries. A flat punch was defined as 1, a paraboloid as 0.75 and a conical indenter as 0.72. They found that the paraboloid better described the unloading behaviour but note that even if a conical geometry had been chosen, the only difference in

their analysis would have been to use the slightly smaller constant of 0.72 (Oliver and Pharr, 1992).

The PDMS elastic modulus is related to the reduced elastic modulus according to $E_{PDMS} = E_r(1 - v_{PDMS}^2) = 0.75E_r$ and thus it is important to remember that the reduced elastic modulus is 25% greater than the elastic modulus (Wang, Volinsky and Gallant, 2015). Nanoindentation has reported widely dispersed values of elastic modulus for 10:1 PDMS between ~ 0.6 MPa – 50 MPa (Lin *et al.*, 2008; Liu *et al.*, 2009; Charitidis, 2011) with many suggesting an elastic modulus ~ 3 - 4 MPa (Deuschle *et al.*, 2008; Shen, Wei and Lin, 2008; Paoli and Volinsky, 2015).

4.1.4.2 Depth dependence of elastic modulus

There is a confusing paradox in the literature regarding the depth dependence of the modulus of PDMS. Whilst some authors state that the elastic modulus values are constant and that there is no depth dependence (White *et al.*, 2005), others have shown a clear depth dependence (Liu *et al.*, 2009; Charitidis, 2011). Some investigators suggest that the stiffness increases at increased depths, due to the increasing contact of the polymer and the indenter (Paoli and Volinsky, 2015) and others suggest the opposite – that the modulus decreases during increased indentations, with higher moduli at the surface. This has been attributed to (i) spherical indenter geometry having a large contact area at the surface (Charitidis, 2011) (ii) a dependence of the film thickness – where a thickness less than 200 µm reports a higher moduli than that from thicker films (Liu *et al.*, 2009), or (iii) as a result of the molecular properties of PDMS – where it is suggested that there is a greater crosslinking density between the surface and up to 300 nm, and bulk properties change after this depth (Charitidis and Koumoulos, 2012).

Nanoindentation of soft materials presents similar problems as also evident for AFM. The sample is assumed to be a linear, isotropic material and the surface forces and longer-range forces can make the contact point difficult to define. This uncertainty can lead to significant errors in the reported modulus (Notbohm, Poon and Ravichandran, 2012). A nanoindenter typically operates with a resolution of hundreds of nN to low µN and is typically used to determine the mechanical properties of very stiff materials, to depths on the order of microns. If very small indentations on the order of nm, on a soft substrate are required, the

nanoindenter may not be an ideal choice. Despite these limitations we performed nanoindentation on a variety of PDMS samples to compare our results obtained by AFM and tensile testing.

4.1.5 Elastic modulus characterisation with the AFM

Because of the problems associated with high loading forces within commercial nanoindenters, the AFM is useful as it permits the application of smaller loading forces (Celik *et al.*, 2009). Notbohm and colleagues performed multiple analyses of a 10:1 ratio cured PDMS sample (Notbohm, Poon and Ravichandran, 2012). They prepared two specimens, at 18 mm x 3 mm and 20 mm x 15 mm respectively, both with ~ 1 mm thickness, and used a motorised translation stage to apply uniaxial tension. They found that the specimens were linear throughout the range of strains tested, and a Young's modulus of 0.89 ± 0.04 MPa was obtained. Poisson's ratio was measured to be 0.47 ± 0.02. They used AFM, with a 0.6 N/m cantilever (an order of magnitude stiffer than ours) functionalised with a 5 µm glass sphere, and collected multiple F-D curves using a range of scan rates. The raw data was fitted to the JKR contact model. They found that their data were nearly identical for rates of 0.06, 0.60 and 6.00 µm/s, suggesting that the PDMS modulus was not rate dependent. Using AFM, the reduced modulus was found to be 1.12 ± 0.01 MPa. The low SD implies that the deformation remained elastic, rather than plastic and implies that the loading curve should be used, rather than the unloading curve – as typically used in nanoindentation experiments. By using a Poisson's ratio of 0.47 the Young's modulus was calculated to be 0.87 MPa, in close agreement with their tensile experiments.

4.1.5.1 Stiffness characterisation with the AFM

Stiffness and elasticity are both related by the concept of flexibility – that is the displacement vs. an applied force. The elastic modulus of a material is an intrinsic material property, and represents the ability of a material to resist deformation and regain its original shape and size following the removal of an applied load. As previously described it can be represented as the stress divided by the strain. It is independent of the geometry of the specimen. The stiffness is a structural property that represents the amount of force required to cause deformation. It is influenced by the material and its geometry. It can be

expressed as the applied force divided by the extension or deflection. It is not uncommon to see both terms used interchangeably (and incorrectly) in the literature.

4.1.5.2 Hertzian contact between a sphere and a flat plane

Under Hertzian contact theory for the contact between a rigid sphere and an elastic half space (Popov, 2010), the pressure, P_0 at the centre of the circular contact area is described according to the equation

$$P_0 = \left(\frac{6FE^{*2}}{\pi^3 R^2}\right)^{\frac{1}{3}} \tag{14}$$

where F is the applied force, $E^*$is the reduced modulus and R is the tip radius. The contact radius area, a is described by the equation.

$$a = \left(\frac{3FR}{4E^*}\right)^{\frac{1}{3}} \tag{15}$$

Assuming a homogeneous normal displacement, the vertical displacement u_z that the indented material may experience can be described by the equation.

$$u_z = \frac{\pi P_0 a}{E^*} \tag{16}$$

4.1.6 Molecular properties

Long-chain polymers typically exist in disordered random coils. The polymeric PDMS has a molecular chain width around 0.7 nm and based on 1000 repeat-units the random coil should be around 10 nm in thickness (Granick, Lin and Bae, 2003; Yamada, 2003). Yamada was able to compress a film of the polymer between two layers of mica and discovered that the polymer chains became ordered into discrete adsorbed layers – 2 to 4 molecular layers in thickness, with mobile layers freely moving between the first layers adjacent to the mica (Fig. 4.1). The author posits that this liquid-like behaviour was possible due to the flexible nature of the siloxane backbone, with free rotation of molecules along the Si – C and Si – O bond axes (Yamada, 2003).

PDMS is hydrophobic, with water contact angles > 90° and typically ~ 94 - 105° (Zhou *et al.*, 2012; Juárez-Moreno *et al.*, 2015). The surface methyl groups that confer the hydrophobicity can be removed by O_2 plasma treatment and replaced by oxygen atoms in the form of hydroxyl groups or a silica-like SiO_x layer, rendering the surface hydrophilic

(Juárez-Moreno *et al.*, 2015). However, PDMS readily undergoes hydrophobic recovery - thought to be caused by the migration of low molar mass uncured siloxanes from the bulk material to the surface (Meincken, Berhane and Mallon, 2005; Zhou *et al.*, 2012). Whilst this phenomenon makes PDMS a great insulator it can be problematic to cell culture and microfluidic applications (Nourmohammadi *et al.*, 2015).

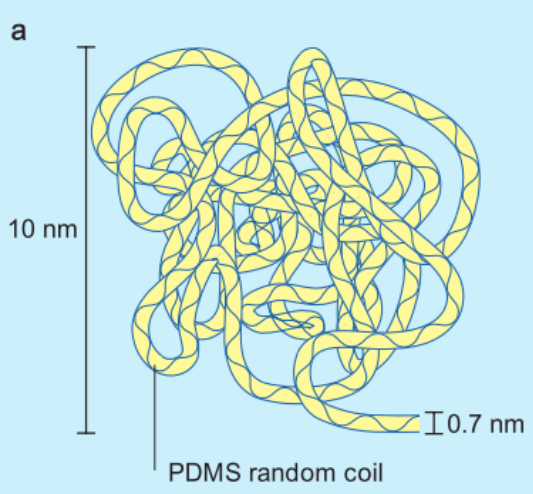

Figure 4.1. PDMS typically exists in a random coil formation. Yamada showed that the thickness of the siloxane backbone is around 0.7 nm and based on 1000 repeat-units the disordered coil should be around 10 nm in thickness (Yamada, 2003). Image adapted from (Granick, Lin and Bae, 2003)

4.1.6.1 Surface roughness

Solid surfaces contain irregular deviations from their prescribed geometry. These are typically characterised by peaks (asperities) or low points (valleys). When two nominally flat surfaces are brought together the surface roughness leads to contact at discrete points along their contacting regions. These discrete points constitute the real contact area, and it is usually only a small proportion of the expected contact area, had the surfaces been perfectly smooth (Bhushan, 1998). Rough surfaces are random, and stochastic models or analysis of 3D roughness maps can be used to characterise the contact between two rough surfaces (Bhushan, 1998). AFM topographic images can be analysed to sub-nanometre resolution.

The mean roughness, R_a or the RMS roughness, R_q of the PDMS surface has been quantified in the literature, and the data are widely dispersed. Values from 0.85 nm to 15 nm (Schrott *et al.*, 2009; Charitidis, 2011; Tang *et al.*, 2015) and up to ~ 66 nm have been reported (Juárez-Moreno *et al.*, 2015). When trying to establish the elastic modulus with indenting probes the roughness characteristics can present problems, as the surface roughness can affect the effective contact area between the probe and the surface (Lopera and Mansano, 2012).

4.1.7 Indenter geometry

Attempts to define the contact angles on rough surfaces involve difficult mathematical and conceptual problems. The difficulty arises when investigating the relationship between the intrinsic contact angle and the apparent contact angle as the apparent contact angle may vary from point to point (Wolansky and Marmur, 1999). The shape at the end of the tip is critical when indenting to small depths (Cohen and Kalfon-cohen, 2013). Whilst the nanoindentation community make great attempts to fully characterise the geometry of the indenter, the AFM community do not appear to be as zealous. Often, the manufacturer designated nominal tip radii or conical half-angles are used in the contact mechanics models employed. Alternatively, blind reconstruction of the tip geometry may be utilised (Cohen and Kalfon-cohen, 2013; Bailey *et al.*, 2014). Here, a tip is scanned across a surface with differing asperities of smaller radii than the probe, and the resultant image is considered to be composed of the artefacts arising from the tip geometry. This technique has proved useful to monitor the changes in tip geometry over the course of repeated scans on hard substrates (Liu *et al.*, 2010; Bailey *et al.*, 2014), but may not be so useful on small indentations of soft materials.

4.1.8 Molecular resolution

The molecular organisation of PDMS does not appear to be very well characterised in the literature. Super-resolution microscopy was employed to investigate PDMS microchannels within a fluidic device (Cheng *et al.*, 2013). These authors developed a photoswitchable micelle to measure nanochannels formed in the PDMS under tensile cracking. Through image reconstruction they suggest that they achieved an imaging resolution ~ 40 nm. Some topography and porosity is evident although their published images were on the order of

microns. SEM and AFM were used to observe the surface of native and coated PDMS (Nourmohammadi *et al.*, 2015). Their AFM images showed considerable topography, but at a length scale of 50 x 50 µm. Yu and co-workers collected AFM topographic images of a polyacrylate-PDMS copolymer. Their images showed considerable porosity of the polymer, but on the order of microns (Yu *et al.*, 2013).

4.1.9 Aims of this chapter

1. Design and produce lithographically patterned silicon wafers to imprint PDMS substrates for bacterial immobilisation.
2. Use tensile testing, nanoindentation and AFM to characterise the elastic modulus of PDMS.
3. Obtain molecular resolution of PDMS and analyse the surface structure and roughness.
4. Investigate any differences between the surface and the bulk properties of PDMS.
5. Infer relationships between tip geometry; contact radii and indentation depth to more accurately define the elastic modulus of PDMS.

4.2 Results

4.2.1 Lithographic patterning of silicon substrates

Three distinct designs with differing geometries were created and transferred onto a glass plate. Using contact mask lithography the mask was placed in contact with a silicon substrate and a UV light source was used to expose the patterns on a layer of positive photoresist (Chapter 3.7). Following exposure and etching, pillars of each design remained bound to the silicon wafer, and these could be used to faithfully transfer the patterns onto PDMS substrates.

4.2.1.1 Repeating circular design

A repeating array of ~ 1.5 µm diameter circular pillars, with a height ~ 750 nm were produced and their geometries verified with SEM (Fig. 4.2). There is charging evident in the micrograph in (Fig. 4.2d) although this does not interfere with the height measurement.

4.2.1.2 Multiple geometries design

It was anticipated that varying the circular diameters might have allowed sufficient immobilisation of SA cells at various stages of growth – either from single or connected cells. A lattice of 10 x ~ 1.5, 2.5 and 3.5 µm diameter circular pillars, with a height ~ 750 nm were produced (Fig. 4.3). These designs were repeated over 8 rows and were topped with 10 x rod-shaped designs, of length ~ 5.5 µm, width ~ 1.5 µm and a height ~ 750 nm, repeated over 2 rows. Together, these formed an array that was repeated numerous times across the silicon wafer. Each array was identifiable with an *XY*-numbered reference, also with a height ~ 750 nm.

4.2.1.3 Four-sided star shaped design

Multiple rows of 5 µm connected circles were arranged to produce a four-sided star shape of ~ 3 µm in diameter and a height ~ 750 nm (Fig. 4.3d).

a

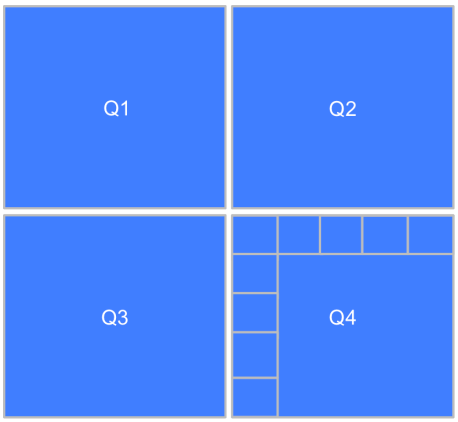

b

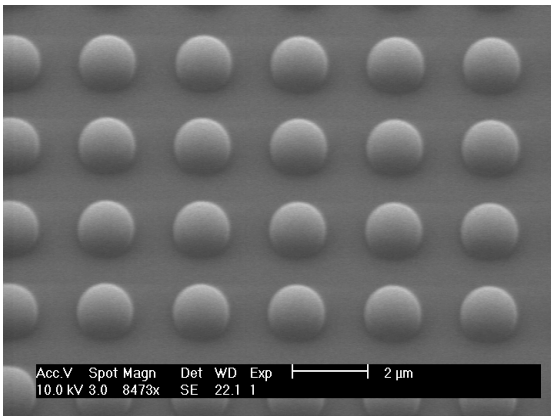

c

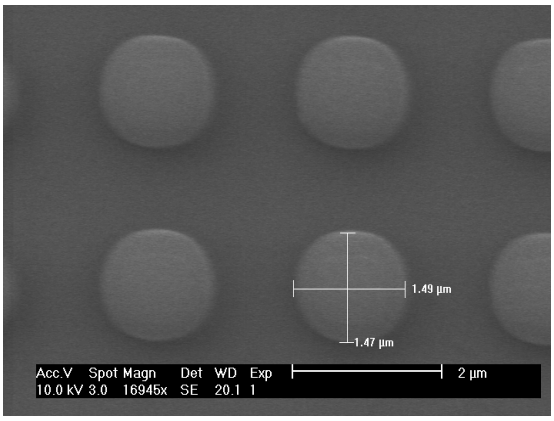

d

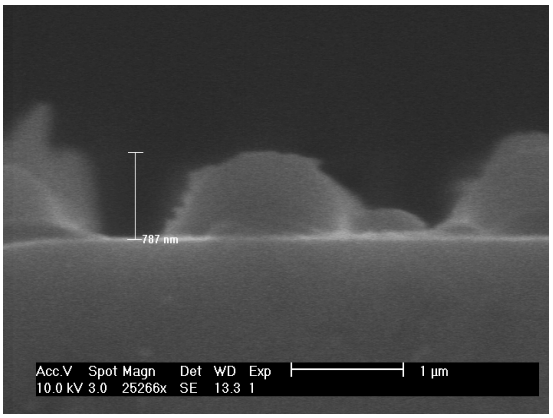

Figure 4.2. Design template and SEM micrographs of lithographically patterned circular pillars. (a) A 4 inch quartz mask was ordered into 4 x 4 cm quadrants. Three designs were created for contact mask photolithography. Each Q contains 5 x 5 sequences of 8 x 8 mm sections (b) A repeating array of circular pillars were produced, with (c) a diameter ~ 1.5 µm and, (d) height ~ 750 nm. Q4 featured a design not used in this study.

a

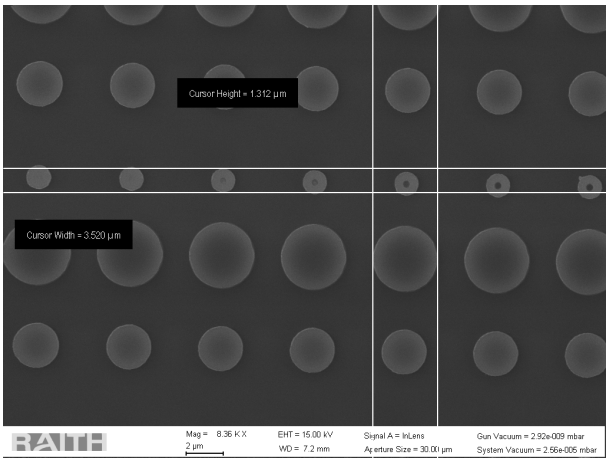

b

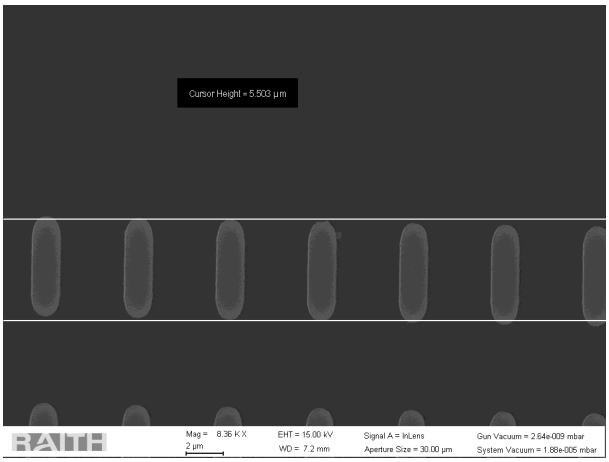

c

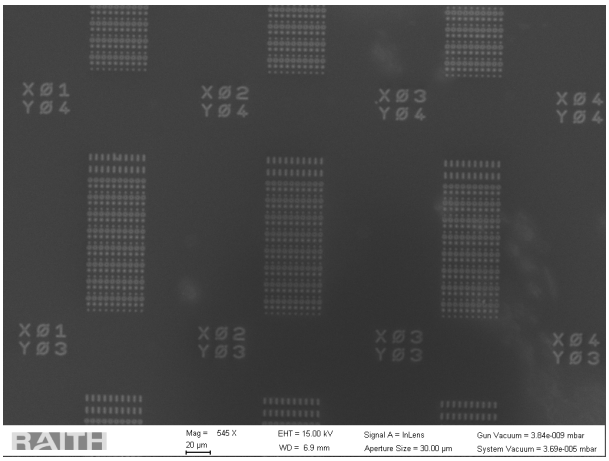

d

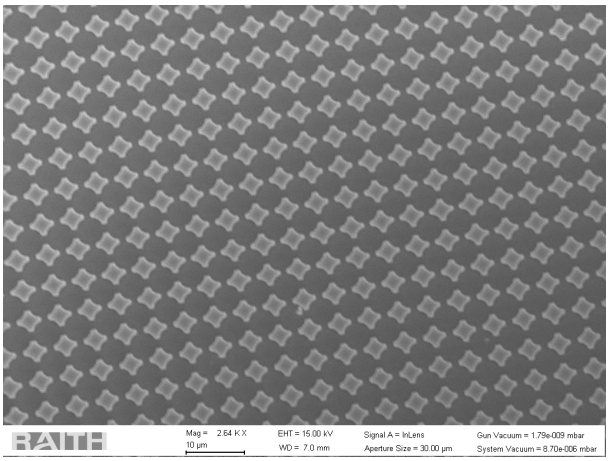

Figure 4.3. SEM micrographs of multiple geometry pillars. (a) A repeating lattice of 1.5, 2.5 and 3.5 µm circular pillars and (b) rod-shaped pillars of 5.5 µm length and 1.5 µm width. (c) This lattice was arranged in a repeating array that was separated by an *XY*-numbered reference. (d) A series of connected 5 µm circles were arranged to create a four-sided star shape between them.

4.2.2 Tensile testing of PDMS

Five different PDMS substrates were mixed in a 10:1 ratio and cured for 2 h at ~ 70° C. The samples varied in thickness and age, between freshly prepared and up to 1 month old. The samples were trimmed with a blade into a rectangle, and mounted into the tensile testing instrument (Fig. 4.4). Their mean dimensions were 5.4 ± 3.7 mm^2. Minimum and maximum were 3.2 mm^2 and 12 mm^2 respectively. The elastic modulus was obtained at a mean strain of 14% along the stress/strain curve. The mean sample yielding was at 69% strain. The maximum applied force at breaking was 3.0 ± 0.56 N. The mean change in length of the substrates was 7.7 ± 2.7 mm. Mean elastic modulus was 1.3 ± 0.23 MPa.

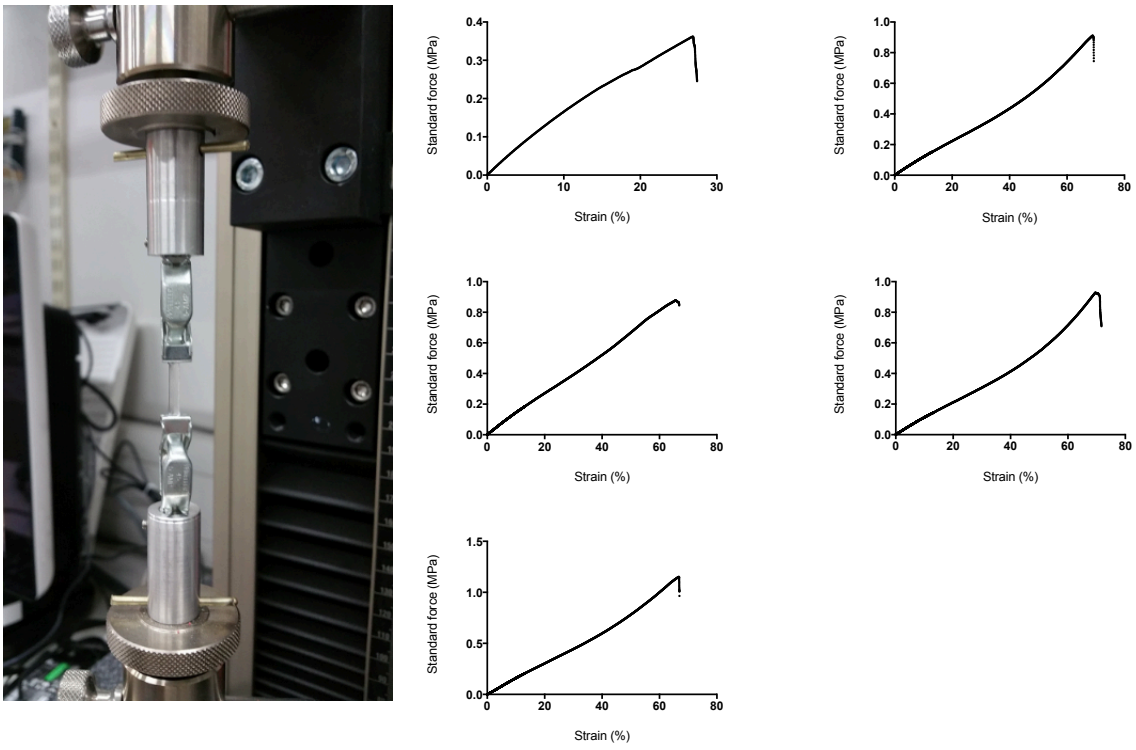

Figure 4.4. Tensile testing strain curves for PDMS. Five individual samples were trimmed into rectangles and mounted into the instrument clamps. The elastic modulus was calculated from a mean strain of 14% along the stress/strain curve. Mean sample yielding was at 69% strain. Mean elastic modulus was 1.3 ± 0.23 MPa. The sample thickness was (clockwise top left to bottom right) 12, 4.03, 4.5, 3.15 and 3.25 mm^2.

4.2.3 Dedicated nanoindentation of PDMS

Similar to the tensile testing experiments, a variety of PDMS substrates, of varying thickness and age were prepared. They were gently pressed around the edges to secure them to the indenter stage.

4.2.3.1 Berkovich indenter

Initial testing was performed in H_2O with a liquid cell, using a Berkovich indenter using load control tests. Two individual indents were performed manually. Loading force was 5 µN, with 5 s and 30 s segment times. The loading rates were automatically calculated. Maximum loads transferred were 3.20 and 3.21 µN respectively. The calculated indentation was 230 nm and 243 nm. Reduced elastic moduli were 10.7 MPa and 11.0 MPa. The mean reduced modulus was 10.9 MPa giving a mean elastic modulus of 8.15 MPa. The different loading rates did not confer a significant difference to the reported depth or moduli. 25 automated indents were performed with loading forces between 3 – 100 µN and a loading speed of 5 s. Minimum and maximum transferred loads were 3.21 and 98.2 µN. Minimum and maximum indentations were 261 nm and 2711 nm. Mean indentation was 1670 ± 730 nm. The reduced elastic modulus at 261 nm was 11.7 MPa. This reduced linearly to 3.35 MPa at the maximum indentation. Mean reduced modulus was 4.54 ± 1.84 MPa giving a mean elastic modulus of 3.40 MPa.

4.2.3.2 100 µm conospherical indenter

Two manual indents were performed in H_2O with a 100 µm conospherical indenter. Loading force was 20 µN, with 5 s – 2 s – 5 s load control. Two lift heights (1 and 2 µm) were investigated to attempt to accurately define the initial surface contact. Maximum transferred loads were 18.1 and 18.6 µN respectively. The calculated indentation was 167 nm and 219 nm. Reduced elastic moduli were 6.58 MPa and 5.78 MPa. Mean reduced modulus was 6.18 MPa giving a mean elastic modulus of 4.64 MPa.

4.2.3.3 1 µm conospherical indenter

A 1 µm conospherical indenter was used in air, and 7 individual indents were performed. A range of loading forces (3, 5 and 15 µN) and lift heights (180, 1000 and 2000 nm) were compared. Minimum and maximum loads transferred were 2.01 and 14.0 µN. Minimum and

maximum indentations were 367 nm and 1338 nm. Mean indentation was 791 ± 330 nm. Mean reduced modulus was 3.8 ± 0.78 MPa giving a mean elastic modulus of 2.9 MPa.

4.2.3.4 Load function and indentation curves

When defining the desired loading speeds a trapezoidal load function was created, where loading times, hold (dwell) times and unloading times could be configured. Loading and unloading speeds were always matched. The hold times were varied between 2 s or 50 s. Single indents with the Berkovich indenter and the 1 µm conospherical indenter were fit to a load function of 5 s load – 50 s hold – 5 s unload (Fig. 4.5a). A representative 5 µN loading/unloading curve from the 1 µm conospherical indenter, with 1000 nm lift height appears in (Fig. 4.5b). The reduced elastic moduli are obtained by fitting a tangent to the steepest portion at the top of the unloading curve in the nanoindenter software (representative line drawn manually here).

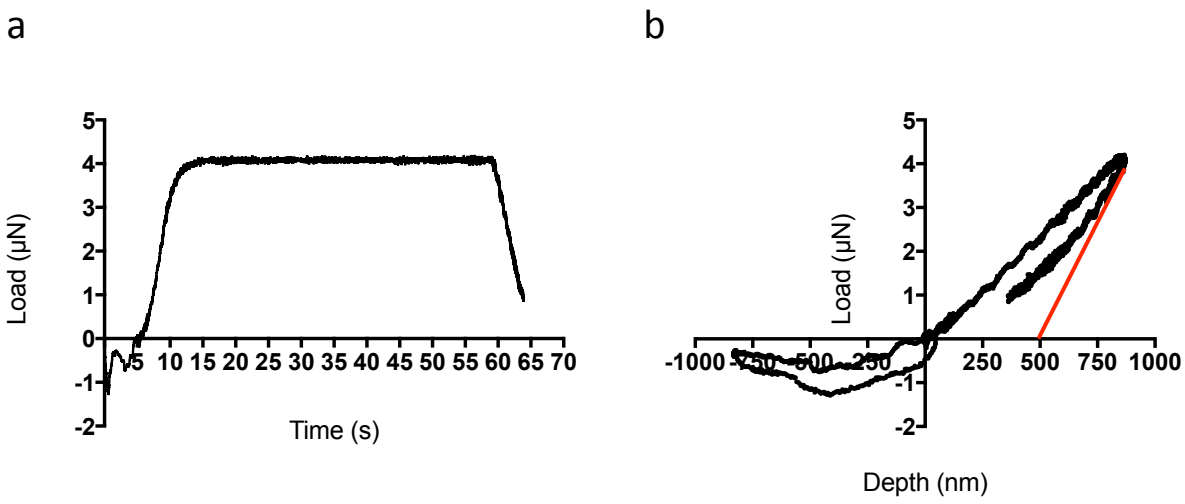

Figure 4.5. Load function and indentation curve on PDMS. (a) A representative trapezoidal load function at 5 µN with 5 s load – 50 s hold – 5 s unload. (b) A representative loading/unloading curve with a 1000 nm lift height and maximum indentation of 870 nm. The reduced elastic modulus is obtained by fitting a tangent to the steepest portion of the unloading curve. Manually drawn here in red.

4.2.3.5 Combined nanoindentation results

Disregarding the different ambient conditions (H_2O vs. air), and the various loading forces, loading speeds or indenter geometries we can combine all the mean reduced elastic moduli to obtain a value of 6.4 ± 3.2 MPa and a mean elastic modulus of 3.6 ± 0.91 MPa. Combining the mean indentation depths gives 885 ± 740 nm.

4.2.4 AFM elastic modulus analysis

Following the wide range of elastic modulus data from our nanoindentation experiments, we reverted to the tensile testing data as a guide for a realistic elastic modulus for our PDMS. The raw F-D curve is first modified with relevant software operators (Chapter 3.9.1) (Figure 4.6 a). The baseline offset is removed to bring the *X* and *Y* axes towards zero (Fig. 4.6 b). The contact position between the tip and sample, where the tip deflects, leading to the steep portion of an F-D curve is approximated using the *X* axis offset (Fig. 4.6 c). In order to determine the actual height and indentation depth of a sample the vertical tip position operator is applied (Fig. 4.6 d). This subtracts the difference between the cantilever vertical deflection and the height of the piezo. The Hertzian model operator used for elastic moduli was applied and the elastic modulus values described here were obtained by using the Sneddon contact model with a conical geometry (Chapter 3.9.5). The contact model was fitted to the approach portion of a F-D curve at 10 nm of indentation, except for the analysis of deeper indentations, described later (section 4.2.9.1). The conical fitting (Fig. 4.6 e) was consistently more accurate than fitting with a spherical geometry (Fig. 4.6 f).

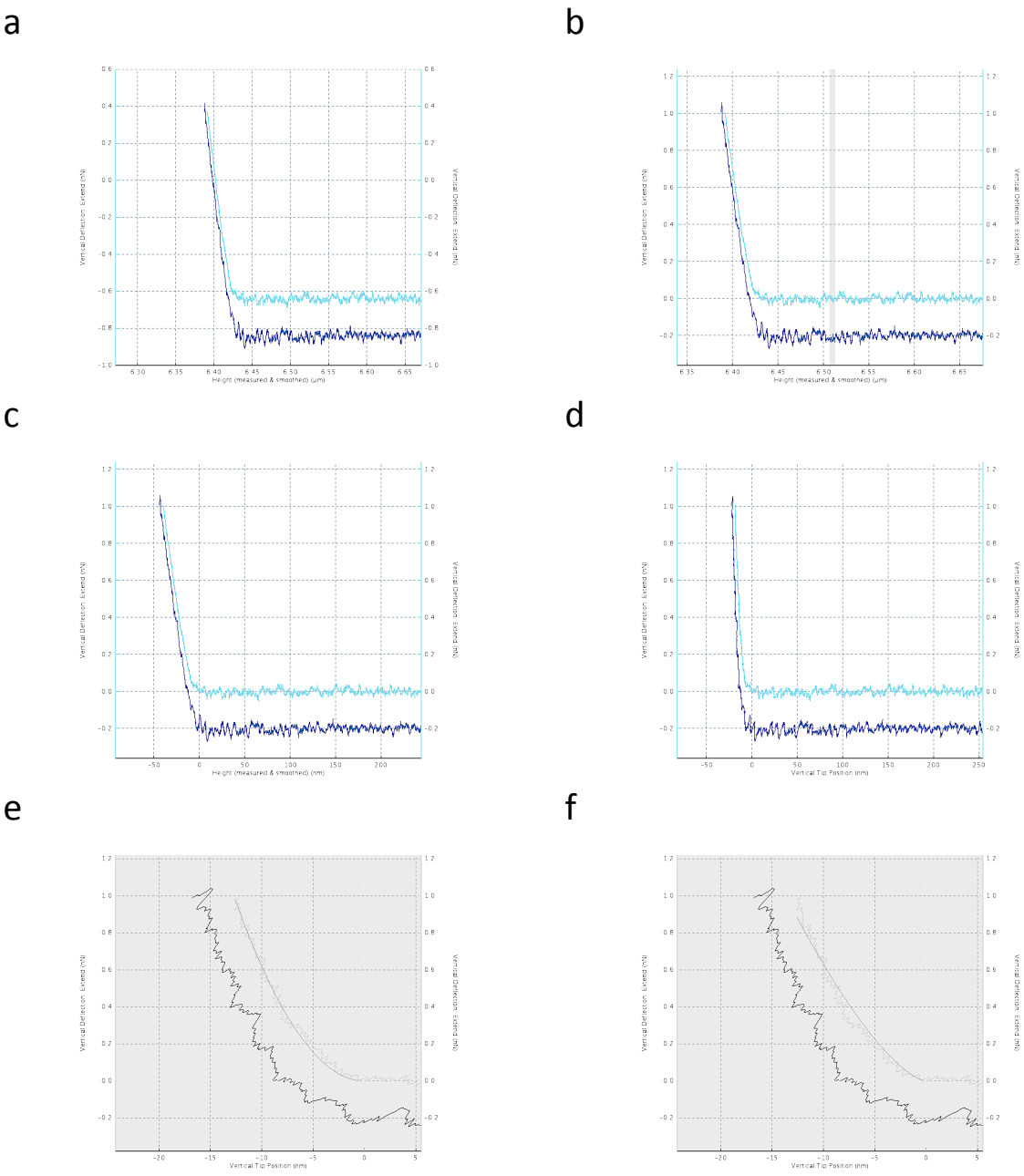

Figure 4.6. Software processing of F-D curves. Representative F-D curves depict the process of applying the AFM software operators. These allow for accurate reporting of sample height, indentation depth and elastic modulus. (a) The raw curve is adjusted to bring the (b) baseline offset towards zero. (c) The contact location between tip and sample is approximated. (d) The cantilever deflection is accurately determined. The Hertzian fitting consistently showed that selecting the (e) conical fit produced more faithful fitting of the F-D curve than when compared to (f) a spherical fit.

4.2.4.1 Software standard conical half-angle vs. modified half-angle

Twenty F-D curves were analysed using the software default conical half-angle of 15°. The reported elastic modulus was 69 ± 27 MPa (± 6.0 SE) from a mean indentation of 10 ± 0.31 nm (0.07 SE). Median elastic modulus was 64 MPa. QI™ setpoint was 6.1 nN. Increasing the conical half-angle to 85° in the software gave a reported elastic modulus of 1.6 ± 0.63 MPa (± 0.14 SE). Median elastic modulus was 1.5 MPa (Fig. 4.7).

4.2.4.2 Elastic moduli with an 85° half-angle

In order to statistically improve the data, further PDMS samples were analysed with an 85° conical half-angle (Chapter 3.9.5 and Chapter 5). Adjusting the angle to 85° consistently reported the elastic modulus of PDMS at ~ 1.3 MPa. A mean elastic modulus of 1.2 ± 0.51 MPa was obtained. The large SD reflects the heterogeneity of the PDMS. The median elastic modulus was 1.2 MPa (Fig. 4.8).

Mean (MPa)	SD (MPa)	SE (MPa)	Median (MPa)
1.2	0.51	0.06	1.2

Table 4.1. 85° half-angle PDMS modulus. The values were calculated by Sneddon contact model fitting at 10 nm indentations of AFM F-D curves. 20 F-D curves per sample *n* = 4 substrates and therefore averages calculated from 80 F-D curves.

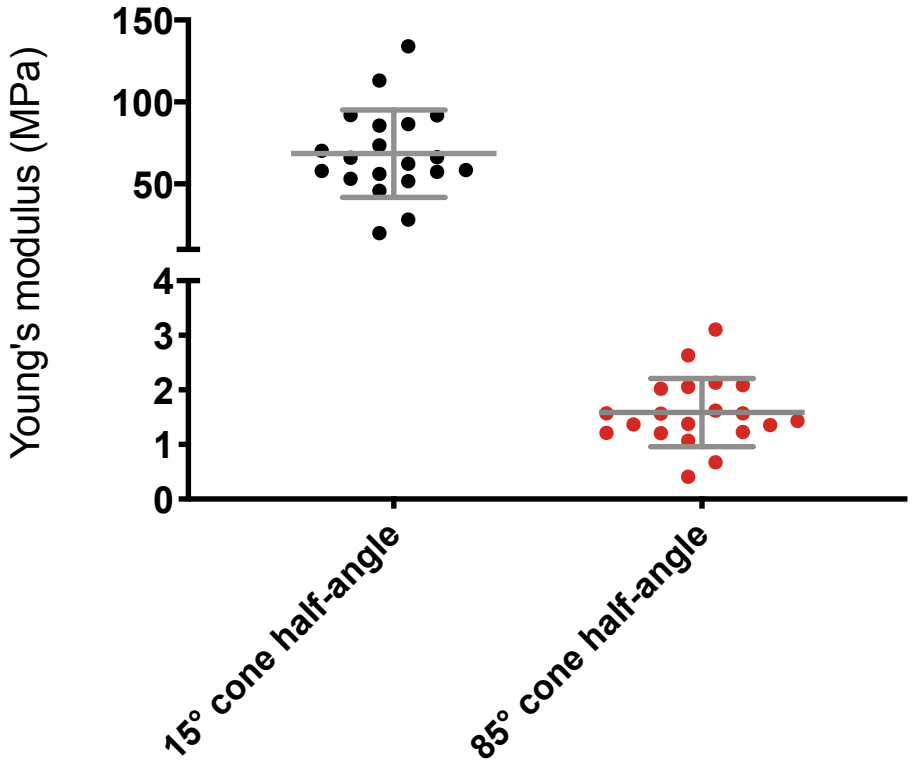

Figure 4.7. PDMS cone angle modulus comparisons. The elastic modulus of PDMS, using the software default 15° cone half-angle setting was compared against a modified cone half-angle setting of 85° as this was found to consistently report the PDMS modulus at ~ 1 .3 MPa. Scatter plot shows the distribution of mean elastic modulus of PDMS. Error bars show mean ± SD. Each dot represents an individual F-D curve. The default 15° half-angle gave a mean elastic modulus of 69 ± 27 MPa. Modifying the cone half-angle gave an elastic modulus of 1.6 ± 0.63 MPa. The left *Y*-axis is split into 2 segments for easier visualisation of the default and modified cone data. Data were derived from 20 F-D curves from a single experiment.

The scatter plot (Fig. 4.8a) shows a dot for each analysed F-D curve. The error bars show the mean ± SD. The frequency distribution histogram (Fig. 4.8b) shows the distribution of values of the PDMS means, with a least squares Gaussian fit. The data are skewed to the right, skewness = 0.99, R^2 = 0.84.

a

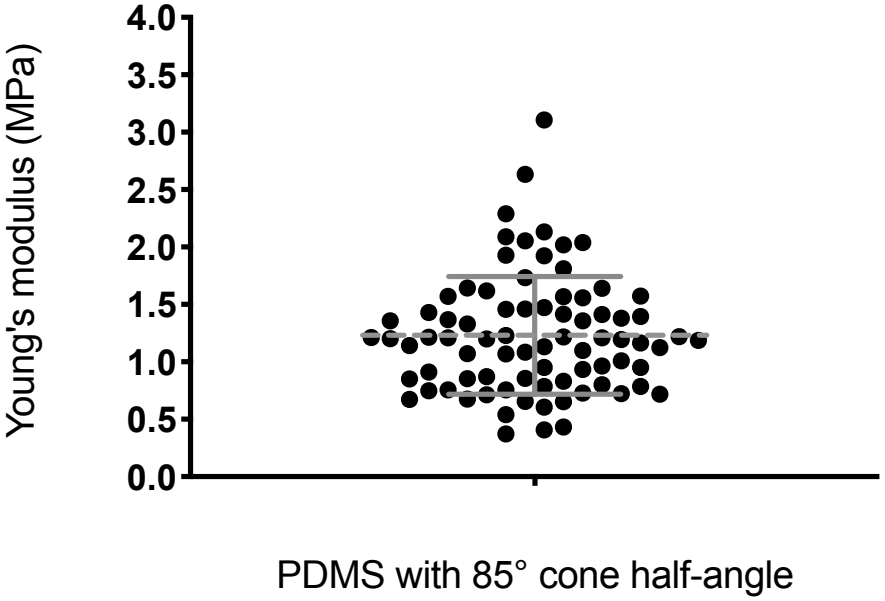

b

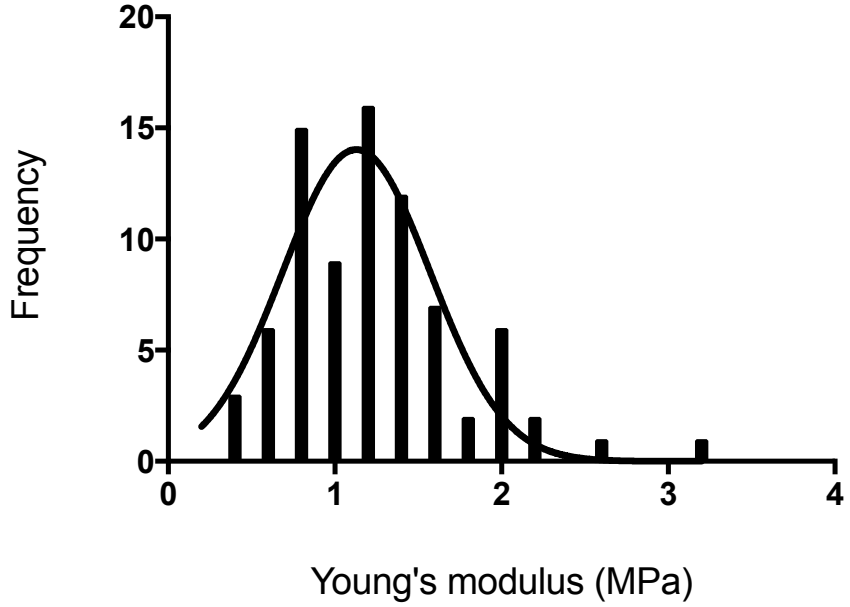

Figure 4.8. Elastic modulus of PDMS with an 85° half-angle. Changing the conical half-angle to 85° consistently reported a PDMS modulus at ~ 1.3 MPa. (a) Scatter plot shows the distribution of mean elastic modulus of PDMS. Error bars show mean ± SD. Each dot represents an individual F-D curve. (b) Frequency distribution histogram of the same data, fitted with a least squares Gaussian fit. Elastic modulus is 1.2 ± 0.51 MPa. *n* = 4 samples from 4 independent experiments.

4.2.4.3 Stiffness of PDMS

To infer alternative assessments of the mechanical properties of PDMS the stiffness was also measured. The stiffness is obtained by fitting a tangent to the approach portion of the F-D curve at 10 nm of indentation Fig. 4.9) and is not affected by any changes in conical half-angles (Chapter 3.9.3). A mean stiffness value of 176 ± 89 nN/µm (0.176 ± 0.089 N/m) was obtained. Again, the large SD reflects the heterogeneity of the samples. SE = 9.9. The median stiffness was 185 nN/µm.

Mean (nN/µm)	SD (nN/µm)	SE (nN/µm)	Median (nN/µm)
176	89	9.9	185

Table 4.2. PDMS stiffness. The values were calculated by applying linear tangents to the curve, at 10 nm indentations of AFM F-D curves. 20 F-D curves per sample were analysed. *n* = 4 substrates and therefore averages calculated from 80 F-D curves.

The scatter plot (Fig. 4.10a) shows a dot for each analysed F-D curve. The error bars show the mean ± SD. The frequency distribution histogram (Fig. 4.10b) shows the distribution of values of the SA cell means, with a least squares Gaussian fit. The data are skewed to the right, skewness = 0.21, R^2 = 0.35.

a b

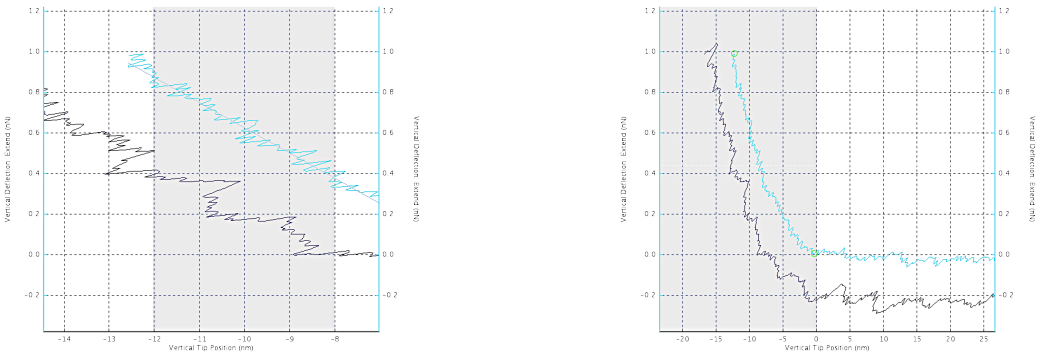

Figure 4.9. Representative slope and statistical fitting of F-D curves. (a) The stiffness of the sample at 10 nm of indentation was measured by fitting a tangent to the curve at 10 nm, constrained by ± 2 nm. (b) The whole indentation region of the F-D curve was selected and the statistical outputs were calculated.

4.2.4.4 Modulus and stiffness characterisation with a spherical indenter

We explored the influence of spherical indenter geometry to test the Hertz contact model against the Sneddon model conical geometry data obtained thus far. A range of AFM cantilevers – with differing spring constants (spanning two orders of magnitude) were functionalised with 10 or 25 μm diameter polystyrene spheres (Fig. 4.11) (Chapter 3.10). The reported elastic modulus and stiffness of 10:1 PDMS and the experimental conditions (loading forces, maximum indentations) are presented in (Table 4.3) and are widely dispersed. Elastic moduli were between 50 – 550 kPa. Stiffness was between 0.054 – 0.38 N/m suggesting that the cantilevers were too stiff to accurately measure the PDMS stiffness.

4.2.4.5 Spherical indenters on a very soft PDMS substrate

Commercially available 15 kPa (Table 4.4) and 28 kPa PDMS (Table 4.5) (Chapter 3.11.1) was tested with various spherical indenters at a range of loading forces. The elastic moduli and stiffness are less dispersed, but still varied - between 41 – 55 kPa and 0.011 – 0.048 N/m respectively. Some curve fitting was poor at 10 nm of indentation. Fitting to the whole curve reduced the moduli to ~ 23 kPa on both samples.

a

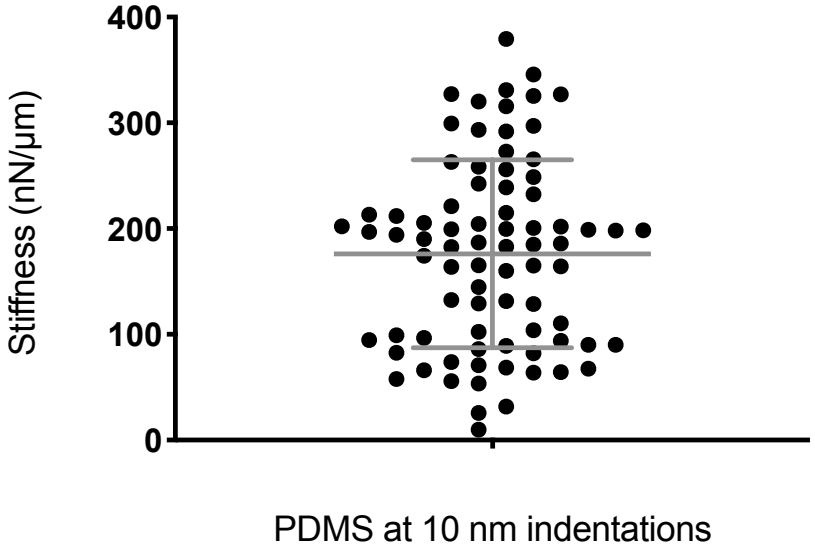

b

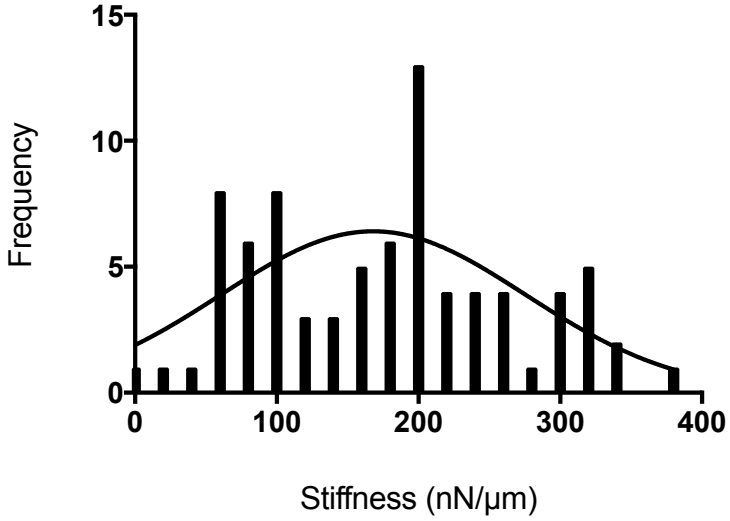

Figure 4.10. PDMS stiffness. (a) Scatter plot shows the distribution of mean stiffness of PDMS. Error bars show mean ± SD. Each dot represents an individual F-D curve. (b) Frequency distribution histogram of the same data, fitted with a least squares Gaussian fit. Stiffness is 176 ± 89 nN/µm. *n* = 4 samples from 4 independent experiments.

a

b

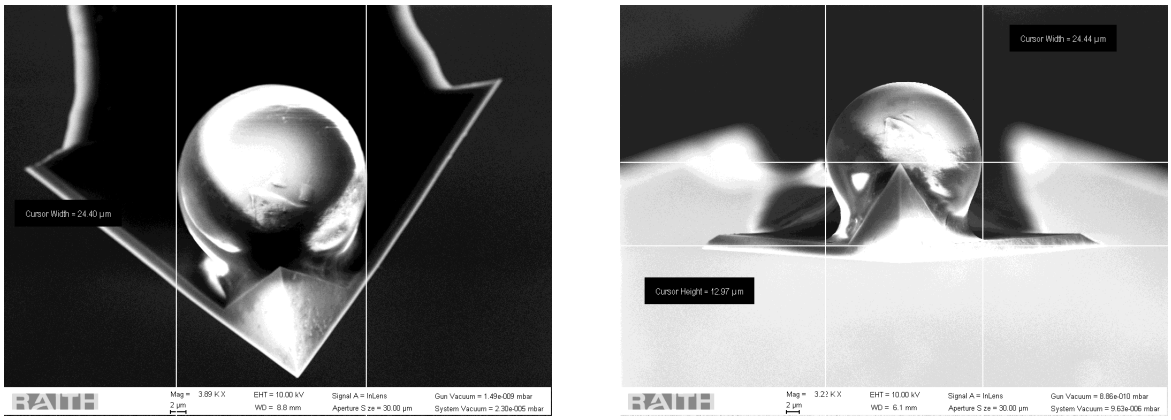

c

d

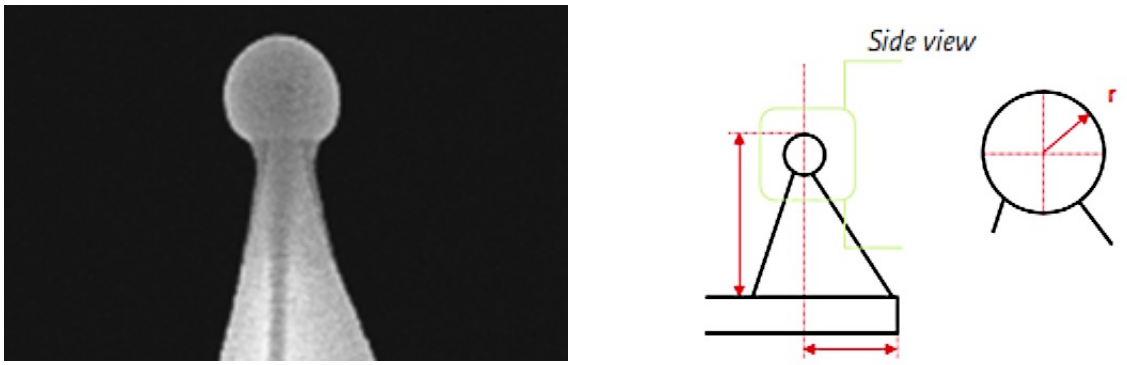

Figure 4.11. Probes with spherical tips. (a, b) SEM micrographs of a 25 µm diameter polystyrene sphere glued onto an Arrow™ CONT cantilever. Measurements were calculated within the SEM software. (c) SEM micrograph of a commercially acquired B500_CONTR probe with 500 ± 10 nm sphere tip. (d) Tip schematic for the B500_CONTR. (c, d) Images adapted from www.nanotools.com.

Sphere diameter (μm)	AFM cantilever	Spring constant (N/m)	Elastic modulus (MPa)	Stiffness (N/m)	Loading force (nN)	Max indentation (nm)
10	MLCT F	1.02	0.22 ± 0.045	0.14 ± 0.3	75	60
25	Arrow™ CONT	0.41	0.05 ± 0.037	0.06 ± 0.06	10	55
25	Arrow™ CONT	0.41	0.13 ± 0.037	0.13 ± 0.06	25	60
25	TESPA-V2	27.5	0.46 ± 0.15	0.33 ± 0.13	50	70
25	TESPA-V2	27.5	0.55 ± 0.18	0.36 ± 0.18	150	100
25	TESPA-V2	27.5	0.55 ± 0.20	0.38 ± 0.21	300	145
25	TESPA-V2	32.1	0.14 ± 0.076	0.087 ± 0.07	500	317
25	TESPA-V2	32.1	0.13 ± 0.038	0.054 ± 0.04	800	430

Table 4.3. The mechanical properties of PDMS tested with various spherical indenters. A range of cantilevers was functionalised with 10 or 25 μm diameter polystyrene spheres. 10:1 PDMS was indented with various loading forces. Fitting the approach portion of AFM F-D curves with the Hertz contact model at 10 nm indentations derived the elastic modulus. The stiffness was reported by fitting tangents to the F-D curves at 10 nm indentations. Elastic modulus and stiffness values listed are the mean ± SD. It can be seen that the cantilevers were between 1 – 3 orders of magnitude stiffer than the measured stiffness of the PDMS and thus were not ideal under these experimental conditions. *n* = 20 F-D curves analysed per condition from 4 independent experiments.

Sphere diameter (µm)	AFM cantilever	Spring constant (N/m)	Elastic modulus (kPa)	Stiffness (N/m)	Loading force (nN)	Max indentation (nm)
10	MLCT F	0.92	41 ± 15	0.011 ± 0.05	10	300
25	TESPA-V2	27.5	55 ± 33	0.048 ± 0.04	46	400

Table 4.4. 15 kPa PDMS tested with spherical indenters. A range of cantilevers was functionalised with 10 or 25 µm diameter polystyrene spheres. PDMS was indented with various loading forces and fitting the approach portion of AFM F-D curves with the Hertz contact model at 10 nm indentations derived the elastic modulus. The stiffness was reported by fitting tangents to the F-D curves at 10 nm indentations. *n* = 20 F-D curves analysed per condition from 2 independent experiments.

Sphere diameter (µm)	AFM cantilever	Spring constant (N/m)	Elastic modulus (kPa)	Stiffness (N/m)	Loading force (nN)	Max indentation (nm)
10	MLCT F	0.92	46 ± 13	0.012 ± 0.04	10	250
25	TESPA-V2	8.24	42 ± 17	0.025 ± 0.02	45	300

Table 4.5. 28 kPa PDMS tested with spherical indenters. A range of cantilevers was functionalised with 10 or 25 µm diameter polystyrene spheres. PDMS was indented with various loading forces and fitting the approach portion of AFM F-D curves with the Hertz contact model at 10 nm indentations derived the elastic modulus. The stiffness was reported by fitting tangents to the F-D curves at 10 nm indentations. *n* = 20 F-D curves analysed per condition from 2 independent experiments.

4.2.4.6 Mechanical characterisation with a commercial spherical indenter

To further test the elastic modulus and stiffness of 10:1 PDMS a commercially available AFM cantilever (B500_CONTR) was utilised (Fig. 4.11 c, d). It has a spring constant of 0.2 N/m (nominal) and a 500 ± 10 nm radius carbon sphere as its tip. The sphere was formed by electron beam-induced deposition. Various PDMS substrates were tested at loading forces between 20 – 60 nN. The mean maximum indentation was ~ 78 nm and the Hertzian fit was applied to the entire F-D curve as it accurately mirrored the geometry. Conversely, fitting at 10 nm of indentation lead to misreporting. Mean elastic modulus was 1.5 ± 0.36 MPa (± 0.046 SE). Median elastic modulus was 1.5 MPa. Mean stiffness was 361 ± 99 nN/µm (± 13 SE). Median stiffness was 362 nN/µm.

4.2.5 PDMS elastic modulus comparisons across different techniques

The mean ± SD of 10:1 PDMS elastic modulus was compared from tensile testing, dedicated nanoindentation, and AFM measurements with an 85° conical half-angle, and a 500 nm radius spherical probe (Fig. 4.12). Both of the AFM measurement methods and the tensile testing data are in close agreement with a combined mean elastic modulus ~ 1.3 MPa.

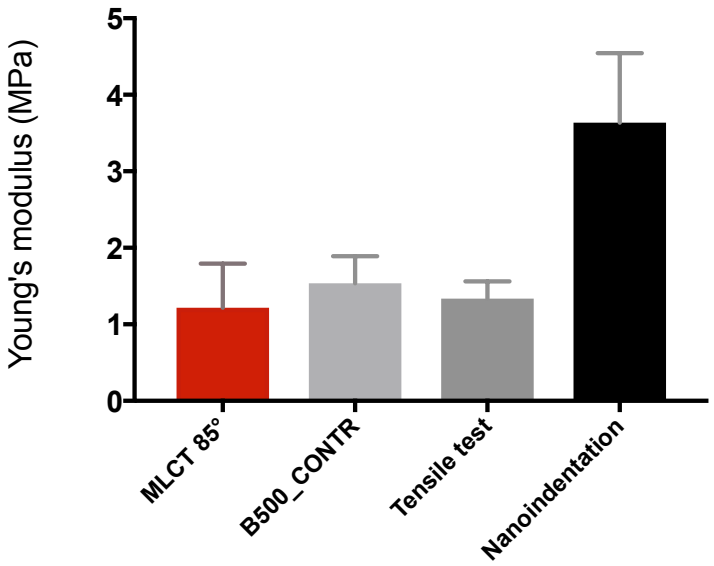

Figure 4.12. Elastic modulus comparisons between AFM and dedicated nanoindentation. The mean elastic modulus from AFM and tensile testing is ~1.3 MPa, and ~ 3.6 MPa from nanoindentation.

4.2.6 QI™ F-D curve and loading time

All elastic moduli in this and subsequent chapters were derived under the same loading conditions (Chapter 3.8.3) unless otherwise stated. A loading force (setpoint) of 1 or 5 nN and an approach and retract speed of 22.5 µm/s equated to an approach and retract time of 40 ms (Fig. 4.13a). The actual surface contact lasted ~ 2.5 ms. There was a typical separation of ~ 200 pN between the approach and retract portions of the F-D curves which were due to hydrodynamic drag (Fig. 4.13b).

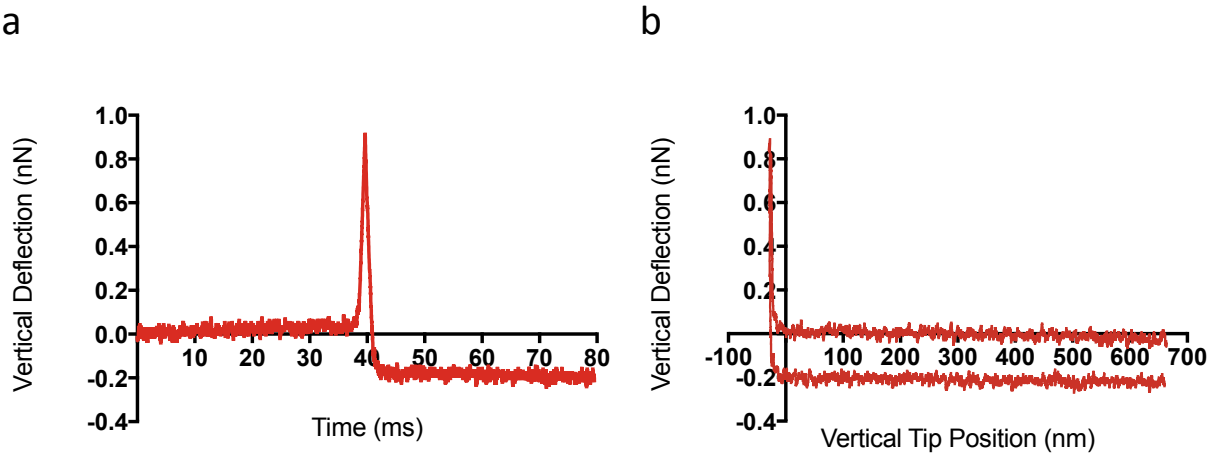

Figure 4.13. QI™ loading time and F-D curve on PDMS. (a) Representative loading function of a QI™ indentation at 1 nN loading force. Approach and retract times are 40 ms, with the surface contact taking ~ 2.5 ms. (b) Representative F-D curve on PDMS at 1 nN loading force.

4.2.7 Molecular organisation of 10:1 PDMS

Intermittent contact mode AFM enabled image capture of the molecular organisation of 10:1 PDMS (Chapter 3.11). Images were gathered at length scales of 1 µm (Fig. 4.14) down to 80 nm (Fig. 4.15d). The surface displays a distinctly porous and heterogeneous morphology at all length scales. All images were edited with 3rd order plane fitting to remove all traces of curvature. To quantify the expected PDMS surface roughness and contact experienced by the MLCT D cantilever tip – with a SEM-derived radius of ~ 40 nm, an 80 x 80 nm 3D topographic profile was generated and three line profiles drawn (Fig.

4.16). Mean height distribution was 0.59 ± 1.6 nm. A 200 nm AFM phase image was measured at multiple points to determine bundle and chain widths (Fig. 4.17). There were dense bundles with ~ 10 nm widths, and individual chains of ~ 2 nm widths and less than 1 nm widths. It is interesting to note how well that these correlate with the work of Yamada and colleagues described previously (Fig. 4.1).

a b

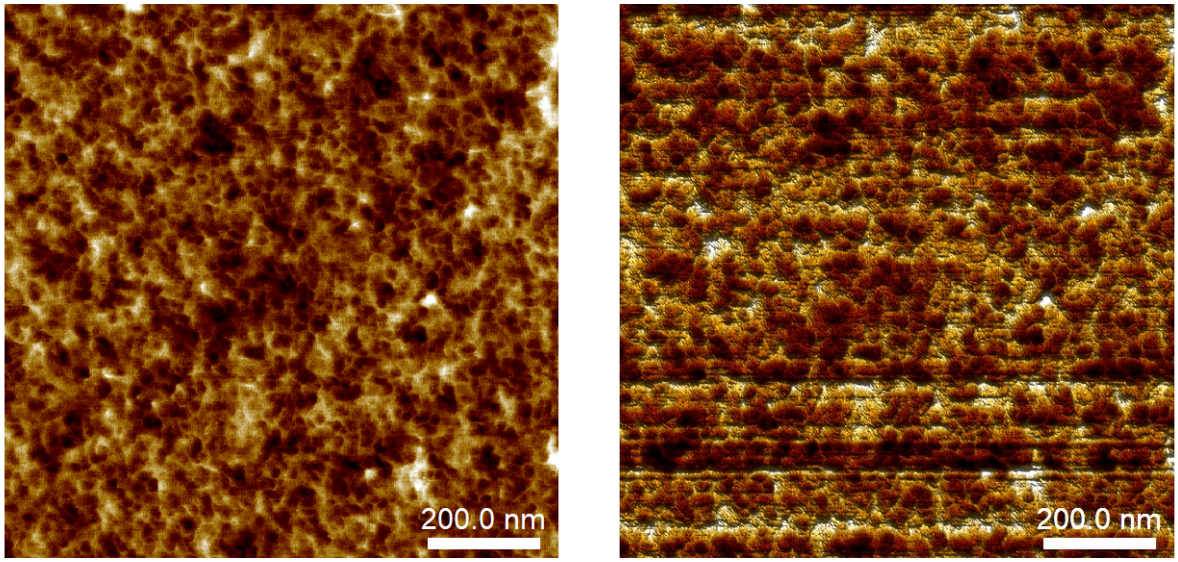

Figure 4.14. Molecular organisation of PDMS surface at 1 µm. The surface displays a heterogeneous and disordered matrix with considerable porosity. (a) AFM height image. Image was 1st order flattened. *Z* scale = 8.1 nm (b) 3D topographical representation of the same data, (without flattening) taken from the AFM height image.

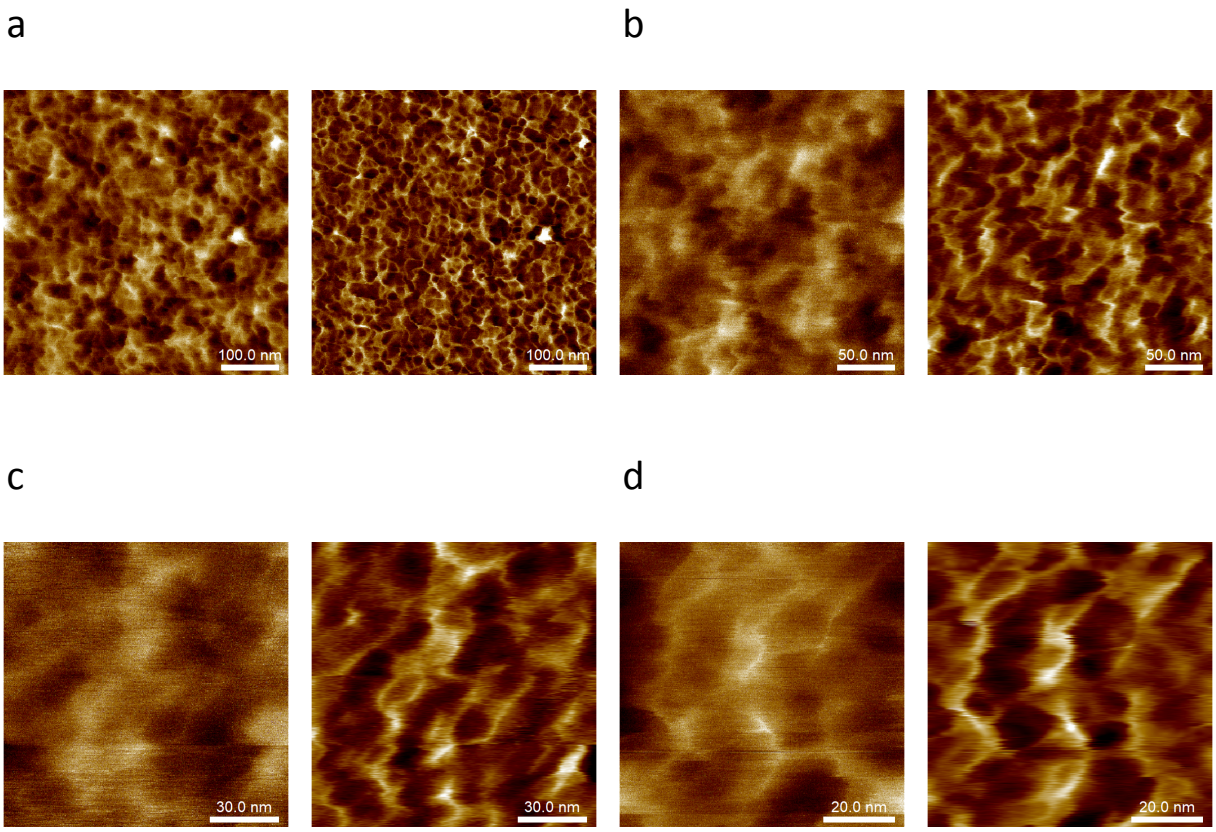

Figure 4.15. Molecular organisation of PDMS surface at nm length scales. AFM height images (left panel) and their corresponding phase images (right panel) of PDMS at (a) 500 nm (b) 250 nm (c) 125 nm and (d) 80 nm scan sizes. The surface is composed of thick bundles ~ 10 nm in width, with smaller interconnecting chains. Around half of the surface is porous at all length scales. *Z* scale = (a) 7.2 nm (b) 5.5 nm (c) 4.9 nm (d) 5.9 nm. Phase angle (dark to light) = (a) - 17.1° to - 6.4° (b) - 23.1° to - 12.7° (c) - 23.4° to - 11.8° (d) - 12.3° to - 2.6°.

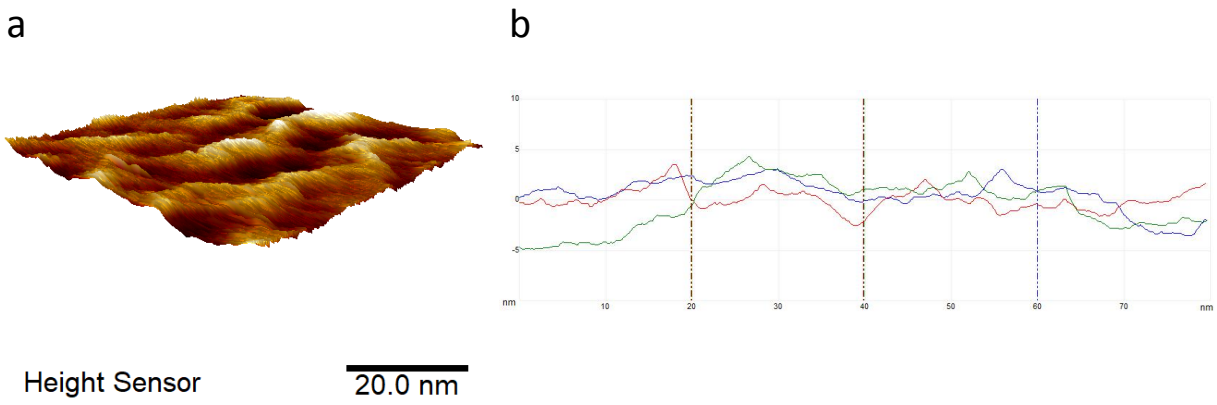

Figure 4.16. Topography of PDMS at 80 nm. (a) AFM 3D topographical height image of PDMS at 80 nm^2. (b) Three line profiles drawn horizontally at even spacing across image a. The vertical lines represent a cumulative width of 40 nm to depict probable contact geometry with a 40 nm radius indenter. Height distribution was calculated as 0.59 ± 1.57 nm.

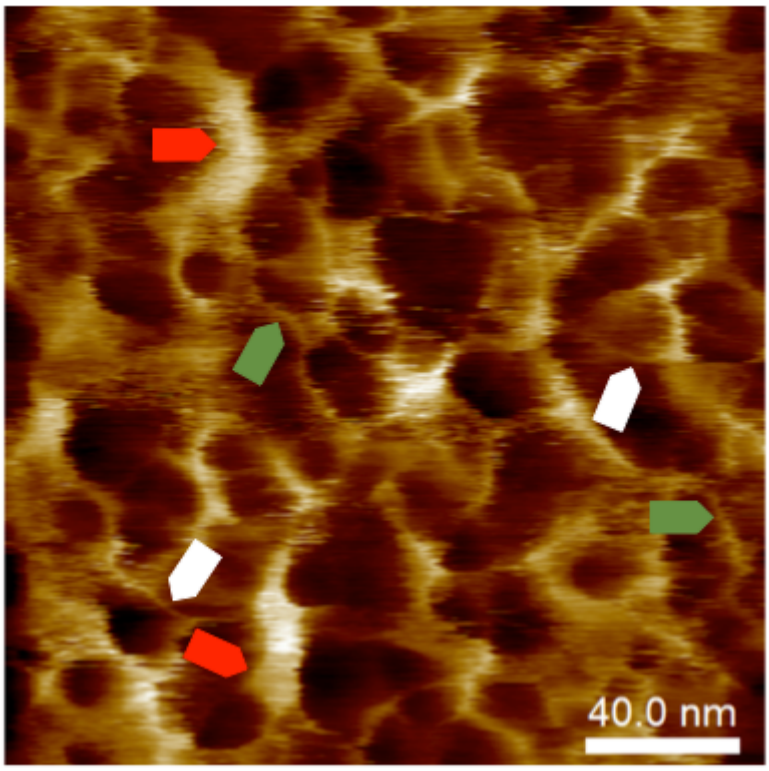

Figure 4.17. PDMS polymer chain and bundle width measurements. AFM phase image shows bundles of ~ 10 nm width (red arrows), and apparent chains of ~ 2 nm width (green arrows), and < 1 nm width (white arrows). Phase angle (dark to light) = - 4.9° to 9.5°.

4.2.7.1 Roughness measurements at different length scales

PDMS was cast from smooth, clean silicon wafers (with no lithographic patterning) and AFM images were collected and analysed for roughness (Chapter 3.12). Two samples were analysed from two independent experiments at 1 µm and 80 nm resolutions. The data were analysed within two software packages – the AFM default (NanoScope Analysis) and Gwyddion respectively. Ten line profiles were assessed for each sample, in each software package. Therefore, the reported mean data are the combined means from 20 line profiles per sample. For the 1 µm sample (using the AFM software) the mean roughness was 1.4 ± 0.57 nm (± 0.13 SE). Median roughness was 1.4 nm. Mean RMS roughness was 1.7 ± 0.73 nm (± 0.16 SE). Median RMS was 1.8 nm. Calculating the data within Gwyddion reported a mean roughness of 1.4 ± 0.61 nm (± 0.14 SE). Median roughness was 1.5 nm. Mean RMS roughness was 1.8 ± 0.78 nm (± 0.178 SE). For the 80 nm sample (using the AFM software) the mean roughness was 1.3 ± 0.47 nm (± 0.11 SE). Median roughness was 1.4 nm. Mean RMS roughness was 1.7 ± 0.54 nm (± 0.12 SE). Median RMS was 1.6 nm. Calculating within Gwyddion, the mean roughness was 1.6 ± 0.45 nm (± 0.10 SE). Median roughness was 1.6 nm. Mean RMS roughness was 1.9 ± 0.55 nm (± 0.12 SE). Median RMS was 1.9 nm. Both software platforms reported very similar data. These combined data were analysed and are detailed in (Table 4.6). The skewness, Rsk and the kurtosis, Rku are included, to infer information about the Gaussian distributions. Both values are dimensionless. Positive values, away from zero, show a distribution with tails to the right. Both mean data sets are skewed to the right. A kurtosis of 3 represents normal peakedness of the distribution. Values >3 suggest more peaks and <3 more valleys. Both mean data sets are slightly less than 3 and suggest more valleys, and thus porosity.

	1 µm			**80 nm**		
	Mean	**SD**	**SE**	**Mean**	**SD**	**SE**
Ra (nm)	1.4	0.58	0.092	1.5	0.47	0.074
Rq (nm)	1.8	0.74	0.12	1.8	0.55	0.088
Rsk	0.065			0.16		
Rku	2.9			2.6		

Table 4.6. PDMS combined roughness measurements. Mean roughness data calculated from AFM height images. Measurements were quantified in two software platforms and combined to report the roughness from a 1 µm and 80 nm image. The roughness remains similar at both length scales.

4.2.8 Surface properties compared to bulk

The molecular organisation of the surface was compared to the molecular organisation deeper within the 10:1 PDMS substrate at nm, µm and mm depths by moving the tip position along the exposed internal surface. Initially, a section was removed with a blade to provide a gently sloping interface (Fig. 4.18). A 1µm image of the surface and ~ 100 nm below the surface were obtained and the molecular morphology appeared to be similar (Fig. 4.19).

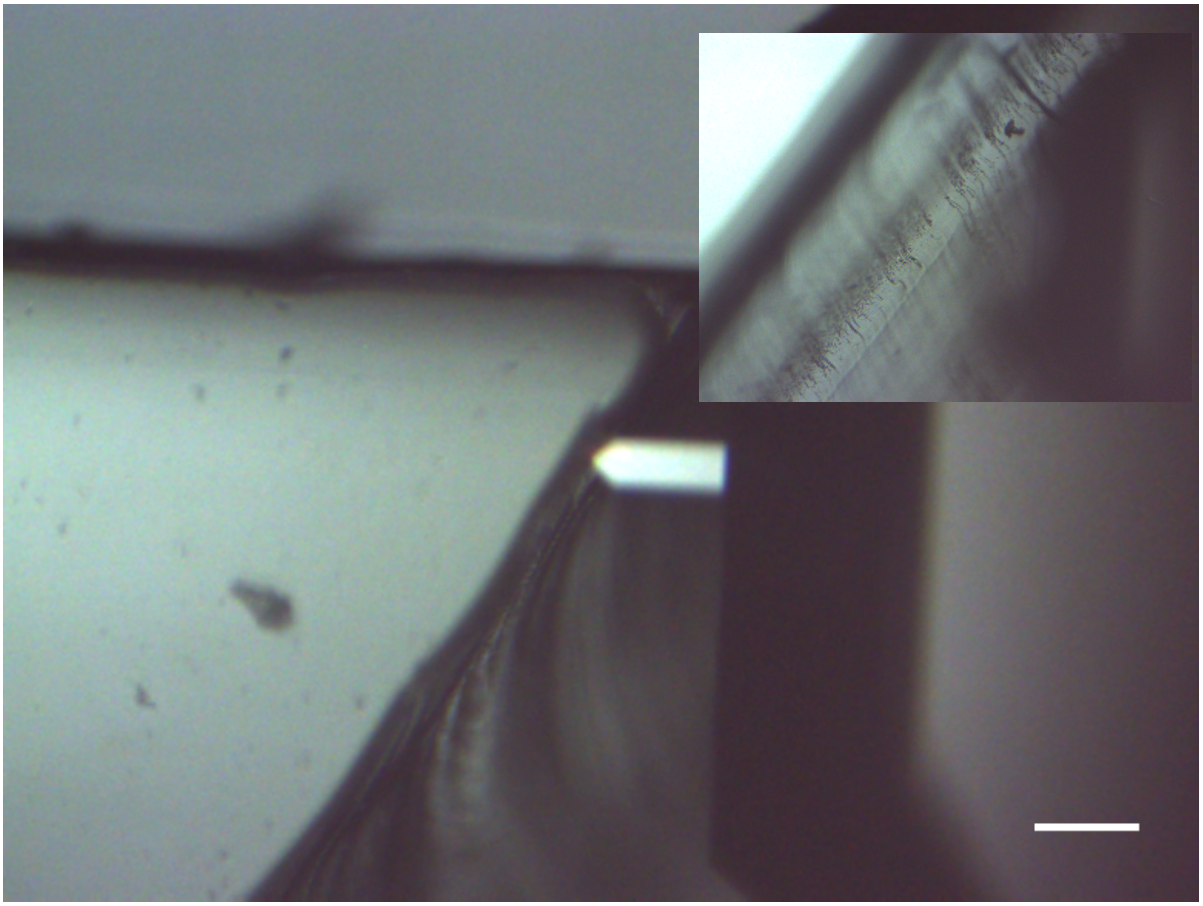

Figure 4.18. Sliced PDMS optical micrograph of surface and sub-surface morphology. A TESPA-V2 cantilever is positioned near a surface and sub-surface (inset) interface prior to AFM image capture of 10:1 PDMS. Scale bar is 100 nm.

a

b

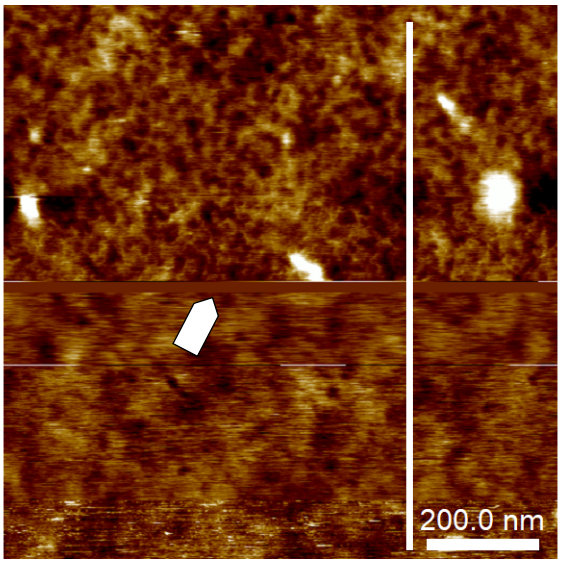

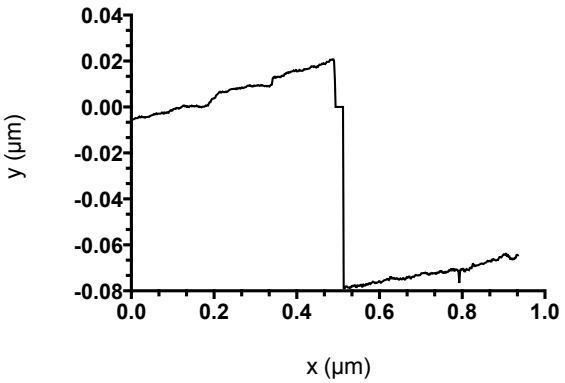

Figure 4.19. Sliced PDMS AFM image of surface and sub-surface molecular morphology. (a) An AFM phase image of the molecular structure at the surface and sub-surface. The thick line (arrowed) represents the interface and the AFM was not able to sufficiently capture image data, due to the steep angle. The white line represents a line profile fitted to the AFM height image of the same data. (b) The line profile data report a sub-surface depth ~ 100 nm. Image was 3rd order flattened. Phase angle (dark to light) = - 28.4° to 5.7°. Image size = 1 x 1 µm.

4.2.8.1 PDMS sub-surface molecular organisation

In order to alleviate any potential for blade cutting artefacts, a section of 10:1 PDMS was briefly immersed in liquid nitrogen, ~ 20 s and quickly cracked with a pestle. This left a clean edge with the interior of the substrate exposed (Fig. 4.20). The PDMS was attached to the microscope stage with the exposed interior facing upwards. There were numerous, seemingly ordered and slightly concentric rings evenly dispersed throughout the interior. Smooth, ring-free areas were scanned with the AFM at increasing distances from the leading (surface) edge to capture images of molecular structure down to mm distances from the surface (Fig. 4.21). The molecular architecture remained constant at all distances explored, and did not differ significantly from the surface architecture.

a b

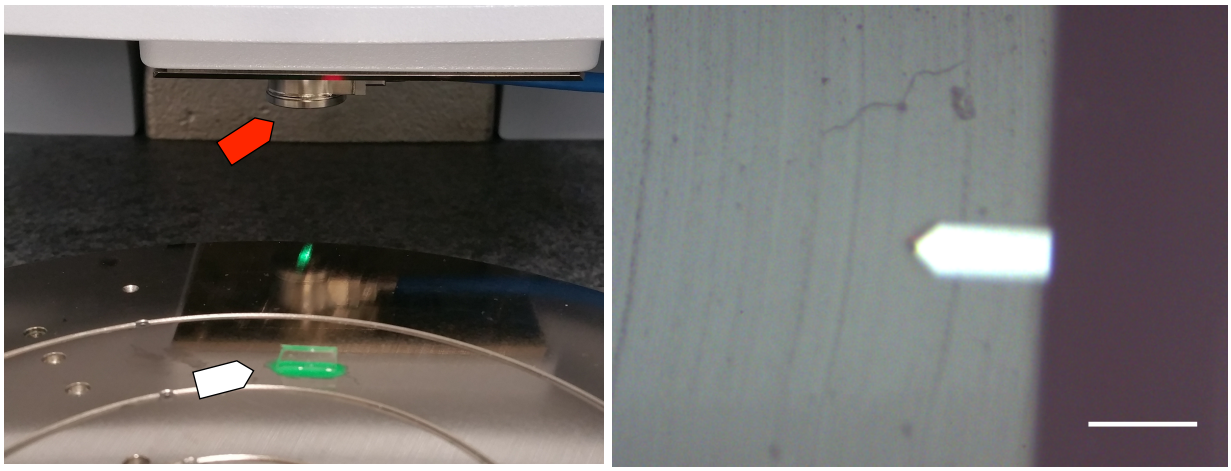

Figure 4.20. Exposed internal structure of PDMS prior to AFM analysis. PDMS has been briefly immersed in liquid nitrogen and cracked to expose a smooth internal surface. (a) The PDMS was secured to the microscope stage (white arrow) and the exposed internal surface was oriented upwards for AFM analysis. The light from the illuminator has created a green reflection from the mounting elastomer. The cantilever is mounted in the *Z* scanner connector (red arrow). (b) An optical micrograph shows a TESPA-V2 cantilever above the internal surface. Multiple concentric rings appear to be evenly distributed throughout. Scale bar = 100 nm.

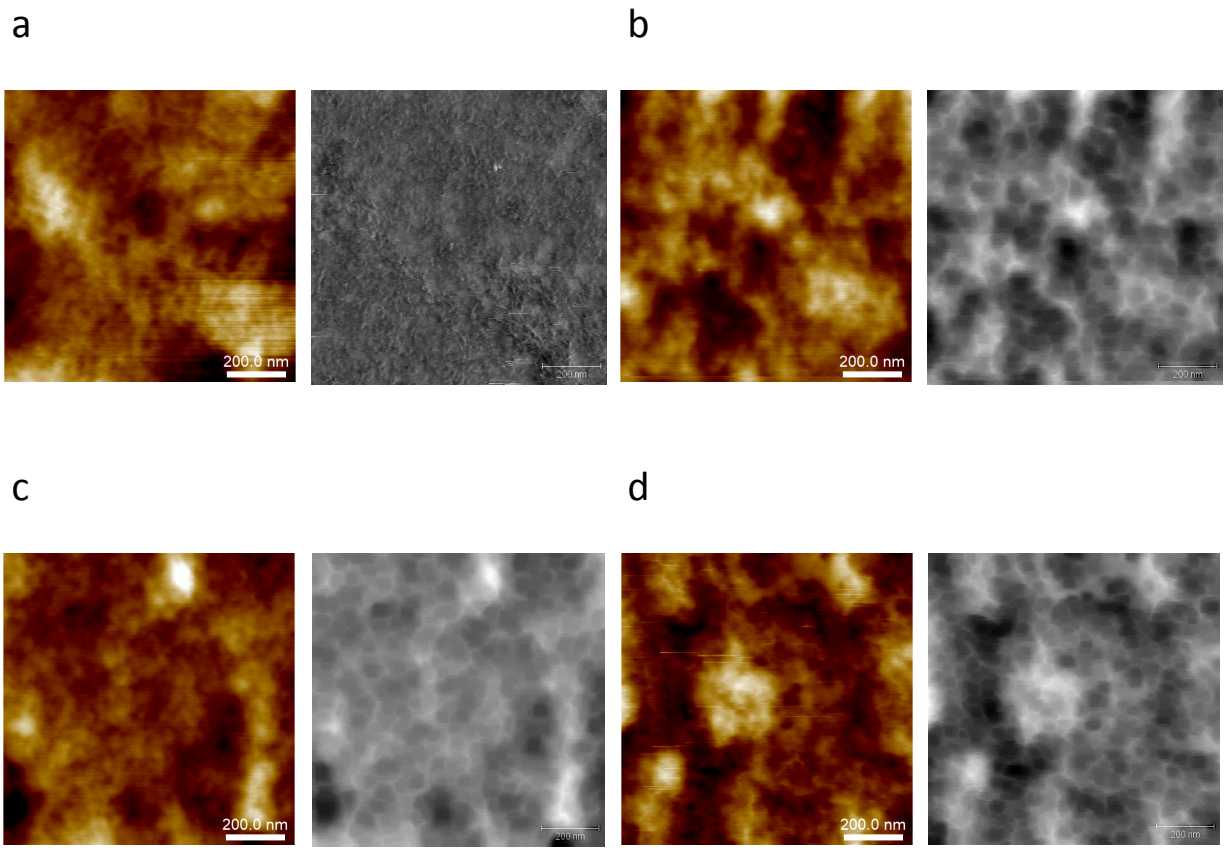

Figure 4.21. Internal molecular architecture of PDMS. (a) AFM height image (left panel) and corresponding phase image (right panel) at a few µm distance from the surface. (b, c, d) AFM height images (left panels) captured at increasing mm distances away from the surface. To reveal finer structural details the right panels of images b, c and d show the same height images that have been binary filtered to remove pixels from the edges of black objects with 8, 10 and 8 pixel size respectively. *Z* scale = (a) 61.8 nm (b) 20.5 nm (c) 32.6 nm (d) 57.7 nm. Phase angle (dark to light) = (a) 8.7° to 22.6° (b) - 21.4° to 31.4° (c) 26.4° to 34.0° (d) 29.7° to 41.7°. Image pixel density = 512 x 512. All images are 1 x 1 µm scan size.

4.2.8.2 PDMS sub-surface roughness

PDMS was prepared as described previously (section 4.2.8.1). Three samples were analysed from a single experiment at 1 µm resolutions. The data were analysed within Gwyddion. Ten line profiles were assessed for each sample; therefore, the reported mean data are the combined means from 30 line profiles. The mean roughness was 3.4 ± 2.2 nm (± 0.40 SE). Median roughness was 2.5 nm. Mean RMS roughness was 4.3 ± 2.7 nm (± 0.49 SE). Median RMS was 3.0 nm. These data appear tabulated (Table 4.7) for easier visualisation. The data are skewed to the right. Skewness = 0.21 and kurtosis = 3.

Mean (nm)	SD (nm)	SE (nm)	Median (nm)
3.4	2.2	0.40	2.5

Table 4.7. PDMS sub-surface roughness. The values were calculated by drawing 10 horizontal 1µm line profiles at spacing's ~ 75 nm apart over a 1 µm AFM image. *n* = 3 substrates and therefore averages calculated from 30 line profiles.

4.2.9 Contact area and deformation

To understand how the AFM probe may interact with the PDMS surface we can look at Hertzian contact theory between a sphere and linear elastic half-space. Taking 10:1 PDMS elastic modulus to be 1.3 MPa (reduced elastic modulus of 1.75 MPa), and using Eq. (14) the pressure applied to the assumed AFM tip-contact radius of 40 nm with an applied load of 1 nN = 718 kPa. This increases to 1.23 MPa at an applied load of 5 nN. The contact area may be smaller than the tip radius. Using Eq. (15), at a 1 nN applied load the contact area = 26 nm and 44 nm at a 5 nN load. This would lead to a pressure of 957 kPa at an applied load of 1 nN, and 1.15 MPa at a 5 nN load. According to Eq. (16) the deformation experienced by the substrate from a 1 nN loading force = 34 nm. This increases to 97 nm at a 5 nN load.

4.2.9.1 Indentation depth as a function of conical half-angle

We routinely found that setting the conical half-angle to 85° reported an elastic modulus ~ 1.3 MPa for PDMS. In this regard, we were using the PDMS as a calibrant (as it has a well defined modulus, both in the literature and from our experimental data) for the collection all of our elastic moduli. As the modulus has not been shown to change from the surface

until the bulk surface many microns below the surface, we explored a range of different indentation depths (up to 100 nm) and investigated what conical half-angle would be required to maintain the elastic modulus ~ 1.3 MPa. Following the work performed with spherical indenters (section 4.2.4.4) we tested the indentation depth of 10:1 PDMS as a function of conical half-angle, using the stiffer MLCT E cantilever. This has the same tip as the MLCT D (used throughout our modulus experiments) but it is mounted on a cantilever with a nominal spring constant of 0.1 N/m (actual 0.17 N/m in our experiments). A variety of loading forces (1, 5, 7 and 10 nN) were applied, and maximum indentation was 79 nm. The conical half-angle was modified within the Sneddon contact model at all depths explored, to keep the elastic modulus ~ 1.3 MPa. Three F-D curves were analysed at each loading force per sample, and two samples were used. The mean angles were calculated for various indentation depths in multiples of 20 nm, i.e. 0-20 nm, 21-40 nm etc. as the range of angles were found to be similar under this grouping. For 0 – 20 nm the mean angle = 84 ± 2.5°; for 21 – 40 nm = 74 ± 9.2°; for 41 – 60 nm = 69 ± 6.5°, and for 61 – 80 nm = 59 ± 4.5° (Fig. 4.22). We approximated these data to suggest a somewhat linear trend of conical half-angle changes at increasing indentation depths (Table 4.8). The conical half-angles show a decreasing change of ~ 5° for every 10 nm of indentation, up to 40 nm. From 40 – 80 nm the half-angle remains similar for every 20 nm indented. Indentations greater than 80 nm were not achieved and thus 81 – 100 nm have been further approximated. To minimise and simplify the range of half-angles used - for all elastic modulus analysis, the first angle of the 5 degree range only was chosen. Thus indentations up to 10 nm were fitted with an 85° half-angle. During fitting, where any ambiguity of the contact point of indentation was present, a range of contact points were explored and the conical angle adjusted to reflect the resultant change in indentation depth (Fig. 4.22 c, d).

a

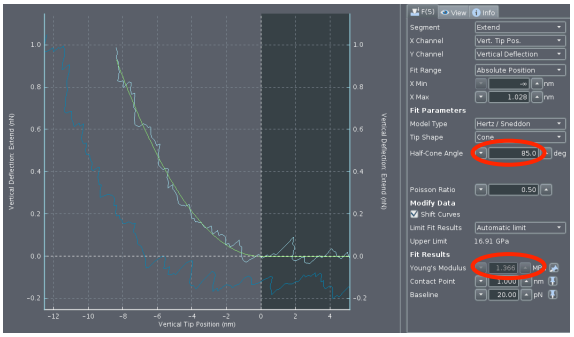

b

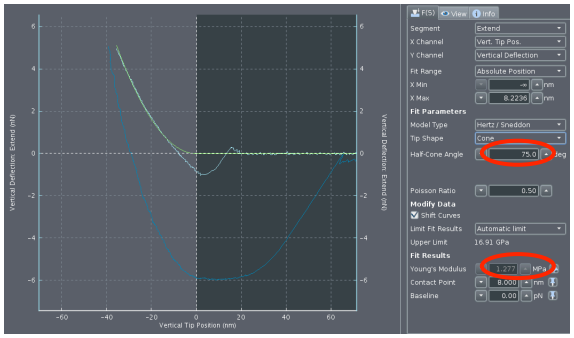

c

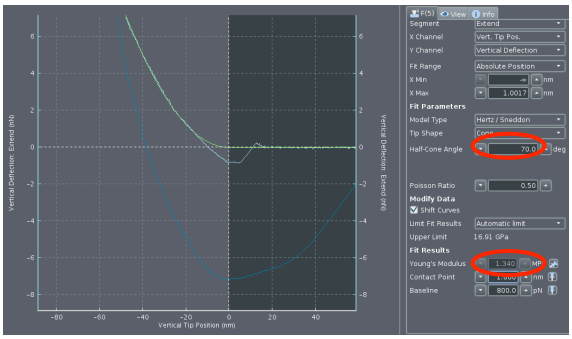

d

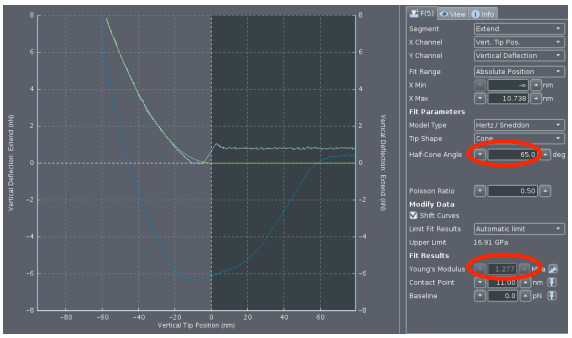

e

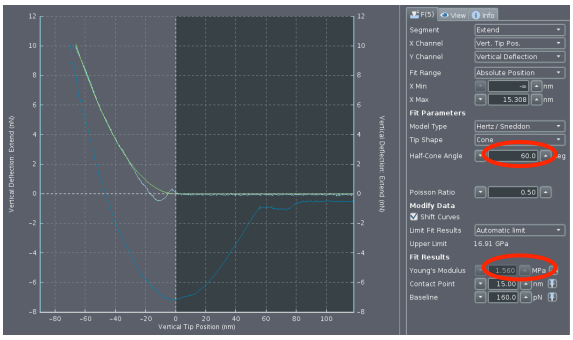

Figure 4.22. F-D curve conical angle fittings on PDMS. Loading forces of 1, 5, 7 and 10 nN were used to indent PDMS to progressively increasing depths and the conical half-angles were adjusted to maintain an elastic modulus ~ 1.3 MPa (circled in red in each image). Indentation depths were (a) 8 nm (b) 36 nm (c) 48 nm (d) 58 nm (e) 67 nm. To check for any ambiguity with actual indentation contact points the same F-D curves were routinely checked at different contact points; represented in (c, d) and the conical half-angle was adjusted to maintain a modulus ~ 1.3 MPa as a result of the concomitant change in indentation depth.

PDMS Indentation Depth (in nanometres)	Tip Half-Angle (in degrees)
0 – 10	85 – 90
11 – 20	80 – 85
21 – 30	75 – 80
31 – 40	70 – 75
41 – 50	65 – 70
51 – 60	65 – 70
61 – 70	60 – 65
71 – 80	60 – 65
81 – 90	55 – 60
91 – 100	55 – 60

Table 4.8. PDMS indentation depth as a function of conical half-angle. PDMS has a well-characterised elastic modulus, both from our experimental data and within the literature. The modulus is not expected to change from a 0 – 100 nm depth. A series of increasing loading forces were used to elicit greater indentation depths on PDMS. Conical half-angles were modified within the Sneddon contact model, to keep the elastic modulus ~ 1.3 MPa. A linear trend of increasing depth and decreasing half-angles were observed and approximated to 5 degree groupings. The first value in the half-angle column was used throughout this study, thus 10 nm indentations were fitted with an 85° half-angle.

4.3 Discussion

4.3.1 Lithographic patterning

The design and fabrication of the geometric patterns were intended to allow for the immobilisation of bacteria for AFM study (Chapter 6). There were occasional errors with the exposure of the patterned masks – leading to pillar heights of tens of nanometres instead of ~ 750 nm (data not shown), but the process was largely efficient and effective. PDMS was able to adopt and maintain the patterns faithfully, and at a depth ~ 750 nm. The *XY*-numbering system included with the multiple geometry design was suitably transferred to the PDMS and was routinely used to allow for finding and re-visiting specific locations on the substrate.

4.3.2 Elastic modulus characterisation with different systems

We sought to address the disparity of reported modulus data and calculate a definitive elastic modulus for 10:1 SYLGARD® PDMS by comparing the data from multiple instruments and methods. Nanoindentation can be problematic when trying to achieve shallow indentations on a soft substrate, as the loading forces are high and determining the actual point of surface contact is difficult. An insensitivity to the to the initial contact can lead to underestimation of contact depth (Cohen and Kalfon-cohen, 2013). White and colleagues found that PDMS needed to be indented by 2000 nm before 10 µN of force was measured (White *et al.*, 2005). The unloading curve is used to derive elastic moduli in nanoindentation, in an attempt to avoid plastic deformations that may be present during loading (Cohen and Kalfon-cohen, 2013). However, the unloading curve of dedicated nanoindentation and AFM are subject to adhesion, which is known to lead to overestimation of elastic moduli. Moreover, PDMS has shown no signs of plastic deformation at up to 50 µm of indentation (Deuschle *et al.*, 2008; Paoli and Volinsky, 2015).

Our tensile testing measurements were consistent, with a mean elastic modulus and low standard deviation of 1.3 ± 0.23 MPa. Using AFM, with an 85° cone half-angle routinely reported moduli around 1.3 MPa – on multiple substrates over a period of ~ 3 years. Such a shallow angle – which almost approximates as a flat punch, could be deemed too arbitrary. Justifications for this angle will be explored in (Chapter 5). However, when using the commercially prepared B500_CONTR cantilever, with a rigid sphere of well-defined geometry, the reported modulus was in agreement. Here, both the Hertz and Sneddon contact models had been utilised, with two distinct and different geometries, and the data correlated. Some confusion exists with our polystyrene-functionalised cantilevers. Minimum and maximum reported moduli were 0.05 and 0.55 MPa – an order of magnitude difference, and at the maximum value, still ~ 3 times lower than we expected. Using the data from (Table 4.3) there does not appear to be a strong correlation between sphere radii or loading forces. As the loading force is increased from 10 to 25 nN using the Arrow™ CONT cantilever, the apparent elastic modulus and stiffness of PDMS are increased. Conversely, increasing the loading forces using a TESPA-V2 cantilever initially reported an increase in elastic modulus and stiffness between 50 – 300 nN, but a sharp decrease in both measurements at 500 and 800 nN forces. When we glued the spheres to the tips some were

seen to move backwards during some AFM scans. Further, when attempting to perform cantilever calibrations at the start of each experiment the approach portion of the F-D curve had a large curved region prior to the steep gradient that would have been expected from the point of initial contact. We ascribe this to an elastic nature of the adhesive used to secure the spheres onto the tips – where we believe that there was some flexion during indentation, both at the calibration and sample analysis stages. Although the elastic moduli were close to the expected values with the 15 and 28 kPa PDMS, this was likely due to the adhesive being less perturbed against such soft substrates.

4.3.3 Tensile vs. compressive testing

It has been widely reported in the literature that there is a disparity between the elastic modulus of polymers obtained between tensile and compressive testing – with compressive (i.e. AFM) methods generally reporting greater values (Hardiman, Vaughan and McCarthy, 2016). Sirghi and Rossi performed tensile testing of SYLGARD® 184 in a 10:1 mix that was cured at 60° C for 4 h. They obtained an elastic modulus of 1.63 ± 0.26 MPa. They subsequently tested the PDMS with an AFM and obtained a similar value of 1.91 ± 0.33 MPa (Sirghi and Rossi, 2006). Their probes were sharp, with a radius of curvature ~ 10 nm and a conical angle of 22°. They make no mention of the spring constant, but searching the manufacturer literature suggests that they were many orders of magnitude stiffer than ours, with nominal values of 5.5 – 11.5 N/m. Investigators explored the tensile vs. compressive problem and performed both tests on a soft silicone. They studied multiple specimens, with differing sizes, under each testing regime. They showed, conversely, that the silicone was softer under compression than it was during tension (Destrade, Murphy and Rashid, 2009).

4.3.4 Modifications to the curve fitting

The data from these soft 15 and 28 kPa PDMS samples were derived from fitting at 10 nm indentations of the approach portion of the F-D curve. However, when fitting to the full curves, which were ~ 400 nm and 250 nm respectively, the moduli became ~ 23 kPa for both samples (data not shown). The contact model fitting faithfully followed the full curve geometry, but did not always, at 10 nm. This suggests that (i) a spherical indenter contact model may be appropriate for deep indentations on a very soft substrate, and (ii) either not appropriate at very small indentations on a very soft substrate, or (iii) it may be difficult to

accurately determine the initial surface contact at high loading forces on a very soft substrate. This final point would seem to agree with the dedicated nanoindentation data, where very high loading forces were applied to a soft substrate and the reported moduli were inconsistent, and the initial surface contact was difficult to determine. Equally, the modulus values were varied for the 10:1 PDMS tested with a TESPA-V2. At loading forces between 50 – 150 nN the moduli were similar, ~ 500 kPa, but they reduced at greater indentation depths. Here, all of these data faithfully followed the F-D curves at ~ 60 nm fitting. Below and above 60 nm the fitting deviated considerably. Fitting the 500 and 800 nN samples at 60 nm adjusted their reported moduli to ~ 500 kPa to match the 50 – 150 nN data. As the conical data consistently reported a similar elastic modulus and as the F-D curve fitting was superior to all other indenter geometries we believe this regime and these data to be accurate.

4.3.5 Asperities and contact area

As briefly mentioned in the materials and methods (Chapter 3.9.5), it was consistently found that the sphere radii – using the Hertz model, had to be set as considerably larger than the actual radius. An MLCT D tip radius is ~ 40 nm, but the value required to obtain a modulus of ~ 1.3 MPa for PDMS was ~ 220 nm – some five times larger. When deriving their contact model in 1971 Johnson and co-workers noted that in their previous work, using rubber or glass spheres at low loads, the observed contact area was considerably larger than those predicted by Hertz (Johnson, Kendall and Roberts, 1971). They suggest that attractive surface forces were operating between the solids at low loads, resulting in these observations. At high loads these attractive forces were of little significance. As the moduli presented in this study are derived from the use of low loads (1 - 5 nN), this could be a causative factor in our observations. However, as the B500_CONTR cantilever did report the expected modulus using the known radius within the Hertz contact model, this suggests that it is the conospherical nature of the MLCT tip that underlies this problem, and further supports our observations that even at shallow indentations, the conical model more accurately defined the tip geometry. The Hertzian calculations performed in (section 4.3) suggested that a 5 nN loading force could cause a 97 nm deformation on PDMS. However, the equations assume that the material is homogenous, and they do not take account of the spring constant and bending of a flexible cantilever. Loading forces of 10 nN only allowed

indentations up to 79 nm in our experiments. The model also assumes a flat surface. The small, but numerous asperities on the surface of PDMS may lead to a contact area lower than expected, as discussed in (section 4.1.6.1).

4.3.6 Adhesion effects

Nanoindentation modulus data are derived from the unloading portion of a F-D curve. In this regime the adhesive forces of the PDMS will be apparent, and this can lead to overestimation of the sample modulus (Charitidis, 2011). The same is true of the unloading (retract) portion of an AFM F-D curve. For this reason we specifically chose to disregard any F-D curves with visible adhesion, where possible, and by fitting to the loading (approach) portion of the F-D curves.

4.3.7 Depth dependence and molecular structure of PDMS

Qian and co-workers examined the effects of depth dependence on SYLGARD® 184 mixed in a 10:1 ratio, on the TI 950 nanoindenter, with a range of different probes. They found large values of elastic modulus at indentation depths less than 800 nm, which they attribute to incomplete unloading of the indenter – leading to large errors with the Oliver and Pharr model. At depths greater than 800 nm the values became almost constant ~ 2.5 MPa (Qian *et al.*, 2018). Further limitations of obtaining quantitative modulus with nanoindentation are the uncertainties in determining the initial tip-sample contact (Charitidis, 2011). Disregarding any problems with defining the initial surface contact within nanoindentation, if the PDMS were actually stiffer at the surface than within the bulk material, this should suggest that the polymer crosslinking was less dense in the bulk. We obtained molecular resolution of the surface and the bulk PDMS at length scales on the order of 100 nm down to a few millimetres in depth. The molecular structure did not seem to alter at any length scale observed and the roughness within the bulk was slightly higher than at the surface. The kurtosis measurements (3 compared to <3) suggest that the bulk is slightly less porous. Although it is difficult to measure the diameter and number of crosslinks at the 1 µm length scales we obtained, the less porous nature suggests more crosslinking. In this regard we would expect the elastic modulus to increase within the bulk.

4.3.8 Depth dependence with a conical indenter

By using a moderately stiff cantilever, with an experimentally calculated spring constant of 0.17 N/m, we were able to increase the loading forces to obtain a maximum indentation of 79 nm. Interestingly, this spring constant is exactly the same as the spring constant we previously calculated for PDMS, thus the cantilever and sample are perfectly matched. This is widely considered to be an ideal scenario for AFM studies, as the cantilever should deflect proportionally to the indentation of the sample under investigation (Gavara, 2017). We found a somewhat linear dependence of indentation depth and apparent conical half-angle where the initial half-angle was 85° (i.e. 170° total angle) at 10 nm indentations. Being nearly 180° this suggests an almost flat punch contact area between the probe and the sample. As the probe is indented further, the contact angle becomes steeper as more material begins to make contact with the sides of the probe. This seems logical, of course. Moreover, using the Hertzian contact model Eqs. (14 – 16) the actual contact area between tip and sample may be less than the actual tip radii – further supporting the notion that 10 nm indentations are essentially achieved with barely any material contacting the sides of the indenter. Materials either sink-in or pile-up when indented. A soft metal, such as aluminium has been shown to pile-up during indentation (Van Vliet, Prchlik and Smith, 2004). Conversely, 10:1 PDMS was extensively studied using a combination of SEM and optical microscopy (Deuschle *et al.*, 2008). These authors used a cube corner tip to indent PDMS at µm length scales. They showed that even at 15 µm, during loading a clear sink-in effect was observed, and that the shape of the impression, rather than being pyramidal, was more conical. They used AFM to collect topographic images, which further supported this finding. All of their indentations recovered fully, confirming true rubber-like properties of PDMS (Deuschle *et al.*, 2008).

4.3.9 Conclusions to this study

We designed and produced photolithographically patterned silicon wafers, which were successfully used to imprint PDMS - receiving faithful representations of the designed geometry. Using a variety of tensile and compressive techniques we attempted to obtain a definitive value of elastic modulus for PDMS, which we estimate to be ~ 1.3 MPa for SYLGARD® 184 mixed in a 10:1 mass ratio and cured at 70° C for 2 h. We have highlighted why the elastic modulus is generally overestimated with dedicated nanoindentation

instruments, and why AFM is more suited to obtain elastic moduli of soft materials at very shallow indentations. One of the most prevalent disparities with the modulus reporting within nanoindentation instruments is the apparent stiffening at the surface compared to the bulk material.

To the best of our knowledge, this study is the first to obtain molecular resolution of PDMS – both at the surface and within the bulk material. Our data suggest that the molecular structure does not appreciably change between the surface and the bulk. The PDMS may, in fact, be slightly denser within the bulk material – between the µm to mm length scales studied here, and thus we would expect it to be slightly stiffer at deeper indentations, and softer at the surface, in contrast to the many published reports. Further, we sought to characterise the roughness of PDMS. The wide-ranging values reported in the literature were not at the molecular resolution that we were able to obtain measurements. Our 80 nm/512 x 512 pixel images = 0.16 nm/pixel. By exploring a range of indenter geometries we sought to better understand how these influence the experimentally obtained mechanical properties of PDMS. We believe that we have addressed the discrepancies between the reported literature values for PDMS and have shown that the AFM – rather than the dedicated nanoindenter is better suited to investigate the mechanical properties of soft materials at nm length scales.

Our AFM contact cantilever tip appears to behave as a conospherical indenter, with an almost flat punch geometry better describing shallow indentations on a soft material, and becoming more conical at greater depths. The conical geometry within the Hertzian model consistently showed more faithful F-D curve fitting than compared to the spherical geometry, and consequently, large differences with the calculated moduli. The differences between the reported elastic modulus may be true for other, similar contact cantilever tips that share a similar radius. This highlights a need for the AFM community to consider the probe geometry in more detail if quantitative mechanical measurements are to be trusted. Ultimately, we used the conical half-angle as an adjustable parameter and fixed it at a range of indentation depths (from 0 – 100 nm) to maintain the elastic modulus of PDMS at ~ 1.3 MPa, which should hold true, based on our mechanical testing and molecular scale imaging. To this end, the PDMS was used as a calibrant against the bacterial cell wall, which we

propose will behave in a similar manner to the PDMS when indented, and is within the same order of magnitude of elastic modulus (Chapter 6.3.6).

4.3.10 Limitations to this study

We disregarded the dedicated nanoindentation data, for many reasons, stated throughout, and we chose to model the AFM elastic modulus data with those obtained by tensile testing. Although some of our AFM data reported elastic moduli ~ 1.5 MPa we chose to match the lower modulus obtained from tensile testing in the formulation of our conical half-angle model. This could lead to our misreporting of the PDMS modulus. However, these disparities would still be within the same order of magnitude, and within ~ 1 MPa.

We attempted to use only F-D curves with little, to no visible adhesion, as the Hertzian contact mechanics models do not factor the influence of adhesive forces. There were instances where adhesion was present throughout – particularly when indenting at higher loading forces. This could lead to an overestimation of our results.

It has been shown that the elastic modulus of PDMS changes markedly following different curing times or temperatures. Our data may only be relevant for PDMS mixed and cured exactly as we did. Other investigators may need to fully characterise their samples accordingly.

Although it has been shown that there is little rate dependence on the reported modulus of PDMS using AFM, our approach and retract F-D curves were quite fast – at 22.5 µm/s, and with a motion time of 40 ms (with an actual ~ 2.5 ms contact) to gather a F-D curve. Although this is not considered fast for the QI™ method, researchers that do not have access to this technique may need to gather their data at slower speeds. This alone may lead to different values. Equally, faster indenting speeds have shown to overestimate the elastic modulus.

During the formulation of our modified conical half-angle model we found a range of ~ 5 degrees (i.e. 85 – 90°) were required to accurately constrain the elastic moduli at a certain indentation depth. We chose to simplify the range of angles and use only 85° in this example. As we intended to use this model to gather elastic moduli from a sample of unknown modulus (Chapter 6) we needed to limit the potential arbitrary use of the half-angle, and to limit any bias.

Chapter 5

Enhanced characterisation of AFM probe geometry

5.1 Introduction

Following the work in Chapter 4, we sought to improve the characterisation of the AFM tip at small nanometre length scales, to determine if the assumed 85° conical half-angle at 10 nm indentations holds a realistic approximation of the geometry at the tip edge.

5.1.1 High-magnification transmission electron microscopy

As previously discussed, the AFM community are typically less concerned with the enhanced characterisation of tip geometry, than their dedicated nanoindentation counterparts. However, some work has sought to characterise the wear of AFM tips following repeated contact on hard surfaces. Using a combination of TEM and blind reconstruction of the tip geometry, a range of AFM tips were seen to degrade (Liu *et al.*, 2010). The authors gathered a series of TEM micrographs before scanning and following 20 scans, and 100 scans. When overlaying these images significant blunting was seen. The micrograph resolution was reasonable and tip radii could easily be calculated. Angle characterisation could have been achieved from these images but at a length scale on the order of 50 – 100 nm.

Molecular dynamics simulation and AFM were also used to study the frictional nature of an AFM tip contacting a hard surface (Dong *et al.*, 2013). The tip was scanned along steep graphite edges under ambient and vacuum conditions and TEM micrographs were obtained. The authors did not perform blind reconstruction or obtain frequent micrographs but rather, obtained TEM images of worn AFM tips at the end of their experiments, where they observed a flattening of the tip apex that agreed with their atomistic simulations. Their TEM micrographs were captured at a high resolution with scale bars at 40 nm. Angle and radii measurements could be easily achievable in some of their images.

Vahdat and colleagues obtained sub-Ångstrom pixel resolution of silicon tips coated with a 10 nm layer of silicon nitride, or a 20 nm layer of diamond-like carbon, before and during up to 45 repeated scans (Vahdat *et al.*, 2013). They found that the diamond-like coating appeared to be removed in an atom-by-atom process with a concomitant decrease in the

tip roughness. Conversely, the silicon nitride showed signs of plastic deformation, with flattening of the tip apex and an increase in tip surface roughness. They compared these data to images they obtained via blind reconstruction to estimate the effective tip radius (Vahdat *et al.*, 2013).

5.1.2 Blind tip reconstruction

Most of the authors in the previous section also used blind tip reconstruction as a secondary means of estimating the tip geometry. Here, a probe is scanned over a series of features with a smaller radius than the probe. The AFM topographic image does not then directly portray the actual sample features and thus contains information of the tip shape. Image processing can reconstruct an image of the tip and be used to approximate the radius and geometry. A major limitation of the technique lies in the fact that the accuracy of the tip radius depends on the amount of noise in the image, and it only provides information of the tip geometry a few nanometres from the apex (Vahdat *et al.*, 2013). Whilst this may have allowed our characterisation around 10 nm from the tip apex, it would not have been sufficient for angle characterisation at greater distances from the apex. The tip wearing under high loads was exploited as a means of directed tip shaping (Vorselen *et al.*, 2016). Here, the authors used a 25 nN loading force to deliberately blunt the apex of a silicon nitride tip followed by imaging at 5 nN for estimation of the tip shape. They found, through blind reconstruction, that the tip apex increased in size, whilst still maintaining the rounded shape observed prior to blunting. Similarly to blind tip reconstruction, tip shape deconvolution is a method that extracts topographical data from an image and applies an algorithm to generate a tip profile. The captured image is then filtered based on this profile to estimate the true morphology (Abdelhady *et al.*, 2005).

5.1.3 High-magnification scanning electron microscopy

Commercial vendors of AFM probes typically provide a SEM micrograph of the cantilever and/or tip to inform the potential purchaser about the features of the chip and some idea of tip geometry. The cantilevers used throughout this study – the MLCT from Bruker Corporation are no exception (Fig. 5.1). The resolution of these images are usually sufficient, but would not allow for detailed radii or angle measurements near the tip apex. There is little in the way of high-magnification of AFM tips using SEM in the literature. Much like the

TEM work, many of the published reports using SEM relate to the wear and damage to the tip following repeated scans on a hard surface (Park *et al.*, 2014; Xue *et al.*, 2014). Whilst the resolution of SEM is considered to be less than is achievable with TEM, it is still easily capable of providing a high-magnification micrograph of the tip apex. Prior to SEM analysis, most samples typically require coating with a layer of metal. This creates a conductive layer that inhibits charging – where electrons may accumulate on the surface of non-conductive materials. It also reduces thermal damage and improves the secondary electron signal, leading to improved topographical resolution. The coatings are readily applied by sputtering onto the surface, or by thermal evaporation. Both techniques were utilised during this study, with no apparent differences observed between them. A major limitation of coating a sample is that the surface topography can be altered. Coatings are routinely <10 nm (Pobelov *et al.*, 2013; Denisin and Pruitt, 2016). When looking at a large sample, such as biological tissue for example, this small layer may be orders of magnitude smaller than the features of interest, but for the purposes of this study – where the resolution at 10 nm is important, any coating could be problematic.

a b

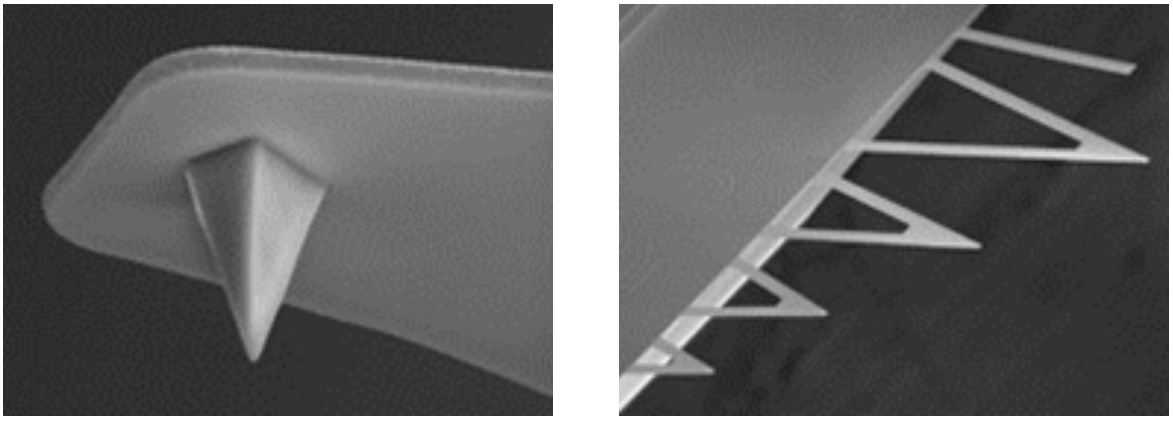

Figure 5.1. Bruker MLCT tip and cantilever. SEM micrographs of (a) an MLCT tip, and (b) five of the six cantilevers supplied on each chip. Cantilever D used throughout this study is in the middle of this array. Image reproduced from Bruker Nano Inc. (2018).

5.1.4 Direct AFM imaging of the tip apex

Using an AFM to directly scan and image another AFM tip may provide an indication of the true tip geometry – particularly if scanned by a tip with a smaller radius. Additionally, there would be no requirement for a metal coating. There should be less potential for tip damage, which may be evident on repeated scans of a hard, steep substrate as used for blind tip reconstruction, or from electron damage within SEM or TEM. Crucially, blind tip reconstruction requires the use of algorithms, whose input parameters are often not obvious or intuitive to the user, but ultimately have a large impact on the reconstruction (Flater *et al.*, 2014).

5.1.5 Power law relation to different geometries

Under Hertzian contact theory, the slope of unloading curves on nanoindentation plots can be described by a power law function where the indenter geometries are well approximated by the exponents; $n = 1$ for a flat punch, $n = 1.5$ (or $\frac{3}{2}$) for a paraboloid of revolution, or $n = 2$ for a cone (Fig. 5.2) (Oliver and Pharr, 2004). TEM was employed to obtain micrographs of blunted AFM tips during high loading rate scans, at ~ 20 nm resolution. The profiles of these tips were extracted from the TEM micrographs and the apex – up to 6 nm were fit using a power-law function (Grierson *et al.*, 2013). Before scanning the tip was described as a paraboloid with a power law ~ 2. Following up to 100 repeated scans the shape of the tip apex changed, and could be described by power-law functions of higher indices, between 3 – 6. The coordinates of AFM F-D curves can be displayed on a logarithmic scale and the gradients used to construct a frequency histogram. From this, the power law exponents can be easily quantified (Bonilla *et al.*, 2015). Previous work in our laboratory extracted F-D curve data of cell wall and whole cell SA into log-log plots of the force vs. indentation. There were two straight lines of non-zero gradients, with the exponents 2 and 4 occurring at an intercept ~ 25 nm of indentation (Bailey *et al.*, 2014). These two distinct regimes were taken to be the influence of the cell wall, with the exponent = 2 and of the whole cell, with the exponent = 4. The authors rejected the Hertz contact model as they could not apply it to the whole curve. However, following deviations from the expected exponent of 2 for an AFM tip, this does not necessarily mean that the Hertzian contact model is not appropriate, as neither the contact area nor the absolute deformation is known (Bonilla *et al.*, 2015). This current study chose to utilise the Hertz model as we fitted

our curve data at only 10 nm indentations, where the contact model fitting more accurately followed the F-D curve and the conical power law (Chapter's 4 and 6) and the power law of our F-D curves was between 1 - 2.

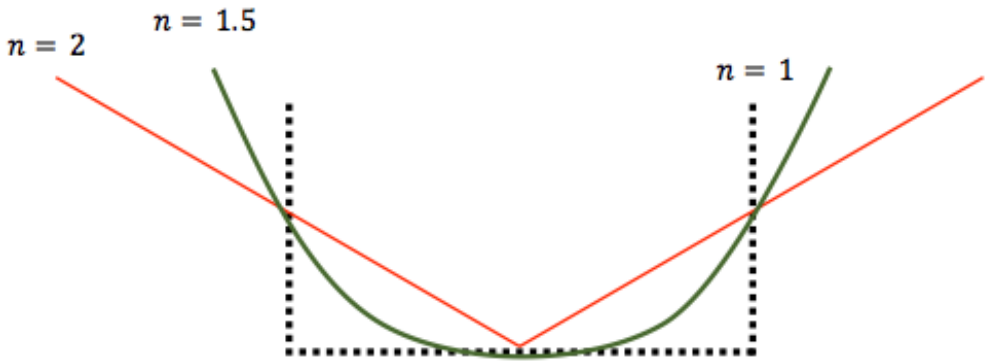

Figure 5.2. Schematic of Hertzian contact power law exponents. The power law relation for different geometries can be described with indices of $n = 1$ for a flat punch, $n = 1.5$ for a paraboloid of revolution and $n = 2$ for a cone.

5.1.6 Aims of this chapter

1. Obtain high-magnification SEM of the AFM cantilever tip apex.
2. Characterise the conical angles at a range of tip heights.
3. Perform AFM scanning of AFM tips and calculate their geometric properties.

5.2 Results

5.2.1 SEM reveals changes in geometry towards the tip apex

The full tip height of the MLCT D cantilever was found to be ~ 7 µm (Fig. 5.3a). Taking the geometric specifications from the manufacturer (Fig. 5.3a inset) the side angle was approximated as 16.3° which agreed with the manufacturer value of 17.5 ± 2.5 °. The angle was found to change very little when increasing the magnification to show ~ 4.4 µm (Fig. 5.3b) and ~ 1.4 µm (Fig. 5.3c). The full angles were calculated as 35.6° and 34.4° respectively; Thus, half-angle measurements of 17.8° and 17.2° respectively. However, when increasing the magnification to show the top 250 nm of the tip the angle became much shallower and the tip apex was broader and flatter, with a spherical end cap (Fig. 5.4a). The white line, showing an angle of 50° (although it extends beyond the tip apex) was applied using the SEM software, following image capture. Signs of charging were evident and the image was edited with a Sobel operator to reveal the true geometry (Chapter 3.14.3) (Fig. 5.4b). The angle did not change following this edit, although the radius became slightly reduced (data not shown). Samples were uncoated. *n* = 2 samples from 2 independent experiments.

a

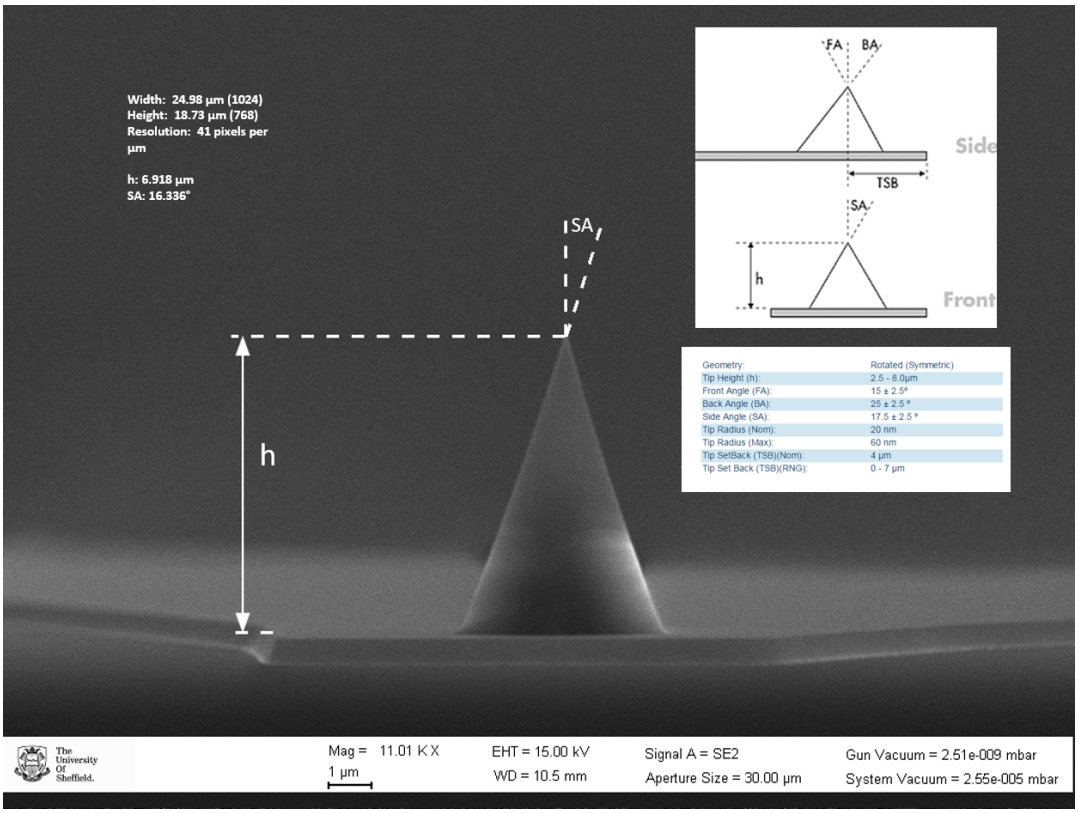

b

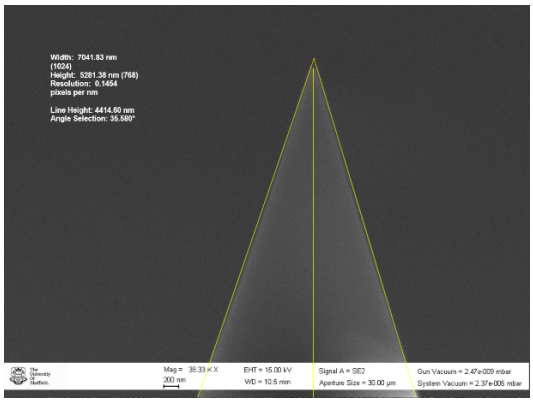

c

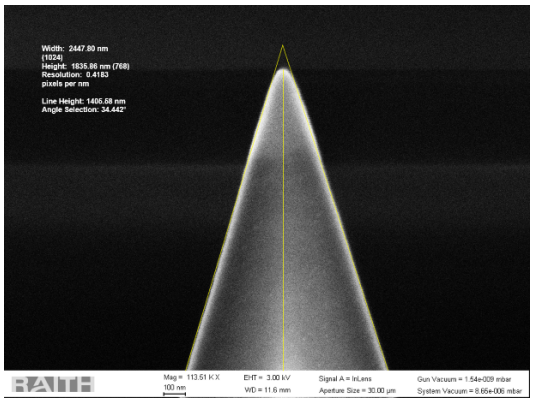

Figure 5.3. MLCT D tip at increasing magnifications. SEM micrographs of (a) The full tip height and (inset) the manufacturer specifications of geometry. The side angle measurement is 16.3°. (b) Higher magnification tip height of 4.4 µm, with a half-angle measurement of 17.8°, and (c) Higher magnification tip height of 1.4 µm, with a half-angle measurement of 17.2°.

a b

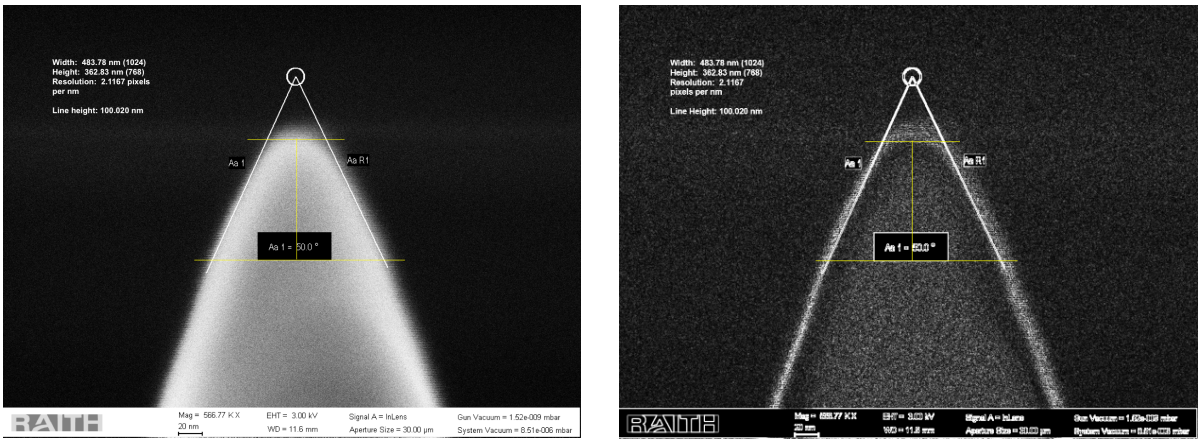

Figure 5.4. Tip geometry changes towards the tip apex. SEM micrograph of the top 250 nm of an MLCT D cantilever tip. The yellow lines represent the top 100 nm from the tip apex. The white lines show a 50° angle calculated by the SEM software (a) The tip shows signs of charging. (b) Edited image reveals the actual geometry.

The edited image above was rotated 180° to enable easier visualisation of its capacity as a vertical indenter and the approximated half-angle values from (Table 4.8) at 10, 50 and 100 nm were added (Fig. 5.5). The half-angles of 85, 65 and 55° respectively were fitted exactly to the tip apex to represent the actual contact geometry that may be evident when indenting the 10:1 PDMS substrate.

5.2.1.1 High-magnification SEM at the tip apex

High-magnification SEM captured the top 89 nm of the AFM tip. Following the half-angle approximations from (Table 4.8) an angle of 170° was fitted at 10 nm from the tip apex (Fig. 5.6a) and an angle of 130° was fitted at 50 nm from the tip apex (Fig. 5.6b). The diameter was measured as ~ 47 nm (white lines and circle) using the SEM software following image capture. After image editing and identification of the charging region the diameter was re-measured to give a value ~ 40 nm (Fig. 5.7).

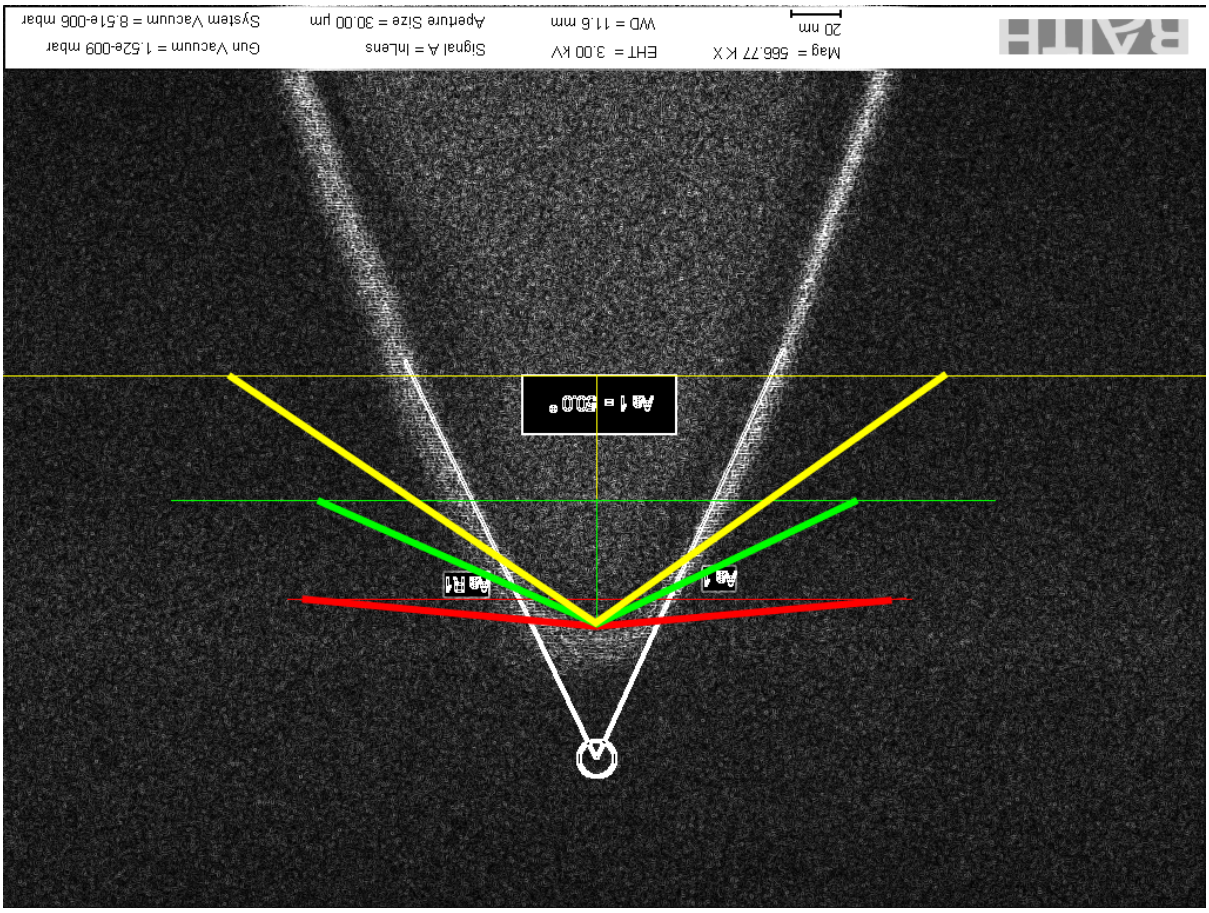

Figure 5.5. Comparisons of approximated conical angles. SEM micrograph of the top 250 nm of the uncoated AFM tip, fitted with the approximated conical angles determined in (Table 4.8). Red angle is 170° at 10 nm. Green angle is 130° at 50 nm. Yellow angle is 110° at 100 nm. The white angle was fitted with the SEM software after image capture. The image was rotated 180° for easier visualisation.

a b

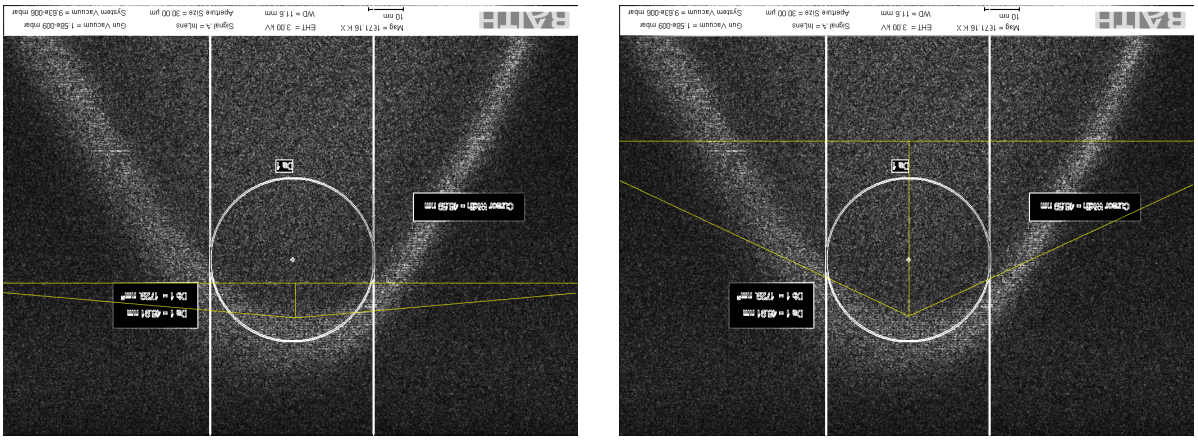

Figure 5.6. High-magnification SEM at the tip apex. Identical micrographs of the tip apex and up to 89 nm. The white lines were added in the SEM software to calculate the tip diameter. The yellow lines depict the approximated angle measurements in (Table 4.8). (a) 170° angle fitted at a measured 10 nm from the leading edge of the tip. (b) 130° angle fitted at a measured 50 nm from the leading edge of the tip. Images were rotated 180° for easier visualisation.

a b

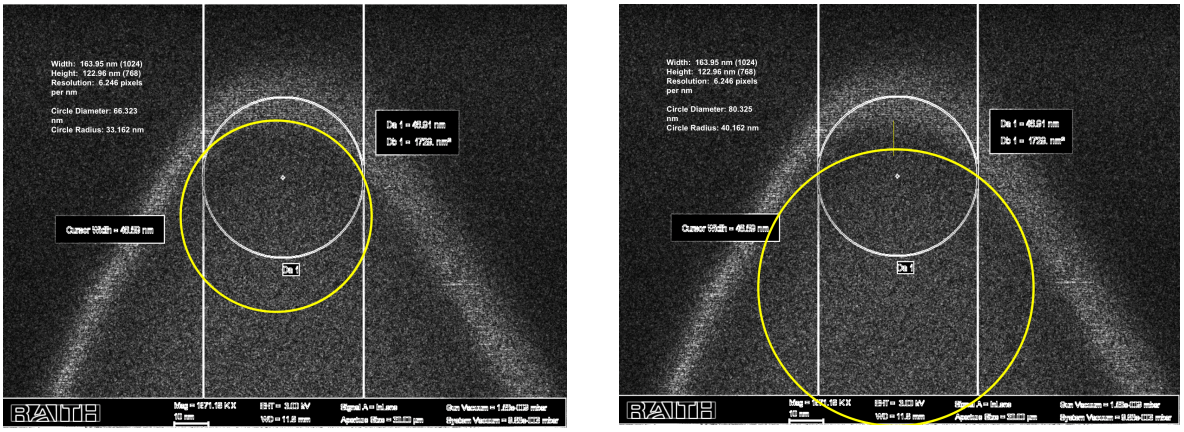

Figure 5.7. Diameter measurements at the tip apex. Identical SEM micrographs of the tip apex. The yellow circle depicts the tip diameter at (a) 66 nm at the tip apex, and (b) 80 nm at 10 nm below the tip apex.

5.2.2 Coated vs. uncoated AFM tips

Initial SEM was performed with a ~ 10 nm layer of gold sputter-coated onto the AFM tip (Fig. 5.8) but the tip was seen to adopt a rough morphology with rounded clumps of coating visible at all length scales. Line measurements at 10 and 100 nm from the tip apex were added using the SEM software following image capture. A diameter of 93 nm was approximated.

a b c

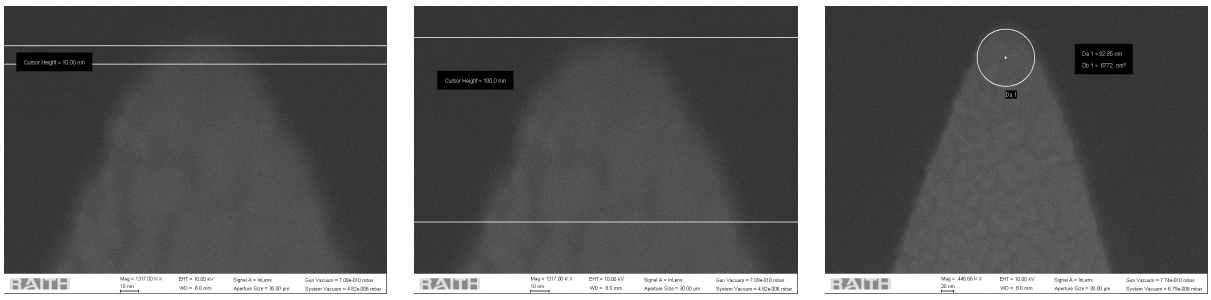

Figure 5.8. Sputter-coated tips show a rough morphology. High-magnification SEM micrographs of gold sputter-coated AFM tips at (a, b) the top 133 nm from the tip apex and (c) 416 nm from the tip apex. The white lines were added in the SEM software following image capture and denote (a) 10 nm from the tip apex (b) 100 nm from the tip apex. The white circle (c) shows an approximation of the tip diameter and measures 93 nm.

5.2.3 Imaging a tip using the AFM

A range of cantilevers were gently removed from the MLCT chip and carefully secured to the bottom of a 35 mm culture dish with optical glue. Initial scans prior to the addition of glue were not stable during AFM scanning, even at low nN forces (data not shown). Multiple tips were scanned using either an MLCT D or TESPA-V2 cantilever in QI™ or intermittent contact mode respectively (Fig. 5.9) (Chapter 3.15).

a b

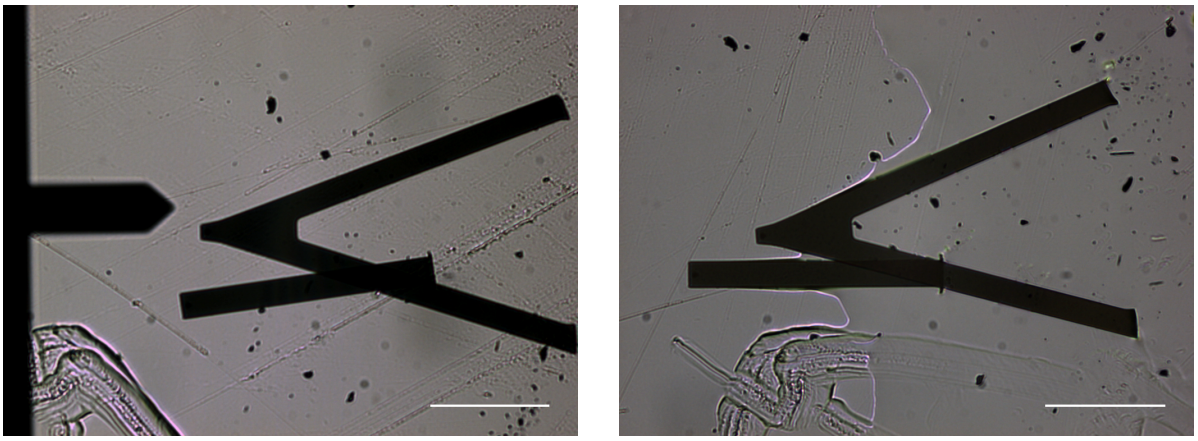

Figure 5.9. AFM scans on a range of cantilever tips. Optical micrographs of two cantilevers from the MLCT chip prior to AFM scans. (a) A TESPA-V2 cantilever on approach towards the unsecured cantilevers. (b) Both cantilevers were gently secured with optical glue, allowing for sufficient immobilisation. Scale bar is 100 µm.

5.2.3.1 3D topographical images of an AFM tip

Two different cantilevers were scanned and AFM height images were acquired and compared to a SEM micrograph of an MLCT D (Fig. 5.10). The tips closely resembled the micrograph at the back angle, but both showed imaging artefacts towards the front angle. The tip scanned with the TESPA-V2 appeared to be rounded at the tip apex, which may be an imaging artefact, as the tip scanned with an MLCT D had previously been scanned with a TESPA-V2 and showed no signs of rounding. The SEM micrograph (Fig. 5.10a) has an 80 nm diameter circle drawn (in yellow) at the tip apex (arrow) to identify the actual maximum contact area at 10 nm indentations on PDMS and SA.

5.2.3.2 3D line profiles of an AFM tip

A line profile was drawn across the full width of the tip, passing over the tip apex on both of the AFM height images (from Fig. 5.10), and the numerical data were used to create a graphical representation (Fig. 5.11). The *XY*-axes were made roughly isometric to gain a suggestion of the true tip apex geometries. The majority of the MLCT tip data were disregarded, leaving only the top ~ 1 µm for a more detailed analysis of the tip apex.

a

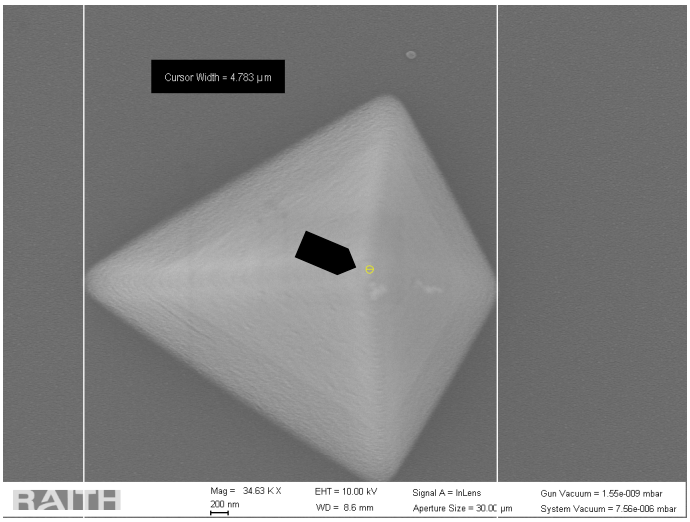

b

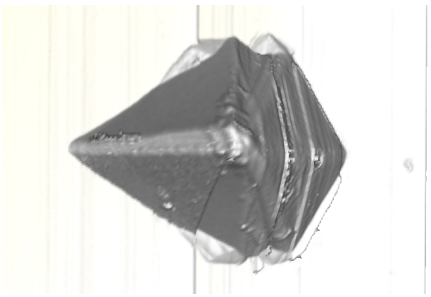

c

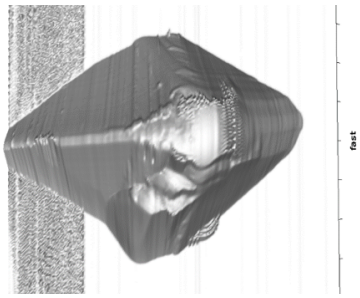

d

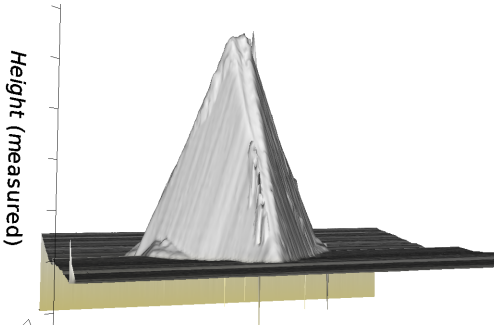

e

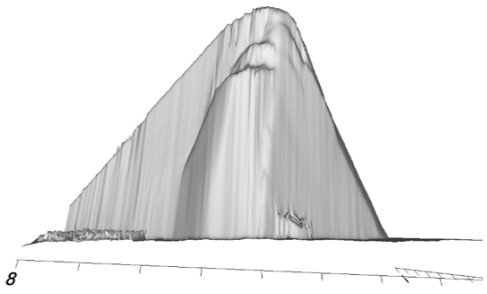

Figure 5.10. Comparisons of SEM micrograph and AFM images of an AFM cantilever tip. (a). SEM micrograph of an MLCT tip. The arrowhead shows an 80 nm diameter circle (yellow) that represents the tip apex. (b, d) AFM 3D height images of an MLCT tip imaged with an MLCT D. (c, e) AFM 3D height images of an MLCT tip imaged with a TESPA-V2.

a

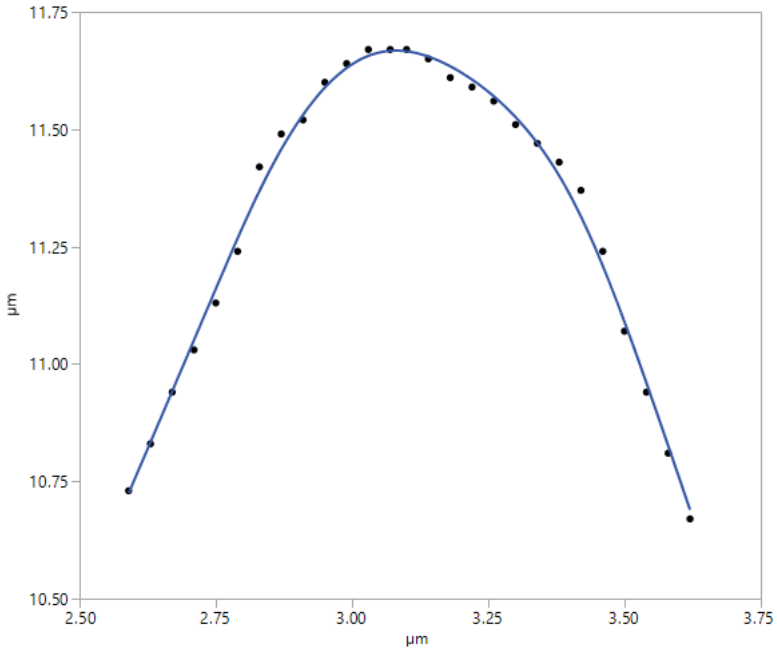

B

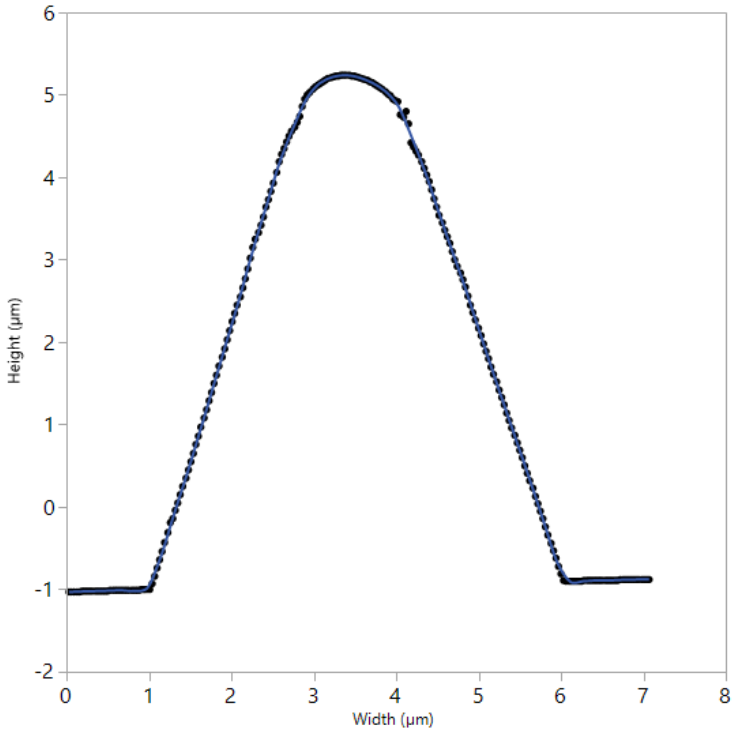

Figure 5.11. AFM tip line profiles. Profiles were drawn over the full width of the height images and across the tip apex, and *XY*-axes made roughly isometric. (a) An MLCT tip scanned with another MLCT. The majority of the numerical data were disregarded to leave the top ~ 1 µm. (b) An MLCT tip scanned with a TESPA-V2.

5.3 Discussion

5.3.1 High-magnification SEM of the AFM tip

We obtained reasonable images of the AFM tip at a range of increasingly magnified SEM length scales. Initially, we had analysed gold-coated samples but clumps and deposits of the metal obscured the true tip morphology. As the MLCT cantilever chip has a reflective coating of gold on the back side and titanium/aluminium on the top layer we reasoned that these may provide enough conductivity and reduce the potential for electronic charging by omitting the coating step. Although some charging was evident at highly magnified length scales it did not inhibit our measurements of radii and conical angles. Additionally, the image editing allowed us to easily distinguish the actual tip geometry – due to its high contrast, from the weakly contrasting charging region. We showed that the half-angle measurements of ~ 17° (which agreed with the manufacturer specifications) were consistent on our images at the full tip height – of ~ 6.9 µm, and down to heights of ~ 4.4 and 1.4 µm. This linear angle behaviour deviated once we approached the end of the tip at ~ 250 nm, with further deviations at ~ 100 nm from the tip apex. Based on our PDMS indentation data and the approximations of conical half-angles (Chapter 4.2.9.1) we fitted these approximated angles at 10, 50 and 100 nm from the tip apex to infer the possible geometry of contact between the tip and the PDMS substrate. Previous work from Deuschle and co-workers showed that there is a clear sink-in effect on PDMS during indentation with a conical indenter (Deuschle *et al.*, 2008). Their data showed that the contour of the contact area was bowed, and was larger than the true contact area. The sink-in was reduced during larger indentations, leading to closer contact of the material and the indenter. They performed very large indentations between 5 – 20 µm. Our measurements suggest the same relationship at the nanoscale. Initially, the contact at 10 nm is almost horizontal, with very little material contact at the tip, presumably due to sink-in effects. During deeper indentations the contact on the tip becomes more pronounced as the sink-in is reduced.

We were able to obtain accurate radius and diameter measurements at the tip apex and showed that the radius was 33 nm at the very edge of the tip apex and 40 nm at 10 nm below the apex. These measurements are half way between the manufacturer specified nominal and maximum radii of 20 and 60 nm respectively.

5.3.2 Direct AFM imaging of a tip

In an attempt to support our high-magnification SEM micrograph data we immobilised a range of MLCT cantilevers (B – F) onto a plastic culture dish and obtained AFM height images using another MLCT cantilever, and a TESPA-V2 cantilever. We had expected a rounding of the tip apex when scanned with another MLCT as both have a radius of ~ 40 nm. However, the apex appeared to be well resolved with little rounding. There were imaging artefacts present at both of the front sides, which were likely due to the relatively blunt nature of the scanning probe, but the AFM image closely resembled our SEM micrograph. Conversely, the AFM image captured by the TESPA-V2, which has a nominal and maximum radius of 7 and 10 nm respectively showed a high degree of rounding at the tip apex. This was confusing, as we would expect an improved resolution with this probe. We considered whether the cantilever, with a stiffness of ~ 40 N/m (compared to ~ 0.05 N/m with the MLCT D) may have damaged the immobilised tip, or even itself – leading to imaging artefacts. This seems unlikely, however, as the tip presented here that was imaged with the MLCT had previously been scanned with the TESPA-V2. Similarly to the MLCT scan there are also imaging artefacts present at both of the front sides. They have an elongated morphology, when compared to the MLCT image and the SEM micrograph. The TESPA-V2 front and side angles are slightly shallower than the MLCT. It is possible that the rounded apex is a combined artefact where the TEPSA-V2 may have had difficulty in tracking the immobilised tip.

The line profiles drawn across the tip apex enabled us to identify the geometry with high precision and in three dimensions. By zooming into the profile data we could quantitatively interrogate and compare the geometry at a range of increasingly smaller nm length scales. This offered a significant advantage over the published SEM and TEM data.

5.3.3 Investigating the power law relationship

Investigators considered the influence of tip roughness to determine the actual contact geometry between the tip and a micronised sample of pharmaceutical particles. Using silicon tips in intermittent contact mode they found a maximum Rq of 12.8 nm (Hooton *et al.*, 2004). We had intended to calculate the roughness parameters of the tip apex but due to the imaging artefacts we were unable to do so (data not shown). The Ra and Rq values

were on the order of ~ 160 nm which cannot be true as silicon wafers have a reported roughness of ~ 0.1 – 1.0 nm (Teichert *et al.*, 1995) and silicon nitride films have a reported roughness ~ 0.2 – 0.3 nm (Xu *et al.*, 2001). In order to approximate how the contact angle of the tip-PDMS combination may arise we obtained molecular resolution of PDMS at 80 nm – this being the tip diameter (Chapter 4.2.7.1). Several steps and valleys could be seen and it is likely that at shallow indentations not all of the steps would be in contact with the tip, leading to the almost linear contact angle approximated at 10 nm. A similar effect can be seen diagrammatically when a cone is indented into a rigid copper substrate. This could lead to the almost flat contact half-angle of 85° that we have identified. (Fig. 5.12) (Nix and Gao, 1998).

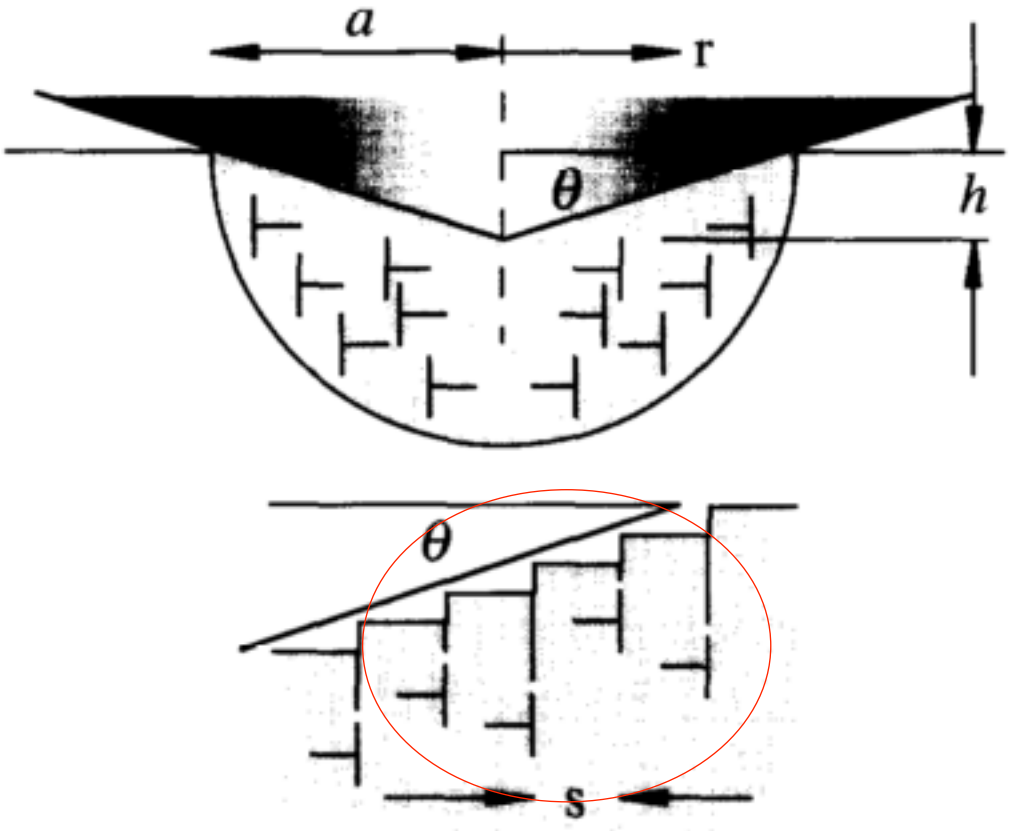

Figure 5.12. Dislocations in copper by a rigid conical indenter. Nix and Gao investigated the strain plasticity of polycrystalline copper and showed that dislocations occurred to account for the permanent shape change at the surface. In an elastic deformation of a soft substrate – such as PDMS, which is subject to considerable sink-in, one can envisage that only some of the surface features would contact the indenter, and that others (circled in red) may not actually make contact with the tip. Image adapted from Nix and Gao (1998).

Lim and Chaudhri performed indentations on a 10:1 SYLGARD™ PDMS with an elastic modulus of 1.55 ± 0.55 MPa, using a variety of conical indenters. The largest included angle was 136°. They performed deep indentations, at ~ 700 μm, and captured the circular radius of contact with an optical camera. The sink-in was clearly visible and the PDMS contact with all the indenters was a considerable distance away from the initial surface position. Their data were well fitted by the Sneddon contact model of rigid cones indenting an elastic half-space (Lim and Chaudhri, 2004).

5.3.4 Conclusions to this study

We sought to characterise the AFM cantilever tip geometry at length scales on the order of tens of nanometres using SEM, and directly scanned an AFM tip with another AFM tip. In doing both of these experiments we have been able to characterise the tip at its apex and upwards towards its full height in three dimensions. We have shown that the included angle of the tip changes considerably towards the tip apex, and at very shallow indentations of a soft elastic surface the contact angle of the tip and substrate is almost linear.

5.3.5 Limitations to this study

Despite the lack of a metal coating on the cantilever tip – reducing the impact of altered geometry due to unevenly distributed coatings, there were signs of charging. We used image editing and made the assumption of the true geometry. However, even in the absence of image editing, the charging outline faithfully followed what we characterised as the true geometry and thus the measured angles should remain the same. The angle fittings were manually drawn and perfectly straight, where the PDMS would be curved, due to the sink-in effects. SEM micrographs are perspective projections and can be interpreted differently depending on the angle and tilt of a mounted sample. To minimise this effect we obtained micrographs of two different tips at a side angle and a front angle. We were unable to obtain high-magnification of the tip apex from the side at the same length scale as achieved from the front (data not shown). Thus, we have formulated our indentation model based on a limited characterisation of tip geometry. Due to the imaging artefacts present on the AFM scans of the AFM tips the true geometry has not been fully characterised.

Chapter 6

Immobilisation of *Staphylococcus aureus* for mechanical property measurements

6.1 Introduction

6.1.1 Cell immobilisation

Immobilisation of bacterial cells can be problematic, especially with regards to scanning – often repeatedly, with an AFM. Bacteria adhere to inanimate surfaces by weak Lifshitz-Van der Waals bonding forces and these can be broken frequently by the tip movement (Touhami, Jericho and Beveridge, 2004; James, Powell and Wright, 2016). The immobilisation needs to constrain the bacterium so that it can withstand the lateral forces exerted by the probe, or the potential thermal or acoustic waves that may be propagated through a liquid medium. Conversely, the method of entrapment should not confer a chemical or mechanical stress to the cell that may interfere with normal physiological processes (Dhahri, Ramonda and Marlière, 2013).

6.1.1.1 Chemical immobilisation

Bacteria are often deposited onto flat substrates, such as glass or mica, allowed to dry and imaged under ambient conditions. This is an effective and easy method of immobilising cells, and structural information can readily be obtained via this method (Kailas *et al.*, 2011). However, for viable cell studies, and to assess the species of interest in an aqueous environment, chemical coatings are often required to immobilise cells. These may be harmful to a cell and could alter the mechanical properties of the cell wall, by inducing cross-linking of cell wall proteins (D'Souza, 2001). Moreover they may not facilitate successful scanning with an AFM. The commonly used polyethlyeneimine has shown the ability to permeabilise the Gram-negative cell membrane and facilitate the transport of hydrophobic solutes into the cell (Helander *et al.*, 1997). Poly-L-lysine is routinely used for cellular immobilisation, but has shown the ability to interfere with the bacterial cell cycle at concentrations as low as 0.001% (w/v), and can even be bactericidal (Colville *et al.*, 2010). Gelatine-coated surfaces have been considered superior to poly-L-lysine coated surfaces and have allowed for repeated scanning SA and *E. coli* in non-contact mode (Doktycz *et al.*,

2003). The Besenbacher group have looked at a variety of immobilisation methods for living bacteria (Louise Meyer *et al.*, 2010). They tried gelatin and 3-Aminopropyltriethoxysilane (APTES) coated surfaces, which are thought to promote cell adherence via electrostatic and hydrophobic interactions. The cells were easily dislodged however, during AFM imaging in PBS. This is thought to arise as the salts in the PBS may interfere with the electrostatic interactions between the cells and the chemical coatings. The authors also used polyphenolic proteins to bind bacteria onto glass surfaces, and could repeatedly scan in both intermittent contact and contact modes. During scanning, 1 – 2 cells detached with each consecutive scan, and eventually, after ~ 3 h, all the observed cells instantaneously detached during a single scan. They suggest that this may be due to cell growth or protein turnover in the cell wall, and a subsequent destabilisation of the contact area (Louise Meyer *et al.*, 2010).

6.1.1.2 Mechanical immobilisation

A diverse range of methods have been utilised to mechanically confine cells. These include holding a cell with a micropipette (Häberle *et al.*, 1992), or holographic optical tweezers (Kirkham *et al.*, 2015), depositing cells onto the surface of aluminium oxide filters (Yao *et al.*, 2002), embedding in agarose (Micic *et al.*, 2004) or agar (Gad and Ikai, 1995). The yeast *Saccharomyces cerevisiae* was immobilised in 3% agar and partially submerged in growth medium. It was shown that the agar was flexible enough to allow increases in height and width of multiple cells, with minimal rotation of the cells and little submerging into the gel matrix. As the cells increased in height during growth, however, there were a number of imaging artefacts present, which limited the resolution (Gad and Ikai, 1995). Additionally, agarose gels may also encourage exponential growth of a bacterium, which may overwhelm the substrate and prevent the imaging of single cells (Moffitt, Lee and Cluzel, 2012b).

A number of methods have been successfully developed, to confine cells in pore sizes similar to the species of interest. If the dimensions of the immobilising pore/s are too restrictive, however, this could impact the ability of the cell to undertake its normal physiological processes (Siryaporn *et al.*, 2014). Porous polymer membranes have been widely used in the literature. *Saccharomyces cerevisiae* was trapped in a Millipore™ filter, made of cellulose acetate and cellulose nitrate (Kasas and Ikai, 1995) and scanned in contact mode. The pore size was just smaller than the cell, at ~ 5 µm, and cells were either loosely

bound on the filter surface, deeply embedded inside the pore, or protruding from the pore. The resolution was quite poor, however, and some cells were easily displaced. The Beveridge group performed high-resolution contact mode imaging of SA cells that were immobilised in a 1.2 µm diameter polycarbonate filter pore (Touhami, Jericho and Beveridge, 2004). Using cells harvested at mid-exponential phase, OD_{600} = 0.2 and immersed in growth medium, they identified signs of cell growth, as a septal hole enlarged, over the course of 1 h at room temperature. Intermittent contact mode has also been used successfully to capture high-resolution images of SA immobilised in a polycarbonate filter, in PBS (Turner *et al.*, 2009), and later to observe invagination of the septal region in growth medium (Turner, Thomson, *et al.*, 2010). These filters have also lead to mechanical deformation of the cell membrane in *Staphylococcus epidermidis* and the potential to influence the AFM F-D curves (Mendez-Vilas, Gallardo-Moreno and Gonzalez-Martin, 2007). The pore dimensions of polycarbonate filters are not entirely uniform and thus the immobilisation of cells can be sporadic and unpredictable (Turner, Thomson, *et al.*, 2010; James, Powell and Wright, 2016). Our study (data not shown) briefly looked into the use of polycarbonate filters to trap SA cells and equally found the process to be poorly reproducible.

Previous work from our laboratory (Kailas *et al.*, 2009) generated silicon wafers with lithographically patterned surfaces. A four sided star shaped array of holes between 1 – 1.8 µm and ~ 450 nm depth enabled contact mode AFM to capture SA cell swelling during growth and division, at room temperature. The cells displayed signs of constrained morphology however, and although the cell was able to grow and divide, it was seen to take on the shape of the confining pore. This effect has been observed with *E. coli*, where it was shown that deliberately confining the cells in chambers of defined shapes, lead to their permanently adopting the defined shape when released (Takeuchi *et al.*, 2005).

Further work from our laboratory used photolithography to pattern silicon wafers with round shaped pore dimensions measuring 1 – 1.2 µm and an increased depth ~ 750 nm (Bailey *et al.*, 2014). The substrate was coated with a thin layer of polystyrene [1 mg/ml] to make the surface more hydrophobic, and to aid in SA cell attachment in liquid.

The use of photolithography to pattern silicon wafers is not unique to this study. The Dague group generated a microstructured silicon master, which they similarly used to create a

PDMS stamp to immobilise yeast cells (Formosa *et al.*, 2015). Their technique is very similar to the one used in this study, and the other studies from our laboratory, albeit they used square patterns of 1.5 – 6 µm in diameter. This wide range of pore sizes was designed so that a variety of different cell types could be studied. However, this silicon master was used merely as a template with which to cast patterned PDMS substrates from, and thus is directly similar to the methods employed in this study. These authors used a convective and capillary setup, with a motorised stage, to drag yeast cells into the pores, at a speed of 2 µm/s. Alternatively, they manually dragged the cells using a glass coverslip. The coverslip method was occasionally employed in this study (Chapter 3.16.5). These authors considered the hydrophobic character of the PDMS substrate and found that it may be necessary to render it more hydrophilic for successful cell deposition. In this case, they briefly treated the PDMS under O_2 plasma for 30 s or under UV-O_3. Equally, both of these methods were employed in this current study to render both PDMS and silicon wafers more hydrophilic, whilst attempting to obtain the most efficient and repeatable method.

6.1.1.3 No immobilisation

Recently, a group from Montpellier successfully used QI™ mode to study bacteria in their native environment with no chemical or mechanical immobilisation on glass (Dhahri, Ramonda and Marlière, 2013). They obtained mechanical measurements of the Gram-positive, non-motile *Rhodococcus wratislaviensis*, and the Gram-negative, motile *Nostoc* cyanobacteria *Anabaenopsis circularis*. Both species, however, are rod-like and filamentous and secrete a sticky extracellular 'slime' matrix. They used high setpoint forces of 6 nN – 10 nN respectively, and very fast scanning rates of 50 – 500 µm/s. Acquisition settings were a 500 nm retract, with an additional 100 nm before moving to the next pixel. They found that the reported turgor values changed in response to the gliding speed of the motile bacteria. At speeds below 100 nm/s their averaged value for the Gram-negative species was 50 ± 10 kPa, whilst it increased to 180 ± 30 kPa when gliding speed was up to 220 nm/s. They obtained stiffness values between 0.07 – 0.36 N/m for the *Nostoc*, and Young's modulus values of 20 – 65 MPa. For the Gram-positive bacterium they obtained a turgor value of 307 kPa, stiffness measurements of 0.23 – 0.64 N/m and a Young's modulus of 104 MPa. The spring constant of the cantilever they used was ~ 0.36 N/m - an order of magnitude stiffer than the ones used in our study. Modulus measurements were obtained using the Sneddon

contact model, with a 35° half-angle and a Poisson's ratio of 0.5. The authors state that mechanical data of Gram-positive bacteria are scarcer in the literature and reveal orders of magnitude disparity with the reported modulus values – something we are inclined to agree with.

We tried multiple times to quantitatively image SA cells in growth medium with no immobilisation (data not shown). As SA cells are spherical and did not produce ECM in the proportions as described above, they were routinely displaced. With careful manipulation of the cantilever, the SA cells could be rolled around the substrate with 'football-like' precision.

6.1.2 Monitoring the mechanical properties over time

Multiple AFM studies of the mechanical properties of eukaryotic cells exist in the literature – particularly with regard to cancer cell lines. For a review, see (Luo *et al.*, 2016). When it comes to elucidating the mechanical properties of bacteria, many studies have looked at stationary phase cells and/or non-actively growing cells in PBS, or ambient conditions. The literature provides very little in the way of bacterial mechanics in actively growing cells, over an extended time period that would be sufficient for the potential generation of daughter cells, during the cell cycle. The actively growing cell studies detailed above, in section 6.1.1, were imaging studies only. Whilst some cell mechanics studies have addressed the adhesive properties (Rodriguez-Emmenegger *et al.*, 2015; Formosa-Dague *et al.*, 2016), or the elastic modulus of living bacteria in a growth medium (Vadillo-Rodriguez, Beveridge and Dutcher, 2008; Smolyakov *et al.*, 2016), these studies looked at single time points only.

The cell wall of SA was seen to degrade by the action of lysostaphin over a 300 min period (Francius *et al.*, 2008) with noticeable swelling and a reduction in the elastic modulus. The authors used mid-exponential phase cells; OD_{600} = 0.6, trapped in polycarbonate filters in PBS. Bacterial cells are generally not considered to be actively growing in a PBS medium and thus these data suggest the lysostaphin action was independent of growth processes. However, Koseki and Yamamoto showed that *E. coli* cells, in PBS, challenged with high hydrostatic pressure, were able to recover from below detectable levels to initial cell count levels after 48 h at 25° C, although no recovery was observed in cells that were stored at 4 or 37° C (Koseki and Yamamoto, 2006). The long- and short-term survival of bacteria stored

in water or PBS was studied and the results are surprising (Liao and Shollenberger, 2003). A total of 148 bacterial strains, including *E. coli* and SA, were observed over a 4 week to 16-year timescale. Plant-associated bacteria were able to survive in sterile distilled water for 12 – 16 years and could be recovered by plating onto agar. Human pathogenic bacteria stored in water remained viable for at least 5 years. SA cells fared better in PBS than water, and *E. coli* fared well in both. Both cultures displayed non-significant population changes after 4 weeks in PBS. The authors suggest that the recovery of the cells was due to repair processes and not bacterial growth. The lysostaphin work of Francius and colleagues (2008) was repeated in our laboratory, using SA cells trapped in a silicon wafer (data not shown). The cells showed no obvious signs of growth or division throughout. They were hydrated in an imaging buffer (Chapter 3.3.2) - not PBS, and a lower concentration of lysostaphin was used – [2 μg/ml], rather than the [16 μg/ml] used by Francius. There was a lag phase of ~ 25 minutes where there were no visible changes in cellular morphology, followed by signs of lysis and eventual bursting of multiple cells within 5 minutes. The enhanced lysing effect of lysostaphin in this experiment (at the lower concentration) suggests that the imaging buffer or the immobilisation in silicon, rather than polycarbonate filters, may be causative factors, or differences with the purity of the enzyme. Lysostaphin has also shown the ability to disrupt the cell wall of sessile, quiescent and actively growing SA cells within biofilms (Wu *et al.*, 2003). Taken together, these studies suggest that the mechanical properties of bacteria could change over time, independent of active growth processes.

Other studies have explored the mechanical changes over time, using alternative methods to AFM. One group embedded rod-shaped bacteria into agarose gels of a known stiffness (Tuson *et al.*, 2012). They modelled the cell wall as a connected chain of linear springs, and by monitoring the perturbations of elongation (balanced by gel compression) at the bacterial poles, they provide an estimate for the cell wall stiffness. They used a variety of rod-shaped Gram-negative bacteria and explored the perturbations between 5 – 30 minutes of growth. Their modulus data however, was only estimated from the first few minutes after embedding in the gels, where the gel compression was considered small. The authors obtained Young's modulus values of 50 – 150 MPa for *E. coli* and state that the range of modulus values could represent a non-linear response of the cell wall. Further, they acknowledge that their values are three to fivefold higher than many AFM-derived modulus

values of extracted cell wall sacculi. The literature suggests that environmental conditions could result in such a spread of values and as the authors specifically observed living cells, they reason that this is why their modulus values differ to sacculi (Tuson *et al.*, 2012).

The mechanical properties of specific regions of the SA cell wall have been studied at single time points (Bailey *et al.*, 2014). This work, from our laboratory, used late-exponential phase cells with an OD_{600} ~ 0.8 immobilised in silicon wafers and using force mapping on the JPK NanoWizard® 3 AFM. Under ideal conditions, i.e. 37° C, in growth medium, with little perturbation from immobilisation, SA should divide in just under 30 minutes. Although this study, and many others, has seen little evidence of true growth and division events over a sustained time period, we propose that even in the absence of any morphological changes, cellular processes must still be occurring. Would these processes lead to noticeable changes in the modulus of the cell wall? By using mid-exponential phase cells - that should still be actively growing, we will investigate any mechanical changes over a 1.5 h period - enough for 3 potential generations of SA.

6.1.3 Extracted cell wall sacculi

An intact bacterium possesses curvature about its circumference and can make AFM imaging difficult, particularly with regard to obtaining high-resolution images and mechanical measurements. Extracting, and purifying, the cell wall polymer from the rest of a cell (Chapter 3.20.1) enables AFM to interrogate the now, relatively flat, material (Hayhurst *et al.*, 2008; Turner, Vollmer and Foster, 2014). Early work with bacterial sacculi enabled structural models of PG arrangement to be formulated (Holtje, 1998; Pink *et al.*, 2000) and by digesting the sacculus, individual glycan chain lengths could be assayed by high performance liquid chromatography (Holtje, 1998) or size-exclusion chromatography (Hayhurst *et al.*, 2008). More recently, locations of PG insertion in the sacculus, by means of fluorescently labelled vancomycin has enabled the formulation of updated structural models (Turner *et al.*, 2013; Lund *et al.*, 2018). The first atomic resolution of a transpeptidase protein, from *Bacillus subtilis*, bound to the PG of an intact sacculi, was determined by solid state nuclear magnetic resonance and revealed that, both the catalytic and recognition domains were important for the interaction – a finding that could offer pathways to novel antimicrobial compounds (Schanda *et al.*, 2014).

The mechanical properties of SA sacculi have been elucidated by AFM in our laboratory (Bailey *et al.*, 2014). The authors were unable to secure the sacculi under liquid and had to investigate the samples in ambient conditions. They recorded a stiffness value of 0.0137 ± 0.0010 N/m from 20 individual sacculi. These data were very similar to the cell wall data they had obtained from whole cells. Although one might expect the sacculi to be less stiff, due to the absence of turgor pressure, the authors suggest that the similar stiffness obtained may be attributed to the dehydrated condition of the sacculi and the influence of the solid substrate. The sacculi thickness was 27 ± 3 nm, which is in agreement with TEM-derived literature values for the cell wall (Giesbrecht, Kersten and Maidhof, 1998).

The structure and mechanical properties of hydrated sacculi can be markedly different to those of the dehydrated sacculus. The sacculi of *E. coli* and *Pseudomonas aeruginosa* were both seen to double in thickness and their elastic modulus was lower in the hydrated condition (Yao *et al.*, 1999). The sacculi were more rigid when dehydrated and more elastic when hydrated in water. Turner and co-workers found that there was significantly more architectural detail in hydrated *E. coli* sacculi than other AFM studies had shown, with periodic banding visible (Turner *et al.*, 2013). Additionally, they devised a novel stretching mechanism to simulate the effect of whole cell turgor on the hydrated sacculi, which retained the banding architecture and revealed multiple pores, with diameters between 4 – 16 nm.

6.1.4 Chemically and genetically challenged cell wall properties

Studies with mutant strains of SA have revealed changes in glycan chain length and stiffness of the cell wall (Wheeler *et al.*, 2015). SagB has been identified as an important glucosaminidase in the regulation of SA cell wall synthesis. The authors generated constructs with gene inactivations of the four key SA glucosaminidase enzymes. In strains lacking any three of these enzyme-encoding genes the cell wall stiffness increased significantly, with the inactivation of SagB leading to the highest stiffness. Inactivation of SagB also lead to a 20% increase in long glycan strands, compared to WT cells, suggesting that it is involved in the post-processing of glycans (Wheeler *et al.*, 2015). In the absence of PBP4, and the concomittant reduction of crosslinking in the cell wall, there was a reduction of the elastic modulus in SA lab strains and hospital acquired and community acquired MRSA (Loskill *et al.*, 2014). Adding ampicillin into a culture of *E. coli* cells resulted in a

dramatic decrease of membrane modulus (Longo *et al.*, 2013). Conversely, an initial stiffening of the cell wall of *Bacillus subtilis* was seen, upon addition of antimicrobial ceragenins, which the authors attribute to the active responses of the bacteria (Pogoda *et al.*, 2017).

6.1.5 Mechanical property characterisation

We have made an assumption that the nanoscale properties of PG will be the same throughout the 25 – 35 nm of cell wall. When indenting with a probe and analysing the mechanical properties of PG at 10 nm of indentation, will the elastic modulus and stiffness be representative of the whole cell wall? Given that the hydrated cell wall may, in fact, be thicker than previously thought (section 6.1.3) – with suggestions of 60 – 80 nm reported in the literature for Gram-positive species (Götz, Bannerman and Schleifer, 2006) this could impede the quality of the results. However, our previous work on the stiffness of the SA cell wall found two distinct stiffness regions, based on the log-log plots of the F-D curves, and a subsequent change in their power law dependence (Bailey *et al.*, 2014). It was shown that the gradient of the curve, and the recorded stiffness values, changed markedly at an indentation depth of 25 nm. This suggested that the influence of intracellular turgor was influential at this indentation depth - whether this was the full thickness of the cell wall or not, and osmotically modifying the turgor confirmed this (Bailey *et al.*, 2014). When considering the structure of SA PG, over 80% of the glycan strands are on average around 6 disaccharides in length, with only the remainder longer than 26 disaccharides (Boneca *et al.*, 2000). The pentaglycine bridges in the PG of SA are highly crosslinked to a density of 79%, and 85% of the pentapeptide stems have glycine bridges attached, leading to a total of 67% of PG crosslinking (Patti, Sung and Schaefer, 2008). The PG of *staphylococci* is exceptional, in that it has almost no free carboxyl groups, as the D-glutamic acid α-carboxyl group is amidated (Tipper *et al.*, 1967) and in SA ~ 50% of muramic acid residues are *O*-acetylated (Tipper, Tomoeda and Strominger, 1971). *E. coli*, and most other Gram-negative species have ~ 70% of glycan strand lengths between 20 – 40 disaccharides, with the remaining strands up to 80 disaccharides (Vollmer and Seligman, 2010). The crosslinking density of *E. coli* PG has been calculated between ~ 23% (Glauner, Holtje and Schwarz, 1988) and 50% (Gumbart *et al.*, 2014). Gram-negative species, such as *E. coli* do not possess WTA (Swoboda *et al.*, 2010). Despite these differences, the glycan strand composition is uniform across all

bacteria (Gumbart *et al.*, 2014). Given that the PG of *E. coli* has a thickness of 3 – 6 nm it stands that the mechanical properties of this PG would be determined at an indentation depth up to a maximum of 3 - 6 nm. The PG of SA is considered to be multi-layered, and it should also hold true that indenting at 10 nm would accurately determine the mechanical properties of the PG. Further, by indenting to this depth, we should largely avoid the influence of turgor, and the dual power law gradients, as previously recorded (Bailey *et al.*, 2014). The elastic moduli values for whole cells widely reported in the literature are typically in the high kPa to low MPa range, 0.5 - 95 MPa (Eaton *et al.*, 2008; Perry *et al.*, 2009; Loskill *et al.*, 2014). Given that these values span 2 orders of magnitude do they simply reflect the heterogeneity of the bacteria or do they arise as a result of experimental differences and models used?

6.1.6 Hertzian contact between two spheres

The equations (Eq. 14, 15 and 16) described in (Chapter 4) consider a spherical indenter on a linear elastic half space. The contact between two spheres can be described by different equations, although Eqs. (17 and 18) are perfectly general and could also be used to describe the contact of a sphere on a plane surface (Budynas and Nisbett, 2010). As the whole cell SA is spherical the pressure, P_{max} at the centre of a circular contact area is described by the equation

$$P_{max} = \frac{3F}{2\pi a^2} \tag{17}$$

where F is the indentation force, and a is the contact area. The contact area is described by the equation

$$a = \sqrt[3]{\frac{3F\frac{(1-\nu_1^2)}{E_1}+\frac{(1-\nu_2^2)}{E_2}}{8\left(\frac{1}{D_1}+\frac{1}{D_2}\right)}} \tag{18}$$

where ν_1 and ν_2 are the Poisson's ratio of the indenter and the sample respectively, E_1 and E_2 are the Young's modulus for the indenter and the sample respectively, and D_1 and D_2 are the indenter and sample diameters respectively. The vertical displacement, d that the sample may experience can be described by the equation

$$d = \frac{a^2}{R} = \sqrt[3]{\frac{9F^2}{16RE^{*2}}} \tag{19}$$

where R is the effective radius, defined as $\frac{1}{R} = \frac{1}{R_1} + \frac{1}{R_2}$

6.1.7 Aims of this chapter

1. To mechanically immobilise SA cells for AFM imaging, using PDMS and silicon.
2. Investigate the mechanical properties of living cells over time, and statistically analyse them for significance.
3. Analyse the mechanical properties of hydrated extracted cell wall sacculi and compare them to intact, living cells.
4. Analyse the mechanical properties of hydrated, antibiotically challenged sacculi, and compare them to native extracted sacculi.
5. Use the Hertzian contact model to investigate the relationships between applied load, pressure and cell wall modulus of whole cell and sacculi.

6.2 Results

6.2.1 Immobilisation of *Staphylococcus aureus* using PDMS

Throughout the course of this study, multiple PDMS substrates were prepared; and initially a single PDMS sample was reused a number of times. The PDMS was given a three-stage wash – as previously described (Chapter 3.2.1) and stored until the next experiment. Considerable mechanical data (not shown) had been obtained for multiple SA cells. However, we discovered that despite the cleaning protocol, there were cells that appeared to be morphologically viable, still immobilised within some of the wells on the substrate. Although these were few in number, we could not rule out the possibility that these cells could be analysed following deposition of fresh bacteria. Thus, we discarded these data and opted to use a fresh PDMS sample for each experiment.

Immobilisation of SA cells was not consistent. Cells were either left to drop out of solution or gently scraped with a glass coverslip, with neither method providing a clear benefit for cell number in the wells of the substrate. Conversely, the glass coverslip method occasionally lead to regions of apparently lysed cells, with large areas > 5 x 5 µm of continuous cellular material. PDMS was rendered more hydrophobic with a coating of polystyrene but this offered no obvious increase in cell numbers. Making the PDMS more hydrophilic also offered no advantage. O_2 plasma treatments lead to a reduced contact angle of the cell sample droplet (data not shown) and a more even coverage of the PDMS surface, but this method also offered no obvious benefits to the amount of cells immobilised. Thus, native PDMS substrates were used for the experimental data presented here.

A differing range of bacterial concentrations was explored, by adjusting the optical density after harvesting. Initially, undiluted cell samples were used and the cell concentrations became too confluent, with little variation between samples that were analysed at room temperature or at 37° C. The high concentrations of cells routinely lead to an inability to perform successful scans, either through multiple cells interfering with the scans, leading to streaks in the images, or by string-like collections of cells binding to the cantilevers (Fig. 6.1). Both disturbances rendered the obtained F-D curves un-usable, as they showed considerable tilt and hydrodynamic drag. A range of optical densities was tried, and a

density of 0.2 was found to offer consistent results. Following sample deposition onto the PDMS at this density, there were only a limited number of cells present at the start of AFM scanning, which enabled easier optical visualisation of the wells, and the ability to locate any immobilised cells. By starting with a low concentration, the sample needed to be diluted once or twice at most, during a typical 4 – 6 h session.

a b

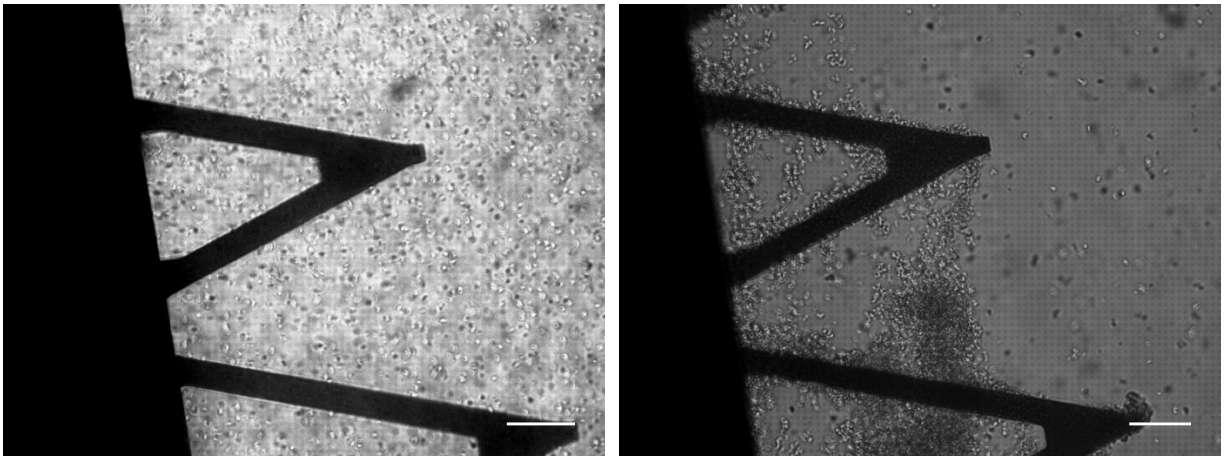

Figure 6.1. High cell concentrations lead to scanning difficulties. 10X optical micrographs of SA cells in growth medium. (a) Over-confluent cells lead to increased hydrodynamic drag of the AFM cantilever, leading to visual disturbances in the obtained AFM images. (b) String-like collections of cells bound to the cantilever were dragged along with each repeating scan. Both disturbances lead to a tilt in the approach and retract portions of the F-D curves and made processing and analysis difficult and unreliable. Scale bar is 50 µm.

It was also found that the growth medium (either BHI or TSB) could affect the cantilever motion. We posited that large molecules, or clumps of material in the media were affecting the cantilever in a similar manner to the bacteria. Following this, all growth media was filtered prior to AFM scans, and the diluted samples were also diluted in the filtered media. In order to test the ability of the filtered media to provide sufficient growth for SA cells, an equal inoculation of overnight cells was added to a tube of filtered media, and non-filtered media, and incubated as previously described (Chapter 3.5). OD_{600} measurements = 0.51 for non-filtered media and 0.35 for filtered media. The high rate of cell growth in the diluted

media, and the requirement to dilute the sample during a typical session suggests that the filtering did not impair cell growth (Fig. 6.2). All data presented here were obtained in filtered growth medium.

a b

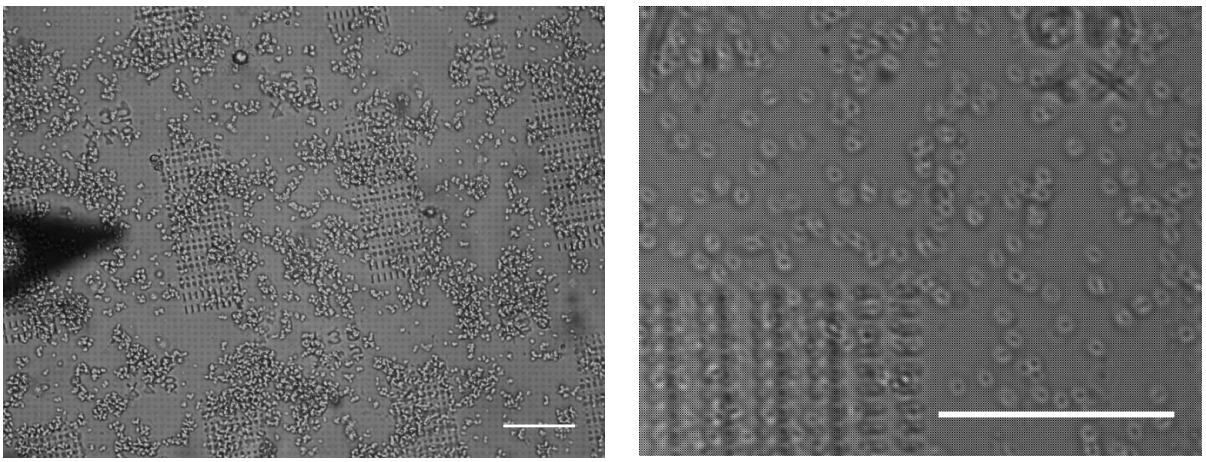

Figure 6.2. SA cell growth in the medium above the PDMS surface. 10X optical micrographs of SA cells demonstrate that they grow and divide in filtered growth medium. (a) Multiple collections of cells randomly oriented themselves close to the PDMS surface. (b) Software-increased magnification and slight defocussing enabled easy visualisation of septal regions, with numerous single cells, and connected sister cells. Scale bar is 50 µm.

6.2.1.1 Alternate PDMS designs

Once the protocol for some cell immobilisation had been established, we sought to improve the yield of immobilised bacteria, and the possibility for unperturbed growth. A range of designs were created (Chapter 3.7.1) and discussed in (Chapter 4.2.1). The multi-sized well substrate did not offer any benefit over the repeating ~ 1 µm diameter holed lattice, and SA cells rarely became immobilised. On occasion a pair of connected sister cells entered the ~ 3.5 µm diameter wells (Fig. 6.3) but became displaced before any scans could be performed.

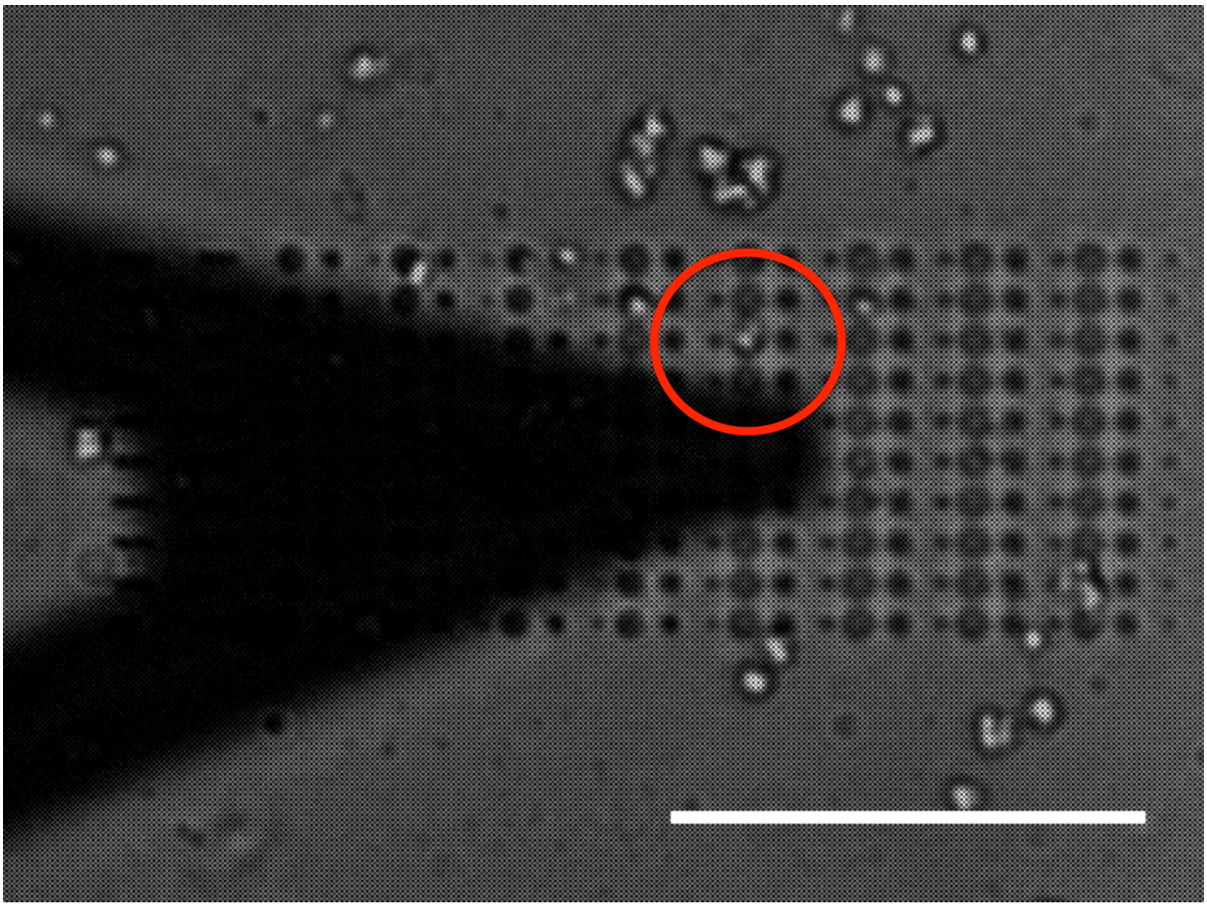

Figure 6.3. Dividing sister cells in PDMS holes were easily displaced. 10X optical micrograph of moderately confluent SA cells in growth medium. A pair of sister cells loosely immobilised in a ~ 3.5 µm diameter well (circled), would be easily displaced during an AFM scan. Scale bar is 50 µm.

Single cells were seen to enter the ~ 1.5 or 2.5 µm diameter wells periodically, but did not remain immobilised for AFM. No cells were observed to enter the ~ 5.5 µm length rod-shaped wells. Consequently, this particular substrate design never afforded immobilised bacteria, and thus, none of the mechanical data presented in this work were obtained from cells immobilised on PDMS cast from it.

The four-sided star shaped design allowed for some growth of a single SA cell once only, with significant swelling observed (Fig. 6.4). The outgrowth of the sister cell filled the narrow confines of one of the corners of the star shape, but did not mature into a whole cell, over the course of 4 h, with no changes in height or volume.

We explored the possibility that the laser, reflected from the back of the cantilever, may be causing toxicity to the cells in solution, and disrupting growth and division as phototoxicity has been reported in the literature. When positioned correctly for the best signal to noise ratio, the laser on the NanoWizard 3™ spills over the edges of the cantilever and could potentially irradiate the sample (Fig. 6.5). The cantilever was left in place, without scanning, and the scanner aligned away from the surface of the star-shaped PDMS substrate, where the cell concentration in the growth medium was the highest. To enable maximum laser intensity, the cantilever was moved out of the path of the laser source, and the laser left activated for 4 h. The cells grew and divided as typically as we normally observed in growth medium, and became overly confluent (data not shown), suggesting that the laser did not prove toxic to the growth processes in SA.

a b

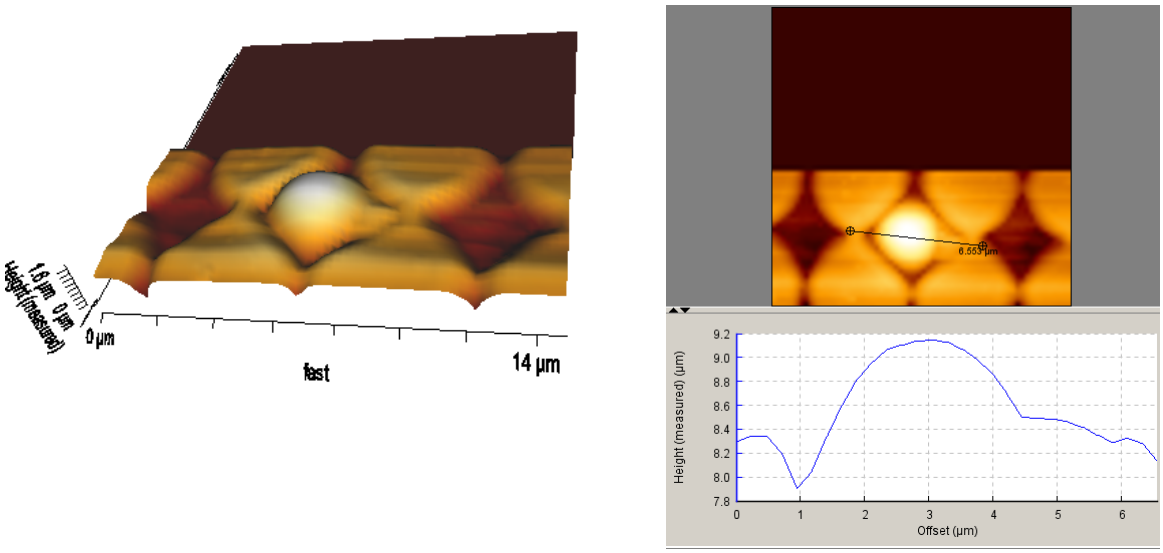

Figure 6.4. Minimal SA growth on star-shaped PDMS. AFM topographic images of a single cell with a sister cell outgrowth filling the edges of the confining substrate geometry. (a) 3D height image allows for easier visualisation of the cell and star shape of the PDMS. *Z*-scale = 1.6 µm. (b) Cross section shows a ~ 3 µm diameter SA cell with ~ 1 µm diameter sister cell protrusion. *Z*-height is just over 1 µm above the lowest recorded depth of the well, and the primary cell is ~ 800 nm above the PDMS surface. The ~ 3 µm diameter shows that the cell has undergone significant swelling. No further changes in morphology were observed, and the height and diameter did not change over 4 h. Scan size = 15 x 15 µm.

a b

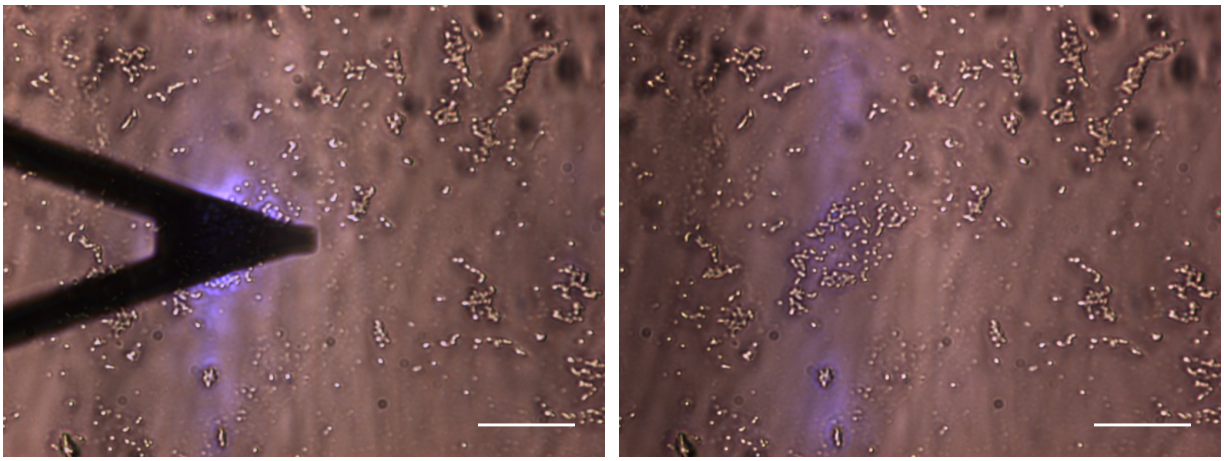

Figure 6.5. Determining the influence of laser toxicity against bacterial cells. 10X optical micrograph of SA cells in growth medium above a PDMS substrate. (a) The AFM laser, when correctly positioned, was still seen to spread over the edges of the cantilever. (b) The cantilever has been removed from the optical path to allow maximum exposure of the laser against the cells. No observed impairment of growth was seen after constant irradiation up to 4 h. Scale bar is 50 µm.

The only PDMS substrate that afforded good immobilisation of SA cells was the repeating ~ 1 µm diameter well lattice. Cells typically remained in place over the course of numerous scans, and over a sustained period. Very few cells were displaced during the ~ 1.5 h time point chosen for the mechanical studies presented here. Although sporadic – and hours could be lost searching for a single cell that remained immobilised, multiple cells were individually immobilised (Fig. 6.6). The cells regularly protruded from the ~ 750 nm depth well by up to ~ 800 nm, suggesting that only ~ 200 nm of cell was confined within the well, and that this small level of entrapment was enough to facilitate AFM scanning. Further, it may suggest that the well size and/or geometry were too restrictive to allow the cell to fit fully within the well dimensions. Grape-like clusters of cells, or connected sister cells, were also immobilised, such that repeat scans could be performed. A collection of cells became immobilised on the surface of the PDMS, and not in a well (Fig. 6.7). The underlying caveat always required that at least one cell was immobilised within a well and that the surface-bound cells were attached to that cell via one or more connections. Approximately half of

the cells analysed for their mechanical properties were immobilised in, or on PDMS. The other half were immobilised in, or on silicon wafers.

a b

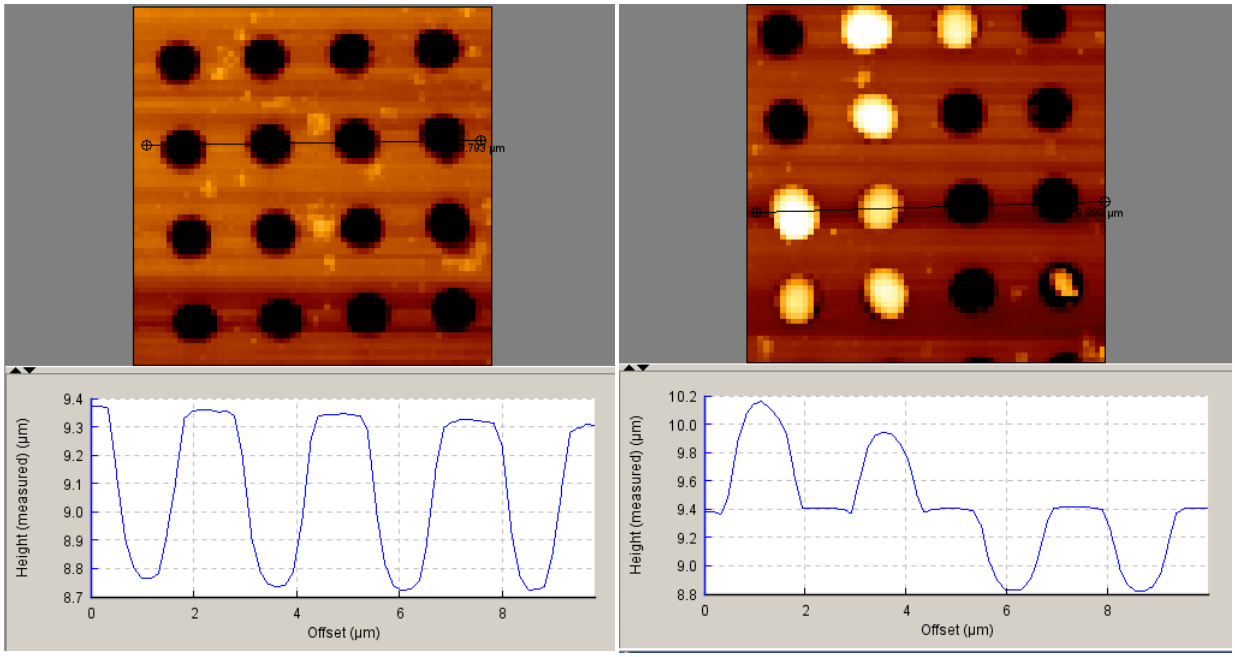

Figure 6.6. AFM topographic images of cells immobilised in PDMS. (a) A PDMS substrate with a repeating lattice of ~ 1 µm diameter wells. (b) The same substrate with individual immobilised SA cells. The cross sections suggest a depth of ~ 600 nm, with SA cells protruding between 500 – 800 nm above the PDMS surface. Scan size = 10 x 10 µm.

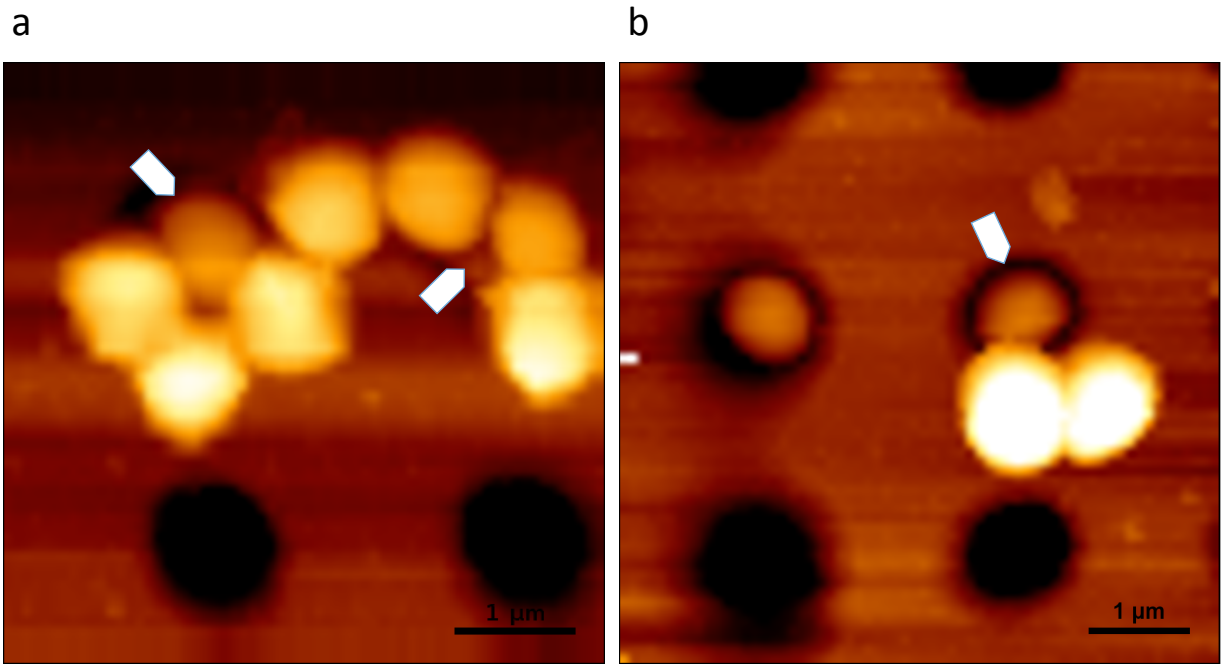

Figure 6.7. SA cells immobilised in, or on PDMS. AFM topographic images show (a) a grape-like cluster of connected cells bound on the surface, (b) a connected pair of sister cells bound on the PDMS surface. To facilitate AFM scanning, the surface-bound cells required single, or multiple connections to at least one other cell that was immobilised in a well (arrows). Images have been cropped. *Z* scale = (a) 1.42 µm (b) 1.04 µm. Scan size 5 x 5 µm (a) and 6 x 6 µm (b).

6.2.1.2 Immobilisation on silicon wafers

The silicon wafers with raised pillars (Chapter 3.7.2) that were used to cast PDMS from were infrequently used to directly deposit onto with SA cell suspension. We explored the possibility that rather than being immobilised within wells of the PDMS, the cells may be immobilised between the raised pillars of the silicon wafers. However, this technique did not allow for sufficient immobilisation. The silicon wafer with ~ 1 µm diameter holes (Chapter 3.7.3) was used successfully for immobilisation of SA cells. The technique used (Chapter 3.16.3) consistently yielded a large number of cells, with most – and occasionally all wells filled. Additionally, the silicon surface between the wells was often populated with immobilised cells, if they were connected to other cells, as discussed in the conditions in section 6.2.1.1. In further contrast to PDMS, all cells were removed following the three-stage wash (Chapter 3.2.1). Earlier work (data not shown) found that when omitting the

drying step under N_2 (Chapter 3.16.3), there were no immobilised cells present. Once the drying step was routinely used, wafers were scanned with the AFM periodically, prior to cell sample deposition, to satisfy that no cells remained from prior experiments.

6.2.1.3 Perturbation of division events

Although the ~ 1 µm diameter holed silicon wafer consistently immobilised SA cells for AFM scanning, there were never any obvious signs of growth and division. A collection of cells were immobilised within a number of consecutive wells, and also bound on the silicon surface, between the wells (Fig. 6.8). They were repeatedly scanned using intermittent contact mode on the Bruker FastScan (Chapter 3.18), in growth medium, at room temperature for 15 h. Each scan lasted ~ 2 min. The bacteria remained immobilised throughout, and the AFM scans were extremely stable, with only a small amount of lateral drift between the first and last images. Crucially, there were no signs of growth, division or morphological changes with any of the bacteria. The lack of growth on this silicon wafer was also observed over 18 h using confocal microscopy (Chapter 7).

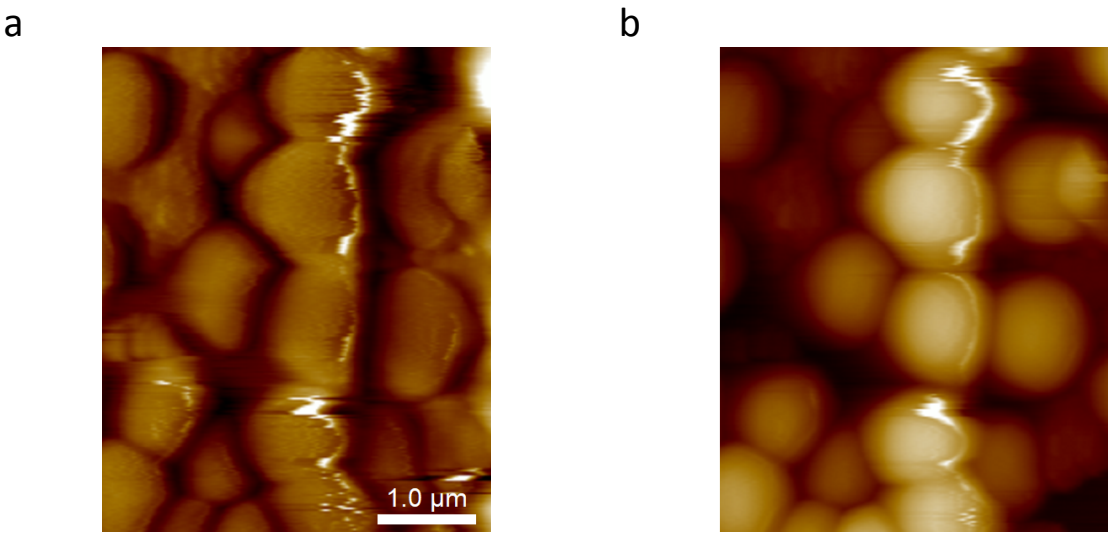

Figure 6.8. SA cells immobilised in, or on patterned silicon. AFM height images show a collection of cells in growth medium at two different time points, during repeated scanning. (a) Initial time point (b) Absence of growth after 15 h. No obvious changes in morphology, or growth were observed throughout. Each scan lasted ~ 2 min and all cells remained immobilised and stable. Panel (b) image has been shifted to the left to correct for lateral drift. Both images were cropped. *Z* scale = (a) 1.57 µm (b) 1.35 µm. Scan size = 5 x 5 µm.

Both the ~ 1 µm diameter holed PDMS and ~ 1 µm diameter holed silicon wafer enabled sufficient immobilisation for repeat AFM scans and the gathering of F-D curves for mechanical property characterisation.

6.2.2 Elastic modulus of whole cell *Staphylococcus aureus*

Following the tip angle characterisation work performed in Chapters 4 and 5, the elastic modulus values described here were obtained by using the Sneddon contact model, with a cone half-angle of 85° (Chapter 3.9.5). The contact model was fitted to the F-D curve at 10 nm of indentation, which was just under half of the ~ 25 nm thickness of the cell wall PG determined by TEM (Fig. 6.9). SA cells were seeded on PDMS or silicon wafers and quantitatively imaged at 37° C in growth medium. 58 cells were analysed, with 10 F-D curves per cell. The mean modulus value from the 10 F-D curves per cell was calculated, thus each inputted mean is the cumulative mean of each individual cell. Each of these values was used to form a data distribution, and statistically analysed. Both the standard deviation, SD and standard error, SE are presented. The SD values appear first in the descriptions and on the scatter plot error bars. As these data were derived from the cumulative mean values, the SE is a better indicator of the variability in the sample means. Additionally, the median values are also presented. These data also appear tabulated, for easier visualisation.

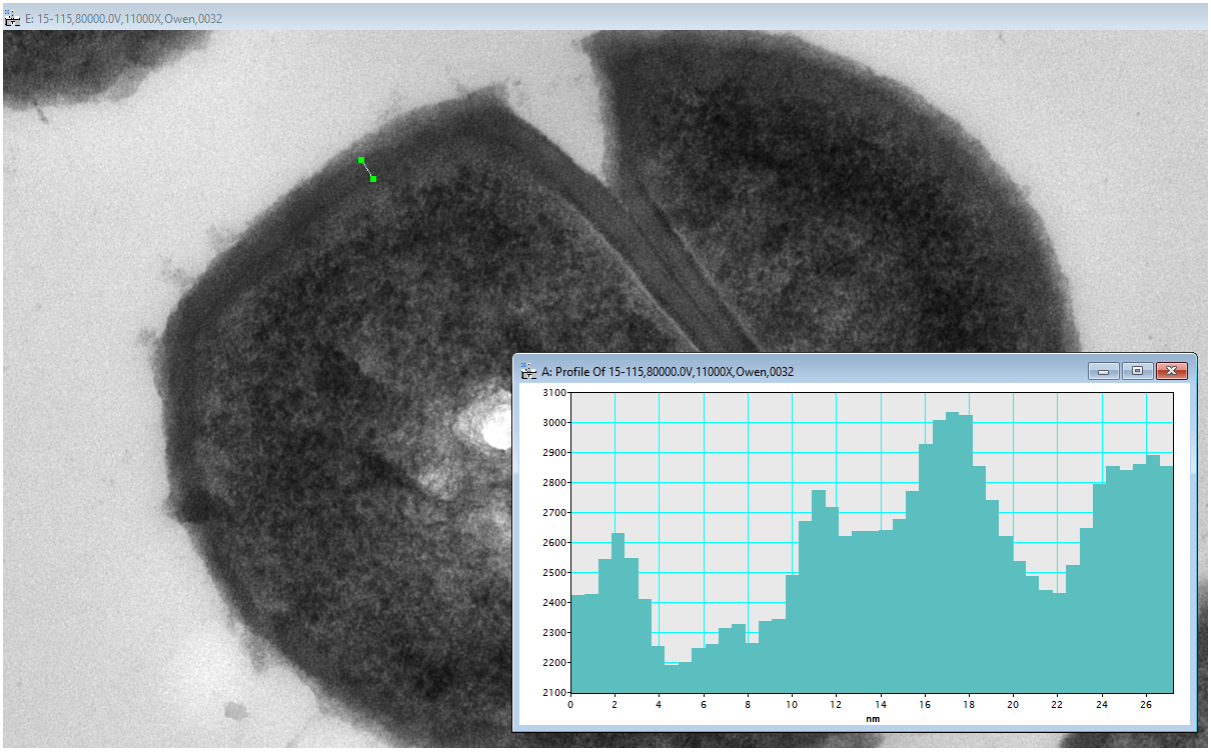

Figure 6.9. Cell wall PG thickness. Representative TEM micrograph of the SA cell wall PG thickness. A line profile and inset measurement shows a thickness ~ 25 nm. The 'fluffy' outer coat is thought to be the WTA as depicted in Fig. 1.1 c.

6.2.2.1 Modulus at time = 0

For cells analysed at an initial time point, t = 0 h, a mean elastic modulus value of 0.31 ± 0.20 MPa was obtained. The large SD reflects the heterogeneity of the samples. Because these data were calculated from the combined means of each set of 10 F-D curves, the standard error about the mean is a better indicator of variability. SE = 0.03. The median elastic modulus was 0.26 MPa.

Mean (MPa)	SD (MPa)	SE (MPa)	Median (MPa)
0.31	0.20	0.03	0.26

Table 6.1. t = 0 h modulus for whole cell SA. The values were calculated by Sneddon contact model fitting at 10 nm indentations of AFM F-D curves. A single average from 10 F-D curves per cell was analysed. *n* = 58 cells and therefore averages calculated from 580 F-D curves.

6.2.2.2 Modulus at time = 1.5 h

For cells analysed at the time point, t = ~ 1.5 h, a mean elastic modulus value of 0.30 ± 0.16 MPa was obtained. SE = 0.02. The median elastic modulus was 0.28 MPa.

Mean (MPa)	SD (MPa)	SE (MPa)	Median (MPa)
0.30	0.16	0.02	0.28

Table 6.2. t = 1.5 h modulus for whole cell SA. The values were calculated by Sneddon contact model fitting at 10 nm indentations of AFM F-D curves. A single average from 10 F-D curves per cell was analysed. *n* = 58 cells and therefore averages calculated from 580 F-D curves.

The scatter plots (Fig. 6.10) show a dot for each cumulative SA cell mean. The error bars show the combined total mean ± SD. The frequency distribution histograms (inset) show the distribution of values of the SA cell means, with a least squares Gaussian fit. (a) The data are skewed to the right, skewness = 1.6, R^2 = 0.93. (b) The data are skewed to the right, skewness = 1.4, R^2 = 0.95.

6.2.2.3 Comparing elastic modulus data for both time points

Both time points, t = 0 and t = ~ 1.5 h were compared against each other with a non-parametric unpaired t-test (Fig. 6.11) (Chapter 3.9.8). The differences were not considered significant. P value = 0.7726.

6.2.3 Stiffness of whole cell *Staphylococcus aureus*

Despite the steps taken in this study to minimise the potential drawbacks of the Hertz/Sneddon elastic contact models, we further analysed the F-D curves using simple linear tangents to the curves at 10 nm of indentation (Chapter 3.9.3). The same 58 cells analysed for their elastic modulus were used for stiffness characterisation. Data is presented in the same manner, with mean stiffness, SD, SE and median stiffness values reported.

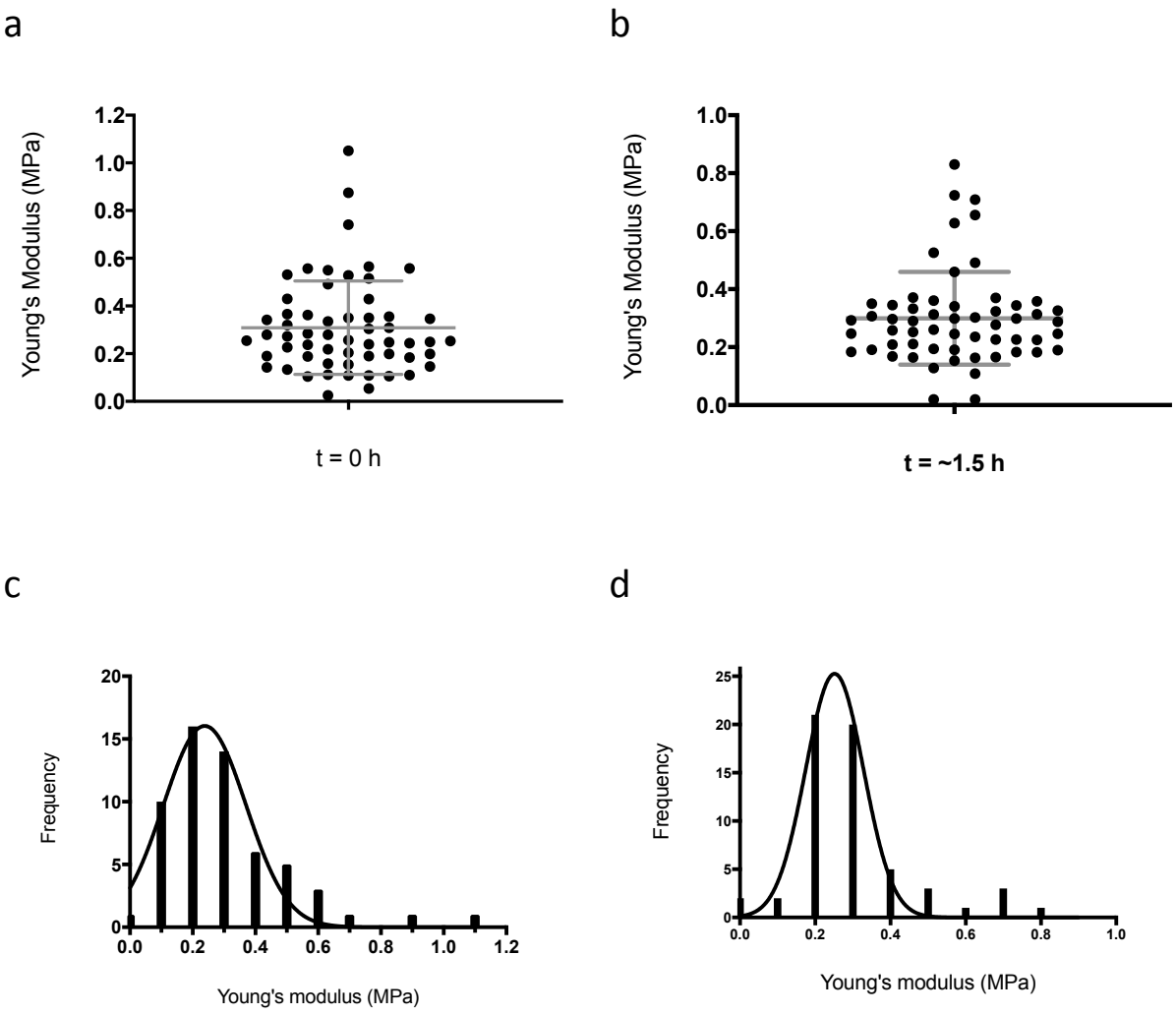

Figure 6.10. Elastic modulus changes over time. (a, b) Scatter plots show the distribution of mean elastic modulus of SA cells in growth medium at 37° C. Error bars show mean ± SD. Each dot represents an individual cell, with the cumulative mean calculated from 10 F-D curves per cell. (c, d) Frequency distribution histogram of the same data, fitted with a least squares Gaussian fit. (a) t = 0 h. Elastic modulus is 0.31 ± 0.20 MPa. (b) t = 1.5 h. Elastic modulus is 0.30 ± 0.16 MPa. *n* = 58 cells from 6 independent experiments.

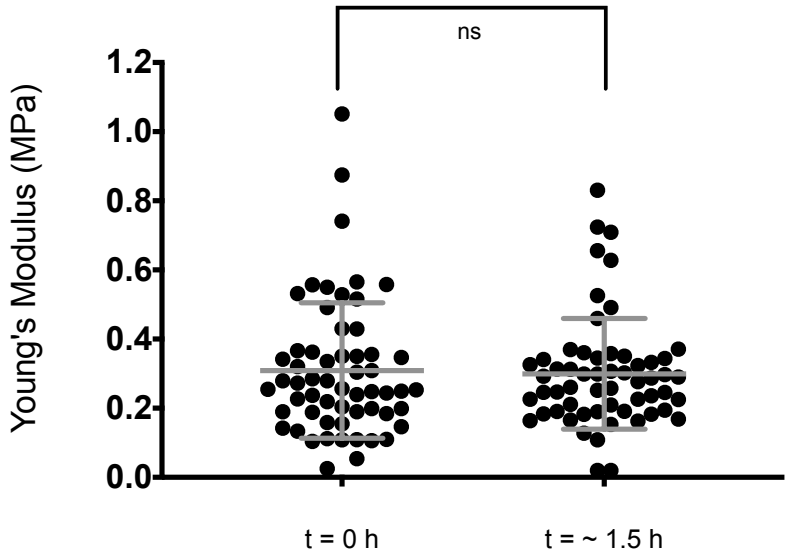

Figure 6.11. Elastic modulus comparison at t = 0 h and t = ~ 1.5 h. Error bars show mean ± SD. Each dot represents an individual cell, with the cumulative mean calculated from 10 F-D curves per cell. Elastic modulus is 0.31 ± 0.20 MPa and 0.30 ± 0.16 MPa respectively. Data were considered not significant. P value = 0.7726. *n* = 58 cells from 6 experiments.

6.2.3.1 Stiffness at time = 0

For cells analysed at an initial time point, t = 0 h, a mean stiffness value of 62.0 ± 44 nN/µm (0.062 ± 0.044 N/m) was obtained. Again, the large SD reflects the heterogeneity of the samples. SE = 5.8. The median stiffness was 54 nN/µm.

Mean (nN/µm)	SD (nN/µm)	SE (nN/µm)	Median (nN/µm)
62	44	5.8	54

Table 6.3. t = 0 stiffness for whole cell SA. The values were calculated by applying linear tangents to the curve, at 10 nm indentations of AFM F-D curves. A single average from 10 F-D curves per cell was analysed. *n* = 58 cells and therefore averages calculated from 580 F-D curves.

6.2.3.2 Stiffness at time = 1.5 h

For cells analysed at the time point, t = ~ 1.5 h, a mean stiffness value of 63.0 ± 42 nN/µm (0.063 ± 0.042 N/m) was obtained. SE = 5.5. The median stiffness was 56 nN/µm.

Mean (nN/µm)	SD (nN/µm)	SE (nN/µm)	Median (nN/µm)
63	42	5.5	56

Table 6.4. t = 1.5 h stiffness for whole cell SA. A single average from 10 F-D curves per cell was analysed. *n* = 58 cells and therefore averages calculated from 580 F-D curves.

The scatter plots (Fig. 6.12) show a dot for each cumulative SA cell mean. The error bars show the combined total mean ± SD. The frequency distribution histograms (inset) show the distribution of values of the SA cell means, with a least squares Gaussian fit. (a) The data are skewed to the right, skewness = 1.6, R^2 = 0.86. (b) The data are skewed to the right, skewness = 2.4, R^2 = 0.93.

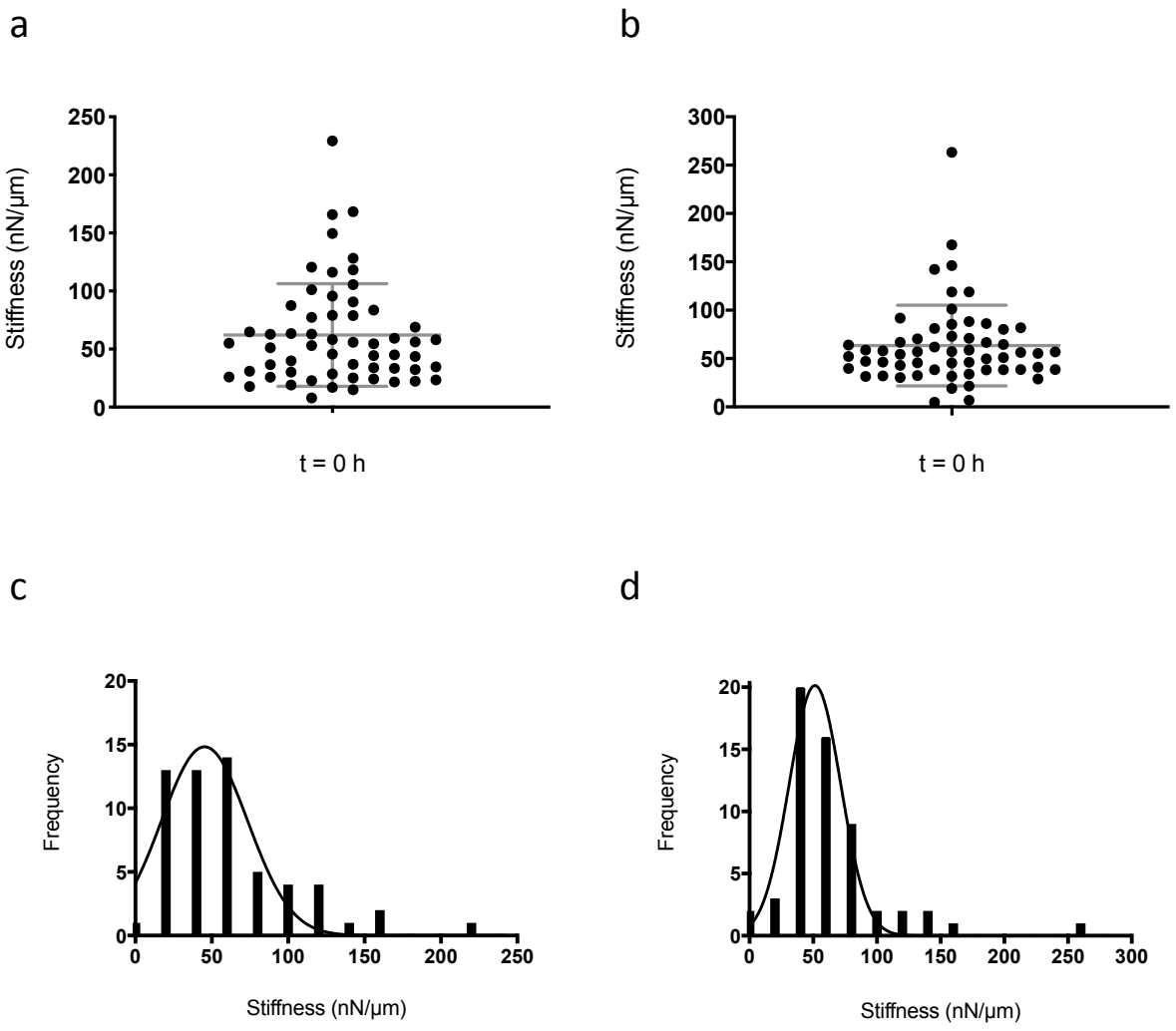

Figure 6.12. Stiffness changes over time. (a, b) Scatter plots show the distribution of mean stiffness of SA cells in growth medium at 37° C. Error bars show mean ± SD. Each dot represents an individual cell, with the cumulative mean calculated from 10 F-D curves per cell. (c, d) Frequency distribution histogram of the same data, fitted with a least squares Gaussian fit. (a) t = 0 h. Stiffness is 62 ± 44 nN/µm. (b) t = 1.5 h. Stiffness is 63 ± 42 nN/µm. *n* = 58 cells from 6 independent experiments.

6.2.3.3 Comparing stiffness data for both time points

Both time points, t = 0 and t = ~ 1.5 h were compared against each other with a non-parametric unpaired t-test (Fig. 6.13) (Chapter 3.9.8). The differences were not considered significant. P value = 0.8751

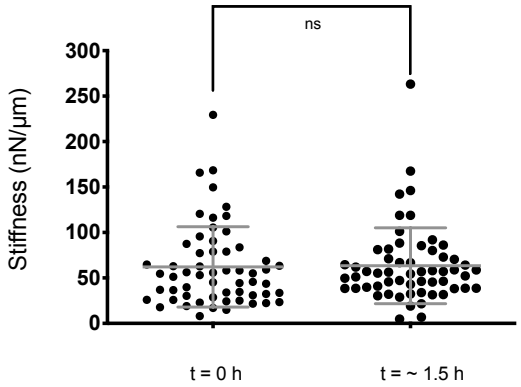

Figure 6.13. Stiffness comparison at t = 0 h and t = ~ 1.5 h. Error bars show mean ± SD. Stiffness is 62 ± 44 nN/µm and 63 ± 42 nN/µm respectively. Data were considered not significant. P value = 0.8751. *n* = 58 cells from 6 independent experiments.

6.2.4 Elastic modulus of extracted cell wall sacculi

Following the methods used for characterising the elastic modulus values of whole cell SA, the elastic modulus values described here were obtained by using the Sneddon contact model, with a cone half-angle of 85° (Chapter 3.9.5). The contact model was fitted to the F-D curve at 10 nm of indentation, or to the full curve if the fitting led to an incorrect estimation of modulus (Chapter 3.9.6). Sacculi were immobilised on glass slides and hydrated in buffer (Chapter 3.21). 59 sacculi were analysed, with 10 F-D curves per sacculi. The mean modulus value from the 10 F-D curves per sacculi was calculated, thus each inputted mean is the mean of each individual sacculi. Each of these values was used to form a data distribution, and statistically analysed. Both the standard deviation, SD and standard error, SE are presented. The SD values appear first in the descriptions and on the scatter plot error bars. Sacculi mean elastic modulus was 0.18 ± 0.074 MPa. SE = 0.0096. The median elastic modulus was 0.15 MPa (Fig. 6.14a).

Mean (MPa)	SD (MPa)	SE (MPa)	Median (MPa)
0.18	0.074	0.0096	0.15

Table 6.5. Elastic modulus for SA extracted cell wall sacculi. The values were calculated by Sneddon contact model fitting at 10 nm indentations of AFM F-D curves. A single average from 10 F-D curves per cell was analysed. *n* = 59 sacculi and therefore averages calculated from 590 F-D curves.

6.2.4.1 Comparison of elastic modulus for whole cell and sacculi

Both whole cell SA (time point, t = 0 h) and extracted cell wall sacculi were compared against each other with a non-parametric unpaired t-test (Chapter 3.9.8) (Fig. 6.14b). The differences were highly statistically significant. P value = <0.0001. Whole cell SA at time point t = ~ 1.5 h was not used in the comparison, as it is not significantly different against whole cell SA t = 0 h.

The scatter plot shows a dot for each cumulative SA cell mean. The error bars show the combined total mean ± SD. The frequency distribution histogram (inset) shows the distribution of values of the sacculi means, with a least squares Gaussian fit. The data are skewed to the right, skewness = 1.6, R^2 = 0.91.

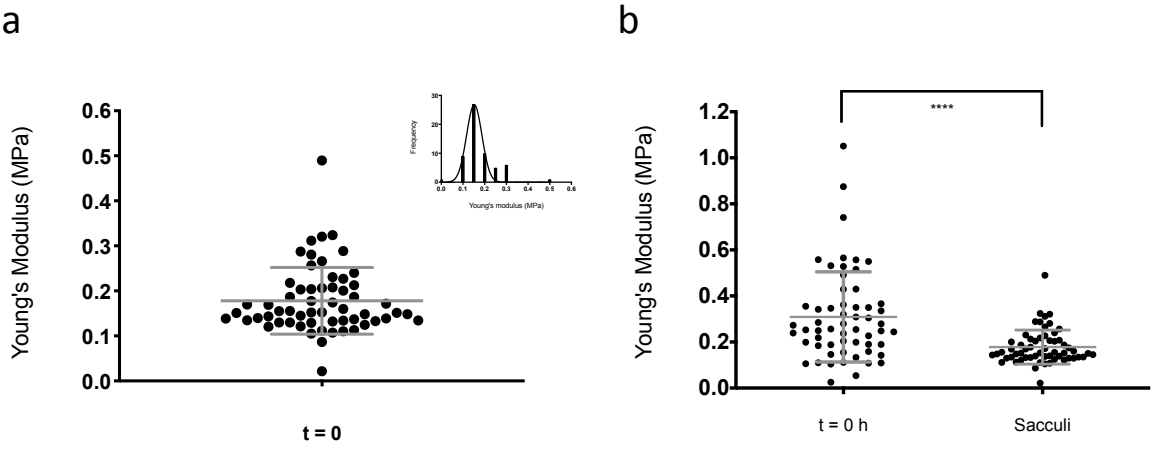

Figure 6.14. Elastic modulus of SA sacculi. Scatter plot shows the distribution of mean elastic modulus of SA sacculi in imaging buffer at room temperature. Error bars show mean ± SD. Each dot represents an individual sacculus, with the cumulative mean calculated from 10 F-D curves per sacculus. (a) Elastic modulus is 0.18 ± 0.074 MPa. (inset) Frequency distribution histogram of the same data, fitted with a least squares Gaussian fit. (b) Whole cell at t = 0 h vs. extracted cell wall sacculi. Elastic modulus is 0.31 ± 0.20 MPa for whole cell wall and 0.18 ± 0.074 MPa for extracted sacculi respectively. Data were considered highly significant. P value = <0.0001. *n* = 58 cells from 6 independent experiments and 59 sacculi from 4 independent experiments respectively.

6.2.4.2 Stiffness of extracted cell wall sacculi

A mean stiffness value of 38 ± 32 nN/µm (0.038 ± 0.032 N/m) was obtained. Again, the large SD reflects the heterogeneity of the samples. SE = 4.2. The median stiffness was 25 nN/µm.

Mean (nN/µm)	SD (nN/µm)	SE (nN/µm)	Median (nN/µm)
38	32	4.2	25

Table 6.6. Stiffness measurements for SA extracted cell wall sacculi. The values were calculated by applying linear tangents to the curve, at 10 nm indentations of AFM F-D curves. A single average from 10 F-D curves per cell was analysed. *n* = 59 sacculi and therefore averages calculated from 590 F-D curves.

The scatter plot (Fig. 6.15) shows a dot for each cumulative sacculi mean. The error bars show the combined total mean ± SD. The frequency distribution histogram (inset) shows the distribution of values of the sacculi means, with a least squares Gaussian fit. The data are skewed to the right, skewness = 3.0, R^2 = 0.95.

6.2.4.3 Comparison of stiffness for whole cell and sacculi

Both whole cell SA (time point, t = 0 h) and extracted cell wall sacculi were compared against each other with a non-parametric unpaired t-test (Chapter 3.9.8) (Fig. 6.15b). The differences were highly statistically significant. P value = 0.0008. Whole cell SA at time point t = ~ 1.5 h was not used in the comparison, as it is not significantly different against whole cell SA t = 0 h.

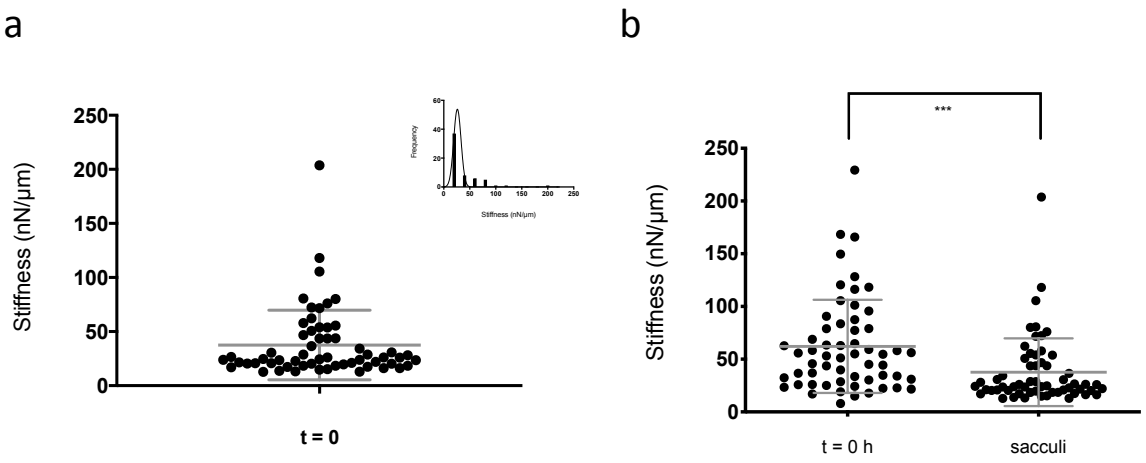

Figure 6.15. Stiffness of SA sacculi. Scatter plot shows the distribution of mean stiffness of SA sacculi in imaging buffer at room temperature. Error bars show mean ± SD. Each dot represents an individual sacculus, with the cumulative mean calculated from 10 F-D curves per sacculus. (a) Stiffness is 38 ± 32 nN/µm. (inset) Frequency distribution histogram of the same data, fitted with a least squares Gaussian fit. (b) Whole cell at t = 0 h vs. extracted cell wall sacculi. Stiffness is 62 ± 44 nN/µm for whole cell wall at t = 0 h and 38 ± 32 nN/µm for extracted sacculi respectively. Data were considered highly significant. P value = 0.0008. *n* = 58 cells from 6 independent experiments and 59 sacculi from 4 independent experiments.

6.2.5 Elastic modulus and stiffness of methicillin-challenged sacculi

Whole cells were grown in the presence of methicillin for 30, 60 and 120 min and extracted cell walls were generated as previously described (Chapter 3.20.2).

Following the methods used for characterising the elastic modulus values of whole cell SA, the elastic modulus values described here were obtained by using the Sneddon contact model, with a cone half-angle of 85° (Chapter 3.9.5). The contact model was fitted to the total F-D curve as 10 nm of indentation lead to incorrect fitting, and thus the reported modulus values (Chapter 3.9.6). Tangents were fitted to the whole curve at 10 nm of indentation. Sacculi were immobilised on glass slides and hydrated in buffer (Chapter 3.21). 10 sacculi were analysed, with 10 F-D curves per sacculi. The mean modulus value from the 10 F-D curves per sacculi was calculated, thus each inputted mean is the mean of each

individual sacculi. Each of these values was used to form a data distribution, and statistically analysed. Both the standard deviation, SD and standard error, SE are presented. The SD values appear first in the descriptions and on the scatter plot error bars. Native sacculi mean modulus was 0.18 ± 0.0096 MPa. Native mean stiffness was 38 ± 4.2 nN/µm.

6.2.5.1 30 min methicillin modulus

Sacculi mean elastic modulus was 0.18 ± 0.040 MPa. SE = 0.013. The median elastic modulus was 0.19 MPa.

Mean (MPa)	SD (MPa)	SE (MPa)	Median (MPa)
0.18	0.040	0.013	0.19

Table 6.7. Elastic modulus for SA extracted cell wall sacculi following methicillin challenge for 30 min. The mean and median values were calculated by Sneddon contact model fitting of AFM F-D curves. A single average from 10 F-D curves per cell was analysed. *n* = 10 sacculi and therefore averages calculated from 100 F-D curves.

The scatter plot (Fig. 6.16a) shows a dot for each cumulative SA cell sacculi mean. The error bars show the combined total mean ± SD. The frequency distribution histogram (Fig. 6.16b) shows the distribution of values of the sacculi means, with a least squares Gaussian fit. The data are skewed to the left, skewness = -1.7, R^2 = 0.89.

6.2.5.2 60 min methicillin modulus

Sacculi mean elastic modulus was 0.068 ± 0.014 MPa. SE = 0.0044. The median elastic modulus was 0.071 MPa.

Mean (MPa)	SD (MPa)	SE (MPa)	Median (MPa)
0.068	0.014	0.0044	0.071

Table 6.8. Elastic modulus for SA extracted cell wall sacculi following methicillin challenge for 60 min. The mean and median values were calculated by Sneddon contact model fitting of AFM F-D curves. A single average from 10 F-D curves per cell was analysed. *n* = 10 sacculi and therefore averages calculated from 100 F-D curves.

The scatter plot (Fig. 6.17a) shows a dot for each cumulative SA cell sacculi mean. The error bars show the combined total mean ± SD. The frequency distribution histogram (Fig. 6.17b) shows the distribution of values of the sacculi means, with a least squares Gaussian fit. The data are skewed to the left, skewness = -1.8, R^2 = 0.96.

6.2.5.3 120 min methicillin modulus

Sacculi mean elastic modulus was 0.065 ± 0.030 MPa. SE = 0.0094. The median elastic modulus was 0.068 MPa.

Mean (MPa)	SD (MPa)	SE (MPa)	Median (MPa)
0.065	0.030	0.0094	0.068

Table 6.9. Elastic modulus for SA extracted cell wall sacculi following methicillin challenge for 120 min. The mean and median values were calculated by Sneddon contact model fitting of AFM F-D curves. A single average from 10 F-D curves per cell was analysed. *n* = 10 sacculi and therefore averages calculated from 100 F-D curves.

The scatter plot (Fig. 6.18a) shows a dot for each cumulative SA cell sacculi mean. The error bars show the combined total mean ± SD. The frequency distribution histogram (Fig. 6.18b) shows the distribution of values of the sacculi means, with a least squares Gaussian fit. The data are skewed to the right, skewness = 0.33, R^2 = -0.59.

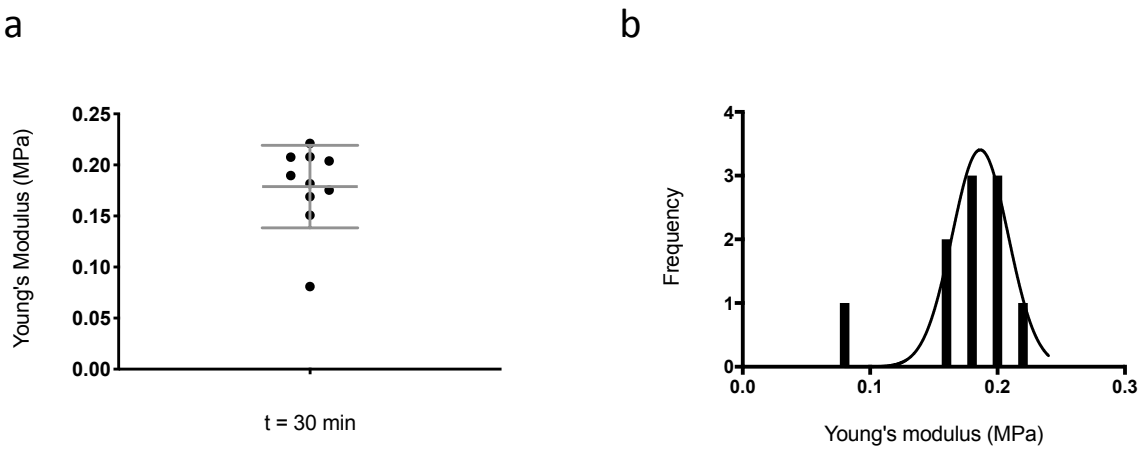

Figure 6.16. Elastic modulus of 30 min methicillin treated SA sacculi. (a) Scatter plot shows the distribution of mean elastic modulus of SA sacculi in imaging buffer at room temperature. Error bars show mean ± SD. Each dot represents an individual sacculus, with the cumulative mean calculated from 10 F-D curves per sacculus. (b) Frequency distribution histogram of the same data, fitted with a least squares Gaussian fit. Elastic modulus is 0.18 ± 0.040 MPa. *n* = 10 sacculi from a single experiment.

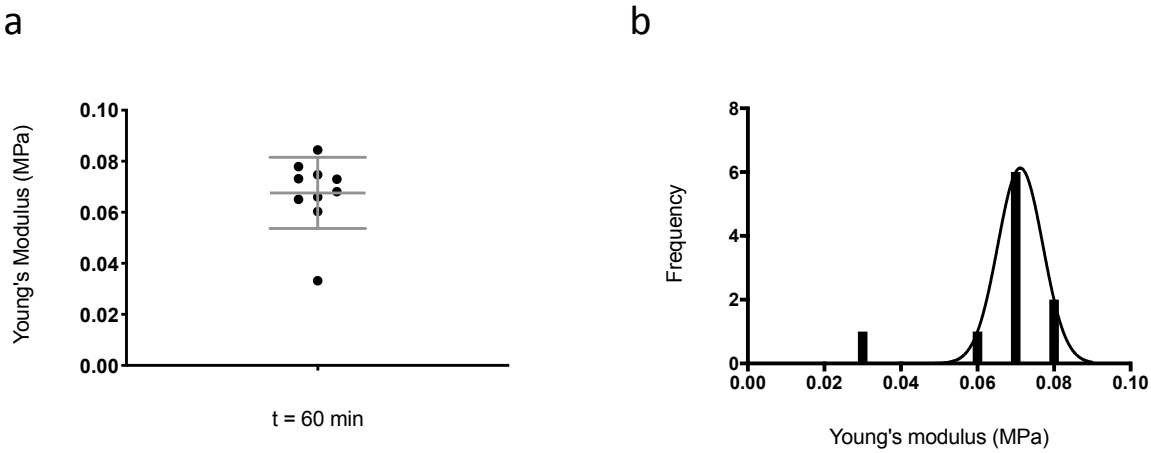

Figure 6.17. Elastic modulus of 60 min methicillin treated SA sacculi. (a) Scatter plot shows the distribution of mean elastic modulus of SA sacculi in imaging buffer at room temperature. Error bars show mean ± SD. Each dot represents an individual sacculus, with the cumulative mean calculated from 10 F-D curves per sacculus. (b) Frequency distribution histogram of the same data, fitted with a least squares Gaussian fit. Elastic modulus is 0.068 ± 0.014 MPa. *n* = 10 sacculi from a single experiment.

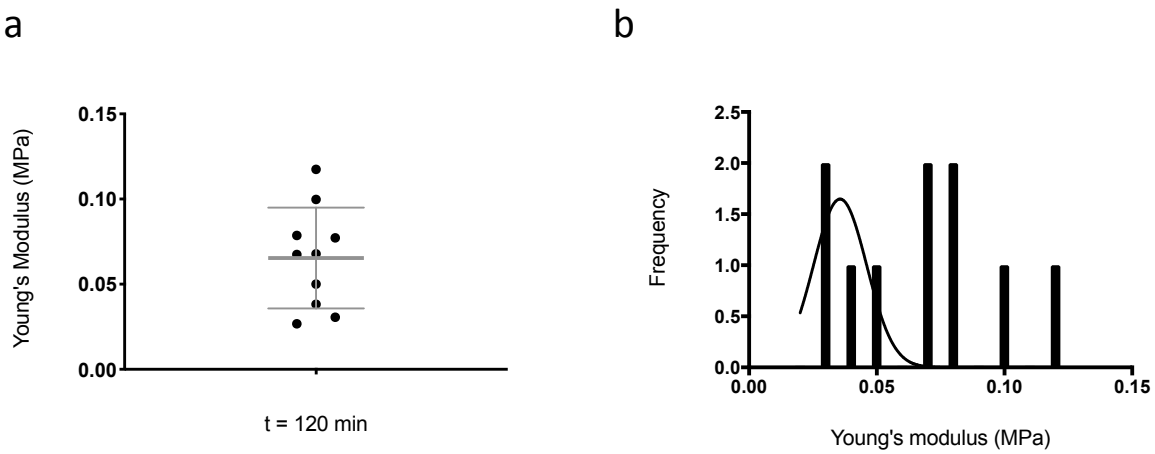

Figure 6.18. Elastic modulus of 120 min methicillin treated SA sacculi. (a) Scatter plot shows the distribution of mean elastic modulus of SA sacculi in imaging buffer at room temperature. Error bars show mean ± SD. Each dot represents an individual sacculus, with the cumulative mean calculated from 10 F-D curves per sacculus. (b) Frequency distribution histogram of the same data, fitted with a least squares Gaussian fit. Elastic modulus is 0.065 ± 0.030 MPa. *n* = 10 sacculi from a single experiment.

As the frequency distribution values from the 120 min methicillin sacculi are more dispersed (Fig. 6.18b) they do not follow a Gaussian distribution. By re-plotting the data from the 100 obtained F-D curves, rather than the 10 cumulative mean data, a Gaussian distribution is observed (Fig. 6.19). The data are skewed to the right, skewness = 1.3, R^2 = 0.85.

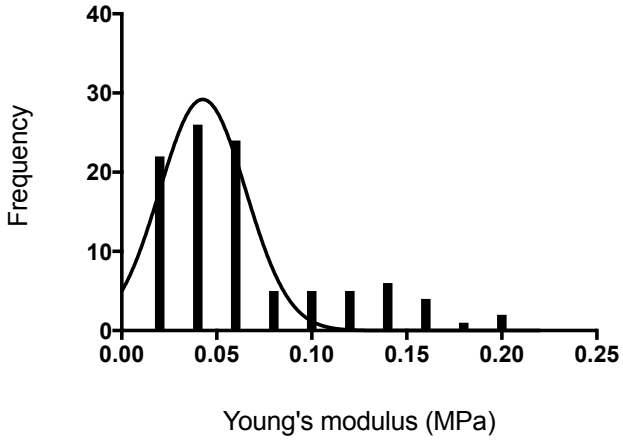

Figure 6.19. Frequency distribution of 120 min methicillin treated SA sacculi. When plotting the distribution of 10 F-D curve means the distribution was not Gaussian. By re-plotting the data from each of the 100 F-D curves the distribution becomes Gaussian.

6.2.5.4 Stiffness of 30 min methicillin-challenged sacculi

A mean stiffness value of 28 ± 6.5 nN/µm (0.028 ± 0.0065 N/m) was obtained. SE = 2.0. The median stiffness was 30 nN/µm.

Mean (nN/µm)	SD (nN/µm)	SE (nN/µm)	Median (nN/µm)
28	6.5	2.0	30

Table 6.10. Stiffness measurements for 30 min methicillin treated SA sacculi. The mean and median values were calculated by applying linear tangents to the curve, at 10 nm indentations of AFM F-D curves. A single average from 10 F-D curves per cell was analysed. *n* = 10 sacculi and therefore averages calculated from 100 F-D curves.

The scatter plot (Fig. 6.20a) shows a dot for each cumulative sacculus mean. The error bars show the combined total mean ± SD. The frequency distribution histogram (Fig. 6.20b) shows the distribution of values from the 100 F-D curves, with a least squares Gaussian fit. The distribution was not Gaussian from the 10 cumulative mean F-D curves. The data are skewed to the right, skewness = 0.64, R^2 = 0.84.

6.2.5.5 Stiffness of 60 min methicillin-challenged sacculi

A mean stiffness value of 14 ± 2.7 nN/µm (0.014 ± 0.0027 N/m) was obtained. SE = 0.85. The median stiffness was 14 nN/µm.

Mean (nN/µm)	SD (nN/µm)	SE (nN/µm)	Median (nN/µm)
14	2.7	0.85	14

Table 6.11. Stiffness measurements for 60 min methicillin treated SA sacculi. The mean and median values were calculated by applying linear tangents to the curve, at 10 nm indentations of AFM F-D curves. A single average from 10 F-D curves per cell was analysed. *n* = 10 sacculi and therefore averages calculated from 100 F-D curves.

The scatter plot (Fig. 6.21a) shows a dot for each cumulative sacculi mean. The error bars show the combined total mean ± SD. The frequency distribution histogram (Fig. 6.21b)

shows the distribution of values from the 100 F-D curves, with a least squares Gaussian fit. The data are skewed to the right, skewness = 0.33, R^2 = 0.91.

6.2.5.6 Stiffness of 120 min methicillin-challenged sacculi

A mean stiffness value of 13 ± 2.9 nN/µm (0.013 ± 0.0029 N/m) was obtained. SE = 0.90. The median stiffness was 14 nN/µm.

Mean (nN/µm)	SD (nN/µm)	SE (nN/µm)	Median (nN/µm)
13	2.9	0.90	14

Table 6.12. Stiffness measurements for 120 min methicillin treated SA sacculi. The mean and median values were calculated by applying linear tangents to the curve, at 10 nm indentations of AFM F-D curves. A single average from 10 F-D curves per cell was analysed. *n* = 10 sacculi and therefore averages calculated from 100 F-D curves.

The scatter plot (Fig. 6.22a) shows a dot for each cumulative sacculus mean. The error bars show the combined total mean ± SD. The frequency distribution histogram (Fig. 6.22b) shows the distribution of values from the 100 F-D curves, with a least squares Gaussian fit. The data are skewed to the left, skewness = -0.082, R^2 = 0.67.

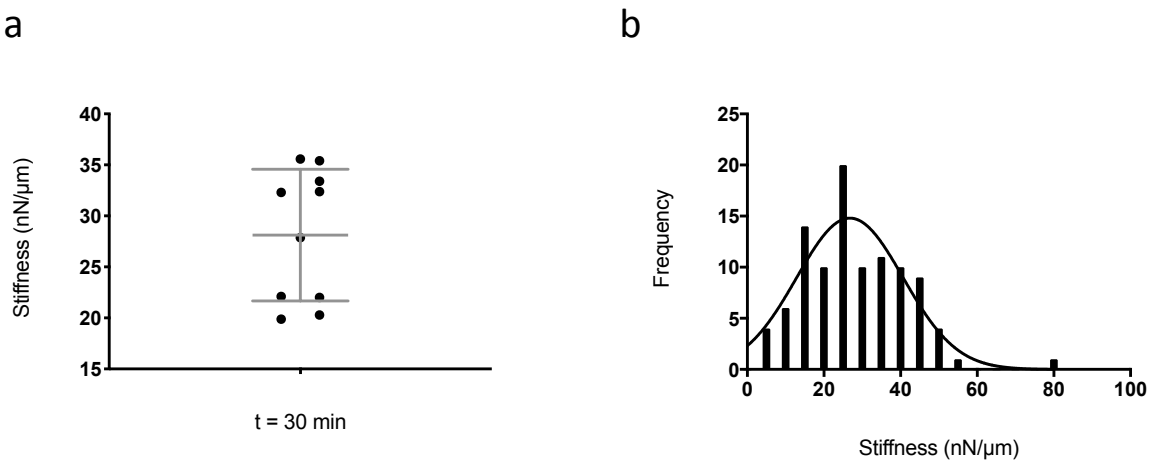

Figure 6.20. Stiffness of 30 min methicillin treated SA sacculi. (a) Scatter plot shows the distribution of mean stiffness of SA sacculi in imaging buffer at room temperature. Error bars show mean ± SD. Each dot represents an individual sacculus, with the cumulative mean calculated from 10 F-D curves per sacculus. (b) Frequency distribution histogram of the 100 F-D curves used to derive the mean stiffness, fitted with a least squares Gaussian fit. Stiffness is 28 ± 6.5 nN/µm. *n* = 10 sacculi from a single experiment.

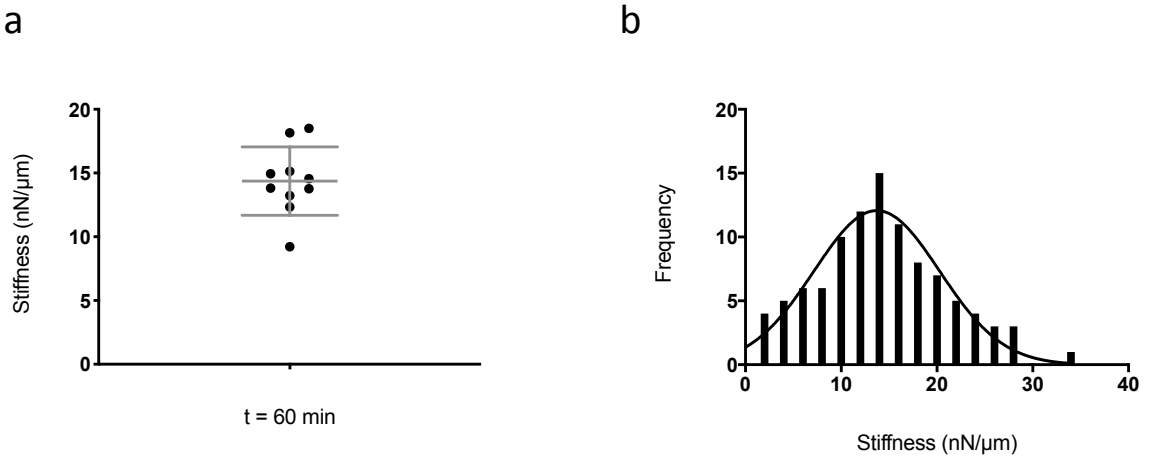

Figure 6.21. Stiffness of 60 min methicillin treated SA sacculi. (a) Scatter plot shows the distribution of mean stiffness of SA sacculi in imaging buffer at room temperature. Error bars show mean ± SD. Each dot represents an individual sacculus, with the cumulative mean calculated from 10 F-D curves per sacculus. (b) Frequency distribution histogram of the 100 F-D curves used to derive the mean stiffness, fitted with a least squares Gaussian fit. Stiffness is 14 ± 2.7 nN/µm. *n* = 10 sacculi from a single experiment.

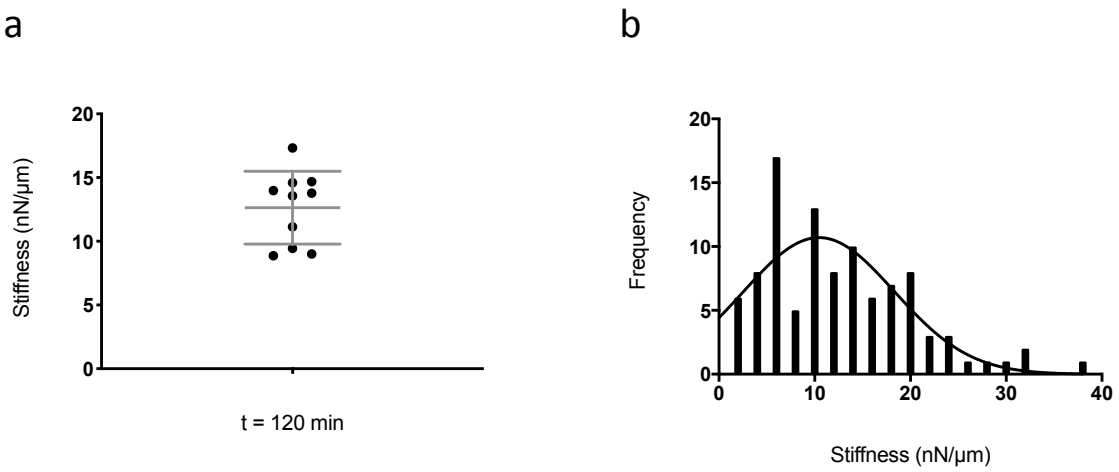

Figure 6.22. Stiffness of 120 min methicillin treated SA sacculi. (a) Scatter plot shows the distribution of mean stiffness of SA sacculi in imaging buffer at room temperature. Error bars show mean ± SD. Each dot represents an individual sacculus, with the cumulative mean calculated from 10 F-D curves per sacculus. (b) Frequency distribution histogram of the 100 F-D curves used to derive the mean stiffness, fitted with a least squares Gaussian fit. Stiffness is 13 ± 2.9 nN/µm. *n* = 10 sacculi from a single experiment.

6.2.5.7 Modulus comparisons of native versus methicillin-challenged sacculi

The elastic moduli of native (unchallenged) sacculi were compared against the methicillin-challenged sacculi at 30, 60 and 120 min time points, using a non-parametric unpaired t-test (Fig. 6.23) (Chapter 3.9.8) Taking the native sacculi as the control, there was no significant difference between the 30 min methicillin-treated sacculi. P value = 0.3175. The 60 min and 120 min methicillin-treated sacculi both showed highly significant differences with a P value = <0.0001 respectively.

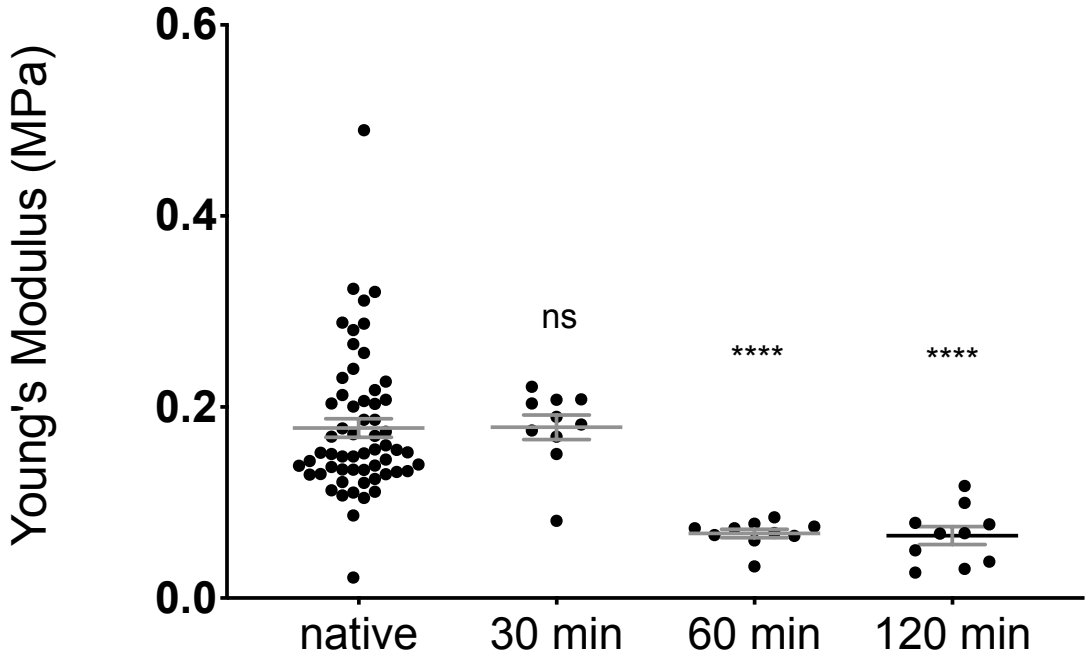

Figure 6.23. Elastic modulus of native SA extracted cell wall sacculi versus methicillin-treated sacculi. Error bars show mean ± SE. Native sacculi modulus = 0.18 ± 0.0096 MPa. 30 min sacculi modulus = 0.18 ± 0.013 MPa. Difference is not significant. P value = 0.3175. 60 min sacculi modulus = 0.068 ± 0.0044 MPa. Difference is highly significant. P value = <0.0001. 120 min sacculi modulus = 0.065 ± 0.0094 MPa. Difference is highly significant. P value = <0.0001.Each column represents the cumulative mean calculated from 10 F-D curves per sacculi. *n* = 59 sacculi from 4 independent experiments (native) and 10 sacculi from a single experiment (30, 60, 120 min).

The elastic moduli of the methicillin-treated sacculi were compared against each other using a non-parametric unpaired t-test. The 30 min sample shows a highly significant median difference of 0.12 MPa against the 60 min sample. P value = <0.0001, and a highly significant median difference of 0.12 MPa against the 120 min sample. P value = <0.0001. The 60 min and 120 min samples displayed no significant difference to each other, with a median difference of 0.0029 MPa. P value = 0.8534.

6.2.5.8 Stiffness comparisons of native versus methicillin-challenged sacculi

The stiffness of native (unchallenged) sacculi was compared against the methicillin-challenged sacculi at 30, 60 and 120 min time points, using a non-parametric unpaired t-test (Fig. 6.24) (Chapter 3.9.8) Taking the native sacculi as the control, there was no significant difference between the 30 min methicillin-treated sacculi. P value = 0.8453. The 60 min and 120 min methicillin-treated sacculi both showed highly significant differences with a P value = <0.0001 respectively.

The stiffness of the methicillin-treated sacculi were compared against each other using a non-parametric unpaired t-test. The 30 min sample shows a highly significant median difference of 16 nN/µm against the 60 min sample. P value = <0.0001, and a highly significant median difference of 16 nN/µm against the 120 min sample. P value = <0.0001. The 60 min and 120 min samples displayed no significant difference to each other, with a median difference of 0.52 nN/µm. P value = 0.2475.

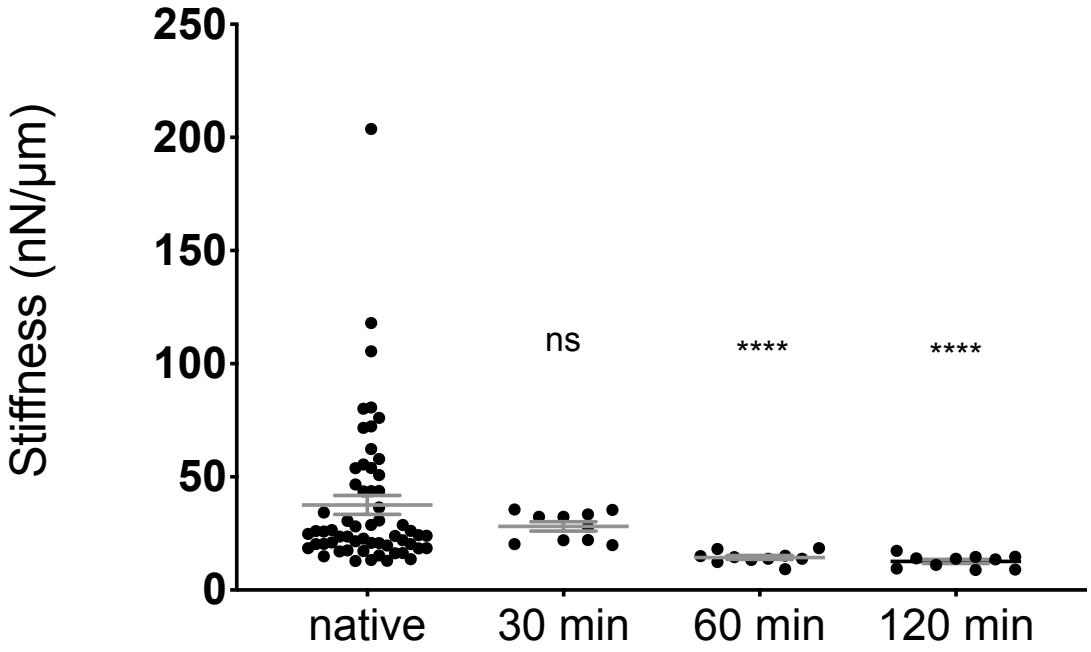

Figure 6.24. Stiffness of native SA extracted cell wall sacculi versus methicillin-treated sacculi. Error bars show mean ± SE. Native sacculi stiffness = 38 ± 4.2 nN/µm. 30 min sacculi modulus = 28 ± 2 nN/µm. Difference is not significant. P value = 0.8453. 60 min sacculi stiffness = 14 ± 0.85 nN/µm. Difference is highly significant. P value = <0.0001. 120 min sacculi stiffness = 13 ± 0.9 nN/µm. Difference is highly significant. P value = <0.0001. Each column represents the cumulative mean calculated from 10 F-D curves per sacculi. *n* = 59 sacculi from 4 independent experiments (native) and 10 sacculi from a single experiment (30, 60, 120 min).

6.2.6 Mechanical property relationship to an applied load

All of the elastic modulus and stiffness data presented thus far were derived from AFM F-D curves at 10 nm of indentation, or as close as possible. As an alternative to the elastic modulus and tangent stiffness data, the mean deflection force required to indent to a given depth gives us an idea of the mechanical properties of the cell wall. Every F-D curve was also statistically analysed within the AFM software to report the actual cantilever deflection force recorded at 10 nm of indentation (Chapter 3.9.4). These data were further statistically analysed for their mean values plus standard deviations and standard errors.

6.2.6.1 Whole cell SA deflection data

As the whole cell at t = 0 h and t = ~ 1.5 h were not significantly different, the t = 0 h only was chosen for analysis. The indentation depth and deflection data were taken from the same 58 cells used for the elastic modulus and stiffness analyses. The mean values from 10 individual F-D curves per cell were used for quantification, thus the 58 cumulative means were derived from 580 F-D curves. From a total applied load of 1 nN, the mean deflection value recorded at 10 ± 0.44 nm (± 0.058 SE) was 135 ± 55 pN (± 7.2 SE). Median indentation value was 10 nm and median deflection was 115 pN. (Fig. 6.25).

6.2.6.2 SA extracted cell wall sacculi deflection data

Extracted cell wall sacculi were analysed as above, with the same 59 sacculi used from the elastic modulus and stiffness analyses. The cumulative means from 10 F-D curves per sacculi were used for quantification, thus they were derived from 590 F-D curves. The mean deflection value recorded at 10 ± 0.17 nm (± 0.023 SE) was 83 ± 30 pN (± 4 SE). Median indentation value was 10 nm and median deflection was 74 pN. (Fig. 6.26).

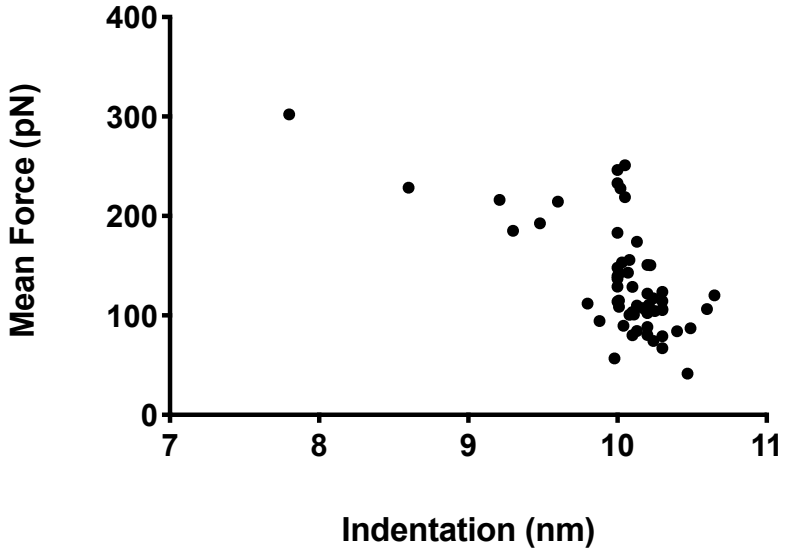

Figure 6.25. Mean cantilever deflection of whole cell SA at 10 nm of indentation. The cantilever deflection of whole cell SA at t = 0 h gives an indication of cell wall mechanical properties. The mean deflection is 135 ± 55 pN (± 7.2 SE) at 10 ± 0.44 nm (± 0.058 SE). Each dot on the scatter plot represents the cumulative mean of 10 F-D curves and therefore averages calculated from 580 F-D curves. *n* = 58 cells from 6 independent experiments.

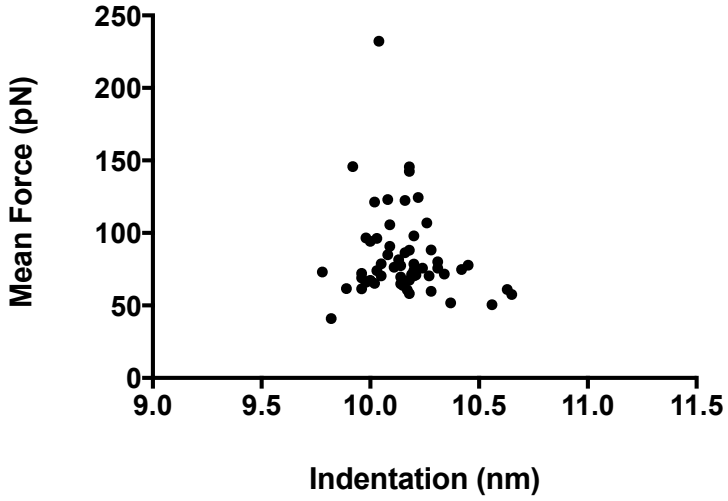

Figure 6.26. Mean cantilever deflection of extracted cell wall sacculi at 10 nm of indentation. The mean deflection is 83 ± 30 pN (± 4 SE) at 10 ± 0.17 nm (± 0.023 SE). Each dot on the scatter plot represents the cumulative mean of 10 F-D curves and therefore averages calculated from 590 F-D curves. *n* = 59 sacculi from 4 independent experiments.

6.2.6.3 Further Hertzian contact model characterisation

The Hertz/Sneddon contact model equations (Chapter 2.10.3) were employed to solve for different terms, to further test the robustness of the reported modulus data. Various properties of the cell wall and extracted cell wall sacculi at 10 nm of indentation were analysed for each term in the Hertz equations to infer the relationships between (i) applied load and actual contact area between the probe and the cell wall; (ii) the likely deformations experienced by the cell wall; and (iii) the magnitude of pressure exerted on the cell wall by the indenter. The AFM tip was regarded as spherical and the Hertzian model equations used were those for contact between two spheres. The numerical values used in the following section are summarised in (Table 6.13).

Parameter	Description	Value (units)	Source
E_1	Young's (elastic) modulus - tip	300 GPa	(Khan, Philip and Hess, 2004)
E_2	Young's (elastic) modulus – cell wall Young's (elastic) modulus – sacculi	300 kPa 180 kPa	This study
E^*	Reduced elastic modulus – cell wall Reduced elastic modulus – sacculi	400 kPa 240 kPa	This study
v_1	Poisson's ratio - tip	0.28	(Vahdat *et al.*, 2013)
v_2	Poisson's ratio – cell wall	0.5	(Pogoda *et al.*, 2017)
D_1	Diameter - tip	80 nm	This study
D_2	Diameter – whole cell	1.2 µm	This study
r_1	Radius – tip	40 nm	This study
r_2	Radius – whole cell	0.6 µm	This study
R	Effective radius	37.5 nm	This study
F	Force applied	135 pN 1 nN 5 nN	This study
t	Thickness – cell wall	25 nm	This study

Table 6.13. Hertzian contact model parameters used for numerical calculations.

6.2.7 Whole cell SA

6.2.7.1 Contact area, deformation and pressure

Using Eq. (9), and the calculations from section 6.2.6.1, the mean applied force on the whole cell wall was 135 pN. Using the SEM micrograph data (Chapter 5) the AFM tip diameter was considered to be 80 nm (radius 40 nm). The estimated contact area between the tip and the cell wall was calculated using Eq. (18). At an applied force of 135 pN the area was 21.2 nm. This increased to 41.3 nm at 1 nN force and 70.6 nm at 5 nN force. The displacement, using Eq. (19) was calculated as 12.0 nm with an applied force of 135 pN, 45.4 nm with an applied force of 1 nN and 133 nm at an applied force of 5 nN. The maximum pressure applied to the cell wall at a range of forces was determined using Eq. (14). Taking the area calculations derived using Eq. (18) above, the maximum pressure exerted on the cell wall at 135 pN was

143 kPa (1.33 atmospheres). This increased to 280 kPa (2.76 atmospheres) at a 1 nN applied force, and 479 kPa (4.73 atmospheres) at a 5 nN force.

6.2.7.2 Cell spring constant estimation

We can infer the spring constant of the bacterium by using the known radius of the indenter and also the estimated contact area between the indenter and the SA cell surface. An applied force of 135 pN over an area of 40 nm would lead to a value of 0.003 N/m according to $135x10^{-12}$ N x $2.5x10^{7}$ m. This increases to 0.025 N/m or 0.125 N/m at applied forces of 1 or 5 nN respectively. The same forces applied over a contact area calculated above (rather than the 40 nm tip radius) leads to a spring constant of 0.006 N/m, 0.024 N/m and 0.07 N/m for applied forces of 135 pN, 1 nN and 5 nN respectively.

6.2.8 Standard, modified and 85° cone angle comparisons

The assumed conical half-angle in relation to the indentation depth (Table 4.8) was tested against the software default half-angle setting. For example, a F-D curve at 35 nm of indentation was fitted with a 70° half-angle. Additionally, the cell wall data at 10 nm of indentation were analysed with an 85° half-angle. Three cells from 2 independent experiments were analysed and the means were calculated from 10 F-D curves per cell. Whole cell mean elastic modulus was 33 ± 15 MPa (± 2.7 SE), using the default cone angle, from a mean indentation of 30 ± 9.4 nm (± 1.7 SE), at a 5.8 ± 0.44 nN (± 0.31 SE) setpoint. Minimum and maximum indentations were 19 and 51 nm respectively. Applying the modified cone half-angle settings gave a mean elastic modulus of 2.4 ± 0.6 MPa (± 0.11 SE). Median elastic modulus was 2.3 MPa. Cell wall mean elastic modulus was 0.65 ± 0.28 MPa (± 0.05 SE), from a mean indentation of 10 ± 0.24 nm (± 0.044 SE) (Fig. 6.27).

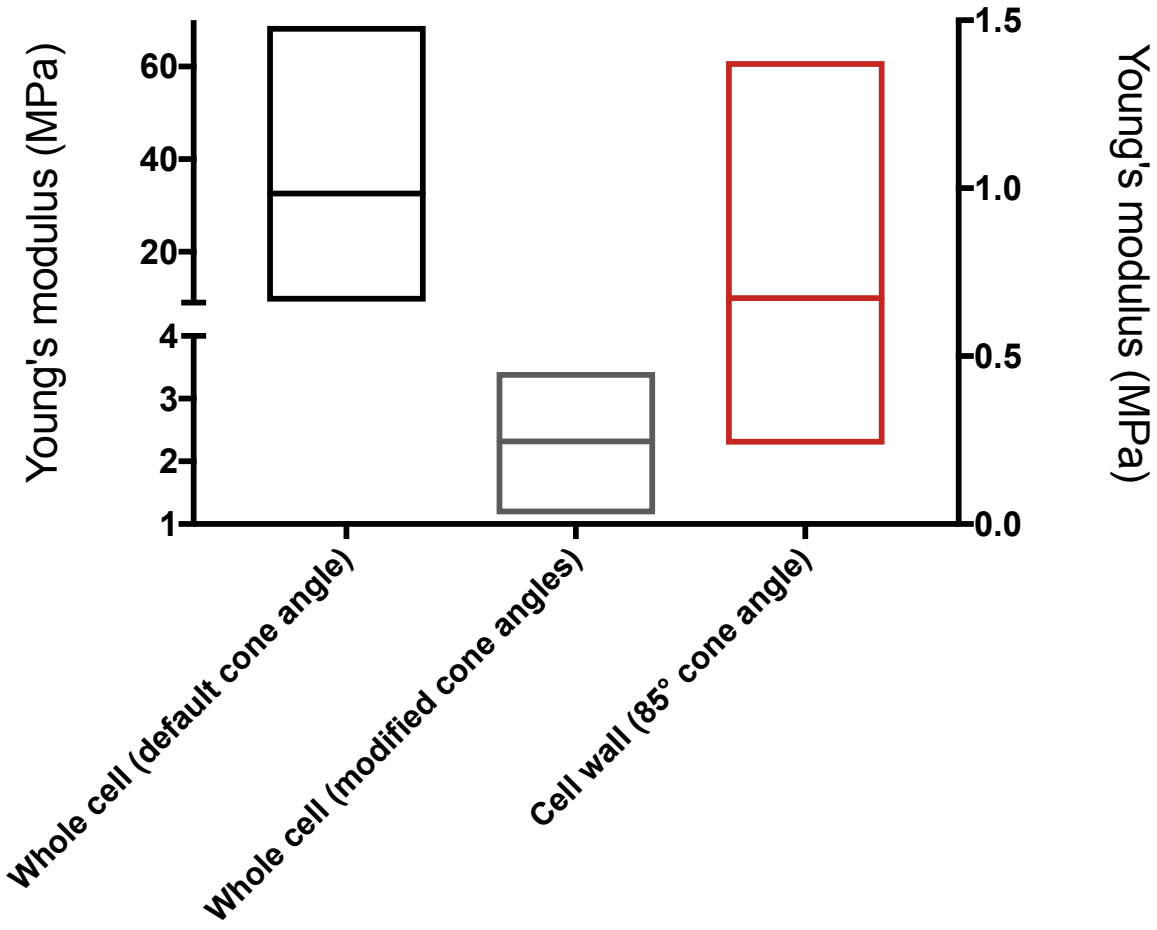

Figure 6.27. SA whole cell cone angle modulus comparisons. The elastic modulus of whole cell SA, using the software default 15° cone half-angle setting was compared against modified cone half-angle settings determined in Table 4.8. Additionally, cell wall data at 10 nm of indentation was assessed. The floating bars represent the minimum to maximum range of data, with the line representing the mean. The default 15° half-angle gave a mean elastic modulus of 33 ± 15 MPa. Modifying the cone half-angles, in relation to different indentation depths, gave an elastic modulus of 2.4 ± 0.6 MPa. Analysing the same data at 10 nm of indentation, using an 85° cone half-angle, gave an elastic modulus of 0.65 ± 0.28 MPa. The left *Y*-axis is split into 2 segments for easier visualisation of the default and modified cone data. The right *Y*-axis shows the modulus values for the 10 nm cell wall data. Data were derived from 10 F-D curves per cell. *n* = 3 cells from 2 independent experiments.

6.3 Discussion

6.3.1 Substrate specificity for cell growth

When choosing a suitable substrate that would allow for both, immobilisation and growth and division, we had hoped that PDMS would fulfil these requirements. It is cheap, easy to produce and widely characterised for its mechanical properties, and biological compatibility. As it is optically transparent we had also intended to perform correlative fluorescence microscopy. PDMS is widely used in microfluidics and has allowed for some growth with *E. coli* (Wang *et al.*, 2010) and SA (Liu *et al.*, 2012), albeit in the absence of an AFM. A custom AFM system was integrated into a PDMS-based microfluidic device, where the authors showed that F-D curves could be obtained (Schoenwald *et al.*, 2010). They gathered F-D curves from a flat glass surface that was sealed within the microfluidic chamber, and tested the laminar flow of 4 µm particles, which showed no adverse interference with the cantilever. They did not test living cells.

The growth of *E.coli* was also observed in an agarose-based microfluidic system (Moffitt, Lee and Cluzel, 2012b). These investigators suggested that PDMS was too stiff and that undersized cavities may induce a mechanical stress upon a bacterium, and that uncured PDMS may leach and possibly induce unknown biological effects. As PDMS is not particularly permeable to aqueous solutions, they further suggest that the local nutrient supply could become quickly depleted over length scales as small as a few bacteria. The buffer flow within microfluidic systems constantly replenishes the nutrient supply and helps to remove excess cells. (Moffitt, Lee and Cluzel, 2012b).

The virulence of *Pseudomonas aeruginosa* was shown to be enhanced when the bacteria were attached to a stiff substrate (Siryaporn *et al.*, 2014). A surface protein was shown to act as a mechanosensor that stretches under the shear stress induced by the movement of fluid across the cell surface. This stretching induces downstream signals for new protein synthesis. The authors tested the role of quorum sensing chemicals on virulence and found that, although important, it was not necessary for cells that were attached to a surface, suggesting that activation of virulence required a mechanical cue (Siryaporn *et al.*, 2014).

SA has been shown to grow on PDMS pillars, with a few cells showing attachment to the top of the pillars after incubation for 4 h, but required time scales of at least 24 h to fully

colonise the PDMS (Jahed *et al.*, 2017). Following this extended incubation period SA were shown to form string-like collections of cells similar to those observed on our AFM cantilevers (Fig. 6.1b).

It has been shown that visible light (400 – 800 nm) at high intensities can kill or disrupt the viability of bacteria (Lipovsky *et al.*, 2009; Ramakrishnan *et al.*, 2016). Equally, infrared light has also proved bactericidal (D'Ercole *et al.*, 2016). We explored if this could have contributed to the apparent lack of growth and division on a substrate surface during AFM. The FastScan AFM used in the 15 h study (section 6.2.1.3) has a laser with a visible light wavelength of 678 nm, a beam diameter of 5 µm and a power of 0.5 mW. The JPK AFM used for all of the mechanical data studies has an infrared wavelength of 950 nm, a beam diameter of 18 µm and a power of 2 mW. We estimated the maximum power density of the FastScan at ~ 2.55 x 10^3 W/cm^2 and the JPK at 800 W/cm^2. The power for both systems is very high, and much greater than the power densities considered as phototoxic in the literature. However, the majority of the laser beam would be reflected from the back of the cantilever, with only some of the energy reaching the sample. We routinely found that the cells in the growth medium grew normally, even when irradiated for 4 h without the cantilever in the path of the laser, suggesting that the lack of growth is not related to phototoxicity.

Taken together, these studies may suggest that the lack of growth and division observed with SA cells in, or on PDMS substrates may be due to (i) insufficient time scales during a typical AFM experiment, (ii) the lack of quorum sensing chemicals in the required vicinity of individual cells – further compounded by the one, or more, removals and replenishments of growth medium during our experiments, and (iii) the PDMS wells may have been too restrictive, inducing a mechanical stress upon the cell. We further postulate that the PDMS is too soft, as SA did grow and divide exponentially on glass, but not as efficiently on non-welled regions of PDMS (Chapter 7). If SA does prefer a rigid surface we would have expected it to grow on silicon wafers. Our 15 h AFM scans showed no growth on silicon. The growth medium was not diluted – suggesting that quorum sensing chemicals were not removed, however, the available nutrient supply may have been depleted. Moreover, the silicon wells may have been too restrictive and possibly induced a mechanical stress to the

cells. Despite these limitations, we were able to analyse ~ 60 individual SA cells that were immobilised in, or on, PDMS and silicon, for extended periods of time.

6.3.2 Mechanical property characterisation of whole cells and sacculi

Through a better understanding of the AFM tip geometry we devised a method that, we believe, offers a more realistic and quantitative assessment of the elastic modulus of the SA whole cell and cell wall. We found that the elastic modulus of hydrated and actively growing cells was ~ 2.4 MPa for cells indented up to 51 nm and 300 kPa at 10 nm of indentation. Values of elastic modulus for SA are widely dispersed in the literature, with many orders of magnitude disparity.

Elastic modulus values of ~ 500 kPa were obtained by Perry and co-workers for whole cell SA under ambient conditions (Perry *et al.*, 2009). Interestingly, they showed that *E.coli* had a greater modulus than SA. Many studies find that Gram-negative species have lower elastic moduli than their Gram-negative counterparts. These authors used cantilevers with spring constants of 0.06 – 0.1 N/m - similar to those used in our study. They also used a Hertzian model but used the retract portion of the F-D curve. The sample was assumed to have a Poisson's ratio of 0.5 and the tip radius was 100 nm. The authors make no mention of the make and model of the cantilevers, but 100 nm seems overly large for a non-functionalised tip. Assuming that this radius is far greater than the actual radius may support why their elastic modulus data is similar to ours; as we found that when using the Hertz model for a spherical indenter, the tip radius had to be described as much larger than the actual radius to report the expected modulus values of PDMS during the formulation of our contact model, described in (Chapter 4.3.5).

PF-QNM AFM was performed on whole cell and extracted cell wall sacculi of the Gram-positive Group B *Streptococci*, in a range of osmotic environments (PBS, 0.5x PBS and H_2O) (Saar Dover *et al.*, 2015). Using 1 nN and 6 nN forces they found that the measured elastic modulus increased when the medium osmolarity was decreased. Further, the measurements from indentations in the higher force regime resulted in higher reported moduli and that the increases due to the shift in osmolarity were more pronounced in the higher force regime. They conclude that this was due to the influence of turgor pressure within the cell and that the 1 nN force measurements were related to the intrinsic elasticity

of the cell wall. Their low force data of whole cells showed just over a 2-fold change in elastic modulus when switching from PBS, 0.5x PBS and H_2O respectively. Under the high force regime these effects were far more pronounced, with a ~ 20-fold difference. These data suggest that the cell is capable of drastically modifying its internal turgor pressure and that the cell wall PG must be capable of accommodating these large increases. Their actual modulus data however, were far greater than proposed here. Their 1 nN force regime reported moduli ~ 2 – 5 MPa and their 6 nN force regime reported values ~ 3 – 53 MPa (although they are similar to our data using the default cone half-angle of 15°). Their sacculi were attached to mica with poly-L-lysine, fixed with 1.5% glutaraldehyde and analysed under ambient conditions with stiff cantilevers (spring constant of 2.6 N/m). The whole cells were trapped in polycarbonate membranes and analysed at room temperature with cantilevers of 0.55 and 0.68 N/m, using PF-QNM at ~ 1 Hz scan rate. The cantilevers they used are between 1 to 2 orders of magnitude stiffer than those used in our study. Moreover, the authors make no mention of the tip radius used in the DMT contact model that generated their data. The dehydrated, and chemically fixed nature of the sacculi may have also contributed to higher moduli.

The observation that the moduli gathered from lower indenting forces is related to the cell wall, and that the intracellular turgor is influential at higher indenting forces is in agreement with our previous study (Bailey *et al.*, 2014) and of others (Loskill *et al.*, 2014). Loskill and co-workers obtained modulus values ~ 6 MPa for the cell wall of hydrated SA cells trapped in polycarbonate filters and hydrated with a 1:10 TSB/PBS solution. Data were gathered using the DMT model at room temperature, with a 1 nN force at a scan rate of 1 kHz using PF-QNM AFM. The authors do not state the spring constant of the cantilever, but suggest that a tip radius ~ 10 nm was used, in addition to a Poisson's ratio of 0.5. (Loskill *et al.*, 2014). They used cantilevers with a maximum tip radius of 12 nm, but a nominal radius of 2 nm (Bruker ScanAsyst-Fluid+). In our experience (with MLCT cantilevers), the true value was somewhere in the middle of the nominal and maximum. If they had chosen a median value of 7 nm, their reported modulus would be even higher under our model. Elastic modulus values of 95 MPa were reported for SA, analysed in ambient conditions with a very stiff cantilever (27 N/m) (Eaton *et al.*, 2008). These authors used the Hertz model with a conical indenter, but make no mention of the cone angle or the Poisson's ratio used. The samples were left for up

to 24 h under ambient conditions - although the authors state that they were not dehydrated. This may not be correct, but equally, this does not suggest that they were dead, as SA cells have shown an ability to survive for over three years, in a dehydrated condition, on the plastic lids of centrifuge tubes (Chaibenjawong and Foster, 2011).

The stiff cantilever seems more suited to intermittent contact mode AFM, however. A very stiff probe on a soft sample can result in excessive indentation and make quantitative force measurements unreliable (Meng *et al.*, 2017). A sharp AFM tip was used to deliberately puncture the cell wall of the Gram-negative bacterium *Salmonella typhimurium* (Suo *et al.*, 2009). Three tips with differing aspect ratios of 1:1, 1.7:1 and 10:1 were used and loading forces between 1 - 4 nN were applied. All of their tips had similar spring constants to those used by us. The cell indented by ~ 50 - 100 nm before the tips ruptured the cell wall. Between 20 and 40 punctures per μm^2 were performed. Although the forces required to rupture the cell varied, due to the nature of the different tips, the pressure required to puncture the cell was the same, at ~ 5 atmospheres (~ 500 kPa). The greatest resistance to puncturing occurred for the pyramidal tip, although this caused greater rupturing due to its lower aspect ratio. The cells were shown to survive multiple punctures and were able to grow and divide successfully, suggesting that the cell membrane and cell wall PG were able to self-repair. The authors found no evidence of cell wall PG damage, or any damage to the proteins connected to the cell wall, from the F-D puncture curves. They further postulate that either the PG layer is sealed within 1 s, or that cell viability is not overly sensitive to the integrity of the PG layer. The measured elastic modulus was 0.4 ± 0.2 MPa and was determined by fitting the indentation curve to a Hertzian model (Suo *et al.*, 2009).

All of these authors, described above, have used a range of different fitting methods to derive their values, including DMT, JKR etc. When scrutinising their methods there are no obvious references to modifying the software model's presets, short of including a tip radius, nor to measuring the substrate stiffness of known values as a control. On a heterogeneous polymer, such as PG that has multiple pores along its surface a sharp tip would be more likely to enter these holes and not accurately measure the mechanical properties at the surface. Pore sizes up to ~ 20 nm have been observed with high resolution imaging (Fig. 1.3) and a tip radius of only 2 nm (nominal), such as that used by (Loskill *et al.*,

2014) may not be an ideal choice. Additionally this probe had a spring constant of 0.7 N/m (nominal), and the stiffer cantilever used by Saar Dover *et al*., (2015) was 2.6 N/m.

It is widely accepted that matching the spring constant of the probe to the spring constant of the sample allows for more accurate imaging as a stiffer probe would be less likely to bend from the opposing force of the sample, and thus less likely to report accurate values. The stiffness of SA PG has been reported to be ~ 0.015 N/m (Francius *et al.*, 2008; Bailey *et al.*, 2014) and we found that intact cell wall, at 10 nm of indentation, gave a stiffness measurement ~ 0.06 N/m, and ~ 0.04 N/m for extracted cell wall sacculi. These are perfectly matched to our cantilever stiffness that had a mean spring constant of 0.061 ± 0.0076 N/m throughout the 6 and 4 individual experiments from which our whole cell and sacculi data were derived. If our data is incorrect, and the cell is actually stiffer than we propose, it could be suggested that our cantilevers were then too soft. If this were true, the cantilever would be more likely to bend too much as it tries to achieve sufficient indentation (Meng *et al.*, 2017). The bending and deflection would arise due to the softness of the cantilever and not the sample stiffness. This would result in a steeper F-D curve, and a greater reported modulus, that may actually be the cantilever modulus. The dehydrated nature of the cells studied in ambient conditions must play a role in the elasticity of the cell wall and the reported modulus values. PG and WTA have many ionisable groups and other hydrophilic groups. There is adequate opportunity for H_2O to compete with the hydrogen bonding sites that provide linking between peptides when dry, and this could explain why a stiff polymer becomes more flexible as the humidity increases (Thwaites and Mendelson, 1991).

The key component of our analysis – in contrast to other studies, is the modification of the probe geometry. As we discovered; whole cell indentations up to 51 nm gave a reported modulus around 33 MPa, which reduced to 2.4 MPa just by changing the conical half-angle from 15° to 85°. However, when checking the Young's modulus of the PDMS substrate with the default 15° half-angle, values up to 100 MPa were found (Chapter 4.2.4.1). Following the work performed in Chapter 4 these values must be incorrect as we know the PDMS is ~ 1.3 MPa. This led to the formulation of using improved tip characterisation as a theoretical model for measuring the Young's modulus of both the PDMS and bacterial samples. By trusting the PDMS modulus measurements the concurrent bacterial measurements should be trusted with some confidence, particularly as PDMS and SA cell wall are within the same

orders of magnitude of elastic modulus and stiffness, and both are essentially viscous elastomers, with a similar porosity. Rather than merely reporting the Young's modulus as a qualitative and non-absolute value, we propose that the new values reported in this study are more accurate than those previously published.

The methicillin-treated sacculi data suggest that the antibiotic had little influence on cell wall elastic modulus or stiffness after 30 min – which is the required time for a generation of daughter cells. The modulus and stiffness were decreased by more than half, after 60 min, suggesting that the antibiotic exerted its effect only at the second generation. There was no further significant change in modulus or stiffness at 120 min. This may suggest that the maximum killing activity was performed at 60 min and subsequent division events were hindered, or that these modulus and stiffness values are at their critical limit and no further loss of integrity could be induced.

6.3.3 Mechanical data from known applied loads

We also attempted to elucidate the mechanical properties of the cell wall by looking at the force required to indent to 10 nm. We showed that from a total loading force of 1 nN a force of 135 pN for intact cells and 83 pN for extracted cell wall sacculi was required. By using a range of applied total loads, and the estimated contact area of the indenter at these loads, we estimated the spring constant of the bacterium and found it to be the same as, or within 1 order of magnitude as the values calculated from our tangent fitting - and also the spring constant of the cantilevers used throughout this study. These data are free from the problems associated with elastic contact models, any cone half-angle modifications and from the potential ambiguity of fitting tangents to a curve. By using the Hertzian contact model we determined that even small-scale indentations, with a relatively blunt probe, could cause a significant amount of localised pressure to the cell. These were shown to be between ~ 1 – 5 atmospheres.

The various indentation speeds used in the studies described here also make direct comparisons difficult (Guz *et al.*, 2014). The scanning rate of 22.5 µm/s that we used in QI™ mode is within the range of other QI™ scan rates reported in the literature for biological systems - and in many respects - slower (Chopinet *et al.*, 2013; Dhahri, Ramonda and Marlière, 2013; Rodriguez-Emmenegger *et al.*, 2015; Formosa-Dague *et al.*, 2016). It has

been shown that increasing the velocity of F-D curves leads to increased modulus values in eukaryotic cells (Braunsmann *et al.*, 2014). This suggests that our reported modulus values may be even lower if we had scanned at a lower rate – assuming that the prokaryotic Gram-positive bacterial cell wall behaves in a similar manner to a eukaryotic cell membrane.

6.3.4 Mechanical data of whole cell

This study was primarily interested in the mechanical properties of the cell wall. The relative or absolute values of intracellular turgor pressure were not a feature of interest – short of their impact upon the stress-stiffening of the cell wall. We showed that the elastic modulus was greater from cells indented at a mean indentation of 30 ± 9.4 nm. This likely represents the influence of turgor as it is beyond the ~ 25 nm that we identified as the cell wall thickness. However, it could reflect the full compression of the cell wall only. The cell wall does not directly contact the cell membrane. There is a periplasmic space between the membrane and cell wall in SA that was discovered, relatively recently, by cryo-TEM of frozen-hydrated sections (Matias and Beveridge, 2006). Although widely characterised within Gram-negative species, this was the first time that a periplasm had been identified within SA. This technique was used to confirm the presence of a periplasm within other Gram-positive species (Matias and Beveridge, 2008). It is thought that, analogous to Gram-negative species, the periplasm is a gel-like compartment composed of highly deformable, low density, soluble components, and with a high LTA content. The authors posit that the membrane and cell wall may be kept apart via charge repulsion between the polyanionic hydrophilic chains of the LTA and the highly anionic WTA within the cell wall, and that membrane-bound polymers, including LTA, PBPs and lipoproteins could form a scaffold that keeps the wall away from the membrane.

The periplasmic space within *Bacillus subtilis* was measured at 21 ± 2 nm. They further showed that only the tip of a growing septum makes intimate contact with the membrane in SA (Matias and Beveridge, 2007). Because the cryo-TEM frozen-hydrated technique does not require chemical fixatives and heavy metal staining, the samples are not dehydrated, and are able to be kept hydrated for observation. However, the authors believe that some structural artefacts may be present (Matias and Beveridge, 2006). The cell wall of SA was shown to consist of two regions; an outer wall zone that measured 19.0 ± 4.3 nm and an inner wall zone that measured 15.8 ± 2.5 nm (Matias and Beveridge, 2006). This leads to a

combined cell wall thickness of 35.8 ± 6.8 nm. This technique was not able to visualise the WTAs and the authors suggest that this was due to a lower density of material that did not provide enough contrast. Thus, the SA cell wall may be thicker than their measurements showed. Interestingly, one might expect that the inner wall zone PG may stretch and compress due to the high turgor within SA, and that there would be a gradual change in density as observed by cryo-TEM. There was no apparent change in density, however, and the authors suggest that the whole cell wall must bear an equal stress (Matias and Beveridge, 2006). They tested this further by osmotically shocking the cells. The plasmolysed SA cell outer wall zone separated further from the protoplast, which shrank, due to water being removed from the cytoplasm. The thickness of the outer wall zone was seen to increase, as the reduction in turgor allowed for its expansion. They extracted sacculi, which they believe were only composed of outer wall zone, as they suggest that the inner wall zone is composed of soluble components that were washed away during isolation and boiling in SDS. They measured the outer wall fragments at 32.8 ± 4.1 nm – an increase of almost double from the whole cell outer wall thickness of 19.0 ± 4.3 nm. They also found that the sacculi only partially retained the shape of the cells, which they suggest is due to the spherical geometry of the cell providing an energetically favourable condition; negating the strict requirement for a rigid exoskeleton within SA (Matias and Beveridge, 2006). We also found that the extracted cell wall sacculi only partially retained their shape and were thicker in our hydrated experiments than our TEM data suggested for the intact cell wall (data not shown).

The mass of a cell increases as the cube, whereas the structural strength increases only as the square of linear dimension. Thus, the structural integrity of bacteria could be maintained by a cell wall structure of low mechanical strength (Beveridge, 1981). The influence of surface charges on the cell wall may also offer structural support. The WTA molecules provide a reservoir of ions close to the cell surface and the ionic gradients could mitigate the differing pressures between the outside and the inside of the cell. (Beveridge, 1981; Swoboda *et al.*, 2010).

6.3.5 Conclusions to this study

Using a new model, based on Hertzian contact mechanics and improved indenter geometry characterisation, we have reported elastic modulus values of ~ 310 ± 200 kPa (0.31 ± 0.2

MPa) for the cell wall at 10 nm of indentation. We sought to reduce the influence of intracellular turgor pressure in an attempt to measure only the local elastic properties of the cell wall. The stiffness was reported as 62 ± 44 nN/µm (0.06 N/m). The modulus and stiffness increased markedly when indenting further, suggesting that we were measuring the influence of intracellular turgor pressure instead. When analysing extracted cell wall sacculi at 10 nm of indentation the elastic modulus was lower, at 180 ± 74 kPa (0.18 ± 0.074 MPa). The stiffness was also lower at 38 ± 32 nN/µm (0.038 ± 0.032 N/m). These data represent ~ 50% reduction in modulus and stiffness of the cell wall, once the turgor is removed. We challenged growing cells with methicillin and extracted the cell walls at various time points. There was no change in modulus or stiffness at 30 min, but the modulus changed from 180 ± 13 kPa (0.18 ± 0.013 MPa) to 65 ± 9.54 kPa (0.065 ± 0.0094 MPa) at 120 min. The stiffness dropped from 38 ± 4.2 nN/µm (0.038 ± 0.004 N/m) to 13 ± 0.9 nN/µm (0.013 ± 0.0009 N/m) at 120 min. These data represent a decrease of ~ 90% and a ratio greater than 2.5:1. This shows that the cell has a high safety margin for the cell wall integrity, and that it must degrade by a large amount before lysis and ultimately cell death occur.

6.3.6 Limitations to this study

Our new model assumes that the AFM tip has a conospherical geometry. Typically, shallow indentations are considered as spherical and become conical at greater depths. We have assumed a conical geometry from the outset, as we consistently failed to report accurate moduli, based on the known spherical radius of the probe. Additionally, many of the fitting curves using a spherical indenter poorly followed the F-D curve.

We postulate that the cell would behave in a similar manner to a PDMS elastomer. The whole cell modulus we reported (~ 2 MPa) is slightly greater than the mean PDMS modulus (~ 1.3 MPa) and the cell wall data (~ 0.3 ± 0.2 MPa) is around 2 to 4 times lower than the PDMS. Both materials are essentially elastomers, with a similar porosity, and assuming they both behave in a similar manner when indented, the contact area and deformation of the SA cell wall may be greater than is experienced on PDMS. In this scenario, we would need to increase the contact area of the indenter, concomitant with a decrease in the conical half-angle. These adjustments would lead to a greater reported elastic modulus for the cell wall. However, this new half-angle would still be much shallower than the 15° software default

value and would still report significantly lower values of modulus than elsewhere in the literature. Further, we have only considered the properties of the cell wall at 10 nm of indentation. We have showed that the modulus and stiffness increase at greater indentation depths. Although we attribute this to intracellular turgor pressure, and that this may not be fully transmitted to the cell wall, due to the periplasmic space, we cannot rule out the possibility that we have only partially measured the mechanical properties of the full cell wall.

Many reports in the literature report the mechanical properties of PG, and some investigators may have removed cell wall proteins and WTA. Our extracted cell wall sacculi did not remove WTA and some covalently bound proteins may still be present, thus we are reporting mechanical data that also include these molecules. Whilst many investigators (ourselves included) chose to use sacculi to obtain mechanical measurements, in the absence of the turgor-induced stress stiffening it may actually be a poor platform to measure cell wall elasticity (Deng, Sun and Shaevitz, 2011).

Defining the actual moment of deflection on a F-D curve can be difficult, particularly when short-range forces or surface asperities may interact with the cantilever, and shifting the assumed location can have a marked difference on the modulus, stiffness and indentation depths reported. The same is true, however, for other investigators. By fitting in a similar manner across all our analysed F-D curves, we can say with confidence, that the reported data show, at the very least, qualitative information.

Some of the elastic modulus fitting curves did not faithfully follow the slope of the F-D curve, and under and over reporting of the modulus was apparent on some curves, although we attempted to minimise these, by choosing alternate F-D curves for analysis and through analysing a large volume of F-D curves – improving our statistics.

There were instances when it was not possible to fit the tangent to a F-D curve at exactly 10 nm of indentation, and the tangent may have been shifted ~ ± 2 nm. We sought to minimise this by choosing alternate F-D curves, and through analysing a large volume of F-D curves.

Chapter 7

Growth, division and cell death on compatible substrates

7.1 Introduction

As we discovered in the previous chapters, the successful immobilisation of SA cells was sporadic on our PDMS substrates, and no obvious signs of unperturbed growth and division have been possible (on PDMS or silicon) when interrogating bacterial cells with an AFM. We identified that in addition to the potential mechanical stress induced by overly restrictive well dimensions using silicon wafers or PDMS, or the dilution of quorum sensing chemicals, we may not have allowed enough time for the cells to adhere in, or on the surfaces.

7.1.1 Finding the ideal substrate

Researchers using SYLGARD™ 184 PDMS mixed in a 10:1 (w/v) ratio showed that SA cells were able to form biofilm colonies on an array of hexagonally patterned pillars of 15 µm diameter and 22.5 µm heights respectively, when left for up to 24 h (Jahed *et al.*, 2017). The authors discovered that due to the hydrophobic nature of the PDMS, air pockets trapped between the pillars prevented the SA solution to efficiently penetrate during incubation times of 1 – 4 h. Cells were likely to remain bound to the very top of the pillars, during aspiration, but it took 24 h before the solution was able to fully penetrate the entirety of the PDMS surface. If such air pockets were present on our PDMS it could explain why the cells did not populate the majority of wells, and why we optically observed cells being easily displaced by the AFM. Jahed and colleagues also found that SA cells formed string-like colonies suspended between the pillars, following as little as 1 h incubation. These resembled the string-like colonies that periodically adhered to our AFM cantilevers (Chapter 6.2.1). Taken together, these results would suggest that SA is able to co-localise and form colonies within a short space of time under favourable conditions, but it may take an increased period of time > 4 h to fully allow for growth and division on an unfavourable surface.

7.1.1.1 Using patterned agarose as a suitable substrate

Agarose is a polysaccharide derived from seaweed and is widely used as a model biopolymer. The mechanical properties are primarily dependent upon the pore dimensions, which are further determined by the type of agarose, and the concentration and curing temperature (Narayanan, Xiong and Liu, 2006). By adjusting the concentration, this could allow for the tuning of the stiffness in a similar manner to the mixing ratio of PDMS. Agarose has been used in microfluidic devices and offers an alternative to PDMS. It is soft and transparent, but porous. This could facilitate the transport and diffusion of nutrients and quorum sensing chemicals, and its softness should impart less mechanical stress against an immobilised bacterium (Moffitt, Lee and Cluzel, 2012b). By casting 6% (w/v) agarose from a lithographically patterned silicon master investigators were able to immobilise *Bacillus subtilis* and observe FtsZ-mediated septal synthesis and division (Bisson-Filho *et al.*, 2017). Their patterned pillars were 4.5 µm in height with a diameter ~ 2 µm. The authors transferred the patterned agarose into a Gene Frame mounted on a glass slide and cut away regions of agarose around the patterning to allow for sufficient oxygen. 4 µl of cell suspension was added and the assembly was covered with a further coverslip (Bisson-Filho *et al.*, 2017). Whilst being effective for their studies, we would not be able to encase the cells under a coverslip for an AFM scan, as the probe has to make direct contact with the cells. We did, however, utilise Gene Frame's in a method similar to these authors, and simply removed the coverslip prior to cell seeding.

Moffit and co-workers employed a similar method to pattern holes into agarose, with concentrations between 3 – 5% (w/v). They created lithographically-patterned silicon wafers with a range of different dimensions; 50 µm length x 50 µm width x 20 µm depth gutters, 100 x 100 x 40 µm, 150 x 50 x 40 µm and 200 x 100 x 20 µm. From these, they cast PDMS intermediates by spin coating the PDMS onto the silicon, in an attempt to reduce the potential silicon damage that may occur due to repeated use. To aid in the wetting of the PDMS they briefly treated it to O_2 plasma or chilled it at 12° C before casting low-melting point agarose on the PDMS and allowing it to cure slowly at 30° C for 1 h. Phase contrast imaging confirmed the patterns were faithfully reproduced onto the agarose (Moffitt, Lee and Cluzel, 2012b). Further, these authors were able to transfer patterns of tracks with a 300 nm width onto a 5% agarose gel, suggesting that this fidelity is an order of magnitude

smaller than previously reported. For the first 5 h of their experiments the bacteria were not subject to any microfluidic flow, to allow for a potential bacterial community to form. Following 12 h of washing, at 10 µl/min any remaining bacteria were allowed to equilibrate for 3 h, to facilitate cell-cell communication (Moffitt, Lee and Cluzel, 2012a).

7.1.1.2 Cell immobilisation on glass

Although we have observed no obvious signs of unperturbed growth and division of SA cells when bound in or onto silicon surfaces, studies have shown that bacteria are able to bind to, and grow on glass surfaces. The bacterium *Caulobacter crescentus* employs a small amount of a polar polysaccharide, termed the holdfast, to bind to a surface. Researchers found that a network of the holdfast created strong attachments to glass coverslips, with a slightly higher affinity for clean untreated glass, compared to a chemically-treated hydrophobic glass, and the affinity increased from acidic to neutral pH (Berne *et al.*, 2013).

The influence of shear forces imparted by flowing growth medium through a glass capillary was investigated for its potential to disrupt microbial attachment (Powell and Slater, 1982). *Bacillus stearothermophilus* at a differing range of growth phases was injected into the glass capillary and given 1 h to form attachments to the glass. Liquid flow with a wall shear stress of ~ 2 N/m^2 was initiated and the removal rates of the cells was quantified. Exponential phase cells were seen to detach very quickly, during the first few minutes of flow, but then the population was seen to increase in number as cell division lead to further attachment. Conversely, stationary phase cells did not show the initial removal following activation of liquid flow, nor display significant growth and division events. The authors suggested that proteins released during cell lysis from late exponential phase samples may adsorb onto the glass wall, providing receptor sites for the living cells, and that polymeric molecules may be excreted from cells in the stationary phase, further promoting adhesion (Powell and Slater, 1982).

The AFM has been used to monitor the attachment and growth of a number of bacteria on glass surfaces, including (but not limited to) *E.coli* (Li and Logan, 2004; Oh *et al.*, 2012), SA (Tiller *et al.*, 2001), *Pseudomonas aeruginosa* and *Bacillus subtilis* (Li and Logan, 2004). The influences of surface energy and roughness of uncoated and metal-oxide coated glass surfaces were explored in relation to bacterial adhesion (Li and Logan, 2004). It was shown

that a variety of coatings increased the surface from hydrophilic to hydrophobic, and progressively increased the surface roughness. Bacterial adhesion was greatest at the roughest, most hydrophobic surface, and was correlated with a lower surface energy. The influence of surface charges (adjusted by differing the ionic strength of the medium) was less pronounced than the surface energies. Importantly, they found that the polymers on the outer surface of the bacteria affected adhesion, with longer LPS molecules and greater EPS production leading to increased adhesion (Li and Logan, 2004).

7.1.2 Protein requirements for attachment and growth

In order to adhere to a surface, to allow for growth, division and ultimately biofilm formation, the expression of a variety of extracellular proteins is required. Biological adhesion is typically mediated by multiple, low-affinity interactions which is thought to allow for plasticity in adhesive junctions (Leckband, 2000). PG and TA account for ~ 90% of the weight of the cell wall. The remainder is composed of proteins and hydrolases (Harris, Foster and Richards, 2002). In a host, SA attachment is mediated by the MSCRAMM family of adhesin proteins. Surface proteins such as fibronectin-binding protein A and B, the fibrinogen-binding proteins clumping factor A and B, and collagen-binding protein Cna are likely to contribute to surface attachment (Harris, Foster and Richards, 2002; Götz, Bannerman and Schleifer, 2006). Cell wall adhesins are under the control of at least three regulator genes; *agr*, *sar* and *sae* (Giraudo, Cheung and Nagel, 1997). In SA, surface proteins are primarily expressed during the exponential phase of growth, and this is when the cell would typically adhere to a substrate. Following this attachment the *agr* locus cuases a down-regulation of the surface proteins and an up-regulation of exoproteins and virulence factors (Harris, Foster and Richards, 2002).

The growth rates of bacteria vary greatly in response to the conditions they encounter. Doubling times of *E.coli* can vary from tens of minutes to tens of hours (Bosdriesz *et al.*, 2015). The maximisation of growth rate is an important strategy and bacteria achieve this by adapting their metabolism. *E.coli* has been extensively studied, and the speed of its ribosomal protein-fraction has been shown to precisely match the increased protein demand, but this rate also depends on the efficiency of the ribosomes and the supply of available nutrients. Further, synthesising more of a particular protein will be at the expense

of other proteins (Bosdriesz *et al.*, 2015). It remains unclear how bacteria perceive their growth rate and regulate their ribosomal quantities.

7.1.3 Cell and substrate chemistries and morphologies

Polyacrylamide gels of differing stiffness were coated with collagen or plamsa polymers and tested for their abilities to allow for adhesion of human mesenchymal cells. These investigators found that the highest cell density was obtained on collagen coated gels, and the spread of cells was greater on stiffer gels independent of the surface chemistry. Conversely, uncoated gels and O_2-plasma treated gels did not allow for cellular adhesion (Lanniel *et al.*, 2011).

The surface potentials of medically relevant surfaces, such as stainless steel and gold, were explored for their ability to allow for SA cell attachment, using Kelvin probe force microscopy (Birkenhauer and Neethirajan, 2014). This technique is an included feature within some AFM systems. It allows for the measurement of the contact potential difference between a conductive cantilever and an ideally conductive sample, although it can be used with non-conductive biological samples. The use of non-conductive surfaces, such as mica, glass and silicon can be used as long as they are thin, and the underlying material is conductive (Birkenhauer and Neethirajan, 2014). These investigators initially left an SA sample to adhere for 3 h and found that the cells did not readily attach to either surface – an observation that we frequently encountered. They measured a negative surface potential on the untreated surfaces and functionalised them with poly-L-lysine, where the surface potentials shifted to positive. They found that SA cells became attached to the functionalised surface within 30 min and longer incubation times led to over-confluent samples. The cell membrane potentials varied between the stainless steel and gold surfaces, with positive and negative potentials respectively. The authors posit that the type of substrate may affect cellular metabolism (Birkenhauer and Neethirajan, 2014).

The porous surface morphology of an anodised alumina substrate was shown to inhibit SA cell adhesion and biofilm formation (Feng *et al.*, 2015). The authors created pore dimensions of 15, 25, 50 and 100 nm by two-step anodisation of high purity aluminium. They cultured *E.coli*, *Listeria monocytogenes*, SA and *Staphylococcus epidermidis* onto vertically positioned substrates, to reflect true attachment and not merely sedimentation

due to gravity. Using confocal microscopy, a thin layer of all bacterial types were present on all surfaces, with SA and *Staphylococcus epidermidis* showing a greater biomass, particularly on the surfaces with 50 and 100 nm diameter pores. However, the bacterial numbers on surfaces with 15 and 25 nm pore diameters were reduced for all bacteria, and markedly reduced for SA, which showed the lowest biomass (Feng *et al.*, 2015). The pore diameters of 15 and 25 nm are similar to those we observed on PDMS (Chapter 4.2.7) and may represent one problem that led to our sporadic SA cell attachment to the substrate.

7.1.4 Cell displacement with AFM

There does not seem to be a single defining method to ensure that bacterial cells are not displaced during AFM scans. We have found that a combination of user settings that facilitates successful scanning during one experiment may ultimately fail in a subsequent (and seemingly identical) experiment. Whilst investigators have been able to calculate the turgor pressure of hydrated *Magnetosprillum gryphiswaldense* immobilised on glass (Arnoldi *et al.*, 2000) and the changing cell wall of *Bacillus pumilus* was observed during challenge by pulsed electric fields (Pillet *et al.*, 2016), other investigators found that four different strains of Gram-negative bacteria; *E.coli*, *Pseudomonas aeruginosa*, *Shewanella oneidensis* and *Geobacter sulfurreducens*, were easily displaced from glass coverslips by an AFM probe when scanning in aqueous conditions, using intermittent contact, or contact mode (Stukalov *et al.*, 2008). All of the bacterial species' used in these studies were rod-shaped and the glass surface was chemically coated in each example. Moreover, the aqueous media were imaging buffers and not active growth media. To the best of our knowledge, there are no studies that have successfully monitored the unperturbed growth and division of spherical bacteria using an AFM, and without chemically coated surfaces, that have been shown to alter bacterial viability (Chapter 6.1.1.1).

7.1.5 Silicon wafers with non-spherical patterning

If the pore dimensions of a relatively stiff substrate, such as PDMS or silicon wafers, are a limiting factor in the growth and division of SA then finding a way to increase the pore dimensions, whilst still being able to immobilise the cells for AFM studies, could prove fruitful. Previous work in our laboratory (currently unpublished) saw us create lithographically designed silicon substrates for the study of *Bacillus subtilis*. These featured

pillars of ~ 750 nm height, which we have used throughout this study, but instead they were ~ 2.5 µm diameter square designs, separated by ~ 2 µm in all directions in a repeated array (Fig. 7.1). We considered if they might allow for sufficient immobilisation of SA, whilst still affording the opportunity for cell growth and division, assuming that at least one bacterium became immobilised on a silicon pillar, which always seemed to be a caveat of successful immobilisation and AFM interrogation in our studies (Chapter 6.2.1.1).

a b

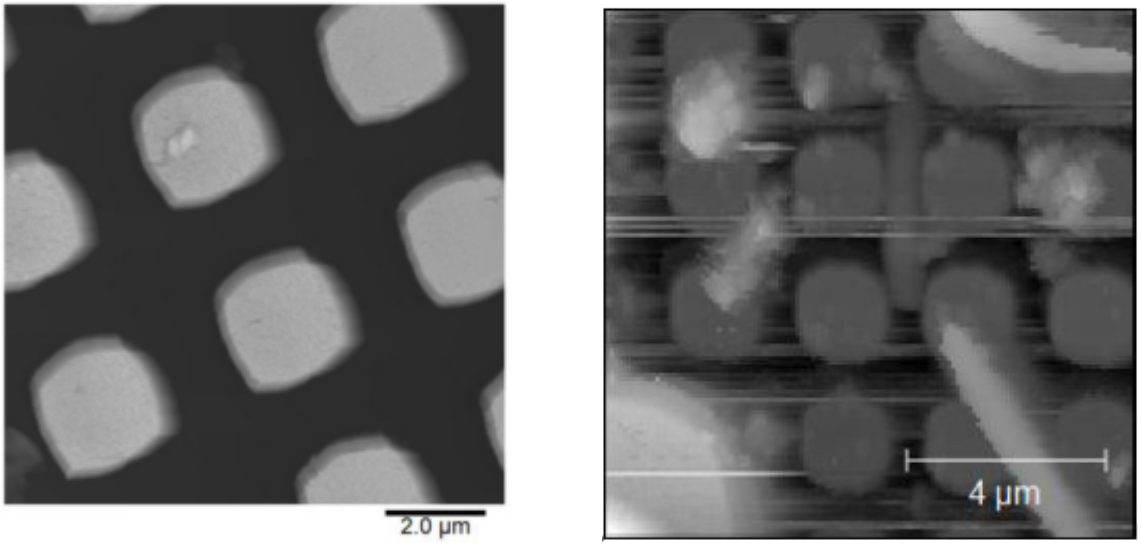

Figure 7.1. *Bacillus subtilis* silicon wafer design. AFM height images of lithographically patterned silicon wafers. (a) Square pillars ~ 750 nm tall and with a ~ 2.5 µm diameter are evenly separated by ~ 2 µm channels in a repeating array. (b) The rod-shaped *Bacillus subtilis* bacteria are trapped on the surface of, or within the pillars of, the silicon substrate. *Z* scale (a) = 845 nm, (b) = 2.8 µm. Images reproduced with permission from Dr Jonathan Burns.

7.1.6 Aims of this chapter

1. Study the attachment of SA cells to PDMS, glass and silicon over long time scales.
2. Produce lithographically patterned agarose and assess SA cell immobilisation.
3. Explore the influence of non-spherical pores on silicon surfaces to aid in cell growth.

7.2 Results

7.2.1 Immobilisation and growth of SA cells over an 18 hour timescale

In order to identify if the incubations of up to ~ 4 h (that we previously employed to measure growth and division) were not sufficient, we tested a range of surfaces at extended incubation time scales of 18 h using confocal microscopy. GFP-expressing SA was seeded and given 5 min for cells to sediment towards the surface, following gentle immersion in growth medium. Cells were resuspended to a similar mid-exponential OD_{600} at the start of each experiment.

7.2.1.1 PDMS surface

A multi-well substrate (Chapter 4.2.1.2) was prepared using SYLGARD™ 184 in a 10:1 (w/v) mixing ratio and trimmed to fit into a 35 mm tissue culture dish, and filled with growth medium. An environmental chamber ensured the temperature remained at 37° C. For the first 2 h frames were captured every 20 s and for the remaining 16 h frames were captured every 1 min. Growth was seen to proceed very slowly up to 2 h with small numbers of cells present. By 4 – 6 h only around 10% of the surface was populated. This increased very little by 18 h where there was only ~ 15% cell coverage. The cells only appeared to be loosely immobilised on the smooth regions of PDMS. There were no obvious signs of any cells immobilised within any of the variously sized wells (Fig. 7.2).

7.2.1.2 Silicon surface

Native and photoresist-coated silicon wafers with repeating ~ 1 µm well diameter arrays were tested and no signs of growth and division were observed. Moreover, cells became displaced by 5 h (data not shown). Silicon was observed for 15 h by AFM, and also showed no growth or division (Chapter 6.2.1.3).

7.2.1.3 Glass surface

SA was seeded onto a 35 mm tissue culture dish with an uncoated glass bottom. The dish was gently filled with growth medium and the temperature maintained at 37° C. Cells grew quickly and by 2 h there was a ~ 15% coverage of the surface. At 4 h large colonies covered ~ 70% of the surface and by 6 – 18 h these colonies appeared to become stacked, leading to an overly confluent coverage (Fig. 7.3).

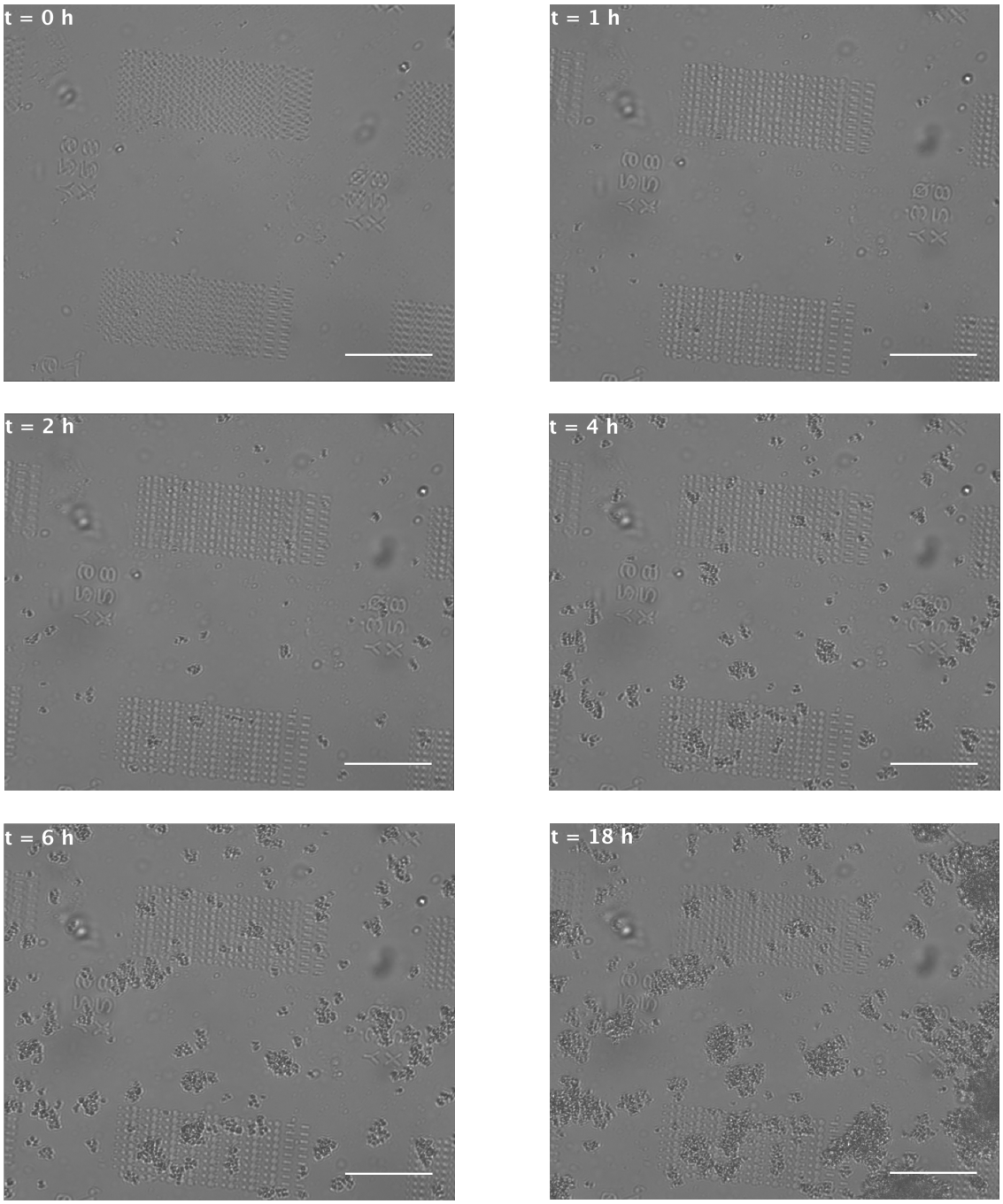

Figure 7.2. SA growth at 18 h on PDMS. Brightfield confocal micrographs show a sequence of temporal events from time = 0 h up to 18 h. SA growth is seen to proceed very slowly up to ~ 4 h, with a steady increase towards 18 h where larger colonies are present. Samples were studied at 37° C in growth medium. Cells appear to be immobilised on the surface only, with no apparent immobilisation within any of the variously sized wells. Scale bar = 50 µm.

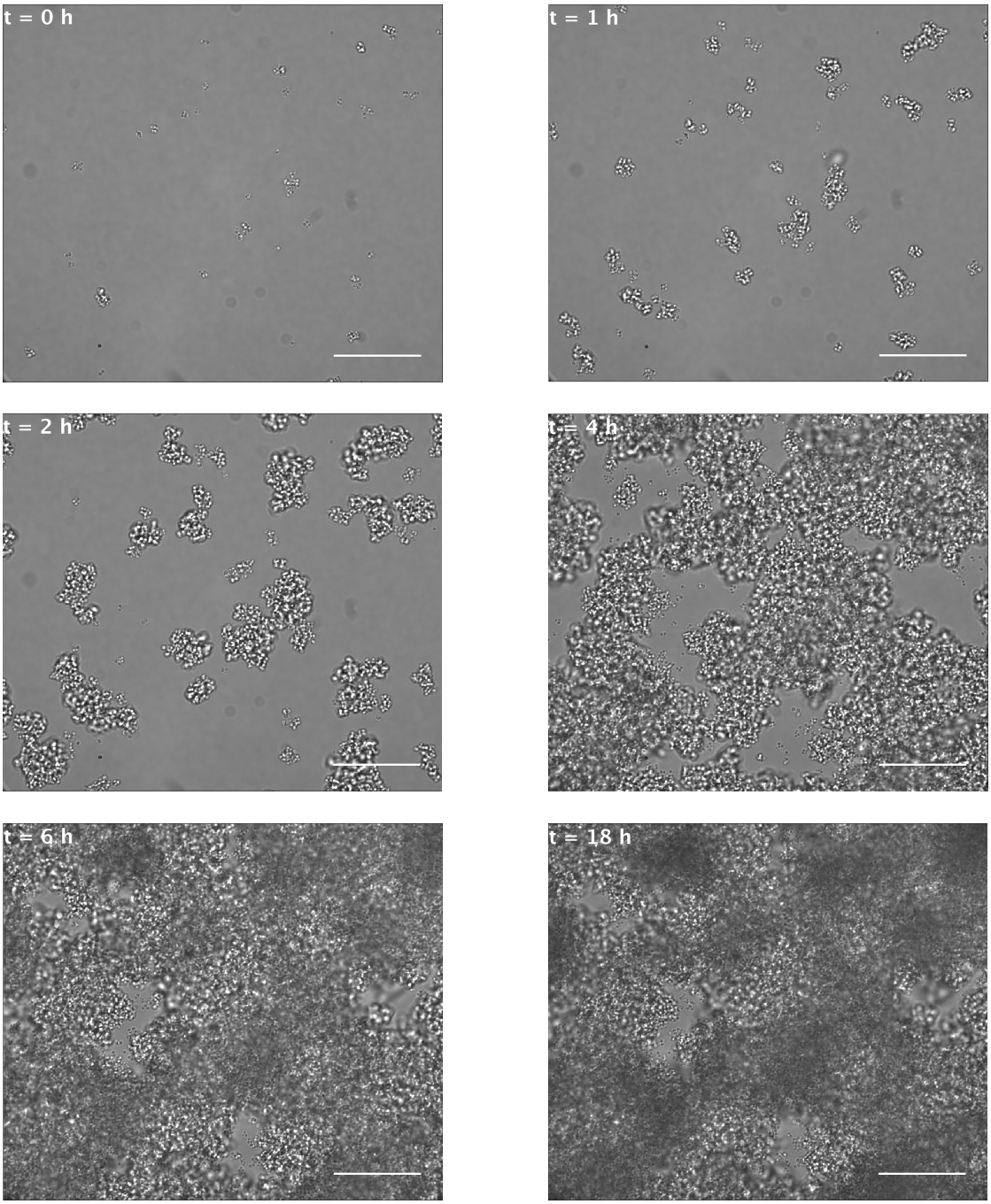

Figure 7.3. SA growth at 18 h on glass. Brightfield confocal micrographs show a sequence of temporal events from time = 0 h up to 18 h. SA growth is seen to proceed slowly up to ~ 2 h, with a large increase towards 4 h, followed by rapid increases up to 18 h where multiple colonies become stacked and over confluent. Samples were studied at 37° C in growth medium. Scale bar = 50 µm.

7.2.2 Modifying agarose for lithographic patterning

We have had no success with growth and division on silicon or on PDMS substrates, for AFM study. Although SA would appear to grow and divide on smooth glass, without the confines of any wells or channels the cells simply roll out of the way of a scanning probe. In order to maintain the optical transparency of PDMS and glass we sought to create patterned agarose from our lithographically produced silicon masters. Numerous methods were employed in an attempt to faithfully transfer the silicon patterns, with a range of agarose concentrations between 2 – 10%. Only the 4 and 6% concentrations were usable. Lower concentrations remained too soluble for patterning and higher concentrations cured too quickly and did not mix or pour adequately. No patterns were transferred using 4% agarose and the ~ 750 nm height pillars (all designs) routinely only imprinted between 30 – 300 nm, with 6% low melting point agarose providing the greatest depth of patterning (Fig. 7.4) (Chapter 3.24.1). In addition to the poor fidelity of the transferred silicon designs the agarose substrates routinely did not adhere to glass or plastic and detached very easily. A method was found that enabled the adhesion of 6% agarose; a thin layer of agarose was poured onto the base of a 35 mm plastic tissue culture dish and allowed to cure. The patterned agarose (prepared separately) was left to cure and trimmed to size. A separate, almost cured agarose sample was spread thinly onto the cured agarose to act as glue, and the trimmed, patterned agarose was gently pressed onto this liquid layer. Following curing of the glue-like layer, the patterned agarose successfully allowed AFM imaging and/or SA sample deposition - although it was difficult to not introduce a bowed effect onto the patterned substrate. Despite this secured layer of agarose no cells remained immobilised during AFM scanning. The 6% agarose was clearly more porous than PDMS, even when viewed at this 64 x 64 pixel density (Fig. 7.4).

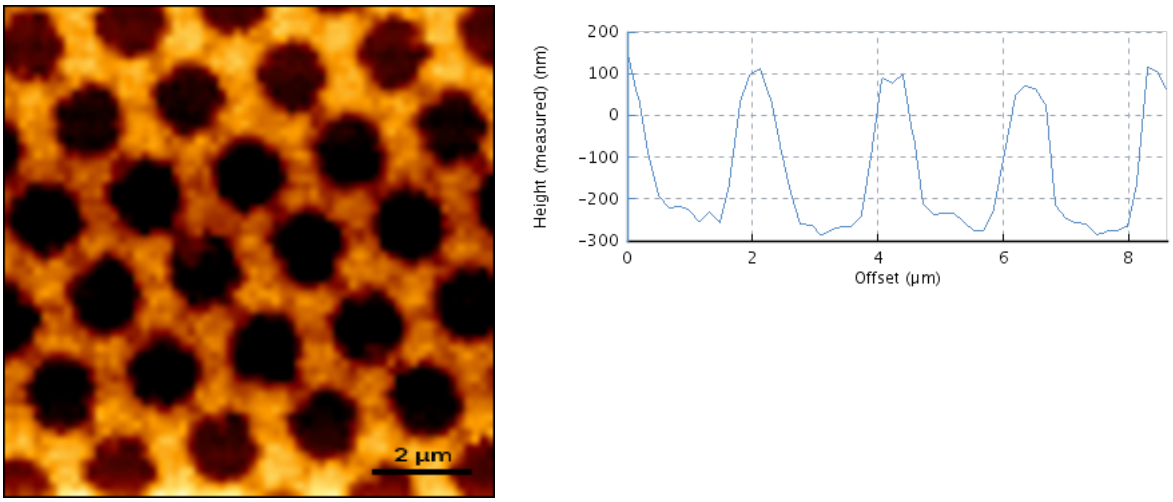

Figure 7.4. 6% agarose only imprints to a maximum of 300 nm. AFM height image of 6% (w/v) low melting point agarose. The expected ~ 750 nm depth wells from a silicon template only imprinted to ~ 300 nm depth, and no cells could remain immobilised. Scale bar = 2 µm.

7.2.3 SA growth and division in silicon channels

In order to test if the previous lack of growth and division was primarily due to mechanical stress induced by the spherical wells, an alternative silicon wafer, with significantly different topographical features was tested. This was lithographically fabricated for a concurrent *Bacillus subtilis* study in our laboratory (data not shown). Being rod-shaped bacteria, this wafer did not feature any circular wells. Instead, an array of ~ 2.5 µm square diameter pillars, of ~ 750 nm height, separated by ~ 2 µm width channels (in all directions) was used (Fig. 7.5). Following mid-exponential SA cell seeding at incubation times > 4 h, (and following removal and replacement of growth medium), cells were routinely found to adhere to the pillars and were able to grow and divide into the channels, with varying degrees of successful immobilisation, during repeated scans with the AFM. Cells were typically left for 1.5 – 2 h following seeding, briefly dried under N_2 and gently rehydrated with growth medium. They were left to adhere for a further ~ 2 h before scanning was performed. The sample was usually overly confluent at this point and the medium was removed, with gentle washing across the silicon surface. Fresh medium was added and the system allowed to equilibrate for a further 30 – 60 min. Growth and division was observed in these diluted, and extended time frames of incubation.

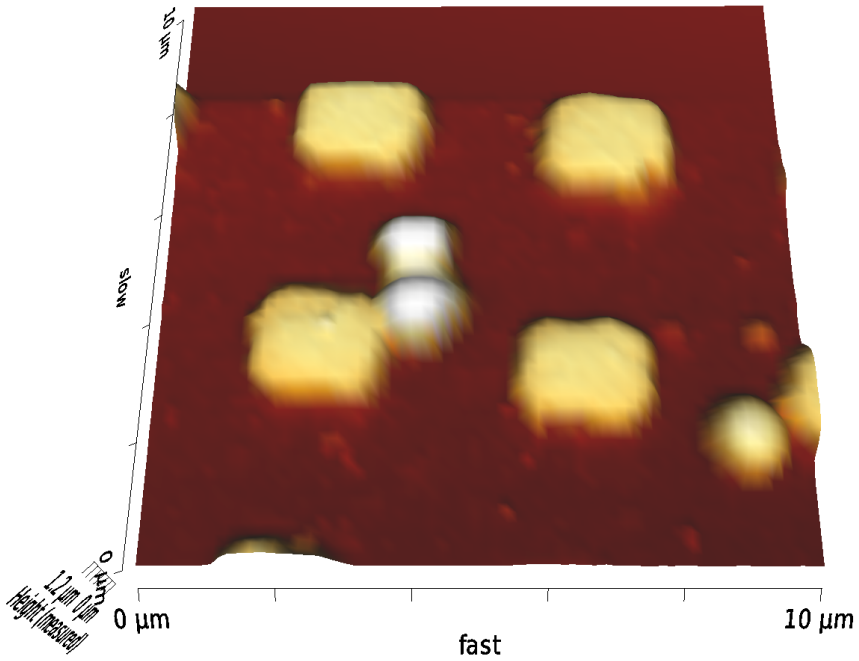

Figure 7.5. *Bacillus* designed silicon wafer with immobilised SA. AFM 3D height image of a rod-shaped channel design wafer, with pillars of ~ 2.5 µm diameter, 750 nm height, separated by ~ 2 µm width channels in the *XY* directions. A connected pair of SA cells are immobilised on one pillar (middle) and a single cell is immobilised (lower right). Z scale = 1.15 µm. Scan size = 10 x 10 µm.

7.2.3.1 Tetrad and sarcinae-like growth and division

Following 4 h 10 min incubation, the growth medium was replaced and the cantilever was left to equilibrate for a further 10 min. A collection of five connected cells were scanned repeatedly for ~ 30 min with no obvious signs of growth, nor displacement. Following this, and within a 9 min period, three new cells were seen to appear (Fig. 7.6). Height profiles were drawn across various locations (not present in these images) to further quantify that the newly formed bacteria were not present previously, and hidden out of view beneath another cell. A 3D topographic image (panel b) provides a useful view of the cells and enables an easier visualisation of their relative heights. Numerous streaks appear in all of the images. These are imaging artefacts caused by cells in the growth medium interacting with the AFM cantilever. All of these cells remained immobilised for a further ~ 30 min of repeated scanning (following the image capture in panel d) before being displaced (data not shown).

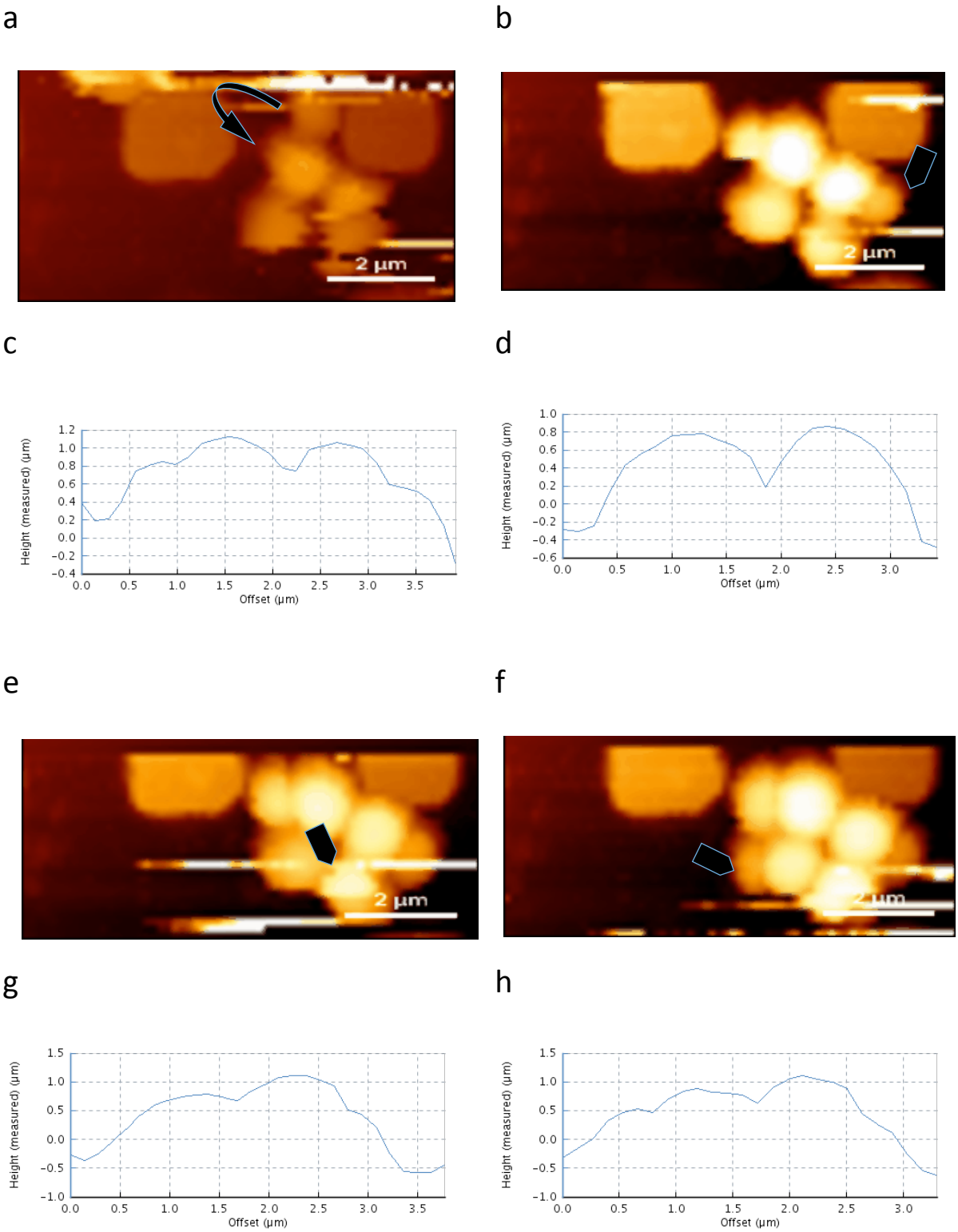

Figure 7.6. SA growth and division in 2 µm channel silicon surface. AFM height images show a collection of SA cells during growth and division. (a) The upper cell will shift position (curved arrow). (b) The mobile cell has assumed a new position, and although it appears to be sliced, this is merely an imaging artefact due to its movement. It will remain in position in

panels e and f. A new cell has also appeared (arrow). (c) A height profile shows the top row of four cells from panel b, now the mobile cell has positioned there. (d) A height profile from the bottom row of cells in panel b. (e) A new cell is appearing above an existing cell (arrow) and is fully formed in panel f. (f) A further cell has divided (arrow). (g) A height profile depicts what are now three cells (bottom row), from left to right, with the newly forming cell, from panel e, occupying the steepest region of the profile. (h) The height profile, from left to right, now depicts the collection of four cells, following the division event in panel f (bottom row), although the fourth cell in the lower right of the image is partially obscured by streaks and the scale bar. The streaks in all of the images are artefacts induced by mobile bacteria in the growth medium interacting with the cantilever. Streaks were temporarily removed prior to obtaining height profiles, and to determine the *Z* scales, and images were levelled with 3rd order plane fitting. Samples were scanned in growth medium at 37° C. Scan time from panel a to panel h = 9 min. *Z* scale = (a) 1.63 µm (b) 1.36 µm (e) 1.43 µm (f) 1.55 µm. Scale bar = 2 µm.

7.2.3.2 Further example of growth and division

A connected pair of cells (numbered 1 and 2 in Fig. 7.7) is pushed apart as a new daughter cell (numbered *) is generated between them. They displayed a large degree of dynamic activity – with cells being reoriented throughout, and they seemingly make new adhesive connections with nearby silicon pillars (Fig. 7.7). The cell, numbered (3) in all of these images appears to be the most mobile and it is being pushed in numerous directions by the scanning probe, ultimately becoming displaced and taking all other cells (except cell 1) in panel f. Following SA cell seeding, the sample was left to incubate at room temperature for 2.5 h. Initial scanning was started 3 h 50 min later. The cells were repeatedly scanned for a further 3 h 50 min before any growth and division was observed, thus growth only began 7 h 40 min after initial seeding. Scan time from panel a to panel f was 61 min.

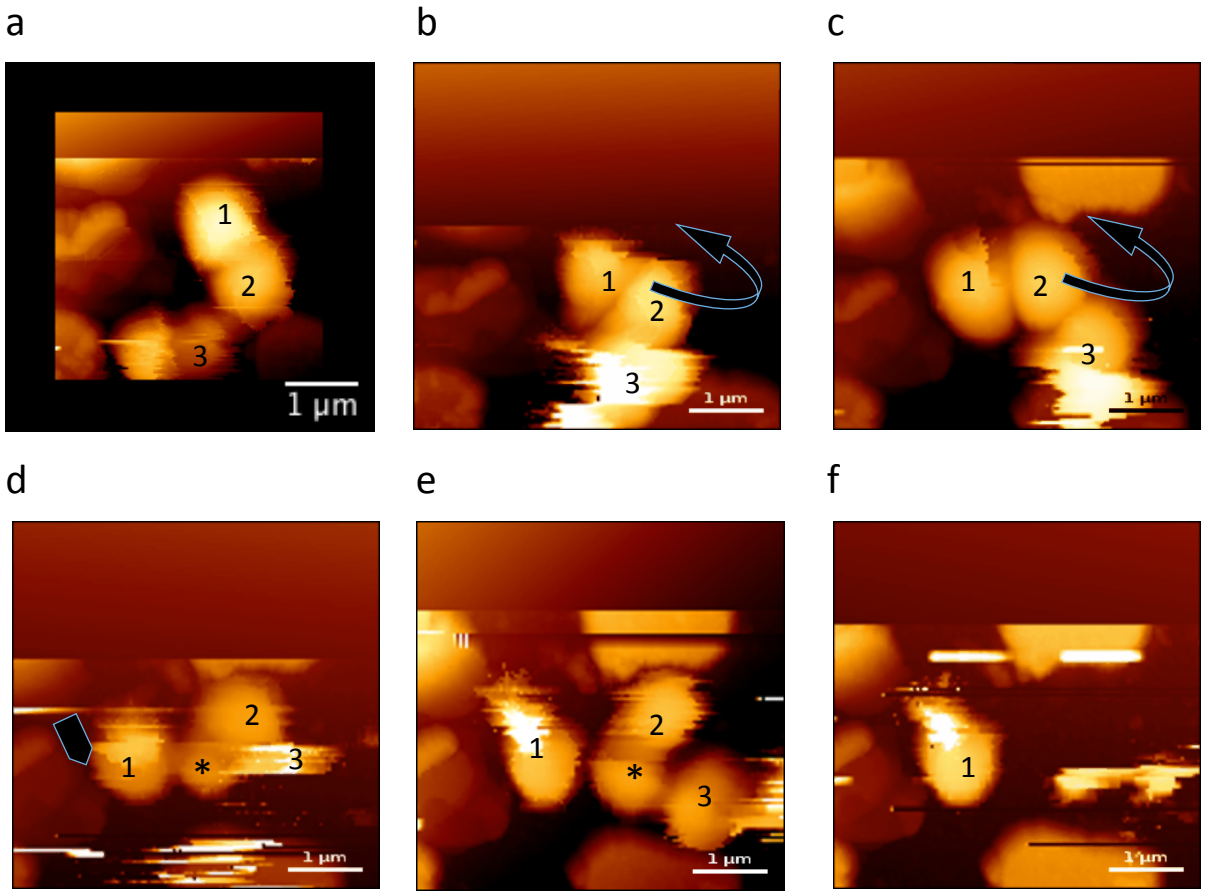

Figure 7.7. SA growth, division and displacement. AFM height images of a sequence of growth and division events. Cells are numbered to enable easier tracking of their paths. (a) A pair of connected cells (1, 2) will shift position and cell (3) and its daughter will be pulled to the right. (b) Cell 2 shows signs of swelling, and cell 3 (and its attached daughter) is being moved (streaks in the image). Cell 2 will move upwards (curved arrow). (c) Cell 2 moves further, and will become bound on a different part of the silicon pillar (curved arrow). (d) A daughter cell appears (asterisk) seemingly pushing cell 1 to make a new contact with cellular debris located between two pillars (arrow), and cell 3 is moved by the scanning probe. (e). Cell 1 shows signs of division (streaks above) and cell 3 is briefly stable, whilst its attached daughter is mobile. (f) Cell 1 remains bound to the cellular debris as all other cells are displaced. Scan time from panel a to f = 61 min. Cells were studied at room temperature which changed from 24.5 – 26.3° C throughout the experiment. Some streaks have been removed for easier visualisation. Images were modified with 3rd order plane fitting. *Z* scale = (a) 1.30 µm (b) 1.69 µm (c) 1.95 µm (d) 1.82 µm (e) 1.63 µm (f) 1.62 µm. Image (a) was scanned at a different scale to all the others (4.961 µm vs. 3.589 µm) and was resized to accurately match the scale of the others. Scale bar = 1 µm.

7.2.3.3 Growth, division and potential antibiotic-induced death

Following SA cell seeding, the sample was left for 1 h 45 min and briefly dried under N_2. The tissue culture dish was gently filled with growth medium and the sample left for a further 2 h 50 min at a room temperature of 23.7° C. Following cantilever equilibration for 10 min multiple scans were performed, to locate any cells of interest. After 50 min a cell of interest was chosen (revisiting from a scan 30 min earlier), as it was beginning to show signs of division (Fig. 7.8). It was repeatedly scanned for a further 3 h 50 min before the cells were all displaced. Specific details (from top left to bottom right) include; a single cell (panel a) was seen to produce a daughter cell 15 min after commencement of the repeated scanning (panel b). This pair of connected cells generated a third cell ~ 38 min later. A 0.5 µg/ml concentration of oxacillin was carefully added to the growth medium 1 h 35 min after the AFM scanning commenced. Almost immediately, and for a further 20 min, the cells became more dynamic and fluctuated more readily with each scan (panel d). The third cell (previously generated) was displaced after a further 20 min (panel e). 35 min after oxacillin addition the pair of connected cells, began to display a near perfect spherical morphology, and no further evidence of dynamic events occurred during a further 30 min of repeated scanning (panel f), until there were signs of moderate cell swelling (panel g). The top cell immediately began to change appearance and became apparently degraded (panel h). The streaks in the images were similar to those seen from the dynamic movements of the previous images, but the cell did not move across the scan region as before, and instead remained relatively motionless. Following a further 45 min of repeated scanning, a protrusion of ~ 300 nm in length was seen to exit from the top of the cell (panel i). The top cell remained relatively motionless, with more streaks being captured until it was displaced, 15 min later (panel k). The bottom (original) cell remained in place for a further 5 min before being displaced (panel l). Scan time from panel a to panel l was 3 h 50 min. Total time of the experiment from initial cell seeding was 9 h 35 min.

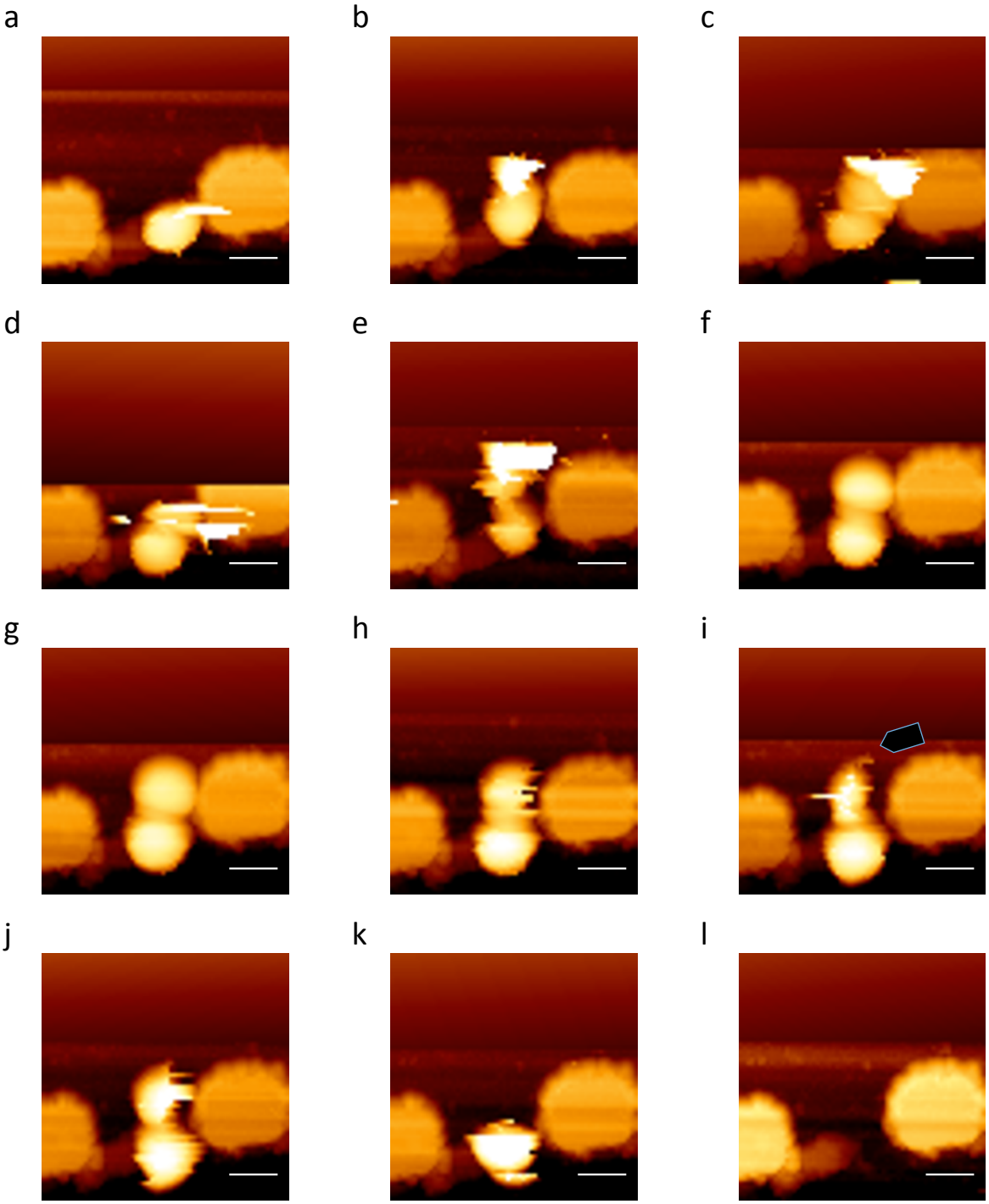

Figure 7.8. Growth, division and potential death of SA. AFM height images show a sequence of events captured during 3 h 50 min of repeated AFM scanning. (a) A single cell immobilised on a silicon pillar shows signs of division. (b) The connected daughter cell becomes more apparent. (c) A further daughter cell is generated and shows lateral fluctuations as a result of the cantilever motion. (d, e) The sample was challenged with 0.5 µg/ml oxacillin and the cells show increased dynamic fluctuations, and are readily perturbed by the cantilever. (f) The third cell has been displaced and the initial pair of connected cells

assume near perfect spherical morphologies. (g) A brief and moderate swelling occurs. (h) Immediately following this swelling, the top cell appears to degrade, with imaging artefacts appearing streak-like, although the cell does not show signs of dynamic, lateral movements. (i) A ~ 300 nm length protrusion exits from the top of the cell (arrow). (j) Further degradation of the top cell. (k) The top cell is displaced. (l) The bottom cell is displaced. Scan time from panel a to panel l = 3 h 50 min. Cells were studied at a room temperature of 23.7° C. *Z* scale = (a) 1.10 µm (b) 1.43 µm (c) 1.86 µm (d) 1.53 µm (e) 1.54 µm (f) 1.44 µm (g) 1.36 µm (h) 1.35 µm (i) 1.42 µm (j) 1.40 µm (k) 1.37 µm (l) 1.07 µm. Scale bar = 1 µm.

7.2.4 Elastic modulus and stiffness of PDMS at 0.5 nN indentations

When SA cells were scanned with 1 nN loading forces they were readily displaced. As such, a reduced loading force of 0.5 nN was required. We had previously found that forces lower than 1 nN (which we have used throughout all of this study) consistently reported lower values of elastic moduli for cells and PDMS. To further test this, during these growth and division experiments, two PDMS substrates, prepared in the same manner as throughout this study were tested at 0.5 nN and immediately after with 1 nN using an 85°conical half-angle (Fig. 7.9). At 1 nN loading forces both substrates reported an elastic modulus ~ 1.3 MPa, in agreement with our previous studies (Chapter 4.2.4.2) – being 1.3 ± 0.31 MPa and 1.3 ± 0.34 MPa respectively. However, at loading forces of 0.5 nN the same substrates reported an elastic modulus of 0.77 ± 0.38 MPa and 2.6 ± 1.1 MPa respectively. These data represent moduli just over less than half, and double the moduli reported at 1 nN and were considered significantly different. Thus, at 0.5 nN loading forces the elastic moduli become varied and difficult to quantify. The stiffness of the PDMS at both loading forces was calculated, by drawing tangents to the curves at 10 ± 2 nm (or as close as possible) (Fig. 7.9b). At 1 nN the stiffness was found to be 248 ± 58 nN/µm and 197 ± 36 nN/µm respectively. The lower value was similar to our previous data, but the greater value was not (Chapter 4.2.4.3). Conversely, at 0.5 nN loading forces the reported stiffness values were 172 ± 56 nN/µm and 171 ± 26 nN/µm respectively and were very similar to our previous data. Data were derived from 10 F-D curves per loading force and per substrate. *n* = 2 substrates from 2 independent experiments.

a

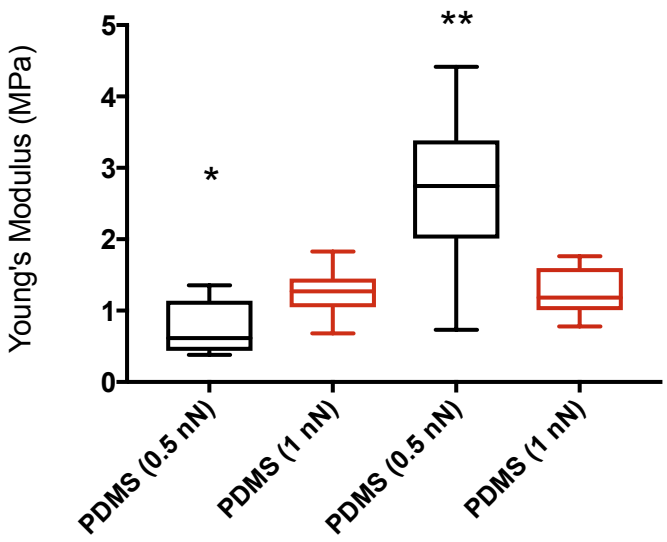

b

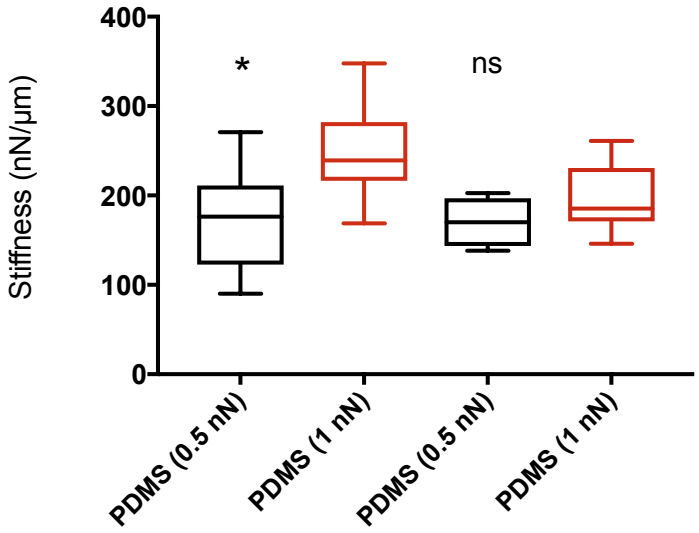

Figure 7.9. Elastic modulus and stiffness of PDMS at 0.5 and 1 nN loading forces. Two PDMS substrates were indented at 0.5 and 1 nN to verify if 0.5 nN forces report similar data. Box and whisker plots show the mean ± SD and min and max range respectively. The line represents the median. Elastic moduli and stiffness at 1 nN loading are in red. (a) At 0.5 nN elastic modulus is 0.77 ± 0.38 MPa and 2.6 ± 1.1 MPa. Data were compared with the PDMS at 1 nN loading with a two-tailed non-parametric t test, and were considered significant. P value = 0.0115 and 0.0089 respectively. (b) At 0.5 nN stiffness is 172 ± 56 nN/µm and 171 ± 26 nN/µm. Data were considered significant and not significant respectively. P value = 0.0115 and 0.1230.

7.2.5 Elastic modulus of SA cells at 0.5 nN loading force indentations

Because the 0.5 nN loading force data from PDMS gave inconsistent results, we must assume that the data derived from the SA cell wall indentations at 10 nm may also report inconsistent data, when compared to the 1 nN-derived data. Previously, we reported a mean elastic modulus of 310 ± 200 kPa for the cell wall at 10 nm indentations, at an initial time point of t = 0 h (Chapter 6.2.2.1).

Fifteen actively growing and dividing SA cells were analysed at a single (initial) time point, t = 0 h, from 10 F-D curves per cell (150 total F-D curves) and the elastic moduli were widely dispersed. The mean modulus value from the 10 F-D curves per cell was calculated, thus each inputted mean is the cumulative mean of each individual cell. Each of these values was statistically analysed. A mean value of 61 ± 42 kPa was calculated. Because these data were calculated from the combined means of each set of 10 F-D curves, the standard error about the mean is a better indicator of variability. SE = 11. The median elastic modulus was 54 kPa.

Mean (kPa)	**SD (kPa)**	**SE (kPa)**	**Median (kPa)**
61	42	11	54

Table 7.1. t = 0 h modulus for whole cell SA at 0.5 nN. The values were calculated by Sneddon contact model fitting at 10 nm indentations of AFM F-D curves. A single average from 10 F-D curves per cell was analysed. *n* = 15 cells and therefore averages calculated from 150 F-D curves.

The scatter plot (Fig. 7.10a) shows a dot for each of the 150 individual F-D curve values. The error bars show the mean ± SD. Minimum and maximum values were 1 kPa and 393 kPa respectively. Although the large spread of data may be due to the heterogeneity of the cells, the movement of the cells most likely influenced the results. The mean value is some 5-fold lower than reported at 1 nN indentations. This is unlikely to represent a true modulus due to the actively growing status of these cells, but more likely represents the influence of lower loading forces and the fact that the cells are freely moving, as they are not immobilised within spherical wells.

7.2.6 Stiffness of SA cells at 0.5 nN loading force indentations

For cells analysed at an initial time point, t = 0 h, a mean stiffness of 13 ± 6.5 nN/µm (0.013 ± 0.0065 N/m) was obtained. SE = 1.7. The median stiffness was 10 nN/µm.

Mean (nN/µm)	SD (nN/µm)	SE (nN/µm)	Median (nN/µm)
13	6.5	1.7	10

Table 7.2. t = 0 stiffness for whole cell SA at 0.5 nN. The values were calculated by applying linear tangents to the curve, at 10 nm indentations of AFM F-D curves. A single average from 10 F-D curves per cell was analysed. *n* = 15 cells and therefore averages calculated from 150 F-D curves.

The scatter plot (Fig. 7.10b) shows a dot for each of the 150 individual F-D curve values. The error bars show the mean ± SD. Minimum and maximum values were 0.97 nN/µm and 76 nN/µm respectively at 10 nm indentations. Previously, we reported a mean stiffness of 62 ± 44 nN/µm for the SA cell wall at 10 nm indentations. The mean stiffness at 0.5 nN was also 5-fold lower than reported for SA indented with 1 nN loading forces at 10 nm indentations, and thus shares the same reduction as found for the elastic moduli.

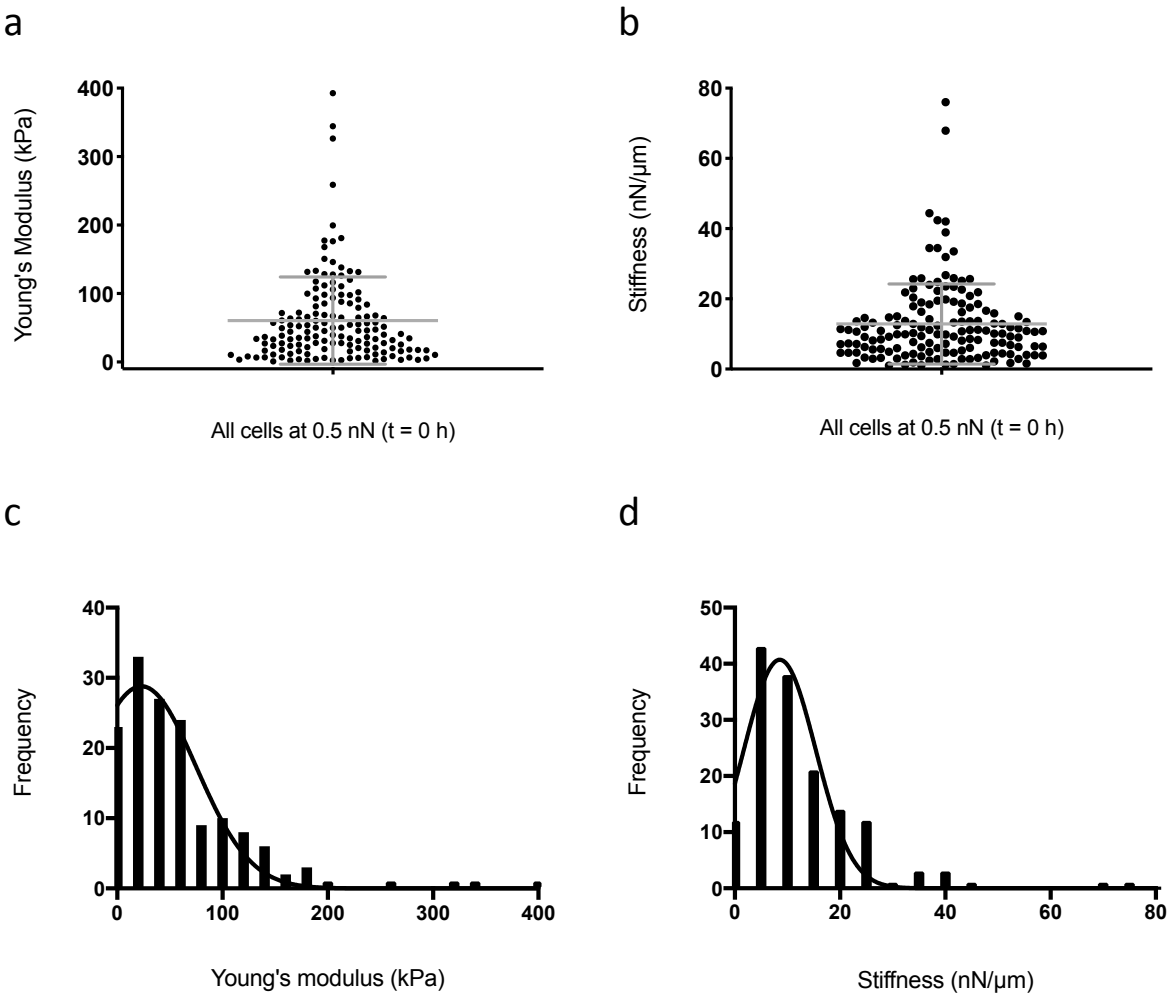

Figure 7.10. Elastic modulus and stiffness of SA cell wall at 0.5 nN loading forces. Scatter plots show the distribution of elastic modulus and stiffness of actively growing and dividing cells. Error bars show mean ± SD. (c, d) Frequency distribution histogram of the same data, fitted with a least squares Gaussian fit. (a) Elastic modulus is 61 ± 42 kPa. (b) Stiffness is 13 ± 6.5 nN/µm. *n* = 15 cells from 4 independent experiments.

7.2.7 Mechanical changes during growth and division

7.2.7.1 Elastic modulus changes during growth and division

The elastic moduli of the cell wall at 10 nm indentations, from cell 1 in section 7.2.3.2 were analysed during various stages of growth (Fig. 7.7 panels a, b, c and f) and represented in box and whisker plots (Fig. 7.11a). The data were compared against t = 0 min. The moduli

were not significantly different at the start and the end (panels a and f) with moduli of 135 ± 58 kPa and 147 ± 57 kPa respectively. P value = 0.6305. During swelling of an attached daughter cell (Fig. 7.7 panel b) the modulus decreased to 108 ± 142 kPa representing a moderately significant change from the starting value. P value = 0.0355. A significant change was observed 29 min after the initial scan (panel c) when the modulus increased to 429 ± 333 kPa. This appears to coincide with cell movement and new attachments being formed with the substrate. P value = 0.0015. Data were derived from 10 F-D curves per time point from a single cell.

7.2.7.2 Stiffness changes during growth and division

The same cell was analysed for any changes in stiffness during the same time points, by drawing tangents to the curve at 10 nm (Fig. 7.11b). The stiffness was not significantly different at the start and end (panels a and f) with values of 25 ± 10 nN/µm and 32 ± 9.8 nN/µm respectively. P value = 0.1431. Conversely, during swelling of the attached daughter cell (panel b) there was no significant change although the stiffness slightly increased to 30 ± 36 nN/µm. P value = 0.2745. A significant change was observed 29 min after the initial scan (panel c) when the stiffness increased to 87 ± 45 nN/µm. P value = 0.0007. Data were derived from 10 F-D curves per time point from a single cell.

a

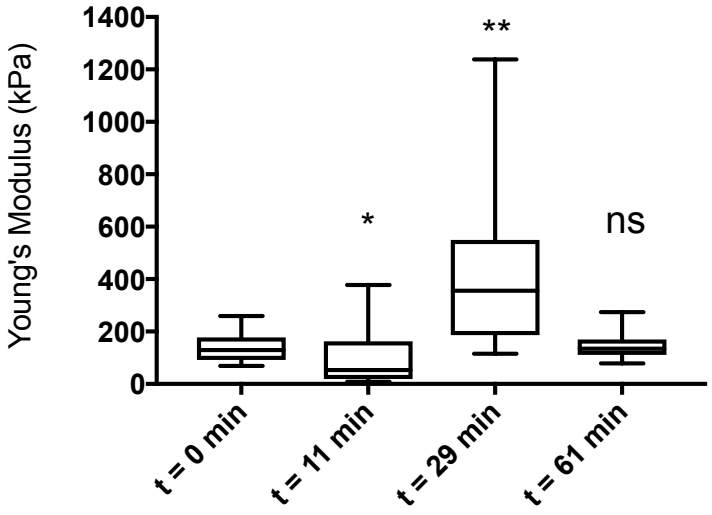

b

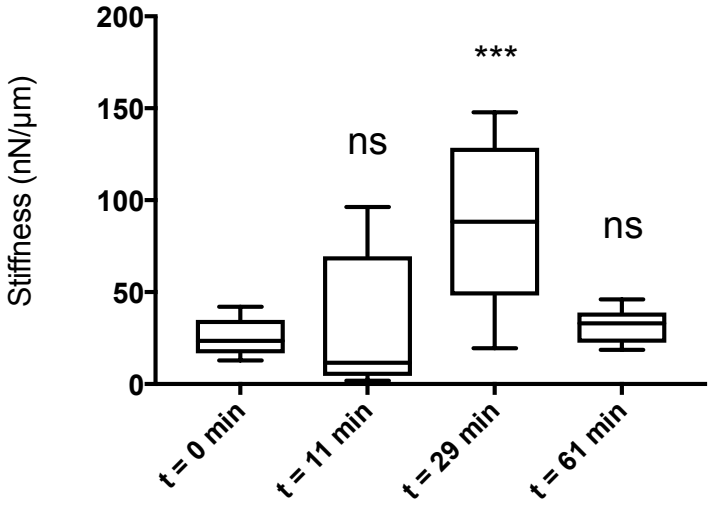

Figure 7.11. Elastic modulus and stiffness changes of a SA cell during growth and division. A single SA cell (cell 1 from section 7.2.3.2) was monitored over a 61 min period of growth and division. Any changes in mechanical properties were compared to the initial time point, t = 0 min. Box and whisker plots show the mean ± SD and min and max range respectively. The line represents the median. (a) The elastic modulus was seen to decrease during the growth and division of an attached cell at t = 11 min and increase at t = 29 min before returning to a similar value at the end of the experiment. (b). Conversely, the stiffness slightly increased at t = 11 min (although not significantly). The stiffness increased at t = 29 min before returning to a similar value at 61 min. Data were derived from 10 F-D curves per time point from a single cell.

7.2.8 Mechanical changes during growth and potential death

7.2.8.1 Elastic modulus changes during growth and death

The elastic moduli of the cell wall at 10 nm indentations, from the pair of cells in section 7.2.3.3 were analysed during various stages of growth and potential death. The lower (original) cell (Fig. 7.12a). was analysed over 3 h 6 min (panels b,c, f, g, i, k of Fig. 7.8). The starting modulus of the lower cell was 64 ± 30 kPa. The other moduli were not significantly different except for when the connected pair of spherical cells were seen to swell and when the ~ 300 nm protrusion exited the top cell (panels g and I of Fig. 7.8). These events lead to elastic moduli of 120 ± 55 kPa during swelling and 24 ± 32 kPa when the protrusion was evident. P value = 0.0052 and 0.0021 respectively. Data were derived from 10 F-D curves per time point from each cell.

The upper cell was analysed over a period of 108 min (Fig. 7.12b) from when it became fully formed to its apparent death and displacement (panels c and j of Fig. 7.8). The starting modulus of the upper cell was 14 ± 12 kPa. The other moduli were not significantly different (including the point when it appears to expel the 300 nm protrusion) until the final moments before apparent cell death and displacement where the modulus increased to 24 ± 10 kPa.

7.2.8.2 Stiffness changes during growth and death

The same cells were analysed for any changes in stiffness during the same time points, by drawing tangents to the curve at 10 nm. The starting stiffness of the lower cell was 16 ± 8.1 nN/µm (Fig. 7.13a) and was not significantly different until the apparent lysing of the upper cell, and the moments before its own potential death and displacement (panels i and k of Fig. 7.8) with reduced values of 8.1 ± 12 nN/µm and 6.2 ± 4.9 nN/µm respectively. P value = 0.0232 and 0.0052 respectively.

The upper cell starting stiffness was 10 ± 7.7 nN/µm (Fig. 7.13b) and no changes were significantly different until its apparent death (panel j of Fig. 7.8), where the stiffness reduced to 4.2 ± 4.1 nN/µm. P value = 0.0232.

Data were derived from 10 F-D curves per cell for each time point.

a

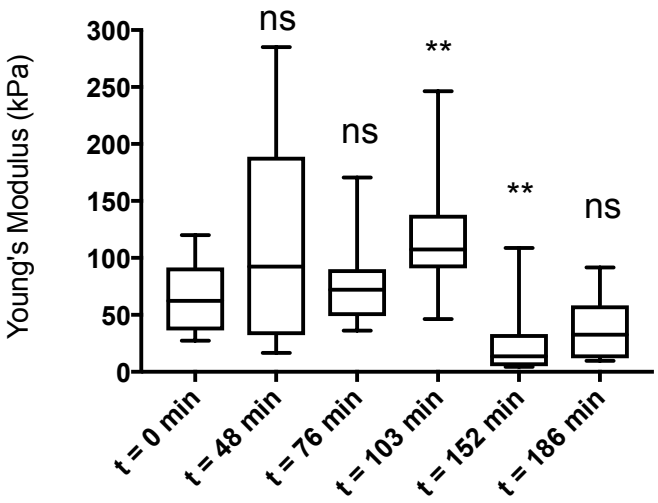

b

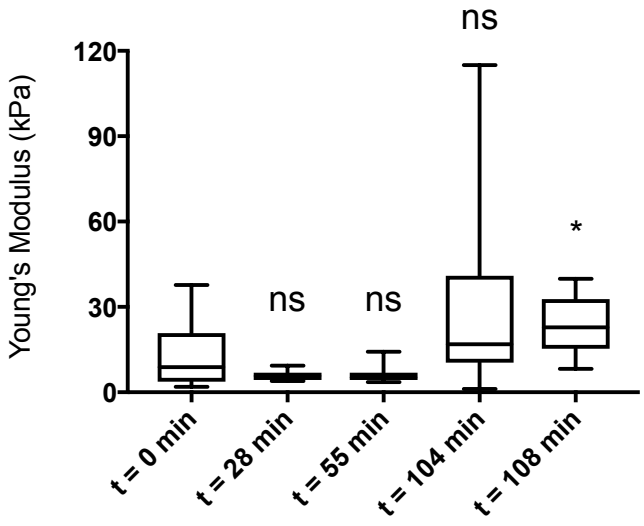

Figure 7.12. Elastic modulus changes of two cells during potential cell death. A pair of cells (from section 7.2.3.3) were monitored over a ~ 2 – 3 h period during growth, division and apparent cell death. Any changes in elastic modulus were compared to the initial time point, t = 0 min. Box and whisker plots show the mean ± SD and min and max range respectively. The line represents the median. (a) The elastic modulus of the lower cell was seen to significantly increase during swelling and significantly decrease when the upper cell was apparently dying, before returning to a similar value at the end of the experiment. (b) The upper cell showed little sign of significant change (even during swelling and its apparent lysing) but conversely showed a moderately significant increase during its apparent death at 108 min.

a

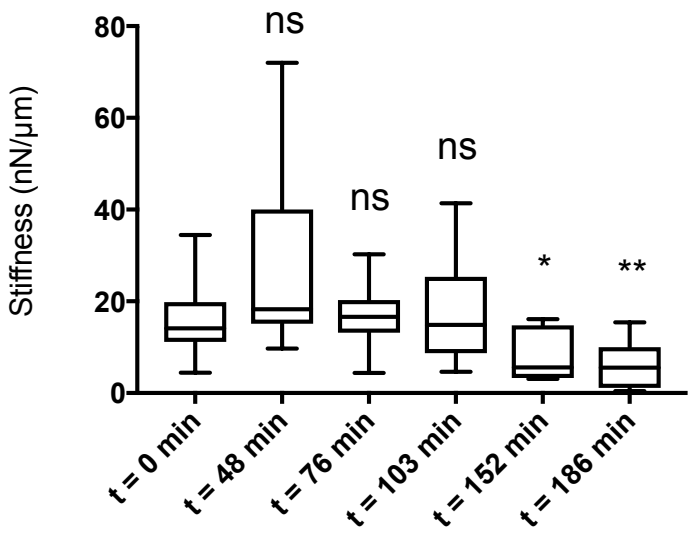

b

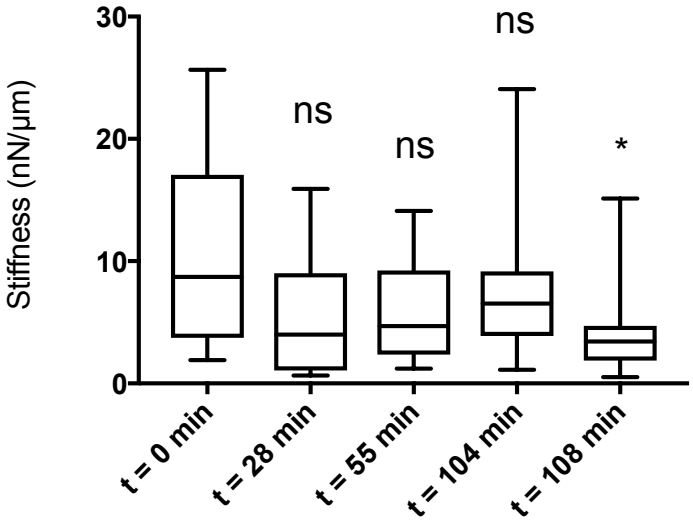

Figure 7.13. Stiffness changes of two cells during potential cell death. A pair of cells (from section 7.2.3.3) were monitored over a ~ 2 – 3 h period during growth, division and apparent cell death. Any changes in stiffness were compared to the initial time point, t = 0 min. Box and whisker plots show the mean ± SD and min and max range respectively. The line represents the median. (a) The stiffness of the lower cell was seen to significantly decrease during the apparent death of the upper cell and moments before its own apparent death. (b) The upper cell showed little sign of significant change (even during swelling and its apparent lysing) but conversely showed a moderately significant decrease during its apparent death.

7.3 Discussion

7.3.1 Testing substrate specificity and chemistry during increased time scales

The body of work performed in Chapter 6 did not seemingly encourage growth and division of immobilised SA cells. We identified that the lack of growth and division observed with SA cells in, or on patterned PDMS and silicon substrates may be due to (i) insufficient time scales during a typical AFM experiment, (ii) the lack of quorum sensing chemicals in the required vicinity of individual cells and (iii) the PDMS or silicon wells may have been too restrictive, inducing a mechanical stress upon the cell. It would be difficult under our experimental conditions not to potentially dilute any quorum-sensing chemicals, as cells became too confluent (even when starting with low cell numbers) and the medium needed aspirating and replenishing. However, by increasing the length of time of our experiments we could address point (i) and indirectly address point (ii) by allowing any quorum-sensing chemicals to become concentrated following dilution.

We showed that SA cells required at least 4 - 6 h incubation on PDMS just to begin to form small colonies. Only ~ 10% of the substrate was populated by this time and at 18 h only ~ 15% of the visible surface was populated. There were no signs of any cells immobilised within the wells of the substrate and thus AFM scans would most likely have been unsuccessful. Conversely, glass showed great promise as a surface that allowed successful growth and division. Cells grew quickly and by 2 h there was ~ 15% coverage of the surface and by 4 h a coverage of ~ 70%. This suggests that even during the ~ 4 h experiments performed in Chapter 6, there would have been a plentiful supply of cells for analysis.

Without the confines of an immobilising well however, SA cells would simply roll away during AFM scans – a problem that we frequently discovered. We had attempted to pattern 1 – 2 µm diameter circular wells into glass surfaces using the same photolithographic methods as used for silicon, but we were unsuccessful (data not shown). It was found that during the UV-alignment step required to expose the photomask the UV-light was internally reflected through the glass leading to sporadic and incorrect pattern geometries. Glass and silicon share very similar chemical and mechanical properties (Trott and Shorey, 2011). Given the lack of growth on patterned silicon surfaces during 15 h scans (Chapter 6.2.1.3) this may suggest that the confines of the wells were the limiting factor for growth and

division (although the cells on the surface of the silicon and not within the wells also displayed no signs of growth). Had we been successful with patterning glass, a similar lack of growth and division may have been encountered.

7.3.1.1 Surface chemistry

In addition to the confines of an immobilising well potentially disrupting the growth and division of SA cells we explored the effects of substrate surface chemistry. Researchers tested a range of hydrophilic and hydrophobic surfaces for their abilities to become functionalised with bovine serum albumin (BSA) or APTES, and for how well bacteria could adhere (Cunliffe *et al.*, 1999). *Listeria monocytogenes* and *E.coli* showed less adhesion to hydrophilic, uncharged substrates, whereas SA and *Salmonella typhimurium* were shown to preferentially adhere to these surfaces, suggesting a different mechanism of cell attachment occurred, and may be related to the surface chemistry of the bacteria themselves. Preadsorption of BSA to selected surfaces resulted in reduced cell adhesion and the authors suggest that coating BSA onto hydrophilic surfaces may be an effective method to prevent bacterial attachment (Cunliffe *et al.*, 1999). We treated glass, silicon and PDMS to O_2-plasma and coated them with porcine serum at varying concentrations and under a variety of different conditions and timings (data not shown) (Chapter 3.22). We had postulated that the abundance of proteins within the serum might have facilitated immobilisation and growth. However, no observable benefits were realised. Previous work in our laboratory did capture division events within SA using AFM (Kailas *et al.*, 2009). The author mentions that the reactive ion-etching step was not always performed during the lithographic patterning of their wafers. This step is used as a final cleaning method and is used to remove any final traces of the photoresist material (BPRS100). There are a number of organic compounds in this material, including propylene glycol, ethyl acetate, and various ethers, esters and ketones. We considered if these may have acted as an alternative carbon source for the growing bacterium and facilitated the observed division events. We spin-coated glass, silicon and PDMS with this photoresist and inoculated SA under varying conditions and time scales, but no obvious benefits were conferred (data not shown).

7.3.1.2 Nutrient availability

Researchers considered the normal colonisation of SA in the human nose and created a synthetic nasal medium based on the analysis of human nasal secretions (Krismer *et al.*, 2014). The human body could be considered as a chemostat, where the nutrients that facilitate bacterial adhesion and growth are constantly being replenished. Conversely, the nutrients in a culture medium in a test tube, or a 35 mm culture dish will be constantly decreasing. When culturing SA in normal medium vs. their synthetic medium the authors found over 340 genes were either up-regulated, or down-regulated with more than a 2-fold difference. They conclude that normal growth medium thus represents a very artificial condition for SA colonisation (Krismer *et al.*, 2014). When utilising agarose as a substrate in their microfluidic studies Moffit and colleagues dissolved amino acids into the matrix and following 5 h incubation removed them, to tailor the growth of various amino acid-deficient auxotrophic bacteria (Moffitt, Lee and Cluzel, 2012a). In this regard, being able to supplement the confining substrate with additional growth promoters offers a distinct advantage over the use of PDMS or silicon wafers in our studies. The use of a flow cell with our substrates may have improved our success, and the use of agarose was tested as a suitable substrate.

7.3.1.3 Agarose substrates

Although we found that 6% (w/v) was an optimal concentration to allow for some transfer of the lithographic patterns, it still did not allow for wells deeper than 300 nm, from an expected 750 nm. Because agarose is not chemically bound to the glass slide or plastic tissue culture dish it could be easily displaced. A similar finding was observed for Moffit and colleagues where their cells could occasionally lift the agarose and grow colonies underneath (Moffitt, Lee and Cluzel, 2012a). We found that the agarose in our work suffered with similar problems – although using agarose as a glue to bind the patterned agarose did offer some success (section 7.2.2). We showed that agarose is more porous than PDMS and would have allowed for solute transfer, and perhaps quorum-sensing chemicals to migrate throughout the matrix. Despite this, we could not immobilise SA suitably for AFM scans and thus were unable to test these properties.

7.3.2 Successful growth and division on silicon surfaces

By using silicon wafers with a different, non-spherical and less confining patterning, we were able to successfully observe unperturbed growth and division of SA using the AFM. The silicon wafer was prepared using standard contact mask photolithography (Chapter 3.7). There were no surface coatings added, or any other chemical changes performed, i.e. 0_2 plasma treatment. Additionally, the photoresist was removed. Although our experiments were performed over longer time scales, of up to over 9 hours in total, our previous 15 h AFM study of unmodified silicon (with 1 µm diameter spherical wells) showed no evidence of growth or division. Thus, the only difference between this substrate and all our others were the lack of confining wells. Based on this observation we must conclude that the limiting factor was mechanical in nature and that the confines of the immobilising wells led to the lack of growth and division with SA.

7.3.2.1 Mechanical properties of growing and dividing cells

We successfully observed SA growth and division in five independent experiments using the AFM. We statistically analysed 15 cells at various stages of growth and division, including newly generated daughter cells, and cells undergoing swelling prior to generating a daughter cell. We obtained a mean elastic modulus of 61 ± 42 kPa. The mean stiffness was reported as 13 ± 6.5 nN/µm. Both of these values are ~ 5-fold lower than we previously obtained in non-actively growing cells at 1 nN loading forces. There are specific factors to consider why this may be; (i) Actively growing cells may be more elastic (thus softer) to allow for septation and generation of daughters. (ii) In addition to, or independent of the growth state, the cells immobilised within tight pores may report greater moduli and stiffness due to metabolic events, or the AFM data may simply be affected by the influence of the substrate. (iii) Due to the lack of confining wells the freely mobile bacteria are more easily pushed away from the scanning probe, thus not providing enough opportunity to challenge the cell wall. (iv) The loading force of 0.5 nN is not great enough to challenge the cell wall to the same extent as 1 nN loading forces. It may be that all of these considerations were involved to some extent. We tested the influence of 0.5 and 1 nN loading forces on two separate PDMS substrates and found that the reported moduli were either around half of those reported at 1 nN, or the polar opposite was also reported, with moduli twice as great at 0.5 nN than compared to 1 nN loading. Both substrates reported a consistent ~ 1.3

MPa at 1 nN. This suggests that we cannot trust the data gathered at 0.5 nN and that the same limit must apply for the SA cell data at 0.5 nN.

When analysing the changing moduli and stiffness over various time scales the data were more widely changing than previously observed with non-actively growing cells at different time points (Chapter 6.2.2.3). This may reflect the actively growing nature of the cell wall or the problems with the freely mobile cells and the reduced loading forces.

7.3.2.2 Mechanical properties of dying cells

Following challenge with oxacillin the previously mobile cells, that were seen to interact with the AFM probe, resulting in numerous imaging artefacts, showed an initial increase in growth and division, leading to a newly generated daughter cell being quickly displaced. The two remaining cells displayed a lot of mobility for 30 min (enough for the generation of a further cell) before both cells very quickly assumed a well-defined spherical morphology. They maintained this morphology for a further 30 min with no mobility, despite the continued and repeated scanning of the AFM probe. After another 30 min both cells were seen to briefly swell and almost immediately the AFM images became streaked with no obvious mobility of either cell. These artefacts continued for 1 h before both cells were displaced. We carefully posit that these events were cell death. Although the streak-like artefacts were similar to those observed with freely mobile cells, neither cell appeared to be freely mobile, suggesting that the streaks were degradation events captured by the probe. This was further supported 15 min prior to cell displacements (45 min after the degradation events began) where a ~ 300 nm protrusion appeared to exit the top of a cell, suggesting damage to the cell wall. However, during lysis and antibiotic-induced cell wall damage one would expect the elastic modulus to decrease. Indeed, we found a greater than 50% reduction in elastic modulus of antibiotically-challenged cell wall sacculi after 60 min than compared to the native sacculi (Chapter 6.2.5.7). Conversely, the apparently lysing cell showed no significant difference in modulus when compared to the pre-challenged t = 0 min scan, and actually reported an increased elastic modulus just prior to being displaced. This could either suggest that the cell was not dying, or further highlight the problems associated with cell mobility and 0.5 nN loading forces. Moreover, it is not unusual for bacteria to retain their integrity for a short time following cell death (Suo *et al.*, 2009).

7.3.3 Conclusions to this study

There is little evidence of morphologically sound, and unperturbed growth and division of immobilised bacteria, imaged by AFM, in the literature. As previously discussed, we have shown SA cells growing and septating during AFM imaging (Kailas *et al.*, 2009). However, in that work the cells appeared to be constrained and changes in the cellular morphology lead to the bacteria taking the shape of the confining pore. The small enlargement of a septal hole observed by the Beveridge group (Touhami, Jericho and Beveridge, 2004) suggests some level of cellular growth processing, and the invagination of the septal region (Turner, Thomson, *et al.*, 2010) also demonstrates some amount of cellular growth. To the best of our knowledge we have shown, for the first time, true unperturbed growth and division of SA captured by the AFM, in addition to obtaining mechanical data during cell growth, division and potential death. Following a large body of work performed in this chapter and the previous chapter, we tested a range of substrates that would confer the ability for cell immobilisation and growth. In contrast to our previous work (Kailas *et al.*, 2009) we discovered that SA does not appear to grow or divide when confined in spherical wells of a similar diameter to itself, and by testing the chemistry of patterned and non-patterned substrates it may suggest that any lack of observed growth and division is mechanical, and not chemical in nature.

By using silicon wafers with pillars of ~ 750 nm in height, and separated by ~ 2 µm in the *XY* directions we afforded the SA cell the ability to bind to a pillar (which appears to be a required step) whilst providing adequate room for cell swelling and daughter cell generation. Following the first use of this silicon wafer we successfully repeated the experiments five times, capturing growth and division each time.

7.3.4 Limitations to this study

Despite the successes with growth and division we were however, unable to repeat the antibiotic challenge experiment, and the data reported here came from a single experiment. Thus, we have drawn conclusions about the potential cell death from a single study and the results should be interpreted with caution. The structural detail of the silicon wafer that afforded growth and division is paradoxically also the weakness of this study. By allowing the cells the freedom to move this also makes the mechanical data unreliable. We assume

that the 5-fold lower modulus and stiffness data reported here (than compared to those obtained with immobilised cells) arise because of this freedom of movement, as cells are likely pushed away from the indenting probe. This problem is further compounded by the requirement to indent with the reduced loading force of 0.5 nN, where all our previous data were gathered at 1 nN loading forces. Thus there exists some ambiguity between both data sets. Of course, it may be that the reduced values of moduli and stiffness are the true values and that previous values arose due to the influence of the substrate and confining wells. Actually, the Sneddon contact model fitting was more faithful to the F-D curves at 0.5 nN than with the F-D curves gathered at 1 nN. However, because a number of F-D curves reported an elastic modulus ~ 300 kPa, which is similar to the mean modulus at 1 nN, we think that they may reflect the true value and, therefore, that these new data may not be correct.

All of the mechanical data reported here rely on a set of assumptions, notably the conical half-angle geometry that we have previously discussed. In order for other investigators to faithfully repeat our work they would need to fully characterise the mechanical properties of their substrate and the AFM tip geometries, or closely follow our methods.

By far, the biggest problem with obtaining growth and division events, as seen here, is the need for extended incubation times of the bacteria. We have shown that when using PDMS or silicon wafers, the bacteria require at least 7 – 10 h of incubation. When considering that SA needs ~ 1 h 30 min to reach a mid-exponential growth phase, it will require ~ 9 – 12 h of attended experimentation to achieve these results. Until such time that a more favourable substrate could be found, resulting in quicker cell growth, or automated AFM becomes widespread in use, the experimenter has to be prepared for lengthy sessions.

Chapter 8

General discussion

8.1 Substrate design for immobilisation of bacteria

This study was designed to elucidate the mechanical properties of the Gram-positive, opportunistic pathogenic bacterium *Staphylococcus aureus* (SA) using atomic force microscopy (AFM). Building on the previous work performed in our laboratory (Kailas *et al.*, 2009; Bailey *et al.*, 2014) we designed a range of lithographically patterned silicon substrates with diverse topographical features on the order of nanometre and micron length scales. By adjusting the photoresist coating during the lithographic processing we could choose whether to obtain silicon substrates with raised, or inverted topographies. The silicon designs with inverted (wells) topographies allowed for bacterial sample deposition directly onto the surface, or afforded the opportunity to cast liquid polydimethylsiloxane (PDMS) from the silicon, leaving PDMS with patterned pillars, which faithfully resembled the lithographic patterning. Conversely, the opposite was true for the silicon substrate with raised topographies. Here, bacterial samples could be seeded onto the raised (pillar) topographies, or PDMS could be cast to faithfully reproduce imprinted patterns. We had hoped that PDMS would be a suitable substrate, allowing for efficient and repeatable immobilisation of SA. Sadly, the bacteria did not appear to find PDMS a favourable substrate, with low numbers of immobilised cells routinely observed. Silicon was found to be a more efficient substrate and cells were regularly immobilised within the wells, or between the raised pillars. However, both substrates successfully allowed for repeated scanning with the AFM, and ~ 50% of the cells analysed in this study were immobilised on each substrate.

8.2 Mechanical properties of PDMS

We identified that adjusting the half-angle geometry of the cantilever tip has a marked influence on the reported moduli of the sample under investigation. The elastic modulus of PDMS has been widely studied and determined to be ~ 1 – 3 MPa. When using the AFM proprietary software half-angle default, or AFM cantilever manufacturer default half-angles (15° and 17.5° respectively) within the software-included Hertzian contact mechanics

models we found a mean elastic modulus up to ~ 100 MPa, which is two orders of magnitude greater than reported. We performed multiple analyses of PDMS using tensile testing, dedicated nanoindentation and further AFM indentation. Tensile testing reported an elastic modulus of ~ 1.3 MPa, which perfectly aligns with many of the literature values. We found that applying an 85° conical half-angle in the Sneddon contact mechanics model routinely produced the tensile testing value of ~ 1.3 MPa modulus. The contact model required a conical half-angle of 85° to report this value at 10 nm indentations, decreasing to 55° at 100 nm indentations in order to keep the elastic modulus ~ 1.3 MPa. In this regard, we treated the PDMS as a calibrant for the mechanical analysis of the SA cell wall, and made the assumption that both materials would deform in a similar manner during AFM indentation.

8.3 Molecular characterisation of PDMS

Nanoindentation literature often suggests that the surface of PDMS is stiffer than the bulk material. We found similar results when performing nanoindentation but identified that the initial point of contact between the probe and the PDMS sample was extremely difficult to identify. The probe typically travelled depths on the order of hundreds of nanometres before the instrument was able to recognise the sample had been indented, leading to incorrect calculations of modulus. This would appear to be a widely reported problem with soft materials, which require piconewton or low nanonewton forces to indent to shallow depths. Conversely, the nanoindenter typically performs indentations on the order of millinewtons or newtons on very hard surfaces. We obtained molecular resolution AFM images of the structural arrangement of the siloxane chains at the surface and sub-surface regions up to millimetre depths. There were few discernable differences, suggesting that the mechanical properties of the surface should be similar to the bulk material – leading us to further trust our assumption of an unchanging modulus between the surface and up to 80 nm indentation depths of PDMS, and our half-angle characterisations. To the best of our knowledge, this is the first time that this level of molecular resolution has been obtained.

8.4 Cantilever tip characterisation

Extensive scanning electron microscopy (SEM) revealed that the manufacturer-specified half-angle of 17.5° was only valid at large length scales and that the geometry markedly

changed at 100 nm from the tip apex, with a large flattening of the half-angle. The angle became flatter still towards the final 10 nm of the tip apex. Using the angle data from the 10 – 80 nm indentations of PDMS we drew the required half-angles at 10, 50 and 100 nm from the tip apex on SEM micrographs to visually determine whether the angles faithfully followed the geometry of the cantilever tip and if they appeared to represent the likely deformation of PDMS. When indented, materials either pile up around the indenter, or sink in, leaving a non-contacting depression around the indenter. PDMS displays sink-in and by comparing to images and data in the literature, our approximations of indenter half-angle geometries supported this behaviour.

We also performed the technically challenging task of scanning an AFM cantilever tip with the AFM. This required the removal, and immobilisation of an isolated cantilever tip and very careful scanning to obtain topographic data, which were analysed for the tip apex geometry at the nanometre length scale. Typically, shallow indentations are considered to be spherical in nature with the geometry changing to conical at increased indentations. We found that the F-D curves generated from indentations of PDMS and SA were fitted with greater accuracy when treating the indenter as conical, with near-perfect fittings in many cases, compared to ill fitting with a spherical geometry. Thus, we postulate that the cantilever tip was better described as conospherical, and remained in the conical regime for the small indentations that we performed. However, this may not be true for all cantilever tip geometries, and the experimenter should take steps to accurately define their indenter geometry if a different cantilever were to be used.

8.5 Mechanical properties of SA

Using Quantitative Imaging (QI™) on the NanoWizard AFM (JPK) we calculated and statistically analysed the elastic modulus (Pascal) and the stiffness (N/m) of the bacterial cell wall at 10 nm indentations. Additionally, we performed larger indentations of ~ 70 nm to determine the influence of intracellular turgor pressure. The elastic modulus was calculated with the widely used Hertzian contact model. Whilst this model has its limitations, notably that the cell is treated as linearly elastic, isotropic and homogenous (which cells rarely are), and that surface forces and adhesion are not accounted for, it is still widely adopted in the materials sciences and AFM communities. We minimised these limitations by only analysing data with a relatively distinct deflection gradient (minimising the influence of short range

surface forces) and where there were no signs of adhesion on the force-distance (F-D) curves. In addition to these analyses we also calculated the stiffness of the cell wall, and whole cell stiffness by drawing tangents to the indentation curve at 10 ± 2 nm, or at the steepest portion of the indentation curve respectively. This allowed us to gain an insight into the mechanical properties of the cell, whilst avoiding any potential ambiguity from the Hertzian contact models. We expanded this further by analysing the applied forces (from the AFM) that were required to indent the cell to the specified depths of interest. These gave us an alternative view into the mechanical properties of the cell and were free from any potential ambiguities of both the contact models and of drawing tangents to a curve. Prior to achieving successful growth and division we analysed the cells at different time points (t = 0 h and t = 1.5 h) to determine if any mechanical changes may have occurred. This expanded upon our previous work where we considered only single time points (Bailey *et al.*, 2014). The previous work however, identified specific regions of the cell wall and characterised differences in their stiffness. This current study did not seek to characterise specific regions, although the sampling of random regions and the spread of our data must include these differences. We studied and compared the modulus and stiffness of extracted cell wall sacculi and found them to be ~ 40 % lower than the intact cell wall, suggesting a role of turgor induced stress stiffening. Further, sacculi from cells grown in the presence of methicillin were reduced by a further ~ 60% compared to native sacculi confirming the assumption that antimicrobial challenge leads to a reduction in the integrity of the cell wall.

The elastic moduli of SA are widely dispersed in the literature, with orders of magnitude variations. When scrutinising the published methods there does not appear to be a single, (or range of) methods to offer a suitable explanation. Incorrectly matching the spring constant of the AFM cantilever and the sample stiffness may be one causative factor, whilst differences in sample preparation and/or instrumentation could be another. We believe that the indenter geometry exerts the greatest influence on the reported moduli. Whilst some authors have chosen to adopt the manufacturer-specified geometries, others are not so clear in their methods. However, our tip characterisation studies showed that the indenter geometry was markedly different towards the tip apex and did not match the manufacturer-specified geometry. Using the calculated conical half-angle of 85° dramatically reduced the reported moduli for the SA cell wall, and whole cell respectively.

8.6 Growth and division of SA

Our previous work (Kailas *et al.*, 2009) successfully allowed for growth and division of SA cells immobilised within tightly confining silicon wells. However, the cells were seen to adopt the shape of the well and although multiple septa were formed, the cells remained as a conjoined mass, with no clear daughter cell separations evident. This current study could not replicate these results when cells were confined tightly, or relatively loosely on silicon or PDMS, and the reasons why remain elusive. We explored whether extended timescales could lead to growth and division on silicon, glass and PDMS. Our results suggested that silicon and PDMS (both the flat surface regions and the confining wells) were not amenable, although some growth did occur on PDMS after ~ 6 h, but increased by very little up to 18 h. Glass, by contrast, allowed for growth and division from as little as 1 h post seeding, and by 18 h cells became over confluent. The glass was smooth, with no topographic patterning and we proposed that the lack of confining wells may have facilitated growth, and thus, that the mechanical constraints of the patterned substrates were the limiting factor in the failure of SA growth. This hypothesis would need to be tested further, as we equally found little evidence of growth and division on the smooth silicon surface. It may be that certain surfaces require longer incubation periods before the bacteria are able to grow. These may be related to protein synthesis, quorum sensing, or other unknown processes.

We were able to show unperturbed growth and division of SA, with clearly defined daughter cell generations in a number of experiments, and to the best of our knowledge this is the first time that this has been successful for analysis with the AFM. These results were obtained by seeding cells on patterned silicon substrates, but with a different topographical geometry to the silicon or PDMS used throughout most of this study, and by adopting vastly longer timescales for study. Cells were left for 4 – 6 h post-seeding to allow for any cellular processes that may be required to facilitate adhesion and growth. Rather than round pillars or wells, this substrate had square pillars ~ 2.5 µm in diameter, although with a similar ~ 750 nm height to the other pillars or wells. However, these pillars were separated by channels (or gutters) around 2 µm in width. Daughter cells were seen to grow and divide into these channels, as long as at least one of the cells was immobilised on a pillar. Although successful at facilitating growth and division, the loosely confining geometry minimised the AFM loading forces that we were able to use. Previously, all of our mechanical data had been

obtained at loading forces of 1 nN, but forces greater than 0.5 nN routinely displaced cells on this substrate. The resulting mechanical data were not able to be directly compared to our previous data, and were prone to errors, thus the features that afforded successful growth and division were paradoxically responsible for limitations with our reported data.

In addition to the growth and division of SA we also observed events that may be cell death. We challenged the medium of actively growing cells with the β-lactam antimicrobial oxacillin. Immediately following the challenge a pair of dynamically moving cells were seen to initially stabilise and remained immobile for ~ 1 h. Following this period of inactivity a rapid cell swelling was followed by a period of apparent degradation of one of the cells before it was eventually displaced. We unsuccessfully attempted to repeat this experiment three more times and currently we have only this single experiment from which to draw any conclusions. We would need to find a reproducible method to obtain more data before a firm conclusion could be made.

8.7 Future work

Further elucidation of the mechanical properties of the bacterial cell wall, particularly during or following antimicrobial challenge, may lead to a better understanding of the cellular processes of cell wall growth and remodelling. Currently, obtaining these data with the AFM is a laborious process, both during acquisition and particularly with the post-processing of the F-D curves. Advances in scanning speeds will improve these outcomes, and automated AFM systems may further enhance data acquisition. The need for extended timescales to allow for growth and division on unfavourable substrates could be improved by finding a surface that better supports cell immobilisation and growth. A porous polymer, such as agarose could provide adequate provision for the migration of quorum sensing chemicals and also provide a carbon source for a growing bacterium, minimising any influence of nutrient depletion with growth media. It would be prudent to explore the lithographic patterning of agarose, perhaps by spin-coating a thin layer onto an existing support, such as patterned silicon. The ~ 750 nm tall pillars and the ~ 2 µm channels of the *Bacillus* shaped silicon wafer supported growth and division, but also resulted in dynamic movements of the cells which lead to difficulty obtaining reliable F-D curves. A reduction in the height of the pillars to perhaps ~ 250 nm may still allow for cellular immobilisation but possibly lead to the cells resting on the surface of the silicon wafer, allowing for less movement when

indented by the AFM probe. Given that SA is routinely found on human epithelium, some kind of epithelial support (perhaps a synthetic skin) substrate may confer successful, and quicker growth.

The splitting of daughter cells occurs on millisecond timescales and it is unlikely the AFM would ever be able to capture these events. However, combining localisation microscopy and AFM may be able to answer some important questions of antimicrobial-mediated cell wall degradation. A fluorescently labelled antimicrobial compound could be targeted to the cell wall and the AFM probe could be directed to that location to capture images and mechanical data at a molecular resolution. Our laboratory is now obtaining molecular resolution of antimicrobially-challenged sacculi, to correlate any structural changes with the mechanical data from this study. The structural models of peptidoglycan arrangement are still unresolved. More high resolution characterisations are required in this regard.

It would be interesting to modify the intracellular turgor pressure, by osmotically challenging cells and monitor any changes in the elastic modulus and stiffness of the cell wall. Obtaining cryo-EM sections of these cells may lead to a better understanding of the role of the periplasmic space and its influence (if any) in mitigating turgor stresses to the cell wall. It would be advantageous to fully determine if the bacterial cell wall sinks in when indented, as we have assumed. Advances in scanning electron microscopy may enable the investigator to visualise an indenting probe on the surface of the cell and capture images of the behaviour of the cell wall.

Our AFM tip geometry characterisation considered only one type of probe. Repeating our work with a range of different indenter geometries would help to further support, or refute our data. Additionally, testing the model on alternative substrates with well-characterised moduli would be a sensible approach. The substrate should ideally be a soft material so that the moduli are similar to the bacterial cell wall. A rigid substrate, such as polycarbonate would be a poor choice as it would not be well matched to the cell modulus and a very stiff cantilever would be required to accurately define these data, which would be unsuitable for analysis of a soft cell. To further test our model, other Gram-positive bacterial species should be assayed, including SA mutants, with genetic constructs that are known to confer changes to the cell wall.

References

Abdelhady, Hosam G., Allen, Stephanie, Ebbens, Stephen J., Madden, Claire, Patel, Nikin, Roberts, Clive J. and Zhang, Jianxin (2005) 'Towards nanoscale metrology for biomolecular imaging by atomic force microscopy', *Nanotechnology*, 16(6), pp. 966–973.

Aguayo, S., Donos, N., Spratt, D. and Bozec, L. (2015) 'Nanoadhesion of Staphylococcus aureus onto titanium implant surfaces', *Journal of Dental Research*, 94(8), pp. 1078–1084.

Aguayo, S., Strange, A., Gadegaard, N., Dalby, M. J. and Bozec, L. (2016) 'Influence of biomaterial nanotopography on the adhesive and elastic properties of Staphylococcus aureus cells', *RSC Advances*. Royal Society of Chemistry, 6(92), pp. 89347–89355.

Alsteens, David, Dupres, Vincent, Yunus, Sami, Latge, Jean-Paul, Heinisch, Jurgen J. and Dufrene, Yves F. (2012) 'High-resolution imaging of chemical and biological sites on living cells using peak force tapping atomic force microscopy', *Langmuir*, 28(49), pp. 16738–16744.

Aminov, Rustam I. (2010) 'A brief history of the antibiotic era: Lessons learned and challenges for the future', *Frontiers in Microbiology*, 1, pp. 1–7.

Ando, Toshio, Uchihashi, Takayuki and Scheuring, Simon (2014) 'Filming biomolecular processes by high-speed atomic force microscopy', *Chemical Reviews*, 114(6), pp. 3120–3188.

Armani, Deniz, Liu, Chang and Aluru, Narayan (1999) 'Re-configurable fluid circuits by PDMS elastomer micromachining', *Proceedings of 12th IEEE International Conference on Micro Electro Mechanical Sytems*, pp. 222–227.

Arnoldi, Markus, Fritz, Monika, Bäuerlein, Edmund, Radmacher, Manfred, Sackmann, Erich and Boulbitch, Alexei (2000) 'Bacterial turgor pressure can be measured by atomic force microscopy', *Physical Review E - Statistical Physics, Plasmas, Fluids, and Related Interdisciplinary Topics*, 62(1 B), pp. 1034–1044.

Bailey, Richard G., Turner, Robert D., Mullin, Nic, Clarke, Nigel, Foster, Simon J. and Hobbs, Jamie K. (2014) 'The interplay between cell wall mechanical properties and the cell cycle in Staphylococcus aureus', *Biophysical Journal*, 107(11), pp. 2538–2545.

Bélanger, Marie Claire, Marois, Yves, Belanger, Marie Claire and Marois, Yves (2001) 'Hemocompatibility, biocompatibility, inflammatory and in vivo studies of primary reference materials low-density polyethylene and polydimethylsiloxane: A review', *Journal of Biomedical Materials Research*, 58(5), pp. 467–477.

Benitez, Rafael and Toca-herrera, José L. (2014) 'Looking at cell mechanics with atomic force microscopy: Experiment and theory', *Microscopy Research and Technique*, 77(11), pp. 947–958.

Berne, Cécile, Ma, Xiang, Licata, Nicholas A., Neves, Bernardo R. A., Setayeshgar, Sima, Brun, Yves V. and Dragnea, Bogdan (2013) 'Physiochemical properties of caulobacter crescentus holdfast: A localized bacterial adhesive', *Journal of Physical Chemistry B*, 117(36), pp. 10492–10503.

Beveridge, T. J. (1981) 'Ultrastructure, Chemistry, and Function of the Bacterial Wall', *International Review of Cytology*, 72, pp. 229–317.

Bhushan, Bharat (1998) 'Contact mechanics of rough surfaces in tribology: multiple asperity contact', *Tribology Letters*, 4, pp. 1–35.

Binnig, G., Quate, C. F. and Gerber, C. (1986) 'Atomic Force Microscope', *Physical Review Letters*, pp. 930–933.

Binnig, G., Rohrer, H., Gerber, C. and Weibel, E. (1982) 'Surface Studies by Scanning Tunneling Microscopy', *Physical review letters*, 49(1), pp. 57–61.

Birkenhauer, Eric and Neethirajan, Suresh (2014) 'Surface Potential Measurement of Bacteria Using Kelvin Probe Force Microscopy', *Journal of Visualized Experiments*, (93), pp. 1–8.

Bisson-Filho, Alexandre W., Hsu, Yen-Pang, Squyres, Georgia R., Kuru, Erkin, Wu, Fabai, Jukes, Calum, Sun, Yingjie, Dekker, Cees, Holden, Seamus, VanNieuenhze, Michael S., Brun, Yves V and Garner, Ethan C. (2017) 'Treadmilling by FtsZ Filaments Drives Peptidoglycan Synthesis and Bacterial Cell Division', *Science*, 355, pp. 739–743.

Boneca, Ivo G., Huang, Zhi-heng, Gage, Douglas A. and Tomasz, Alexander (2000) 'Characterization of Staphylococcus aureus Cell Wall Glycan Strands , Evidence for a New β - N- Acetylglucosaminidase Activity *', *The Journal of biological chemistry*, 275(14), pp. 9910–

9918.

Bonilla, M. R., Stokes, J. R., Gidley, M. J. and Yakubov, G. E. (2015) 'Interpreting atomic force microscopy nanoindentation of hierarchical biological materials using multi-regime analysis', *Soft Matter*. Royal Society of Chemistry, 11(7), pp. 1281–1292.

Bosdriesz, Evert, Molenaar, Douwe, Teusink, Bas and Bruggeman, Frank J. (2015) 'How fast-growing bacteria robustly tune their ribosome concentration to approximate growth-rate maximization', *FEBS Journal*, 282(10), pp. 2029–2044.

Boussinesq, J. (1885) *Application des potentiels à l'étude de l'équilibre et du mouvement des solides élastiques*. Paris: Gauthier-Villars.

Braunsmann, Christoph, Seifert, Jan, Rheinlaender, Johannes and Schäffer, Tilman E. (2014) 'High-speed force mapping on living cells with a small cantilever atomic force microscope', *Review of Scientific Instruments*, 85(7307), pp. 1–8.

Brown, Lisa, Wolf, Julie M., Prados-Rosales, Rafael and Casadevall, Arturo (2015) 'Through the wall: Extracellular vesicles in Gram-positive bacteria, mycobacteria and fungi', *Nature Reviews Microbiology*. Nature Publishing Group, 13(10), pp. 620–630.

Budynas, R. G. and Nisbett, J. K. (2010) *Shigley's Mechanical Engineering Design*. 9th edn, *Mechanical Engineering*. 9th edn. New York: McGraw-Hill Education.

Butt, H. J., Siedle, P., Seifert, K., Fendler, K., Seeger, T., Bamberg, E., Weisenhorn, a. L., Goldie, K. and Engel, A. (1993) 'Scan speed limit in atomic force microscopy', *Journal of Microscopy*, 169(1), pp. 75–84.

Butt, Hans Jürgen, Cappella, Brunero and Kappl, Michael (2005) 'Force measurements with the atomic force microscope: Technique, interpretation and applications', *Surface Science Reports*, 59, pp. 1–152.

Celik, Emrah, Oterkus, Erkan, Guven, Ibrahim and Madenci, Erdogan (2009) 'Mechanical characterization of ultra-thin films by combining AFM nanoindentation tests and peridynamic simulations', *Proceedings - Electronic Components and Technology Conference*, pp. 262–268.

Chaibenjawong, Plykaeow and Foster, Simon J. (2011) 'Desiccation tolerance in Staphylococcus aureus', *Archives of Microbiology*, 193(2), pp. 125–135.

Chang, J., Coffman, L. and Kim, S. J. (2017) 'Inhibition of d-Ala incorporation into wall teichoic acid in: Staphylococcus aureus by desleucyl-oritavancin', *Chemical Communications*. Royal Society of Chemistry, 53(41), pp. 5649–5652.

Charitidis, C. A. and Koumoulos, E. P. (2012) 'Nanomechanical properties and nanoscale deformation of PDMS nanocomposites', *Plastics, Rubber and Composites*, 41(2), pp. 88–93.

Charitidis, Costas (2011) 'Nanoscale Deformation and Nanomechanical Properties of Soft Matter Study Cases: Polydimethylsiloxane, Cells and Tissues', *ISRN Nanotechnology*, 2011(4), pp. 1–13.

Chen, J. (2014) 'Nanobiomechanics of living cells: a review', *Interface Focus*, 4(2), pp. 20130055–20130055.

Cheng, Mou-chi, Leske, Austin T., Matsuoka, Toshiki, Kim, Byoung C., Lee, Jaesung, Burns, Mark A., Takayama, Shuichi and Biteen, Julie S. (2013) 'Super-Resolution Imaging of PDMS Nanochannels by Single- Molecule Micelle-Assisted Blink Microscopy', *The Journal of Physical Chemistry B*, 117, pp. 4406–4411.

Chopinet, L., Formosa, C., Rols, M. P., Duval, R. E. and Dague, E. (2013) 'Imaging living cells surface and quantifying its properties at high resolution using AFM in QI^{TM} mode', *Micron*. Elsevier Ltd, 48, pp. 26–33.

Cleveland, J. P., Manne, S., Bocek, D. and Hansma, P. K. (1993) 'A nondestructive method for determining the spring constant of cantilevers for scanning force microscopy', *Review of Scientific Instruments*, 64(2), pp. 403–405.

Cleveland, Jason P., Proksch, Roger, Higgins, Michael J., McEndoo, S. and Polcik, Martin (2006) 'Non-invasive Determination Of Optical Lever Sensitivity in Atomic Force Microscopy', *Review of Scientific Instruments*, 77(1), pp. 13701–4.

Cohen, Sidney R. and Kalfon-cohen, Estelle (2013) 'Dynamic nanoindentation by instrumented nanoindentation and force microscopy : a comparative review', *Beilstein Journal of Nanotechnology*, 4, pp. 815–833.

Colville, Keegan, Tompkins, Nicolas, Rutenberg, Andrew D. and Jericho, Manfred H. (2010) 'Effects of poly(L-lysine) substrates on attached escherichia coli bacteria', *Langmuir*, 26(4), pp. 2639–2644.

Costa, Sofia Santos, Viveiros, Miguel, Amaral, Leonard and Couto, Isabel (2013) 'Multidrug Efflux Pumps in Staphylococcus aureus: an Update.', *The open microbiology journal*, 7(SPEC.ISSUE.1), pp. 59–71.

Cross, Sarah E., Jin, Yu Sheng, Rao, Jianyu and Gimzewski, James K. (2007) 'Nanomechanical analysis of cells from cancer patients', *Nature Nanotechnology*, 2(12), pp. 780–783.

Cunliffe, D., Smart, C. a, Alexander, C. and Vulfson, E. N. (1999) 'Bacterial Adhesion at Synthetic Surfaces', *Applied and Environmental Microbiology*, 65(11), pp. 4995–5002.

D'Costa, Neill P. and Hoh, Jan H. (1995) 'Calibration of optical lever sensitivity for atomic force microscopy', *Review of Scientific Instruments*, 66(10), pp. 5096–5097.

D'Ercole, S., Spoto, G., Trentini, P., Tripodi, D. and Petrini, M. (2016) 'In vitro inactivation of Enterococcus faecalis with a led device', *Journal of Photochemistry & Photobiology, B: Biology*. Elsevier B.V., 160, pp. 172–177.

D'Souza, S. F. (2001) 'Microbial biosensors', *Biosensors and Bioelectronics*, 16(6), pp. 337–353.

Dague, E., Jauvert, E., Laplatine, L., Viallet, B., Thibault, C. and Ressier, L. (2011) 'Assembly of live micro-organisms on microstructured PDMS stamps by convective/capillary deposition for AFM bio-experiments', *Nanotechnology*, 22(39).

Davies, S. C. (2013) *Annual Report of the Chief Medical Officer, Volume Two, 2011, Infections and the rise of antimicrobial resistance*. London: Department of Health.

Dejun, M. A., Ong, Chung Wo, Jianmin, LIU and Jiawen, H. E. (2004) 'Determination of Young's modulus by nanoindentation', *Science in China Series E: Engineering & Materials Science*, 47(4), pp. 398–408.

Deng, Yi, Sun, Mingzhai and Shaevitz, Joshua W. (2011) 'Direct measurement of cell wall stress stiffening and turgor pressure in live bacterial cells', *Physical Review Letters*, 107(15), pp. 7–10.

Denisin, Aleksandra K. and Pruitt, Beth L. (2016) 'Tuning the Range of Polyacrylamide Gel Stiffness for Mechanobiology Applications', *ACS Applied Materials and Interfaces*, 8(34), pp. 21893–21902.

Derjaguin, B. V, Muller, V. M. and Toporov, Y. U. P. (1975) 'Effect of contact deformation on

the adhesion of particles.', *Journal of colloid and interface science*, 52(3), pp. 105–108.

Destrade, Michel, Murphy, Jerry G. and Rashid, Badar (2009) 'Differences in tension and compression in the nonlinearly elastic bending of beams', *International Journal of Structural Changes in Solids*, 1(1), pp. 73–81.

Deuschle, J. K., Buerki, G., Deuschle, H. M., Enders, S., Michler, Goerg H. and Arzt, E. (2008) 'In situ indentation testing of elastomers', *Acta Materialia*, 56(16), pp. 4390–4401.

Dhahri, Samia, Ramonda, Michel and Marlière, Christian (2013) 'In-Situ Determination of the Mechanical Properties of Gliding or Non-Motile Bacteria by Atomic Force Microscopy under Physiological Conditions without Immobilization', *PLoS ONE*, 8(4).

Dmitriev, Boris A., Toukach, Filip V, Schaper, Klaus-jürgen, Holst, Otto, Rietschel, Ernst T. and Ehlers, Stefan (2003) 'Tertiary Structure of Bacterial Murein : the Scaffold Model', *Journal of bacteriology*, 185(11), pp. 3458–3468.

Doerner, M. F. and Nix, W. D. (1986) 'A method for interpreting the data from depth-sensing indentation instruments', *Journal of Materials Research*, 1(4), pp. 601–609.

Doktycz, M. J., Sullivan, C. J., Hoyt, P. R., Pelletier, D. A., Wu, S. and Allison, D. P. (2003) 'AFM imaging of bacteria in liquid media immobilized on gelatin coated mica surfaces', *Ultramicroscopy*, 97, pp. 209–216.

Domke, J. and Radmacher, M. (1998) 'Measuring the elastic properties of thin polymer films with the atomic force microscope', *Langmuir*, 14(12), pp. 3320–3325.

Dong, Yalin, Liu, Xin Z., Egberts, Philip, Ye, Zhijiang, Carpick, Robert W. and Martini, Ashlie (2013) 'Correlation between probe shape and atomic friction peaks at graphite step edges', *Tribology Letters*, 50(1), pp. 49–57.

Drake, B., Prater, C. B., Weisenhorn, A. L., Gould, S. A. C., Albrecht, T. R., Quate, C. F., Cannell, D. S., Hansma, H. G. and Hansma, P. K. (1989) 'Imaging Crystals , Polymers , and Processes in Water with the Atmic Force Microscope', *American Association for the Advancement of Science*, 243(4898), pp. 1586–1589.

Ducker, William A. and Cook, Robert F. (1990) 'Rapid measurement of static and dynamic surface forces', *Applied Physics Letters*, 56(24), pp. 2408–2410.

Dufrene, Yves F., Martinez-Martin, David, Medalsy, Izhar, Alsteens, David and Muller, Daniel

J. (2013) ‘Multiparametric imaging of biological systems by force-distance curve-based AFM’, *Nature Methods*. Nature Publishing Group, 10(9), pp. 847–854.

Eaton, Peter, Fernandes, João C., Pereira, Eulália, Pintado, Manuela E. and Xavier Malcata, F. (2008) ‘Atomic force microscopy study of the antibacterial effects of chitosans on Escherichia coli and Staphylococcus aureus’, *Ultramicroscopy*, 108(10), pp. 1128–1134.

Ebenstein, D. M. and Pruitt, L. A. (2004) ‘Nanoindentation of soft hydrated materials for application to vascular tissues’, *Journal of Biomedical Materials Research*, 69A(2), pp. 222–232.

Feng, Guoping, Cheng, Yifan, Wang, Shu Yi, Borca-Tasciuc, Diana A., Worobo, Randy W. and Moraru, Carmen I. (2015) ‘Bacterial attachment and biofilm formation on surfaces are reduced by small-diameter nanoscale pores: How small is small enough?’, *npj Biofilms and Microbiomes*. Nature Publishing Group, 1(15022).

Flater, Erin E., Zacharakis-Jutz, George E., Dumba, Braulio G., White, Isaac A. and Clifford, Charles A. (2014) ‘Towards easy and reliable AFM tip shape determination using blind tip reconstruction’, *Ultramicroscopy*. Elsevier, 146, pp. 130–143.

Formosa-Dague, Cécile, Fu, Zhuo-Han, Feuillie, Cécile, Derclaye, Sylvie, Foster, Timothy J., Geoghegan, Joan A. and Dufrêne, Yves F. (2016) ‘Forces between Staphylococcus aureus and human skin’, *Nanoscale Horiz.*, 1(4), pp. 298–303.

Formosa, Cécile, Pillet, Flavien, Schiavone, Marion, Duval, Raphaël E., Ressier, Laurence and Dague, Etienne (2015) ‘Generation of living cell arrays for atomic force microscopy studies’, *Nature Protocols*, 10(1), pp. 199–204.

Foster, Timothy J. (2017) ‘Antibiotic resistance in Staphylococcus aureus . Current status and future prospects’, *FEMS microbiology reviews*, 41, pp. 430–449.

Francius, Grégory, Domenech, Oscar, Mingeot-Leclercq, Marie Paule and Dufrêne, Yves F. (2008) ‘Direct observation of Staphylococcus aureus cell wall digestion by lysostaphin’, *Journal of Bacteriology*, 190(24), pp. 7904–7909.

Francois, Jean Marie, Formosa, Cécile, Schiavone, Marion, Pillet, Flavien, Martin-Yken, Hélène and Dague, Etienne (2013) ‘Use of atomic force microscopy (AFM) to explore cell wall properties and response to stress in the yeast Saccharomyces cerevisiae’, *Current*

Genetics, 59(4), pp. 187–196.

Frederix, Patrick L. T. M., Bosshart, Patrick D. and Engel, Andreas (2009) 'Atomic force microscopy of biological membranes', *Biophysical Journal*. Biophysical Society, 96(2), pp. 329–338.

Fujii, Teruo (2002) 'PDMS-based microfluidic devices for biomedical applications', *Microelectronic Engineering*, 61–62, pp. 907–914.

Fukuma, T., Onishi, K., Kobayashi, N., Matsuki, a and Asakawa, H. (2012) 'Atomic-resolution imaging in liquid by frequency modulation atomic force microscopy using small cantilevers with megahertz-order resonance frequencies', *Nanotechnology*, 23(13), p. 135706.

Gad, M. and Ikai, A. (1995) 'Method for immobilizing microbial cells on gel surface for dynamic AFM studies', *Biophysical Journal*, 69(6), pp. 2226–2233.

Gavara, Nuria (2017) 'A beginner's guide to atomic force microscopy probing for cell mechanics', *Microscopy Research and Technique*, 80(1), pp. 75–84.

Gazzè, Salvatore A., Saccone, Loredana, Smits, Mark M., Duran, Adele L., Leake, Jonathan R., Banwart, Steven A., Ragnarsdottir, K.Vala and McMaster, T. J. (2013) 'Nanoscale Observations of Extracellular Polymeric Substances Deposition on Phyllosilicates by an Ectomycorrhizal Fungus', *Geomicrobiology Journal*, 30(8), pp. 721–730.

Giesbrecht, Peter, Kersten, Thomas and Maidhof, Heinrich (1998) 'Staphylococcal Cell Wall : Morphogenesis and Fatal Variations in the Presence of Penicillin', *Microbiology and Molecular Biology Reviews*, 62(4), pp. 1371–1414.

Giesbrecht, Peter, Kersten, Thomas, Maidhof, Heinrich and Wecke, Jörg (1997) 'Two alternative mechanisms of cell separation in staphylococci: One lytic and one mechanical', *Archives of Microbiology*, 167(4), pp. 239–250.

Giraudo, Ana T., Cheung, Ambrose L. and Nagel, Rosa (1997) 'The sae locus of Staphylococcus aureus controls exoprotein synthesis at the transcriptional level', *Archives of Microbiology*, 168(1), pp. 53–58.

Glauner, B., Holtje, J. V. and Schwarz, U. (1988) 'The composition of the murein of Escherichia coli', *Journal of Biological Chemistry*, 263(21), pp. 10088–10095.

Götz, Friedrich, Bannerman, Tammy and Schleifer, Karl-heinz (2006) *The Genera*

Staphylococcus and Macrococcus, *Prokayotes*.

Granick, Steve, Lin, Zhiqun and Bae, Sung Chul (2003) 'Molecules squeezed and stroked', *Nature*, 425(October), pp. 467–468.

Grierson, David S., Liu, Jingjing, Carpick, Robert W. and Turner, Kevin T. (2013) 'Adhesion of nanoscale asperities with power-law profiles', *Journal of the Mechanics and Physics of Solids*. Elsevier, 61(2), pp. 597–610.

Gross, Leo, Mohn, Fabian, Moll, Nikolaj, Liljeroth, Peter and Meyer, Gerhard (2009) 'The Chemical Structure of a Molecule Resolved by Atomic Force Microscopy', *Science*, 325(August), pp. 1110–1114.

Gross, Matthias, Cramton, Sarah E., Götz, Friedrich and Peschel, Andreas (2001) 'Key Role of Teichoic Acid Net Charge in Staphylococcus aureus Colonization of Artificial Surfaces Key Role of Teichoic Acid Net Charge in Staphylococcus aureus Colonization of Artificial Surfaces', *Infection and Immunity*, 69(5), pp. 3423–2426.

Gumbart, James C., Beeby, Morgan, Jensen, Grant J. and Roux, Benoît (2014) 'Escherichia coli Peptidoglycan Structure and Mechanics as Predicted by Atomic-Scale Simulations', *PLoS Computational Biology*, 10(2).

Guz, Nataliia, Dokukin, Maxim, Kalaparthi, Vivekanand and Sokolov, Igor (2014) 'If Cell Mechanics Can Be Described by Elastic Modulus: Study of Different Models and Probes Used in Indentation Experiments', *Biophysical Journal*. Biophysical Society, 107(3), pp. 564–575.

Häberle, W., Hörber, J. K. H., Ohnesorge, F., Smith, D. P. E. and Binnig, G. (1992) 'In situ investigations of single living cells infected by viruses', *Ultramicroscopy*, 42–44, pp. 1161–1167.

Hansma, P. K., Cleveland, J. P., Radmacher, M., Walters, D. a., Hillner, P. E., Bezanilla, M., Fritz, M., Vie, D., Hansma, H. G., Prater, C. B., Massie, J., Fukunaga, L., Gurley, J. and Elings, V. (1994) 'Tapping mode atomic force microscopy in liquids', *Applied Physics Letters*, 64(13), pp. 1738–1740.

Hardiman, M., Vaughan, T. J. and McCarthy, C. T. (2016) 'The effects of pile-up, viscoelasticity and hydrostatic stress on polymer matrix nanoindentation', *Polymer Testing*. Elsevier Ltd, 52, pp. 157–166.

Harris, L. G., Foster, S. J. and Richards, R. G. (2002) 'An introduction to Staphylococcus aureus, and techniques for identifying and quantifying S. aureus adhesisn in relation to adhesion to biomaterials: Review', *European Cells and Materials*, 4, pp. 39–60.

Hayhurst, Emma J., Kailas, Lekshmi, Hobbs, Jamie K. and Foster, Simon J. (2008) 'Cell wall peptidoglycan architecture in Bacillus subtilis.', *Proceedings of the National Academy of Sciences of the United States of America*, 105(38), pp. 14603–8.

Helander, Ilkka M., Alakomi, Hanna Leena, Latva-Kala, Kyösti and Koski, Pertti (1997) 'Polyethyleneimine is an effective permeabilizer of Gram-negative bacteria', *Microbiology*, 143(10), pp. 3193–3199.

Hertz, Heinrich (1882) 'Ueber die Berhürung fester elastischer Körper', *Journal für die Reine und Angewandte Mathematik*, 1882(92), pp. 156–171.

Hocheng, Hong, Chen, Chao Ming, Chou, Yu Chang and Lin, Chien Hung (2010) 'Study of novel electrical routing and integrated packaging on bio-compatible flexible substrates', *Microsystem Technologies*, pp. 423–430.

Holtje, J. V (1998) 'Growth of the stress-bearing and shape-maintaining murein sacculus of Escherichia coli.', *Microbiology and molecular biology reviews*, 62(1), pp. 181–203.

Hoogenboom, Bart and Leung, Carl (2013) 'Probe miniaturisation for improving the resolution of atomic force microscopy for soft samples in liquid', *Microscopy and Analysis*, 27(3), pp. 26–29.

Hooton, Jennifer C., German, Caroline S., Allen, Stephanie, Davies, Martyn C., Roberts, Clive J., Tendler, Saul J. B. and Williams, Philip M. (2004) 'An Atomic Force Microscopy Study of the Effect of Nanoscale Contact Geometry and Surface Chemistry on the Adhesion of Pharmaceutical Particles', *Pharmaceutical Research*, 21(6), pp. 953–961.

Horimizu, Makoto, Kawase, Tomoyuki, Tanaka, Takaaki, Okuda, Kazuhiro, Nagata, Masaki, Burns, Douglas M. and Yoshie, Hiromasa (2013) 'Biomechanical evaluation by AFM of cultured human cell-multilayered periosteal sheets', *Micron*. Elsevier Ltd, 48, pp. 1–10.

Horsburgh, Malcolm J., Aish, Joanne L., White, Ian J., Shaw, Les, Lithgow, James K. and Foster, Simon J. (2002) 'σB modulates virulence determinant expression and stress resistance: Characterization of a functional rsbU strain derived from Staphylococcus aureus

8325-4', *Journal of Bacteriology*, 184(19), pp. 5457–5467.

Hua, Feng, Sun, Yugang, Gaur, Anshu, Meitl, Matthew A., Bilhaut, Lise, Rotkina, Lolita, Wang, Jingfeng, Geil, Phil, Shim, Moonsub, Rogers, John A. and Shim, Anne (2004) 'Polymer imprint lithography with molecular-scale resolution', *Nano Letters*, 4(12), pp. 2467–2471.

Hutter, J. L. (2005) 'Comment on Tilt of Atomic Force Microscope Cantilevers', *Langmuir*, 21, pp. 2630–2632.

Hutter, Jl and Bechhoefer, John (1993) 'Calibration of atomic force microscope tips', *Review of Scientific Instruments*, 64(7), pp. 1868–1873.

Jahed, Zeinab, Shahsavan, Hamed, Verma, Mohit S., Rogowski, Jacob L., Seo, Brandon B., Zhao, Boxin, Tsui, Ting Y., Gu, Frank X. and Mofrad, Mohammad R. K. (2017) 'Bacterial Networks on Hydrophobic Micropillars', *ACS Nano*, 11(1), pp. 675–683.

James, Sean A., Powell, Lydia C. and Wright, Chris J. (2016) 'Atomic Force Microscopy of Biofilms- Imaging, Interactions, and Mechanics', in Dhanasekaran, Dr.Dharumadurai (ed.) *Microbial Biofilms- Interactions and Application*. InTech, pp. 95–118.

Jensen, S. and Lyon, B. (2009) 'Genetics of antimicrobial resistance in Staphylococcus aureus.', *Future Microbiology*, 4(5), pp. 565–582.

Johnson, K. L., Kendall, K. and Roberts, A. D. (1971) 'Surface Energy and the Contact of Elastic Solids', *Proceedings of the Royal Society A: Mathematical, Physical and Engineering Sciences*, 324(1558), pp. 301–313.

Johnston, I. D., McCluskey, D. K., Tan, C. K. L. and Tracey, M. C. (2014) 'Mechanical characterization of bulk Sylgard 184 for microfluidics and microengineering', *Journal of Micromechanics and Microengineering*, 24(3), p. 35017.

JPK Instruments AG (2011) *Quantitative Imaging with the NanoWizard*.

Juárez-Moreno, J. A., Ávila-Ortega, A., Oliva, A. I., Avilés, F. and Cauich-Rodríguez, J. V. (2015) 'Effect of wettability and surface roughness on the adhesion properties of collagen on PDMS films treated by capacitively coupled oxygen plasma', *Applied Surface Science*. Elsevier B.V., 349, pp. 763–773.

Kailas, L., Ratcliffe, E. C., Hayhurst, E. J., Walker, M. G., Foster, S. J. and Hobbs, J. K. (2009) 'Immobilizing live bacteria for AFM imaging of cellular processes', *Ultramicroscopy*, 109(7),

pp. 775–780.

Kailas, Lekshmi, Terry, Cassandra, Abbott, Nicholas, Taylor, Robert, Mullin, Nic, Tzokov, Svetomir B., Todd, Sarah J., Wallace, B. A., Hobbs, Jamie K., Moir, Anne and Bullough, Per A. (2011) 'Surface architecture of endospores of the Bacillus cereus/anthracis/thuringiensis family at the subnanometer scale', *Proceedings of the National Academy of Sciences*, 108(38), pp. 16014–16019.

Kasas, S. and Ikai, A. (1995) 'A method for anchoring round shaped cells for atomic force microscope imaging', *Biophysical Journal*, 68(5), pp. 1678–1680.

Kennedy, Ciara A. and O'Gara, James P. (2004) 'Contribution of culture media and chemical properties of polystyrene tissue culture plates to biofilm development by Staphylococcus aureus', *Journal of Medical Microbiology*, 53(11), pp. 1171–1173.

Khan, A., Philip, J. and Hess, P. (2004) 'Young's modulus of silicon nitride used in scanning force microscope cantilevers', *Journal of Applied Physics*, 95(4).

Khan, Shah Haidar and Hoffmann, Peter Manfred (2016) 'Young's modulus of nanoconfined liquids?', *Journal of Colloid and Interface Science*, 473, pp. 93–99.

Kirkham, Glen R., Britchford, Emily, Upton, Thomas, Ware, James, Gibson, Graham M., Devaud, Yannick, Ehrbar, Martin, Padgett, Miles, Allen, Stephanie, Buttery, Lee D. and Shakesheff, Kevin (2015) 'Precision assembly of complex cellular microenvironments using holographic optical tweezers', *Scientific Reports*, 5, pp. 1–7.

Koch, A. L. (1998) 'Length distribution of the peptidoglycan chains in the sacculus of Escherichia coli.', *Research in Microbiology*, 149, pp. 689–701.

Koseki, Shigenobu and Yamamoto, Kazutaka (2006) 'Recovery of Escherichia coli ATCC 25922 in phosphate buffered saline after treatment with high hydrostatic pressure', *International Journal of Food Microbiology*, 110(1), pp. 108–111.

Krismer, Bernhard, Liebeke, Manuel, Janek, Daniela, Nega, Mulugeta, Rautenberg, Maren, Hornig, Gabriele, Unger, Clemens, Weidenmaier, Christopher, Lalk, Michael and Peschel, Andreas (2014) 'Nutrient Limitation Governs Staphylococcus aureus Metabolism and Niche Adaptation in the Human Nose', *PLoS Pathogens*, 10(1).

Kumar, Sandip, Cartron, Michaël L.Michael L., Mullin, Nic, Qian, Pu, Leggett, Graham J.,

Hunter, Christopher Neil and Hobbs, Jamie Kayne (2017) 'Direct Imaging of Protein Organization in an Intact Bacterial Organelle Using High-Resolution Atomic Force Microscopy', *ACS Nano*, 11(1), p. acsnano.6b05647.

Lanniel, Mathieu, Huq, Ejaz, Allen, Stephanie, Buttery, Lee, Williams, Philip M. and Alexander, Morgan R. (2011) 'Substrate induced differentiation of human mesenchymal stem cells on hydrogels with modified surface chemistry and controlled modulus', *Soft Matter*, 7(14), pp. 6501–6514.

Leckband, Deborah (2000) 'Measuring the forces that control protein interactions', *Annual Review of Biophysics and Biomolecular Structure*, 29, pp. 1–26.

Leclercq, S., De Timary, P., Delzenne, N. M. and Stärkel, P. (2017) 'The link between inflammation, bugs, the intestine and the brain in alcohol dependence', *Translational Psychiatry*, 7(2).

Lecuit, Thomas and Lenne, Pierre-François (2007) 'Cell surface mechanics and the control of cell shape, tissue patterns and morphogenesis.', *Nature reviews. Molecular cell biology*, 8(8), pp. 633–644.

Lee, Timothy K. and Huang, Kerwyn Casey (2013) 'The role of hydrolases in bacterial cell-wall growth', *Current Opinion in Microbiology*. Elsevier Ltd, 16(6), pp. 760–766.

Li, Baikun and Logan, Bruce E. (2004) 'Bacterial adhesion to glass and metal-oxide surfaces', *Colloids and Surfaces B: Biointerfaces*, 36(2), pp. 81–90.

Liao, Ching Hsing and Shollenberger, L. M. (2003) 'Survivability and long-term preservation of bacteria in water and in phosphate-buffered saline', *Letters in Applied Microbiology*, 37(1), pp. 45–50.

Lim, Yong Yee and Chaudhri, M.Munawar (2004) 'Indentation of elastic solids with rigid cones', *Philosophical Magazine*, 84(27), pp. 2877–2903.

Lin, I.Kuan, Liao, Yen Ming, Liu, Yan, Ou, Kuang Shun, Chen, Kuo Shen and Zhang, Xin (2008) 'Viscoelastic mechanical behavior of soft microcantilever-based force sensors', *Applied Physics Letters*, 93(25).

Lipovsky, Anat, Nitzan, Yeshayahu, Friedmann, Harry and Lubart, Rachel (2009) 'Sensitivity of Staphylococcus aureus Strains to Broadband Visible Light', *Photochemistry and*

Photobiology, 85, pp. 255–260.

Liu, Jingjing, Notbohm, Jacob K., Carpick, Robert W. and Turner, Kevin T. (2010) 'Method for characterizing nanoscale wear of atomic force microscope tips', *ACS Nano*, 4(7), pp. 3763–3772.

Liu, Miao, Sun, Jianren, Sun, Ying, Bock, Christopher and Chen, Quanfang (2009) 'Thickness-dependent mechanical properties of polydimethylsiloxane membranes', *Journal of Micromechanics and Microengineering*, 19(3), p. 35028.

Liu, Yu Hsin, Wang, Chih Hung, Wu, Jiunn Jong and Lee, Gwo Bin (2012) 'Rapid detection of live methicillin-resistant Staphylococcus aureus by using an integrated microfluidic system capable of ethidium monoazide pre-treatment and molecular diagnosis', *Biomicrofluidics*, 6(3).

Liu, Zhiguo, Wei, Zhuang, Song, Yonghai, Wang, Li and Sun, Lanlan (2006) 'Manipulation, Dissection, and Lithography Using Modified Tapping Mode Atomic Force Microscope', *Microscopy Research and Technique*, 69, pp. 998–1004.

Longo, Giovanni, Rio, Laura Marques, Trampuz, Andrej, Dietler, Giovanni, Bizzini, Alain and Kasas, Sandor (2013) 'Antibiotic-induced modifications of the stiffness of bacterial membranes', *Journal of Microbiological Methods*. Elsevier B.V., 93(2), pp. 80–84.

Lopera, S. and Mansano, R. D. (2012) 'Plasma-Based Surface Modification of Polydimethylsiloxane for PDMS-PDMS Molding', *ISRN Polymer Science*, 2012, pp. 1–5.

Loskill, Peter, Pereira, Pedro M., Jung, Philipp, Bischoff, Markus, Herrmann, Mathias, Pinho, Mariana G. and Jacobs, Karin (2014) 'Reduction of the peptidoglycan crosslinking causes a decrease in stiffness of the staphylococcus aureus cell envelope', *Biophysical Journal*, 107(5), pp. 1082–1089.

Louise Meyer, Rikke, Zhou, Xingfei, Tang, Lone, Arpanaei, Ayyoob, Kingshott, Peter and Besenbacher, Flemming (2010) 'Immobilisation of living bacteria for AFM imaging under physiological conditions', *Ultramicroscopy*. Elsevier, 110(11), pp. 1349–1357.

Lowy, Franklin D. (2000) 'Is Staphylococcus aureus an intracellular pathogen?', *Trends in Microbiology*, 8(8), pp. 341–343.

Lund, Victoria A., Wacnik, Katarzyna, Turner, Robert D., Cotterell, Bryony E., Walther,

Christa G., Fenn, Samuel J., Grein, Fabian, Wollman, Adam J. M., Leake, Mark C., Olivier, Nicolas, Cadby, Ashley, Jones, Simon and Foster, Simon J. (2018) 'Molecular coordination of Staphylococcus aureus cell division', *eLife*, 7(e32057), pp. 1–31.

Luo, Qing, Kuang, Dongdong, Zhang, Bingyu and Song, Guanbin (2016) 'Cell stiffness determined by atomic force microscopy and its correlation with cell motility', *Biochimica et Biophysica Acta - General Subjects*. Elsevier B.V., 1860(9), pp. 1953–1960.

Magonov, S. N., Elings, V. and Whangbo, M. H. (1997) 'Phase imaging and stiffness in tapping-mode atomic force microscopy', *Surface Science*, pp. L385–L391.

Magonov, Sergei N. and Reneker, Darrell H. (1997) 'Characterization of Polymer Surfaces With Atomic Force Microscopy', *Annual Review of Materials Science*, 27(1), pp. 175–222.

Marchand, David J., Hsiao, Erik and Kim, Seong H. (2013) 'Non-contact AFM imaging in Water using electrically driven cantilever vibration', *Langmuir*, 29(22), pp. 6762–6769.

Martin, Y., Williams, C. C. and Wickramasinghe, H. K. (1987) 'Atomic force microscope-force mapping and profiling on a sub 100-Å scale', *Journal of Applied Physics*, 61(10), pp. 4723–4729.

Matias, V. R. F. and Beveridge, Terry J. (2007) 'Cryo-electron microscopy of cell division in Staphylococcus aureus reveals a mid-zone between nascent cross walls', *Molecular Microbiology*, 64(1), pp. 195–206.

Matias, V. R. F. and Beveridge, Terry J. (2008) 'Lipoteichoic acid is a major component of the Bacillus subtilis periplasm', *Journal of Bacteriology*, 190(22), pp. 7414–7418.

Matias, Valério R. F. and Beveridge, Terry J. (2006) 'Native cell wall organization shown by cryo-electron microscopy confirms the existence of a periplasmic space in Staphylococcus aureus', *Journal of Bacteriology*, 188(3), pp. 1011–1021.

Meincken, M., Berhane, T. A. and Mallon, P. E. (2005) 'Tracking the hydrophobicity recovery of PDMS compounds using the adhesive force determined by AFM force distance measurements', *Polymer*, 46(1), pp. 203–208.

Mendez-Vilas, Antonio, Gallardo-Moreno, Amparo M. and Gonzalez-Martin, M.Luisa (2007) 'Atomic Force Microscopy of Mechanically Trapped Bacterial Cells', *Microscopy and Microanalysis*, 13, pp. 55–64.

Meng, Xianghe, Zhang, Hao, Song, Jianmin, Fan, Xinjian, Sun, Lining and Xie, Hui (2017) 'Broad modulus range nanomechanical mapping by magnetic-drive soft probes', *Nature Communications*. Springer US, 8(1), pp. 1–10.

Mesarovic, S. D. and Fleck, N. A. (1999) 'Spherical indentation of elastic-plastic solids', *Proceedings of the Royal Society A:*, 455(1987), pp. 2707–2728.

Meyer, G. and Amer, N. (1988) 'Novel optical approach to atomic force microscopy', *Applied Physics Letters*, 53(12), pp. 1045–1047.

Micic, Miodrag, Hu, Dehong, Suh, Yung Doug, Newton, Greg, Romine, Margaret and Lu, H.Peter (2004) 'Correlated atomic force microscopy and fluorescence lifetime imaging of live bacterial cells', *Colloids and Surfaces B: Biointerfaces*, 34(4), pp. 205–212.

Mitchell, P. and Moyle, J. (1957) 'Autolytic Release and Osmotic Properties of " Protoplasts " from Staphylococcus aureus', *Journal of general microbiology*, 16, pp. 184–194.

Moffitt, Lee, J. B. and Cluzel, P. (2012a) 'Supplementary Information (SI) The single-cell chemostat: an agarose-based, microfluidic device for high-throughput, single-cell studies of bacteria and bacterial communities', *Lab on a Chip*, 12(8).

Moffitt, Lee, J. B. and Cluzel, P. (2012b) 'The single-cell chemostat: An agarose-based, microfluidic device for high-throughput, single-cell studies of bacteria and bacterial communities', *Lab on a Chip*, 12(8), pp. 1487–1494.

Moormeier, D. E., Bose, J. L., Horswill, A. R. and Bayles, Kenneth W. (2014) 'Temporal and Stochastic Control of Staphylococcus aureus Biofilm Development', *mBio*, 5(5), pp. 1–12.

Moormeier, Derek E. and Bayles, Kenneth W. (2017) 'Staphylococcus aureus biofilm: a complex developmental organism', *Molecular Microbiology*, 104(3), pp. 365–376.

Morita, S., Abe, M., Yokoyama, K. and Sugawara, Y. (2000) 'Defects and their charge imaging on semiconductor surfaces by noncontact atomic force microscopy and spectroscopy', *Journal of Crystal Growth*, 210(1), pp. 408–415.

Müller, Daniel J., Sass, Hans Jürgen, Müller, Shirley A., Büldt, Georg and Engel, Andreas (1999) 'Surface structures of native bacteriorhodopsin depend on the molecular packing arrangement in the membrane.', *Journal of molecular biology*, 285(5), pp. 1903–1909.

Narayanan, Jaaky, Xiong, Jun-Ying and Liu, Xiang-Yang (2006) 'Determination of agarose gel

pore size: Absorbance measurements vis a vis other techniques', *Journal of Physics: Conference Series*, 28, pp. 83–86.

Neumann, Yvonne, Ohlsen, Knut, Donat, Stefanie, Engelmann, Susanne, Kusch, Harald, Albrecht, Dirk, Cartron, Michael, Hurd, Alexander and Foster, Simon J. (2014) 'The effect of skin fatty acids on Staphylococcus aureus', *Archives of Microbiology*, 197(2), pp. 245–267.

Nix, W. D. and Gao, H. J. (1998) 'Indentation size effects in crystalline materials: A law for strain gradient plasticity', *Journal of the Mechanics and Physics of Solids*, 46(3), pp. 411–425.

Notbohm, Jacob, Poon, Benny and Ravichandran, Guruswami (2012) 'Analysis of nanoindentation of soft materials with an atomic force microscope', *Journal of Materials Research*, 27(1), pp. 229–237.

Nourmohammadi, Jhamak, Hajibabaei, Tohid, Amoabediny, Ghassem, Jafari, Seyed Hassan and Salehi-Nik, Nasim (2015) 'Aminosilane layer formation inside the PDMS tubes improves wettability and cytocompatibility of human endothelial cells', *Trends in Biomaterials and Artificial Organs*, 29(2), pp. 123–131.

O'Shea, S. J. and Welland, M. E. (1998) 'Atomic Force Microscopy at Solid−Liquid Interfaces', *Langmuir*, 14(15), pp. 4186–4197.

Oh, Yoo Jin, Cui, Yidan, Kim, Hyunseok, Li, Yinhua, Hinterdorfer, Peter and Park, Sungsu (2012) 'Characterization of curli a production on living bacterial surfaces by scanning probe microscopy', *Biophysical Journal*, 103(8), pp. 1666–1671.

Oliver, W. C. and Pharr, G. M. (1992) 'An improved technique for determining hardness and elastic modulus using load and displacement sensing indentation experiments', *Journal of Materials Research*, 7(6), p. 1564.

Oliver, W. C. and Pharr, G. M. (2004) 'Measurement of hardness and elastic modulus by instrumented indentation: Advances in understanding and refinements to methodology', *Journal of Materials Research*, 19(1), pp. 3–20.

Palchesko, Rachelle N., Zhang, Ling, Sun, Yan and Feinberg, Adam W. (2012) 'Development of Polydimethylsiloxane Substrates with Tunable Elastic Modulus to Study Cell Mechanobiology in Muscle and Nerve', *PLoS ONE*, 7(12).

Paoli, Federico De and Volinsky, Alex A. (2015) 'Obtaining full contact for measuring

polydimethylsiloxane mechanical properties with flat punch nanoindentation', *MethodsX*. Elsevier B.V., 2, pp. 374–378.

Park, Byong Chon, Song, Woon, Hyun Kim, Dal, Lee, Ju-Yeop, Hong, Jaewan and Seung Kim, Jin (2014) 'Cross-sectional atomic force microscope in scanning electron microscope', *Journal of Vacuum Science & Technology B*, 32(6), p. 06FC04.

Patti, Gary J., Sung, Joon Kim and Schaefer, Jacob (2008) 'Characterization of the peptidoglycan of vancomycin-susceptible Enterococcus faecium', *Biochemistry*, 47(32), pp. 8378–8385.

Perry, Christopher C., Weatherly, Monique, Beale, Tiffany and Randriamahefa, Alexandrine (2009) 'Atomic force microscopy study of the antimicrobial activity of aqueous garlic versus ampicillin against Escherichia coli and Staphylococcus aureus', *Journal of the Science of Food and Agriculture*, (December 2008), pp. 958–964.

Pillet, Flavien, Formosa-Dague, Cécile, Baaziz, Houda, Dague, Etienne and Rols, Marie-Pierre (2016) 'Cell wall as a target for bacteria inactivation by pulsed electric fields', *Scientific reports*, 6(19778), pp. 1–8.

Pink, D., Moeller, J., Quinn, B., Jericho, M. and Beveridge, T. (2000) 'On the architecture of the gram-negative bacterial murein sacculus', *Journal of Bacteriology*, 182(20), pp. 5925–5930.

Piruska, Aigars, Nikcevic, Irena, Lee, Se Hwan, Ahn, Chong, Heineman, William R., Limbach, Patrick a and Seliskar, Carl J. (2005) 'The autofluorescence of plastic materials and chips measured under laser irradiation.', *Lab Chip*, 5(12), pp. 1348–1354.

Pobelov, Ilya V, Mohos, Miklós, Yoshida, Koji, Kolivoska, Viliam, Avdic, Amra, Lugstein, Alois, Bertagnolli, Emmerich, Leonhardt, Kelly, Denuault, Guy, Gollas, Bernhard and Wandlowski, Thomas (2013) 'Electrochemical current-sensing atomic force microscopy in conductive solutions.', *Nanotechnology*, 24(11), p. 115501.

Pogoda, Katarzyna, Piktel, Ewelina, Deptuła, Piotr, Savage, Paul B., Lekka, Małgorzata, Bucki, Robert, Deptu, Piotr, Savage, Paul B. and Bucki, Robert (2017) 'Stiffening of bacteria cells as a first manifestation of bactericidal attack', *Micron*, 101(February), pp. 95–102.

Pollitt, Eric J. G., Szkuta, Piotr T., Burns, Nicola and Foster, Simon J. (2018) 'Staphylococcus

aureus infection dynamics', *PLoS Pathogens*, 14(6), pp. 1–27.

Poon, B., Rittel, D. and Ravichandran, G. (2008) 'An analysis of nanoindentation in linearly elastic solids', *International Journal of Solids and Structures*. Elsevier Ltd, 45(24), pp. 6018–6033.

Popov, Valentin L. (2010) *Contact Mechanics and Friction*. Berlin: Springer-Verlag Heidelberg.

Powell, Martin S. and Slater, Nigel K. H. (1982) 'Removal Rates of Bacterial Cells from Glass Surfaces by Fluid Shear', *Biotechnology and Bioengineering*, 24, pp. 2527–2537.

Qian, Zhiyuan, Risan, Jared, Stadnick, Benjamin and McKenna, Gregory B. (2018) 'Apparent depth-dependent modulus and hardness of polymers by nanoindentation: Investigation of surface detection error and pressure effects', *Journal of Polymer Science, Part B: Polymer Physics*, 56(5), pp. 414–428.

Quinn, Roswell (2013) 'Rethinking antibiotic research and development: World War II and the penicillin collaborative', *American Journal of Public Health*, 103(3), pp. 426–434.

Radmacher, M., Cleveland, J. P., Fritz, M., Hansma, H. G. and Hansma, P. K. (1994) 'Mapping interaction forces with the atomic force microscope', *Biophysical Journal*. Elsevier, 66(6), pp. 2159–2165.

Radmacher, M., Cleveland, J. P. and Hansma, P. K. (1995) 'Improvement of thermally Induced bending of cantilevers used for atomic force microscopy', *Scanning*, 17(2), pp. 117–121.

Ramakrishnan, Praveen, Maclean, Michelle, MacGregor, Scott J., Anderson, John G. and Grant, M.Helen (2016) 'Cytotoxic responses to 405 nm light exposure in mammalian and bacterial cells: Involvement of reactive oxygen species', *Toxicology in Vitro*. The Authors, 33, pp. 54–62.

Rea, Kieran, Dinan, Timothy G. and Cryan, John F. (2016) 'The microbiome: A key regulator of stress and neuroinflammation', *Neurobiology of Stress*. The Authors, 4, pp. 23–33.

Rodriguez-Emmenegger, Cesar, Janel, Sébastien, de los Santos Pereira, Andres, Bruns, Michael and Lafont, Frank (2015) 'Quantifying bacterial adhesion on antifouling polymer brushes via single-cell force spectroscopy', *Polym. Chem.* Royal Society of Chemistry, 6(31),

pp. 5740–5751.

Rodríguez, Tomás R. and García, Ricardo (2003) 'Theory of Q control in atomic force microscopy', *Applied Physics Letters*, 82(26), pp. 4821–4823.

Rubin, M. (1985) 'Optical properties of soda lime silica glasses', *Solar Energy Materials*, 12(4), pp. 275–288.

Saar Dover, Ron, Bitler, Arkady, Shimoni, Eyal, Trieu-Cuot, Patrick and Shai, Yechiel (2015) 'Multiparametric AFM reveals turgor-responsive net-like peptidoglycan architecture in live streptococci', *Nature Communications*. Nature Publishing Group, 6(May), p. 7193.

Schanda, Paul, Triboulet, Sebastien, Laguri, Cedric, Bougault, Catherine M., Ayala, Isabel, Callon, Morgane, Arthur, Michel and Simorre, Jean-Pierre (2014) 'Atomic model of a cell-wall cross-linking enzyme in complex with an intact bacterial peptidoglycan', *Journal of the American Chemical Society*.

Schiebener, P., Straub, J., Levelt Sengers, J. M. H. H. and Gallagher, J. S. (1990) 'Refractive index of water and steam as function of wavelength, temperature and density', *Journal of Physical and Chemical Reference Data*, 19(3), pp. 677–717.

Schindelin, Johannes, Arganda-Carreras, Ignacio, Frise, Erwin, Kaynig, Verena, Longair, Mark, Pietzsch, Tobias, Preibisch, Stephan, Rueden, Curtis, Saalfeld, Stephan, Schmid, Benjamin, Tinevez, Jean Yves, White, Daniel James, Hartenstein, Volker, Eliceiri, Kevin, Tomancak, Pavel and Cardona, Albert (2012) 'Fiji: An open-source platform for biological-image analysis', *Nature Methods*, 9(7), pp. 676–682.

Schneider, Florian, Draheim, Jan, Kamberger, Robert and Wallrabe, Ulrike (2009) 'Process and material properties of polydimethylsiloxane (PDMS) for Optical MEMS', *Sensors and Actuators, A: Physical*, 151(2), pp. 95–99.

Schneider, Tanja, Senn, Maria Magdalena, Berger-Bächi, Brigitte, Tossi, Alessandro, Sahl, Hans Georg and Wiedemann, Imke (2004) 'In vitro assembly of a complete, pentaglycine interpeptide bridge containing cell wall precursor (lipid II-Gly5) of Staphylococcus aureus', *Molecular Microbiology*, 53(2), pp. 675–685.

Schoenwald, K., Peng, Z. C., Noga, D., Qiu, S. R. and Sulchek, T. (2010) 'Integration of atomic force microscopy and a microfluidic liquid cell for aqueous imaging and force spectroscopy',

Review of Scientific Instruments, 81(5).

Schrott, Walter, Slouka, Zdeněk, Červenka, Petr, Ston, Jiří, Nebyla, Marek, Přibyl, Michal and Šnita, Dalimil (2009) 'Study on surface properties of PDMS microfluidic chips treated with albumin', *Biomicrofluidics*, 3(4), pp. 1–15.

Senden, Tim J. (2001) 'Force microscopy and surface interactions', *Current Opinion in Colloid & Interface Science*, 6(2), pp. 95–101.

Shen, Yan Xing, Wei, Pal Jen and Lin, Jen Fin (2008) 'Initial and adhesive contact between a diamond indenter and polydimethylsiloxane', *Review of Scientific Instruments*, 79(9), pp. 2006–2009.

Shih, C. W., Yang, M. and Li, J. C. M. (1991) 'Effect of tip radius on nanoindentation', *Journal of Materials Research*, 6(12), pp. 2623–2628.

Silhavy, Thomas J., Kahne, Daniel and Walker, Suzanne (2010) 'The bacterial cell envelope.', *Cold Spring Harbor perspectives in biology*, 2(5), p. a000414.

Sirghi, L. and Rossi, F. (2006) 'Adhesion and elasticity in nanoscale indentation', *Applied Physics Letters*, 89(243118).

Siryaporn, Albert, Kuchma, Sherry L., O'Toole, George A. and Gitai, Zemer (2014) 'Surface attachment induces Pseudomonas aeruginosa virulence', *Proceedings of the National Academy of Sciences*, 111(47), pp. 16860–16865.

Smolyakov, G., Formosa-Dague, C., Severac, C., Duval, R. E. and Dague, E. (2016) 'High speed indentation measures by FV, QI and QNM introduce a new understanding of bionanomechanical experiments', *Micron*. Elsevier Ltd, 85, pp. 8–14.

Sneddon, Ian N. (1948) 'Bousslnesq's Problem for a Rigid Cone', *Mathematical Proceedings of the Cambridge Philoophical Society*, 44(4), pp. 492–507.

Sneddon, Ian N. (1965) 'The relation between load and penetration in the axisymmetric boussinesq problem for a punch of arbitrary profile', *International Journal of Engineering Science*, 3(1), pp. 47–57.

Solopova, Ana, Formosa-Dague, Cécile, Courtin, Pascal, Furlan, Sylviane, Veiga, Patrick, Péchoux, Christine, Armalytė, Julija, Sadauskas, Mikas, Kok, Jan, Hols, Pascal, Dufrêne, Yves F., Kuipers, Oscar P., Chapot-Chartier, Marie-Pierre and Kulakauskas, Saulius (2016)

'Regulation of cell wall plasticity by nucleotide metabolism in Lactococcus lactis', *Journal of Biological Chemistry*, 291(21), pp. 11323–11336.

Strange, Adam P., Aguayo, Sebastian, Ahmed, Tarek, Mordan, Nicola, Stratton, Richard, Porter, Stephen R., Parekh, Susan and Bozec, Laurent (2017) 'Quantitative nanohistological investigation of scleroderma: An atomic force microscopy-based approach to disease characterization', *International Journal of Nanomedicine*, 12, pp. 411–420.

Stukalov, Oleg, Korenevsky, Anton, Beveridge, Terry J. and Dutcher, John R. (2008) 'Use of atomic force microscopy and transmission electron microscopy for correlative studies of bacterial capsules', *Applied and Environmental Microbiology*, 74(17), pp. 5457–5465.

Suo, Zhiyong, Avci, Recep, Deliorman, Muhammedin, Yang, Xinghong and Pascual, David W. (2009) 'Bacteria survive multiple puncturings of their cell walls', *Langmuir*, 25(8), pp. 4588–4594.

Swoboda, Jonathan G., Campbell, Jennifer, Meredith, Timothy C. and Walker, Suzanne (2010) 'Wall Teichoic Acid Function, Biosynthesis, and Inhibition', *Chembiochem.*, 11(1), pp. 35–45.

Takeuchi, Shoji, DiLuzio, Willow R., Weibel, Douglas B. and Whitesides, George M. (2005) 'Controlling the Shape of Filamentous Cells of Escherichia Col', *Nano letters*, 5(9), pp. 1819–1823.

Tamayo, J., Humphris, a D., Owen, R. J. and Miles, M. J. (2001) 'High-Q dynamic force microscopy in liquid and its application to living cells.', *Biophysical journal*. Elsevier, 81(1), pp. 526–537.

Tang, Jun, Guo, Hao, Zhao, Miaomiao, Yang, Jiangtao, Tsoukalas, Dimitris, Zhang, Binzhen, Liu, Jun, Xue, Chenyang and Zhang, Wendong (2015) 'Highly Stretchable Electrodes on Wrinkled Polydimethylsiloxane Substrates', *Scientific Reports*. Nature Publishing Group, 5, pp. 1–9.

Teichert, C., MacKay, J. F., Savage, D. E., Lagally, M. G., Brohl, M. and Wagner, P. (1995) 'Comparison of surface roughness of polished silicon wafers measured by light scattering topography, soft-x-ray scattering, and atomic-force microscopy', *Applied Physics Letters*, 66(18), pp. 2346–2348.

Thwaites, John J. and Mendelson, Neil H. (1991) 'Mechanical Behaviour of Bacterial Cell Walls', *Advances in Microbial Physiology*, 32, pp. 173–222.

Tiller, J. C., Liao, C. J., Lewis, K. and Klibanov, A. M. (2001) 'Designing surfaces that kill bacteria on contact', *Proceedings of the National Academy of Sciences*, 98(11), pp. 5981–5985.

Tipper, D. J., Tomoeda, M. and Strominger, J. L. (1971) 'Isolation and Characterization of β-1,4-N-Acetylmuramyl-N-acetylglucosamine and its O-Acetyl Derivative', *Biochemistry*, 10(25), pp. 4683–4690.

Tipper, Donald J., Katz, Walther, Strominger, Jack L. and Ghuysen, Jean Marie (1967) 'Substituents on the α-Carboxyl Group of D-Glutamic Acid in the Peptidoglycan of Several Bacterial Cell Walls', *Biochemistry*, 6(3), pp. 921–929.

Tortonese, Marco (1997) 'Cantievers and tips for atomic force microscopy', *IEEE engineering in medicine and biology*, (April), pp. 28–33.

Touhami, Ahmed, Jericho, Manfred H. and Beveridge, Terry J. (2004) 'Atomic force microscopy of cell growth and division in Staphylococcus aureus', *Journal of Bacteriology*, 186(11), pp. 3286–3295.

Trott, Gary R. and Shorey, Aric (2011) 'Glass wafer mechanical properties: A comparison to silicon', in *6th International Microsystems, Packaging, Assembly, and Circuits Technology Conference, IMPACT*, pp. 359–362.

Tsai, Long-Fang, Dahlquist, William C., Kim, Seunghyun and Nordin, Gregory P. (2011) 'Bonding of polydimethylsiloxane microfluidics to silicon-based sensors', *Journal of Micro/Nanolithography, MEMS and MOEMS*, 10(4), p. 43009.

Turner, Robert D., Hurd, Alexander F., Cadby, Ashley, Hobbs, Jamie K. and Foster, Simon J. (2013) 'Cell wall elongation mode in Gram-negative bacteria is determined by peptidoglycan architecture.', *Nature communications*. Nature Publishing Group, 4, pp. 1496–1503. Available at: (Accessed: 23 September 2014).

Turner, Robert D., Kirkham, Jennifer, Devine, Deirdre and Thomson, Neil H. (2009) 'Second harmonic atomic force microscopy of living Staphylococcus aureus bacteria', *Applied Physics Letters*, 94(4), pp. 2012–2015. Available at: (Accessed: 15 October 2014).

Turner, Robert D., Ratcliffe, Emma C., Wheeler, Richard, Golestanian, Ramin, Hobbs, Jamie K. and Foster, Simon J. (2010) 'Peptidoglycan architecture can specify division planes in Staphylococcus aureus.', *Nature communications*. Nature Publishing Group, 1(3), p. 26. Available at: (Accessed: 15 October 2014).

Turner, Robert D., Thomson, N. H., Kirkham, J. and Devine, D. (2010) 'Improvement of the pore trapping method to immobilize vital coccoid bacteria for high-resolution AFM: A study of Staphylococcus aureus', *Journal of Microscopy*, 238(2), pp. 102–110.

Turner, Robert D., Vollmer, Waldemar and Foster, Simon J. (2014) 'Different walls for rods and balls: the diversity of peptidoglycan.', *Molecular microbiology*, 91(5), pp. 862–74. Available at: (Accessed: 15 October 2014).

Tuson, Hannah H., Auer, George K., Renner, Lars D., Hasebe, Mariko, Tropini, Carolina, Salick, Max, Crone, Wendy C., Gopinathan, Ajay, Huang, Kerwyn Casey and Weibel, Douglas B. (2012) 'Measuring the stiffness of bacterial cells from growth rates in hydrogels of tunable elasticity', *Molecular Microbiology*, 84(5), pp. 874–891.

Typas, Athanasios, Banzhaf, Manuel, Gross, Carol A. and Vollmer, Waldemar (2012) 'From the regulation of peptidoglycan synthesis to bacterial growth and morphology', *Nature Reviews Microbiology*. Nature Publishing Group, 10(2), pp. 123–136.

Vadillo-Rodriguez, Virginia, Beveridge, Terry J. and Dutcher, John R. (2008) 'Surface viscoelasticity of individual gram-negative bacterial cells measured using atomic force microscopy', *Journal of Bacteriology*, 190(12), pp. 4225–4232.

Vahdat, Vahid, Grierson, David S., Turner, Kevin T. and Carpick, Robert W. (2013) 'Mechanics of Interaction and Atomic- Scale Wear of Amplitude Modulation Atomic Force Microscopy Probes', *Acs Nano*, 7(4), pp. 3221–3235.

Van Vliet, Krystyn J., Prchlik, Lubos and Smith, James F. (2004) 'Direct measurement of indentation frame compliance', *Journal of Materials Research*, 19(1), pp. 325–331.

Vollmer, Waldemar, Blanot, Didier and de Pedro, Miguel a (2008) 'Peptidoglycan structure and architecture.', *FEMS microbiology reviews*, 32(2), pp. 149–67. Available at: (Accessed: 6 August 2014).

Vollmer, Waldemar and Seligman, Stephen J. (2010) 'Architecture of peptidoglycan: more

data and more models', *Trends in Microbiology*, 18(2), pp. 59–66.

Vorselen, Daan, Kooreman, Ernst S., Wuite, Gijs J. L. and Roos, Wouter H. (2016) 'Controlled tip wear on high roughness surfaces yields gradual broadening and rounding of cantilever tips', *Scientific Reports*. Nature Publishing Group, 6(July), pp. 1–7.

Wang, Ping, Robert, Lydia, Pelletier, James, Dang, Wei Lien, Taddei, Francois, Wright, Andrew and Jun, Suckjoon (2010) 'Robust growth of escherichia coli', *Current Biology*. Elsevier Ltd, 20(12), pp. 1099–1103.

Wang, Zhixin, Volinsky, Alex A. and Gallant, Nathan D. (2015) 'Nanoindentation study of polydimethylsiloxane elastic modulus using berkovich and flat punch tips', *Journal of Applied Polymer Science*, 132(5), pp. 1–7.

Wheeler, Richard, Turner, Robert D., Bailey, Richard G., Salamaga, Bartłomiej, Mesnage, Stéphane, Mohamad, Sharifah A. S., Hayhurst, Emma J., Horsburgh, Malcolm, Hobbs, Jamie K. and Foster, Simon J. (2015) 'Bacterial Cell Enlargement Requires Control of Cell Wall Stiffness Mediated by Peptidoglycan Hydrolases', *The American society for microbiology*, 6(4), pp. 1–10.

White, C. C., Vanlandingham, M. R., Drzal, P. L., Chang, N. K. and Chang, S. H. (2005) 'Viscoelastic characterization of polymers using instrumented indentation. II. Dynamic testing', *Journal of Polymer Science, Part B: Polymer Physics*, 43(14), pp. 1812–1824.

Wolansky, Gershon and Marmur, Abraham (1999) 'Apparent contact angles on rough surfaces: The Wenzel equation revisited', *Colloids and Surfaces A: Physicochemical and Engineering Aspects*, 156(1–3), pp. 381–388.

Workman, R. K. and Manne, S. (2000) 'Variable temperature fluid stage for atomic force microscopy', *Review of Scientific Instruments*, 71(2), pp. 431–436.

Wu, Julie A., Kusuma, Caroline, Mond, James J. and Kokai-Kun, John F. (2003) 'Lysostaphin Disrupts Staphylococcus aureus and Staphylococcus epidermidis Biofilms on Artificial Surfaces', *Antimicrobial Agents and Chemotherapy*, 47(11), pp. 3407–3414.

Wu, Ling Juan and Errington, Jeff (2012) 'Nucleoid occlusion and bacterial cell division', *Nature Reviews Microbiology*. Nature Publishing Group, 10(1), pp. 8–12.

Xu, Wentao, Boquan, Li, Fujimoto, Toshiyuki and Kojima, Isao (2001) 'Suppressing the

surface roughness and columnar growth of silicon nitride films', *Surface and Coatings Technology*, 135, pp. 274–278.

Xue, Bo, Yan, Yongda, Hu, Zhenjiang and Zhao, Xuesen (2014) 'Study on effects of scan parameters on the image quality and tip wear in AFM tapping mode', *Scanning*, 36(2), pp. 263–269.

Yamada, Shinji (2003) 'Layering transitions and tribology of molecularly thin films of poly(dimethylsiloxane)', *Langmuir*, 19(18), pp. 7399–7405.

Yao, X., Jericho, M., Pink, D. and Beveridge, T. (1999) 'Thickness and Elasticity of Gram-Negative Murein Sacculi Measured by Atomic Force Microscopy Thickness and Elasticity of Gram-Negative Murein Sacculi Measured by Atomic Force Microscopy', *Journal of Bacteriology*, 181(22), pp. 6865–6875.

Yao, X., Walter, J., Burke, S., Stewart, S., Jericho, M. H., Pink, D., Hunter, R. and Beveridge, T. J. (2002) 'Atomic force microscopy and theoretical considerations of surface properties and turgor pressures of bacteria', *Colloids and Surfaces B: Biointerfaces*, 23, pp. 213–230.

Yu, Dongmei, Zhao, Yunhui, Li, Hui, Qi, Hengzhi, Li, Bo and Yuan, Xiaoyan (2013) 'Preparation and evaluation of hydrophobic surfaces of polyacrylate- polydimethylsiloxane copolymers for anti-icing', *Progress in Organic Coatings*, 76(10), pp. 1435–1444.

Zhong, Q., Inniss, D., Kjoller, K., Elings, V. B., Innuss, D., Kjoller, K. and Elings, V. B. (1993) 'Fractured polymer/silica fiber surface studied by tapping mode atomic force microscopy', *Surface Science*, 290(1–2), pp. L688–L692.

Zhou, Jinwen, Khodakov, Dmitriy A., Ellis, Amanda V. and Voelcker, Nicolas H. (2012) 'Surface modification for PDMS-based microfluidic devices', *Electrophoresis*, 33(1), pp. 89–104.

Zhou, Xiaoxue, Halladin, David K., Rojas, Enrique R., Koslover, Elena F., Lee, Timothy K., Huang, Kerwyn Casey and Theriot, Julie A. (2015) 'Mechanical crack propagation drives millisecond daughter cell separation in Staphylococcus aureus', *Science*, 348(6234), pp. 574–578.